Fixed Structure Methods for Flight Control Analysis and Automated Gain Scheduling

by

Piero Miotto

Laurea in Aeronautics and Astronautics
University of Rome "La Sapienza", 1987

SUBMITTED TO THE DEPARTMENT OF AERONAUTICS AND ASTRONAUTICS
IN PARTIAL FULFILLMENT OF THE REQUIREMENTS FOR THE DEGREE OF

DOCTOR OF PHILOSOPHY

AT THE

MASSACHUSETTS INSTITUTE OF TECHNOLOGY

JUNE 1997

Signature of Author _____
Department of Aeronautics and Astronautics
May 29, 1997

Certified by _____
James D. Paduano
Associate Professor of Aeronautics and Astronautics
Thesis Supervisor

Certified by _____
John J. Deyst
Professor of Aeronautics and Astronautics

Certified by _____
Eric Feron
Assistant Professor of Aeronautics and Astronautics

Certified by _____
Walter M. Hollister
Professor of Aeronautics and Astronautics

Authorized by _____
Jaime Peraire
Associate Professor of Aeronautics and Astronautics
Chair, Graduate Office

This page intentionally left blank.

Fixed Structure Methods for Flight Control Analysis and Automated Gain Scheduling

by

Piero Miotto

Submitted to the Department of Aeronautics and Astronautics
on May 29, 1997 in partial fulfillment of the requirements for the
degree of Doctor of Philosophy

Abstract

Flight control law validation issues raised at NASA Dryden Flight Research Center are described, and these problems are recast into the real-μ analysis framework. To solve these problems, a recently developed algorithm for computing real-μ is extended to include repeated real perturbations. Worst-case direction information also is provided; such information is useful in applications that require proper weighting of the perturbation block structure. An iterative weighting procedure that indicates the relative importance of the real uncertainties being analyzed is described. Other developments motivated by flight-test issues are also described: block structures for analyzing phase margin and transport delay, robustly guaranteed gain and phase margins, and in-flight robustness measurements. These tools and techniques are demonstrated on the X-31 flight control laws.

The problem of gain adjustment in an existing control law is cast into the framework of modern control theory, which results in a real-diagonal block structure of gains and time constants to be adjusted. The desire to recover performance in the form of input-output properties, as well as handling qualities, is introduced as a mixed cost functional. Linear Matrix Inequality (LMI) based solutions for H_∞ and H_2 based costs are discussed, as well as a Quasi-Newton approach. The handling qualities of the F/A-18 HARV during refueling serves as a motivating example for the method. Eight gains in the existing flight control system are adjusted to recover the performance and handling qualities of the standard F/A-18. The eight gains are gain scheduled against dynamic and static pressure throughout the flight envelope. The functional dependence of these gains on the scheduling parameters results in the definition of 39 coefficients. A Fixed-Structure Linear Parameter Varying (LPV) synthesis method is used to gain schedule the longitudinal and lateral-directional control augmentation system of the F/A-18. The goal is to retune the control law so that it could be used as the Control Augmentation System (CAS) for the F/A-18 HARV, which has much different dynamics. The example illustrates how modern methods can be used to improve both the handling qualities and the input-output characteristics of an existing control system, and to do so automatically over a wide range of operating. Automated tuning of the gain schedule is achieved via optimization over a large region of the flight envelope. The presented approach is systematic and emphasizes the reuse of conceptual structures and architecture. The CAS with the new gains was implement on the fixed base NASA Dryden flight simulator. Several tracking maneuvers were performed by six different pilots on the flight simulator. The fine tracking performance of the F/A-18 HARV with the new gain schedule received a Cooper-Harper (CH) rating identical to that of the standard F/A-18 HARV.

Thesis Supervisor: James Donald Paduano
Title: Associate Professor of Aeronautics and Astronautics

This page intentionally left blank.

Acknowledgments

The submission of this thesis puts an end to my formal education, a task which has taken most of my life and that I will never consider completed.

I acknowledge Professor James D. Paduano for the large part he has played in the course of the research culminating in this thesis. Thank you Jim for your guidance and for providing the "Big Picture" perspective of this work; for your unbending trust and kind encouragement at all the times; for your friendship and financial support. I would like to thank Professor Eric Feron for his ideas and the "Mathematical Sights" in this work. I benefited greatly from the stimulating discussions we had. Special thanks also go to the other members of my Doctoral Committee: Professor John Deyst and Professor Walter Hollister.

My sincerest appreciation goes to John Burken and to all the members of the NASA Dryden Flight Research Center. I very much enjoyed being there the last three summers. In particular I would like to acknowledge Patrick Stoliker, Joseph Pahle, John Bosworth, Lothar Juraschka, Marlin Pickett, and Ken Norlin. Their interest and enthusiasm really made this project possible. I also want to thank the pilots who spent hours with me in the flight simulator: Charles Fullerton, Thomas Mc Murtry, Dana Purifoy, Rogers Smith, and Marc Stucky.

The folks in the Instrumentation, Control, and Estimation Laboratory deserve my thanks and gratitude. Thanks to my fellow graduate students for providing ideas and most importantly diversions from thesis work. It was a pleasure to share the office with many of you: Jerry Wohletz, Laurent Duchesne, Marc Shewchun, and Karen Gondoly. During my four years at MIT I had the opportunity to interact with many other students and I would like to acknowledge them for their ideas and expertise on a wide range of topics.

Above all I thank my wife Andreola. You have been an endless source of strength, tenacity, and attentions (when not too stressed in writing your own dissertation!). Many thanks to my cat Macchia who inspired me while sleeping long hours on top of my thesis. My thoughts are now for my parents and parents in law Mary, Oscar, Paola, and Paolo; your are an endless source of support and love. I couldn't have done it without all of you.

This page intentionally left blank.

Table of Contents

List of Figures

List of Tables

Acronyms

CAS	Control Augmentation System
CH	Cooper Harper
FCL	Flight Control Law
HARV	High Alpha Research Vehicle
HQ	Handling Quality
LPV	Linear Parameter Varying
LQG	Linear Quadratic Gaussian
LQR	Linear Quadratic Regulator
LMI	Linear Matrix Inequality
MIMO	Multi Input Multi Output
PIO	Pilot Induced Oscillations
PMP	Pitch Multiple Pulses
PSP	Pitch Single Pulse
SRA	System Research Aircraft
PI	Proportional and Integral
NS	Neal Smith criteria for Handling Qualities
SISO	Single Input Single Output
TF	Transfer Function

Symbols

Variable	Symbol	Description	Units
PK15		Pitch stick proportional gain	
PK16		Normal acceleration, n_z, proportional gain	
PK18		Pitch rate proportional gain	
RK5		Lateral stick gain	
RK6		Roll rate feedback gain	
YK13		Lateral acceleration gain	
YK17		Yaw rate feedback gain	
YK19		Pedal gain increment	
psf		Pound Square Feet	
QC		Impact pressure	psf
PS		Static pressure	psf
RI		Impact to static pressure ratio	
H	h	Altitude	ft
P	p	Roll rate	ft/sec
Q	q	Pitch rate	ft/sec
R	r	Yaw rate	ft/sec
PHI	ϕ	Bank angle	rad/sec
THETA	θ	Pitch angle	rad/sec
PSI	ψ	Heading angle	rad/sec
UB	u	X body axis velocity	ft/sec
VB	v	Y body axis velocity	ft/sec
WB	w	Z body axis velocity	ft/sec
NZ	n_z	Normal acceleration	g
DAP	dap	Pilot roll stick input	in
DEP	dep	Pilot pitch stick input	in
DRP	drp	Pilot rudder input	pounds
DLEFL	δ_{Ll}	Left leading edge position	deg
DLEFR	δ_{Lr}	Right leading edge position	deg
DTEFL	δ_{Tl}	Left trailing edge position	deg
DTEFR	δ_{Tr}	Right trailing edge position	deg
DLHTD	δ_{Hl}	Left stabilator position	deg
DRHTD	δ_{Hr}	Right stabilator position	deg
DLAD	δ_{Al}	Left aileron position	deg
DRAD	δ_{Ar}	Right aileron position	deg
DRUDL	δ_{Rl}	Left rudder position	deg
DRUDR	δ_{Rr}	Right rudder position	deg

Variable	Symbol	Description	Units
DLEFD	δ_{Ls}	Symmetric leading edge position $(\delta_{Ll} + \delta_{Lr})/2$	deg
DTEFD	δ_{Ts}	Symmetric trailing edge position $(\delta_{Tl} + \delta_{Tr})/2$	deg
DHTD	δ_{Hs}	Symmetric stabilator position $(\delta_{Hl} + \delta_{Ar})/2$	deg
DAD	δ_{Ad}	Differential aileron position $(\delta_{Al} - \delta_{Ar})$	deg
DDLEF	δ_{Ld}	Differential leading edge position $(\delta_{Ll} - \delta_{Lr})$	deg
DTEFDI	δ_{Td}	Differential trailing edge position $(\delta_{Tl} - \delta_{Tr})$	deg
DDTD	δ_{Hd}	Differential stabilator position $(\delta_{Hl} - \delta_{Hr})$	deg
VLEFL		Left leading edge command	deg
VLEFR		Right leading edge command0	deg
VTEFL		Left trailing edge command	deg
VTEFR		Right trailing edge command	deg
VCASHTL		Left stabilator command	deg
VCASHTR		Right stabilator command	deg
VCASAIL		Left aileron command	deg
VCASAIR		Right aileron command	deg
VCASRDL		Left rudder command	deg
VCASRDR		Right rudder command	deg
VLED		Differential leading edge command	deg
VTED		Differential trailing edge command	deg
VCASHTD		Differential stabilator command	deg

This page intentionally left blank

Chapter 1

Introduction

Modern control theory can be divided into two main branches: analysis and synthesis. Analysis deals with the performance and robustness of an existing control law while synthesis deals with the design of control laws that meet specified requirements of performance and robustness. In this thesis we will consider some of the major problems arising in flight control law design and analysis. Our goal is to develop low level tools based on modern control theory, to help control engineers face current problems, such as stability and robustness of multivariable systems, gain scheduling, and design of fixed structure controllers.

For this reason the thesis is divided in two major parts; the first dedicated to flight control law analysis and verification, and the second to flight control law design. In the next two sections a brief description of the main aspects of these two parts is given.

1.1 Controller Analysis: low level tools for engineers

Recent years have seen the steady maturation of real-μ and mixed-μ as a framework for analyzing the robustness of multivariable control systems, as well as algorithms for computing upper and lower bounds for μ [Ref.1-1, Ref.1-2, and Ref.1-3]. The primary application of the methodology is often considered to be design: once algorithms are in place to reliably and efficiently compute μ, they are folded into a synthesis procedure which attempts to define a controller that minimizes its maximum value [Ref.1-4].

The application considered in this thesis will be fundamentally different. In a flight test and control law validation environment, such as NASA Dryden, robustness characterization is an end in itself: given a complex flight control system and a nonlinear model of the flight dynamics, determine *what can go wrong* in flight, during maneuvers, or at the next flight point in an envelope expansion. The problems which must be dealt with in

this environment often involve delays, nonlinearities, actuator position and/or rate saturation, mode switching pathologies, handling qualities, and pilot/cockpit interactions. The goal of the thesis will be to address some of these problems, by recasting them in the real-μ framework [Ref.1-5 and Ref.1-6].

Specifically this thesis will address questions like:

- How can we iteratively select the weighting, so that the parameters that are most important for the stability of the system are made apparent?
- How can phase and transport delay be included in the real-μ robustness problem?
- How can robustness to several aerodynamic parameters be characterized in a way which is useful to flight test engineers?
- How ca a measure of multivariable robustness be derived during a flight test and presented in the control room?

We have developed a set of algorithms which are explicitly aimed at solving the problems described above. These tools have properties that we feel will make them useful to the practicing engineer: they are straight-forward to use in the context of flight control design, they are sufficiently low level and versatile enough to be incorporated into various analysis scenarios, and the results are easily interpreted as standard engineering measures.

Admittedly, these problems constitute only a narrow subset of the issues faced during flight test and control law validation. However, these relatively simple questions are important application issues which must be addressed before even the most rudimentary implementation of structured singular value analysis is attempted.

1.2 Controller Synthesis

In the last two decades, control theory has evolved in an unprecedented manner, and various attractive design approaches have been conceived. Unfortunately a large gap between theory and practice has emerged. There are only few examples of modern control theory

applied to real flight control systems. In this section we will first describe the current control law design practice and how it translates into a lack of acceptance of modern control theory, and then we will introduce an alternative approach whose goal is to reduce the gap between some of the theories and practice.

In order to achieve the highest level of aircraft performance, modern fighters utilize multiple actuation devices — such as aerodynamic surfaces, thrust vectoring, and pneumatic vectoring — and different sensors for attitude determination. Even as aircraft become more and more sophisticated in their physical layout, the ever-present drive for simplicity in control system design remains, and possibly becomes stronger. Simplicity not only results in reduced hardware (which means cheaper, lighter, and less voluminous control system), but also allows control engineers to understand the physical interpretation of the control law and adapt the controller to changes in the aircraft or in the environment it has to operate — we call this property maintainability. The aircraft design process is a highly iterative process, and the aircraft's configuration goes through several major changes during the development phase and some minor changes during the operative phase. As a result, the flight control system is often redesigned and tuned with changes in the aircraft's configuration: this redesign is enabled by the simplicity and accessibility of current control law designs. It is a matter of fact that minor changes late in the development or when the aircraft is already operative can be very expensive.

Simplicity in the control law design must be balanced with the desire to achieve ever increasing performance levels, and to do so over expanded flight envelopes (especially in terms of angle of attack), where the aircraft dynamics are highly nonlinear. Specialized gain scheduling schemes (including blends, and switches) constitute the most common design approach used to capture the nonlinear behavior of the airplane and insure high performance levels. The design process involves obtaining a set of linear plants for a set of values of the scheduling parameters, designing controllers for each of these points, and then linearly interpolating the linear controllers to cover the whole flight envelope.

The SISO classical control design approach naturally gives rise to control laws that have a well defined structure and are suitable for gain scheduling. For this reason, gain scheduling of classical SISO designs has been the most common approach to flight control law design. Unfortunately there is very little in the way of a theoretical foundation for scheduling. There is a lack of tests which can be applied to guarantee stability of the scheduled system. Stability and performance analyses rely on point-by-point analysis and extensive time-simulations, that make the engineer confident but do not guarantee anything (see Ref.1-7 and Ref.1-8).

The process of tuning a flight control system is thus extremely long and expensive, especially as the inherent complexity of the control system increases. Several gains and filters may need to be simultaneously adjusted for best performance; this translates into a multivariable optimization even when the system is originally classically designed. In order to reduce the design cost and time, we aim in this research for a rigorous and automated approach to controller design that addresses tuning, gain scheduling, accessibility, and maintainability, as described above.

MIMO modern control theory addresses a completely different set of issues than those described above. Typically these procedures are concerned with robustness, multivariable synthesis, and automation (i.e. creating an optimized point design automatically). To address these concerns, unfortunately, design methods such as LQG, H_∞, LPV, Dynamic Inversion, and feedback linearization rely on extremely complex control laws, requiring a large number of calculations for a large number of parameters, which conflicts with the essential need of simplicity, accessibility, and maintainability. For instance these systems are not well suited for gain scheduling, because of the large number of parameters that are re-optimized at every design point, and the fact that the control law itself is not sufficiently constrained. Thus controllers can change dramatically between nearby flight points, and switching between control laws presents serious problems. Clearly what is needed is an approach which marries the automation capabilities of modern control design methodologies and the practicality of current flight control design practice.

The concept of automated gain scheduling is not new. What we hope to provide here is a procedure in which both the control law and the design goal (for instance, the target performance) are more highly constrained by the flight control engineer, and which is flexible and modular enough to be incorporated into existing practice. These are the goals that set the desired procedure apart from, for instance, LPV, optimal control based approaches, and previous attempts to fixed-structure control law design.

In Fig. 1-1, a specific road map for flight vehicle modeling and control law validation is illustrated. Flying and handling qualities requirements are the starting point of the design process; as a result they can be defined as a measure of the ease with which the pilot can carry out specific tasks. With full-authority augmentation systems, the flying qualities of the aircraft can be adapted as the operating envelope is traversed and as the mission task is changed. Thus the controller's task is to achieve acceptable performance throughout the flight envelope.

The most common approach is to design a set of linear controllers on linearizations of the plant for a set of values of the key parameters (altitude, Mach number, dynamic pressure, static pressure, angle of attack, and sideslip angle) which covers the operating envelope. Based on this approach, some controller blending scheme must be implemented as the flight envelope is traversed. Control switching and control scheduling are subject to particularly tough design specifications; pilots desire a highly predictable response from the controlled aircraft, and any perceivable transient effect on actuators or aircraft states will be considered unacceptable. Regarding this particular aspect the military specification MIL-8785-C states that:

> *The transient motions and trim changes resulting from the intentional engagement or disengagement of any portion of the primary flight control system by the pilot shall be such that dangerous flying qualities never result. ..... With the controls free, the transients shall not exceed ±0.1 g normal or lateral acceleration at the pilot's station, and ±3 degrees per second roll.*

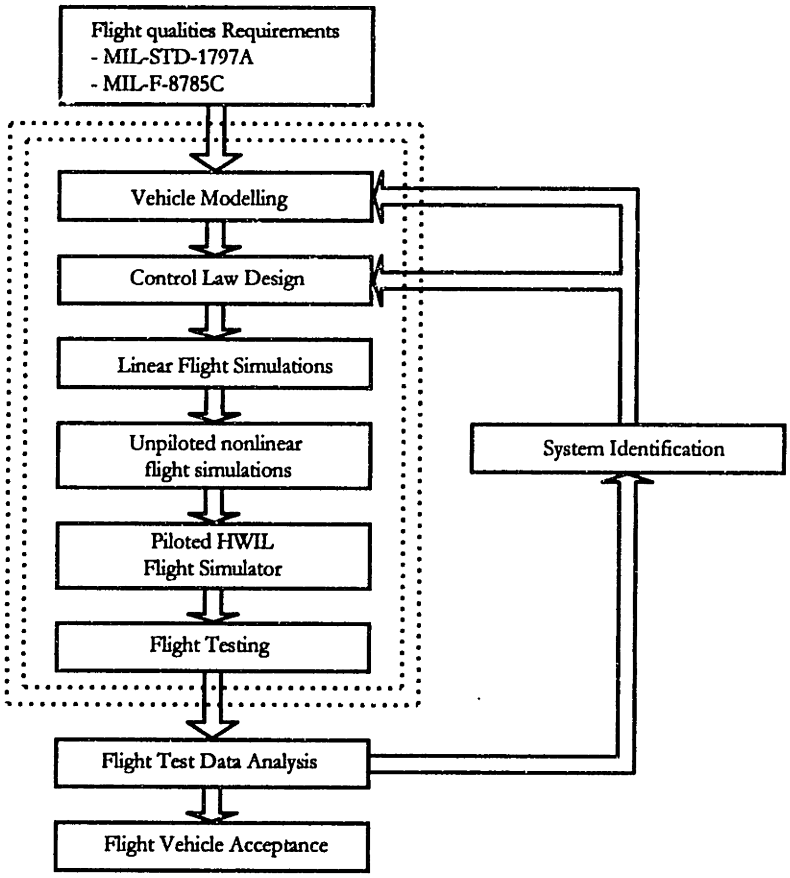

Fig. 1-1 Aircraft Modeling and Flight Control Law Validation

The scope of this thesis will be to define a control methodology that meets the requirements of simplicity, maintainability, controller scheduling, and controller switching. Stability will also be guaranteed throughout the entire flight envelope.

The first two objectives — simplicity and maintainability — will be achieved by considering a fixed structure flight control. This means that only the parameters (gains, time constants, etc.) in a pre-specified control structure will be allowed to change. Conventional controllers, of the type we will consider, have been successfully used for many years in flight control systems and they still often perform as well as very complicated controllers (H_∞ and dynamic inversion based control laws) and they are very well suited for gain scheduling. H_∞ controllers in general do not have such an explicit structure and scheduling still represents a problem.

The second objective — controller scheduling — will be accomplished by predefining the dependence of the controller gains on the key parameters which capture the nonlinear behavior of the system. In this way smoothness of the control law when traversing the flight envelope will be a built in feature. We will also recast this gain scheduling technique in the general framework of LPV theory, giving to the methodology that theoretical foundation that has long been missing.

1.3 References

Ref.1-1 Young P. M., and Doyle J. C., "Computation of μ with Real and Complex Uncertainties," *Proceedings of the 29th IEEE Conference on Decision and Control* (Honolulu, HI), Inst. of Electrical and Electronics Engineers, New York, 1990, pp. 1230-1235.

Ref.1-2 Sideris A., and Sanchez Peña R. S., "Fast computation of the Multivariable Stability Margin for Real Interrelated Uncertain Parameters," *Proceedings of the American Control Conference* (Atlanta, GA), Inst. of Electrical and Electronics Engineers, New York, 1988, pp. 1483-1488.

Ref.1-3 Dailey R. L., "A New Algorithm for the Real Structured Singular Value," *Proceedings of the American Control Conference* (San Diego, CA), Inst. of Electrical and Electronics Engineers, New York, 1990 pp. 3036-3040.

Ref.1-4 Balas G. J., Doyle J. C., Glover K., Packard A., and Smith R., *μ-Analysis and Synthesis Toolbox*, MuSyn Inc., Minneapolis, MN, 1991.

Ref.1-5 Morton B. G., and McAfoos R. M., "A μ Test for Robustness Analysis of a Real Parameter Variation Problem," *Proceedings of the American Control Conference* (Boston, MA), Inst. of Electrical and Electronics Engineers, New York, 1985 pp. 135-138.

Ref.1-6 J.D. Paduano and D.R. Dowing, "Sensitivity Analysis of Digital Flight Control Systems Using Singular Values Concepts", *Journal of Guidance, Control, and Dynamics*, Vol. 12, No. 3, May 1984.

Ref.1-7 J.S. Shamma and M. Athans, "Analysis of gain scheduled control of nonlinear plants", IEEE Transactions on Automatic Control, Vol. 35, No. 8, 1990, pp. 898-907.

Ref.1-8 J.S. Shamma and M. Athans, "Gain scheduling: Potential hazards and possible remedies", *IEEE Control System Mag.*, Vol. 12, No. 3, 1992, pp. 101-107.

This page intentionally left blank.

Chapter 2

Robustness Measures via Real Structured Singular Values

2.1 Introduction

At the beginning of the 80' Doyle and Safonov introduced the notion of Structured Uncertainties as a framework for analyzing the robustness of multivariable control systems (Ref.2-1, Ref.2-2, Ref.2-3, and Ref.2-4). Doyle and Young then extended the concept of structured uncertainties and defined the real structured singular value μ. Since the definition of μ succinctly captures practically motivated robustness questions, much of the recent literature has concentrated on methods for computing tight bounds while reducing computation time (Ref.2-5, Ref.2-6, Ref.2-9, Ref.2-10, Ref.2-11, Ref.2-12, and Ref.2-13). In this chapter we present a method to calculate a lower bound of the real-μ that has the valuable property of identifying the direction of the worst case perturbation. Once the element or the elements that strike the stability boundary are identified an iterative weighting procedure is then used to maximize the size of the stable hypercube.

The approach that will be used is to develop methods to answer specific questions raised during the analysis of the flight control laws of the X-31 Enhanced Fighter Maneuverability Demonstrator. These methods form building blocks for analysis of more complex robustness questions. The X-31 lateral-directional flight control system will be used to motivate the analyses and demonstrate the procedures.

This chapter is organized as follows: the definition of the robustness problem is first given, and Dailey's algorithm for computing a lower bound of real-μ is described and extended to the repeated-real case. Then the issue of iterative weighting is discussed and an illustrative example is used to highlight the importance of iteratively re-weighting for detailed

robustness analysis. Next, block structures are developed that allow phase and delay to be included as part of the real-μ problem. These block structures become part of a second example, where we use the concept of "robustly guaranteed" gain and phase margin as a bridge between classical robustness measures and the modern techniques used here. Finally, we briefly describe the methods used to include flight test information in the analysis problem, and show how an experimental μ-plot might be useful as part of flight test envelope expansion procedures.

2.2 Stability Robustness Analysis With Iterative Weighting Procedure

The notation that will be used is fairly standard. Superscript * denotes the complex conjugate transpose of a complex matrix M, a $k \times k$ identity matrix is denoted by I_k, and the largest singular value is denoted by $\bar{\sigma}(M)$.

The first step in the real-μ analysis is to transform the problem into the interconnection structure of Fig. 2-1, in which $M(s)$ represents the nominal closed loop dynamics, and all perturbations are captured in the structured uncertainty Δ.

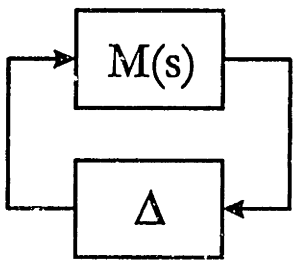

Fig. 2-1 The standard robustness problem.

The matrix $M(j\omega)$ is defined at each frequency ω with $M(j\omega) \in C^{n \times n}$. The structured uncertainty Δ is composed by m diagonal blocks, with $m \leq n$. The block structure $K(m)$ is a set of positive integers

$$K(m) = (k_1, k_2, \ldots, k_m)$$

that specifies the dimensions of the perturbation blocks (these dimensions must sum to n for compatibility with M).

The set of all allowable perturbations then is defined as

$$X_K = \left\{ \Delta : \Delta = \text{block diag}\left(\delta_1 I_{k_1}, \delta_2 I_{k_2}, \delta_3 I_{k_3}, \ldots, \delta_m I_{k_m} \right) \right\}$$

If the dimensions k_i is different from 1 for some i, $k_i \neq 1$, we say that we have 'repeated real' uncertainties in Δ. If $k_i = 1 \ \forall i$, then a conceptually simpler uncertainty structure exists (see sections 2.3.1 and 2.3.2).

The size of the smallest destabilizing perturbation in X_K is characterize by calculating $\mu_K(M)$ at each frequency where μ_K is defined below.

Definition 1. The structured singular value $\mu_K(M)$ of a matrix $M(j\omega) \in C^{n \times n}$ with respect to a block structure $K(m)$ is defined as

$$\mu_K(M) = \left\{ \min_{\Delta \in X_K} \left[\bar{\sigma}(\Delta) : \det(I - \Delta M) = 0 \right] \right\}^{-1}$$

with $\mu_K(M) = 0$ if no $\Delta \in X_K$ solves $\det(I - \Delta M) = 0$.

The preceding definition if applied to our set of allowable perturbations X_K, can be simplified. In this case the 2-norm $\|\Delta\| = \bar{\sigma}(\Delta)$ is identical to the norm

$$\max_{i=1\ldots m} |\delta_i|$$

which is more easily interpreted in applications. Because the size of Δ is often of interest, it is convenient to define $K_\mu = \mu_K^{-1}$. Thus the size of the smallest Δ (where size is defined in terms of the preceding norms) that destabilizes the system in Fig. 2-1 is by definition K_μ. The next statements follow in a straightforward manner:

1) The system in Fig. 2-1 is stable for all $\Delta \in X_K$ such that

$$\max_{i=1\ldots m} |\delta_i| < K_\mu$$

This inequality defines a hypercube of perturbations for which the system is guaranteed to remain stable.

2) If a weighting matrix $W(j\omega)$ is introduced as in Fig.2-2, the resulting system is stable for all $\Delta \in X_K$ with $\|\Delta\| < 1$ if and only if

$$\mu_K[W(j\omega)M(j\omega)] < 1 \qquad \forall \omega \in (0,\infty)$$

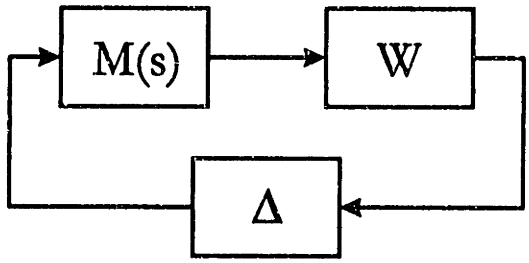

Fig.2-2 Standard robustness problem with weighting matrix.

3) If W is a diagonal frequency independent weighting matrix,

$$W = diag(w_1, w_2, \ldots, w_m)$$

then the system in Fig.2-2 is stable for all $\Delta \in X_K$ such that

$$\max_{i=1\ldots m} \left|\frac{\delta_i}{w_i}\right|$$

This inequality defines an elongated hypercube of guaranteed stable perturbations.

2.3 A New Algorithm for Computing Real-μ

Several algorithms have been proposed for the calculation of upper and lower bounds of μ; we adopt the approach outlined by Dailey. Although this algorithm is not as efficient or general as other approaches it provides valuable insights into the robustness scenario, which we translate into procedures for iterative weighting.

The main assumption that is made in this algorithm is that the worst-case perturbation at a given frequency, the size of which determines μ, is in the vicinity of one of the corners of the largest stable hypercube in the uncertain parameter space. What we mean by vicinity is that all but two elements of the worst-case Δ are equal to $1/\mu$; the remaining two elements are less than or equal to $1/\mu$. In most of the cases we will see that one of the

two elements is in fact equal to $1/\mu$ and the other is bigger. Our experience with this procedure has supported the validity of the assumption, especially in the frequency region were μ is maximum. In all the cases that we run the distance between the upper bound computed using Young's approach (Ref.2-9) and the lower bound computed using Dailey's approach (Ref.2-15) was always less than *20%*. Dailey's algorithm does not include the possibility to have repeated real uncertainties in the Δ block; in section 2.3.2 we will extend the analysis to include repeated real uncertainties.

2.3.1 Distinct Real Uncertainties

In this case all uncertain elements have multiplicity one. The set of allowable perturbations is then defined as

$$X_K = \left\{\Delta : \Delta = \text{block diag}\left(\delta_1, \delta_2, \delta_3, \ldots, \delta_m\right), \quad \delta_i \in \Re\right\}$$

To direct our search in the region of each of the corners of the stable hypercube, we fix all but two elements of the Δ block at initial values of $\pm k_g$. (All combinations of the sign of each element must be checked and all possible couples δ_i and δ_j must be considered.) The values of the remaining two elements, which we designate δ_1 and δ_2, for which $\det(I-\Delta M)=0$ can be computed by solving a quadratic equation. Manipulating the Δ and M matrices it is always possible to put the couple (δ_i, δ_j) as the first two elements of the Δ block. We thus have the following general equation

$$\det\left(I - \begin{bmatrix} \Delta_{12} & 0 \\ 0 & k_g R \end{bmatrix}\begin{bmatrix} M_{11} & M_{12} \\ M_{21} & M_{22} \end{bmatrix}\right) = 0$$

Where k_g is the current estimate of k_μ, R is a diagonal matrix of ± 1 which define the direction of the corner of the actual search, and $\Delta_{12} = \text{diag}(\delta_1, \delta_2)$. Rearranging this determinant,

$$\det\begin{pmatrix} I_2 - \Delta_{12} M_{12} & -\Delta_{12} M_{12} \\ -k_g R M_{21} & I_{m_r-2} - k_g R M_{22} \end{pmatrix} = 0$$

$$\det\left(I_{m_r-2} - k_g RM_{22}\right)\det\left(I_2 - \Delta_{12}\left(M_{11} + M_{12}(I - k_g RM_{22})^{-1} k_g RM_{21}\right)\right) = 0$$

Where the $\det\left(I_{m_r-2} - k_g RM_{22}\right)$ is different from zero except under pathological circumstances. Now if we let

$$P(k_g) = M_{11} + M_{12}(I - k_g RM_{22})^{-1} k_g RM_{21}$$

and also partition P appropriately, we can write

$$\det\left(I_2 - \begin{bmatrix}\delta_1 & 0\\ 0 & \delta_2\end{bmatrix}\begin{bmatrix}P_{11}(k_g) & P_{12}(k_g)\\ P_{21}(k_g) & P_{22}(k_g)\end{bmatrix}\right) = 0$$

The condition to be met with minimum norm of (δ_1, δ_2) is then

$$\left(1 - \delta_1 P_{11}(k_g)\right)\left(1 - \delta_2 P_{22}(k_g)\right) - \delta_1\delta_2 P_{12}(k_g)P_{21}(k_g) = 0$$

Given a certain value of k_g the last equation can be solved for δ_1 and δ_2. If δ_1 and δ_2 are complex, or if their norm is greater than k_g, then no solution exists with $\|\Delta\| = k_g$; we therefore increase k_g and repeat. On the other hand, if the norm of (δ_1, δ_2) is smaller than k_g, then a solution with $\|\Delta\| = k_g$ does exists; in this case, we decrease k_g and repeat. The possible search scenarios are shown in Fig. 2-3. On the left side is described the situation when δ_1 and δ_2 are real, the search stops when k_g is equal in magnitude to the norm of (δ_1, δ_2). In this case all but one element in the Δ-block have the same magnitude k_μ. On the right side is described the situation when (δ_1, δ_2) are sometimes complex during the search. In this case it may be necessary for the search to stop on the lower right branch when the norm of (δ_1, δ_2) is lower than k_μ; in this case all but two elements in the Δ-block will have the magnitude k_μ. The latter case is very rare, and in practical situations we never encountered this situation, especially when we are dealing with a large number of uncertainties.

In three dimensions the first search scenario corresponds to a solution on the edge, i.e. the stability boundary is hit by an edge of the stable hypercube. The second scenario corresponds instead to a solution on the side, the stability boundary is tangent to one side of the stable hypercube.

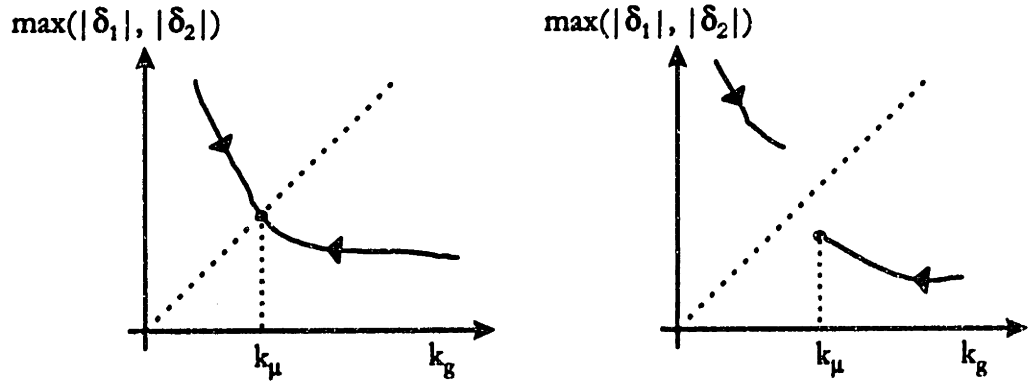

Fig. 2-3 Single direction possible μ search scenarios.

The search thus converges toward the minimum value of k_g for which a solution exists with $\|\Delta\| = k_g$, and this gives us a lower bound on μ:

$$\mu_K = k_\mu^{-1} \geq \max(k_g^{-1})$$

This search is repeated for all combinations of "all but two elements fixed," and the maximum lower bound obtained is, in practice, an excellent lower bound on μ_k. Because of the combinatorial nature of the procedure (the number of searches conducted is $m(m-1)^{2n-3}$), the practical use of the algorithm currently is limited to a maximum of nine uncertainties.

It is possible to avoid searching in all directions using some simple expedients. Normally this procedure is applied to a transfer function matrix $M(j\omega)$ over a range of frequencies. At most frequencies, the norm of (δ_1, δ_2) converges to the tightest lower bound during the first search because one simply chooses to search in the direction that worked at the previous frequency. The remaining searches are then unnecessary; as soon as the minimum value of k_g is found, one simply verifies that there are no other directions for which a solution exists with $\|\Delta\| = k_g$. Only when a solution actually exists in a separate direction does one switch faces and search in the new direction.

The main advantage of this algorithm is that together with the value of μ we also know which single uncertain element is actually causing the minimum k_g. This information is

particularly valuable when we want to weight the variables to find the most voluminous stable hypercube. A weighting procedure based on this information is described later.

Hundreds of test were run using this algorithm and the one available in the *Matlab* μ-toolbox (Ref.2-19). Complex random matrices were used to compare the two algorithms. One of the main disadvantages of the *Matlab* μ-toolbox was its inability to calculate a lower bound when random complex matrices were used. Tab. 2-1 summarizes the results of the test conducted on a sample of 200 complex matrices.

Size of the uncertainty block Δ	n=4	n = 6	n = 8
Mean Difference Between Upper and Lower Bound *	23.22 %	18.86 %	17.64 %
Maximum Difference Between Upper and Lower Bound **	77.78 %	32.07 %	29.05 %
Minimum Difference Between Upper and Lower Bound ***	3.28 %	4.80 %	3.59 %
Mean CPU time for the *Matlab* μ upper bound calculation	0.4036 sec	0.4503 sec	0.5244 sec
Mean CPU time of Dailey's algorithm	0.4637 sec	1.8708 sec	11.0761 sec

* Calculated as: $\Delta\mu = (\mu_{up}-\mu_{lo})/\mu_{up}*100$

** Calculated as: $\max(\Delta\mu)$

*** Calculated as: $\min(\Delta\mu)$

Tab. 2-1 Comparison between the *Matlab* μ-toolbox upper bound and Dailey's lower bound on the real μ

As expected the computational time necessary to calculate the lower bound with Dailey's algorithm is higher than the *Matlab* computational time. The computation time of Dailey's algorithms increases exponentially with the size of the uncertainty Δ-block, and as already mentioned it becomes not practical if the number of real uncertainty is greater than 10. On the other hand Young's algorithm, implemented in *Matlab*, was never able to converge for randomly generated complex matrices.

Example

We are going to apply the algorithm described in the previous section to a single complex matrix M, $M \in C^{6x6}$. In this case the structured uncertainty Δ is composed of *6* non repeated real blocks. The matrix M is given by:

$$M = \begin{bmatrix} 0.16-0.17i & -0.48+0.20i & 0.02-0.04i & -0.17-0.21i & 0.44+0.36i & -0.34-0.04i \\ -0.38+0.21i & 0.09-0.11i & 0.27-0.10i & -0.05-0.40i & 0.46-0.26i & 0.02-0.27i \\ 0.45+0.08i & 0.22+0.44i & -0.43-0.26i & 0.24-0.28i & -0.25+0.21i & -0.39+0.30i \\ -0.02+0.37i & 0.00+0.11i & -0.06-0.42i & -0.29+0.30i & -0.43-0.24i & 0.34-0.01i \\ 0.12+0.26i & -0.45-0.14i & 0.48-0.08i & -0.33+0.03i & -0.38-0.12i & -0.13-0.50i \\ 0.41+0.34i & -0.06+0.04i & -0.03-0.03i & -0.13+0.17i & 0.03-0.42i & -0.08-0.23i \end{bmatrix}$$

Using Dailey's algorithm we were able to calculate a lower bound on the real structured singular value μ, that is $\mu = 1.1483$. The worst case perturbation, i.e. the Δ-block that gives the maximum μ is:

$$\Delta = diag \begin{bmatrix} -0.87084705969641 \\ -0.87085586461396 \\ -0.87085586461396 \\ -0.20962260018560 \\ 0.87085586461396 \\ -0.87085586461396 \end{bmatrix}$$

It is immediate to verify that $\det(I - \Delta M) = 0$. The real structured singular value of the same matrix M was also calculated using the *Matlab* μ-toolbox. As is often the case, *Matlab* was not able to calculate the lower bound while the upper bound found was, $\mu = 1.2943$. The difference between our lower bound and the *Matlab* upper bound is *0.1460*, or *11.28 %*.

In the worst case perturbation we have four elements that have the same magnitude and two elements with different magnitude, the first and the sixth. The first element is equal (to within the tolerance of the search) to the other four elements, this means that the solution that we found lies along an edge of the stable hypercube. The first element is thus the one fixing the norm of the worst case perturbation vector. If we intend to apply the iterative weighting procedure, described in section 2.5, this is the element whose weighting must be reduced in order to enlarge the stability boundaries at the next iteration.

2.3.2 Repeated Real Uncertainties

The k_g search, in the direction of each corner, required in the case of a repeated real block structure is more complicated than the one described above. In this case, we still fix all but two elements and perform a search, but the solution for a given k_g is not given by a

simple quadratic equation. Instead, a sub-search for the (δ_1, δ_2) with minimum norm must be conducted for each value of k_g. Otherwise the procedure is unchanged.

Let us describe the sub-search. Suppose that the current direction of our search is defined by the diagonal $n_R \times n_R$ matrix R with diagonal elements equal to +1 or -1 defining the direction of the search. The remaining two uncertainties form a two-block structure of diagonal uncertainties whose multiplicity are k_1 and k_2:

$$\Delta' = \begin{bmatrix} I_{k_1}\delta_1 & 0 \\ 0 & I_{k_2}\delta_2 \end{bmatrix} \qquad n_{\Delta'} = k_1 + k_2$$

We are looking for the minimum norm Δ' such that

$$\det\left\{ I - \begin{bmatrix} \Delta' & 0 \\ 0 & k_g R \end{bmatrix} \begin{bmatrix} M_{11} & M_{12} \\ M_{21} & M_{22} \end{bmatrix} \right\} = 0$$

where k_g is the current estimate of k_μ and M has been suitably partitioned. Rearranging this determinant,

$$\det\left\{ I - \begin{bmatrix} \Delta' & 0 \\ 0 & k_g I_{n_R} \end{bmatrix} \begin{bmatrix} I_{n_{\Delta'}} & 0 \\ 0 & R \end{bmatrix} \begin{bmatrix} M_{11} & M_{12} \\ M_{21} & M_{22} \end{bmatrix} \right\} = 0$$

we have

$$\det\begin{bmatrix} I_{n_{\Delta'}} - \Delta' Q_{11} & -\Delta' Q_{12} \\ -k_g Q_{21} & I_{n_R} - k_g Q_{22} \end{bmatrix} = 0$$

where the definitions of Q_{ij} are obvious. Because $\det\left[I_{n_R} - k_g Q_{22}\right]$ is different from zero except under pathological circumstances, the matrix inversion lemma allows us to convert the preceding condition to

$$\det\left[I_{n_{\Delta'}} - \Delta' Q_{11} - \Delta' Q_{12}\left(I_{n_R} - k_g Q_{22}\right)^{-1} k_g Q_{21} \right] = 0$$

Now, if we let

$$P(k_g) = Q_{11} + Q_{12}\left(I_{n_R} - k_g Q_{22}\right)^{-1} k_g Q_{21}$$

and also partition $P(k_g)$ appropriately, we can write

$$\det\left\{I_{n_A} - \begin{bmatrix} I_{k_1}\delta_1 & 0 \\ 0 & I_{k_2}\delta_2 \end{bmatrix}\begin{bmatrix} P_{11}(k_g) & P_{12}(k_g) \\ P_{21}(k_g) & P_{22}(k_g) \end{bmatrix}\right\} = 0$$

The condition to be met with minimum norm of (δ_1, δ_2) is then

$$\det\begin{bmatrix} I_{n_1} - \delta_1 P_{11}(k_g) & -\delta_1 P_{12}(k_g) \\ -\delta_2 P_{21}(k_g) & I_{n_2} - \delta_2 P_{22}(k_g) \end{bmatrix} = 0$$

Again, we apply the matrix inversion lemma, which gives

$$\det\left(I_{n_1} - \delta_1 P_{11}(k_g)\right)\det\left\{I_{n_2} - \delta_2\left[P_{22}(k_g) + P_{21}(k_g)\left(I_{n_1} - \delta_1 P_{11}(k_g)\right)^{-1}\delta_1 P_{12}(k_g)\right]\right\} = 0$$

As before $\det\left(I_{n_1} - \delta_1 P_{11}(k_g)\right)$ is not equal to zero, so we have the following result: Given a value of k_g, and a guess at the size of δ_1, the minimum value of δ_2 that makes $\det(I - \Delta M) = 0$ is given by

$$\delta_2 = \min_{\lambda_i \in R}\left|\frac{1}{\lambda_i\{B(\delta_1, k_g)\}}\right|$$

where

$$B(\delta_1, k_g) = P_{22}(k_g) + P_{21}(k_g)\left(I_{n_1} - \delta_1 P_{11}(k_g)\right)^{-1}\delta_1 P_{12}(k_g)$$

Here we have used the fact that

$$\det\left(I_{n_B} - \delta_2 B\right) = \prod_{i=1}^{n_B}\left[1 - \delta_2\lambda_i\{B\}\right]$$

where $n_B = k_1 + n_R$. Clearly, the minimum δ_2 to perturb the determinant to zero is determined by the maximum real eigenvalue of $B(\delta_1, k_g)$, — the sub-search for the value of δ_1 that minimizes $max(|\delta_1|, |\delta_2|)$ thus can be conducted.

2.4 Algorithm Performance

In order to develop the upper and lower bounds on the real μ it is necessary to define some sets of block diagonal scaling matrices.

$$Q_K = \{\Delta \in X_K : \delta_i^r \in [-1 \quad 1]\}$$
$$D_K = \{block\ diag(D_1,\ldots,D_{m_r}) : D_i = D_i^* > 0,\ D_i \in C^{k_i x k_i}\}$$
$$G_K = \{block\ diag(G_1,\ldots,G_{m_r}) : G_i = G_i^*,\ G_i \in C^{k_i x k_i}\}$$

The following theorems give us the theoretical basis for the calculation of a lower and upper bound of the real μ.

Theorem 1 *For any matrix* $M \in C^{nxn}$, *and any compatible block structure* K

$$\max_{Q \in Q_K} \rho_R(QM) = \mu_K(M)$$

This theorem, taken from Ref.2-5, gives us a theoretical lower bound since for any $Q \in Q_K$, $\rho_R(QM) \leq (M)$. Unfortunately this is a non convex optimization problem and only local maxima can be found. An efficient algorithm based on a power iteration is described in Ref.2-5 and is implemented in *Matlab* in the μ-Analysis and Synthesis Toolbox. The iteration scheme converges very quickly but it is not very robust. As we will show later, in many situations the algorithm is not able to converge to a lower bound.

The calculation of the real μ upper bound is based on the following theorem taken from Ref.2-7.

Theorem 2 *For any matrix* $M \in C^{nxn}$, *and any compatible block structure* K *suppose* α_* *is the result of the following minimization problem*

$$\alpha_* = \inf_{D \in D_K,\ G \in G_K} \left[\min_{\alpha \in R} \{\alpha : (M^* DM + j(GM - M^* G) - \alpha D) \leq 0\} \right]$$

then $\mu_K(M) \leq \sqrt{\max(0, \alpha_*)}$.

This is a convex optimization problem that can be solved via LMI or a whole array of other numerical techniques. An efficient algorithm described in Ref.2-9 is implemented in the *Matlab* μ Toolbox.

For the purpose of testing the algorithm it is highly desirable to be able to generate matrices $M \in C^{n\times n}$ for which the solution is know a priori. In Ref.2-10 an algorithm was developed for the purely complex case and in Ref.2-9 the same algorithm was extended to the mixed μ case. We are going to describe how to obtain such matrices $M \in C^{n\times n}$ for the pure real case. The algorithm is divided into the following steps

a) Randomly generate the matrices $D \in D_K$, $G \in G_K$, and $Q \in Q_K$ with the additional restriction that Q is unitary, $Q^* Q = I$. In addition create a random matrix $Y \in C^{n\times m}$, and a real non-negative diagonal matrix $\Sigma = diag(\sigma_1 \ldots \sigma_n)$ with

$$\sigma_i = 1 \quad for \quad i = 1 \ldots r$$
$$\sigma_i < 1 \quad for \quad i = r+1 \ldots n$$

where r is some integer satisfying $1 \le r \le n$. Then generate a random unit vector $\eta \in C^n$ with the condition that:

$$\eta_i = 0 \quad for \quad i = r+1 \ldots n$$

b) Compute a unitary matrix $X \in C^{n\times m}$ which satisfies the equation:

$$X\eta = (Q^{-1} - jG)(I_n + G^2)^{-0.5} Y\eta$$

This can be done in the following way. First calculate the vector v as

$$v = T\eta \quad \text{where} \quad T = (Q^{-1} - jG)(I_n + G^2)^{-0.5} Y$$

Then define a matrix P as

$$P = \begin{bmatrix} v & p_2 & \cdots & p_n \end{bmatrix}$$

where $v, p_2, \ldots, p_n$ are independent columns. Then using the Gram-Schmidt method we can orthogonalize the columns of P and define an orthogonal matrix Q. The first column of Q will be a multiple of v, such that $Q^* v = v$. We can then write

$$v = QEQ^* v$$

where E is defined as follows:

$$E = \begin{bmatrix} 1 & 0 \\ 0 & H \end{bmatrix}$$

and H is any unitary matrix, $H \in R^{(n-1)x(n-1)}$. At this point we can calculate the unitary matrix X as

$$X\eta = T\eta = TQEQ^*\eta \qquad \Rightarrow \qquad X = TQEQ^*$$

c) Now we can compute M as

$$M = D^{-1}\left(X\Sigma Y^*(I_n + G^2)^{0.5} + jG\right)D$$

This algorithm allows us to generate random matrices M with μ equal to the upper bound defined in Theorem 2, and equal to one. It is also clear that in this case there is no gap between the upper and lower bounds, even if we have to solve a non convex optimization problem to find the lower bound and thus there is no guarantee that there will be no gap in the final solution.

We are going to apply the algorithm presented in section 2.3.1 and 2.3.2 to a set of random matrices generated with the procedure just described. It is important to point out that Dailei's algorithm gives the exact value of μ. The way we generate the random matrices puts the worst case perturbation vector in the direction of a corner, exactly were Dailey's algorithm is searching. The matrix Q, defined at point (a), is diagonal with its elements equal to +1 or -1, this is also the direction of the worst case perturbation. The results of the tests are reported in the next two sections.

Test 1: Distinct Real Uncertainties

The scope of this test is to verify the *Matlab* function that implements Dailey's algorithm for the case of distinct real uncertainties. During the test, matrices from size 2 to size 8 were considered. Thousand of matrices were generated and in all cases the lower bound calculated with the new function was always equal to 1. The worst case perturbation vector was always in the direction defined by the Q matrix (a part from some sporadic cases).

This confirms that the algorithm was correctly coded. Tab. 2-2 summarizes the results of the tests conducted on the new algorithm and compares it with *Matlab mu* function.

The upper bound mean error stays around 3% even for Δ blocks larger than 8. The lower bound calculated with *Matlab*, using power iteration, converges to a solution that is exact almost 70% of the time. The function implementing Dailey's algorithm was always calculating the correct μ and was always converging. Unfortunately we can see that the CPU time increases exponentially with the size of Δ. Up to uncertainty blocks of size 6, the CPU time of the new algorithm is comparable to that of *Matlab* lower bound.

	n = 2	n = 3	n = 4	n = 5	n = 6	n = 7	n = 8
Matlab upper bound mean error *	0.60 %	1.34 %	2.49 %	3.05 %	3.36 %	3.40 %	3.46 %
Matlab lower bound mean error **	0.00 %	0.01 %	0.00 %	0.00 %	0.00 %	0.00 %	0.00 %
New algorithm lower bound mean error	0.00 %	0.01 %	0.00 %	0.00 %	0.00 %	0.00 %	0.00 %
Matlab upper bound mean CPU time [sec]	0.4269	0.4582	0.4356	0.4525	0.4033	0.5288	05484
Matlab lower bound mean CPU time [sec]	1.7900	0.8956	0.9698	0.9630	1.4183	1.8284	1.8323
New algorithm mean CPU time [sec]	0.0171	0.3703	0.3745	0.8603	2.0941	6.4396	14.9339
Matlab lower bound average convergence ratio	1.0 %	84.5 %	65.5 %	77.0 %	67.5 %	73.0 %	67.0 %

* Calculated as $(\mu-1)*100$ ** Only when converging

Tab. 2-2 Summary of the tests conducted on the algorithm for distinct real uncertainty Δ block

Test 2: Repeated Real Uncertainties

This test was conducted to check the algorithm implemented in *Matlab* for the case of repeated real uncertainties. We considered an uncertainty Δ with four blocks of different sizes. The scope of the test was to compare the new lower bound with the upper and lower bounds calculated from *Matlab*. There was always an almost perfect match between the two lower bounds when *Matlab* was able to converge.

	n = 8	n = 12	n = 16	n = 20	n = 24	n = 28	n = 32
Matlab upper bound mean error *	5.11 %	6.28 %	6.82 %	7.03 %	7.10 %	7.16 %	7.22 %
Matlab lower bound mean error **	0.00 %	0.00 %	0.00 %	0.00 %	0.00 %	0.00 %	0.00 %
New algorithm lower bound mean error	0.01 %	0.01 %	0.01 %	0.01 %	0.01 %	0.01 %	0.01 %
Matlab upper bound mean CPU time [sec]	0.3825	0.4764	0.6043	0.7882	1.0553	1.4235	2.1316
Matlab lower bound mean CPU time [sec]	0.9256	1.0729	1.2564	1.4925	1.8517	2.3118	3.2245
New algorithm mean CPU time [sec]	2.9689	3.2948	3.7519	4.3102	5.1224	6.1294	7.3924
Matlab lower bound average convergence ratio	81.5 %	87.0 %	87.5 %	87.0 %	88.5 %	87.0 %	84.0 %

* Calculated as $(\mu\text{-}1)*100$ ** Only when converging

Tab. 2-3 Summary of the tests conducted on the algorithm for repeated real uncertainty Δ block

We understand that several other tests need to be done to check the algorithm. In this section we only gave the results of some tests to give an idea of the benefits and the limitations of the new algorithm with respect to the one implemented in *Matlab*.

2.5 Iterative weighting procedure

When analyzing several uncertainties in an engineering environment, it is of tremendous interest to determine which uncertain elements dominate the robustness measure, which elements are interrelated, and which elements do not greatly affect the stability of the system.

The iterative weighting procedure that we are going to describe is one way to address these questions. Fig. 2-4 illustrates why weightings are important.

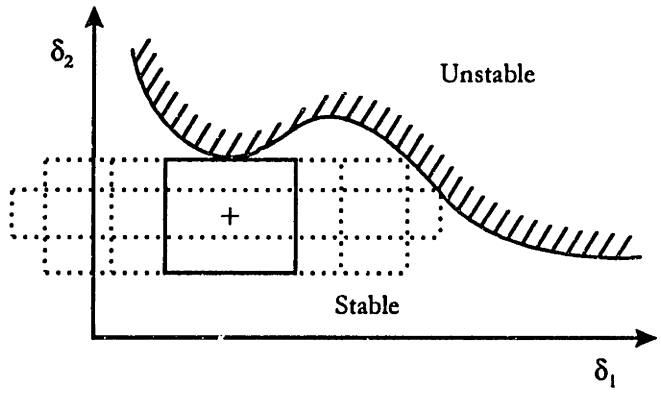

Fig. 2-4 Effect of weighting on guaranteed stable region.

In this simple example the stability of the system is less sensitive to uncertainty in δ_1. However, with equal weighting on these two parameters, μ analysis will not uncover this fact without additional analysis of the sub-blocks. From Fig. 2-4, we can see how reweighting the parameters in the Δ block using a real diagonal weighting matrix W helps to improve our knowledge of the stable space. As the relative weighting on δ_2 goes down, the guaranteed box becomes elongated in the δ_1 direction. In the two-dimensional case, this continues until the corner of the box strikes the stability boundary; in multidimensional cases, a different edge of the stable hypercube usually strikes the boundary; weighting on the new edge is then necessary. Thus, reweighting gives a more complete picture of the robustness interrelationships. Reweighting also, in general, enlarges the guaranteed stable region, because the union of any two guaranteed stability regions is also stable.

In the previous section, we described an algorithm for calculating a lower bound of μ that is based on determining the specific uncertain element that is actually causing the maximum μ. It is reasonable then to argue that by reducing the weighting on this element we will allow larger stability bounds on the other elements, just as in our 2x2 example.

Let us say that we have 6 uncertainties and that we start with the following weighting matrix:

$$W_0 = diag(1,\ 1,\ 1,\ 1,\ 1,\ 1)$$

After running the algorithm we find a certain value of the structured singular value μ_0. We then know that stability is guaranteed in the following n-dimensional box:

$$S_0 = \left\{ \delta_i :\ \max_{i=1..m_i} |\delta_i| \le \frac{w_{0i}}{\mu_0} = \frac{1}{\mu_0} \right\}$$

We also know, based on the parameters that the algorithm must iterate, that the element causing the maximum μ is, for example, the second one, weighted by $W(2,\ 2)$. For the next weighting matrix we choose

$$W_1 = diag(1,\ 0.9,\ 1,\ 1,\ 1,\ 1)$$

We then solve for μ_1. The associated guaranteed stable region is

$$S_0 = \left\{ \delta_i : \max_{i=1...m_r} |\delta_i| \le \frac{w_{1i}}{\mu_1} \right\}$$

In many cases, $\mu_1 \le \mu_2$, such that the new guaranteed stable region is more voluminous.

If the reduction in the weighting $W(2, 2)$ is not too large, the stability boundaries on all of the elements other than $\Delta(2, 2)$ are larger than before. The bound on $\Delta(2, 2)$ is tighter than before, because we reduced the weighting on this element.

As we continue changing weights, the elements that never strike the stability boundary represent uncertainties that tend not to affect the stability of the system. At the end of this process, the overall guaranteed stable region is

$$S = (S_0 \cup S_1 \cup S_2 \cdots)$$

From Fig. 2-4, we can see how the union of all of the stability regions can provide extra information about the shape of the stability boundary. In many practical situations after only five or six reweightings, we gain a good deal of information about the robustness picture.

2.6 Phase and Delay as Real Uncertainties

The algorithm and weighting procedure described is applicable to the general class of problems described in the previous sections. In applications, however, an interesting step is often that of creating the Δ-block structure to be analyzed, based on commonly asked engineering questions. For instance, classic measures of robustness (gain margin and phase margin) are still common tools for assessing the stability of flight control systems. Although singular values and structured singular values are more general measures of robustness, their interpretation is sometimes difficult; the intuition that engineers have developed for phase and gain margins is still valuable. Furthermore, the concept of delay margin is a very important variant on phase margin — transport delays are often a primary concern during

flight system development, because they can change as the flight code grows. For these reasons we would like to incorporate gain changes, phase changes, and delays into our toolbox of available perturbations to the flight system. After describing block structures for these types of perturbations, a useful way to present the resulting analysis for engineering interpretation is presented in the following sections.

2.6.1 Gain Margin

It is straightforward to incorporate gain-margin concepts into a robustness problem. The interconnection of Fig. 2-5 shows how we have chosen to do this using a multiplicative uncertainty in the feedback path.

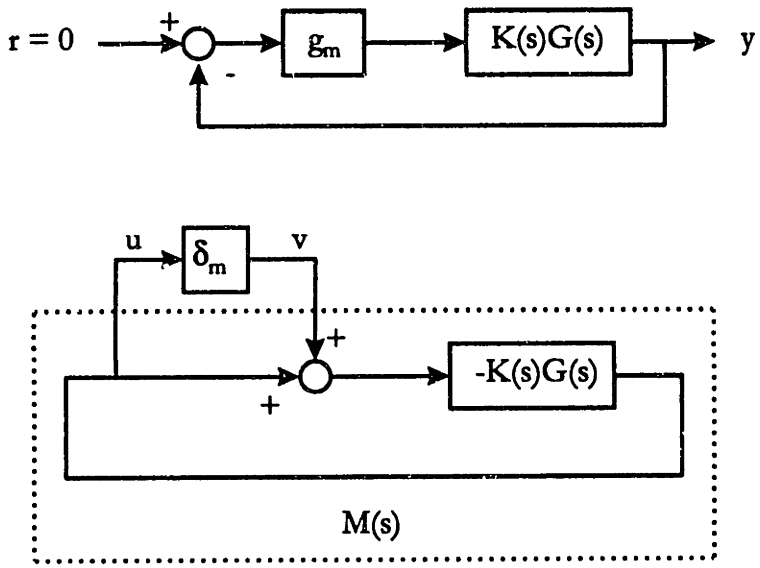

Fig. 2-5 Gain margin g_m and gain uncertainty δ_m.

If the uncertain gain δ_m is the only uncertainty in the system, then the single loop gain margin is computed as $g_m = 1 \pm \delta_m$.

2.6.2 Time delay and phase margin as real uncertainties

Although a direct relationship exists between gain margin and a real uncertainty, no such relationship exists for time delay and phase margin. Instead, we use a n^{th}-order Padè approximation of a delay, and thus break out the magnitude of the delay as a real uncertainty.

We know that the Laplace transform of a pure delay τ is

$$L[f(t-\tau)] = e^{-\tau s}F(s)$$

An n^{th}-order Padè approximation provides a way to incorporate delay (or phase change at a specific frequency) without subsequently changing the gain of the system:

$$e^{-\tau s} = \frac{1 - p_1(\tau s) + p_2(\tau s)^2 \cdots p_n(\tau s)^n}{1 + p_1(\tau s) + p_2(\tau s)^2 \cdots p_n(\tau s)^n}$$

To incorporate τ into a real μ perturbation structure, we start with a first-order Padè and then do some block-diagram manipulation to isolate τ from the rest of the block diagram.

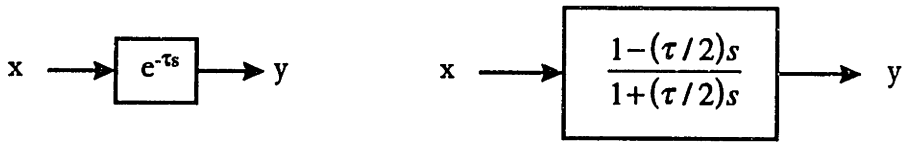

Delay First order Pade approximation

Fig. 2-6 Time delay and first order Padè approximation.

In order to isolate the magnitude of the time delay we need to transform the first order Padè approximation shown in Fig. 2-6 as an additive perturbation (Fig. 2-7).

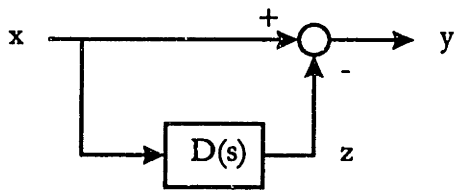

Fig. 2-7 First order Padè alternative block diagram.

The transfer function of the block diagram shown in Fig. 2-7 must be the same as the transfer function of the first order Padè approximation. The transfer function *D(s)* is then

$$1 - D(s) = \frac{1-(\tau/2)s}{1+(\tau/2)s} \qquad \Rightarrow \qquad D(s) = \frac{\tau s}{1+(\tau/2)s}$$

We can now rearrange the transfer function from x to z as follows

$$z = \frac{\tau s}{1+(\tau/2)s}x \quad \Rightarrow \quad z+z(\tau/2)s = x\tau s \quad \Rightarrow \quad z = \tau s\left(x-\frac{1}{2}z\right)$$

These manipulations result in the rearranged block diagram shown in Fig. 2-8, this block diagram can be incorporated easily into, for instance, a Simulink representation of the flight system. During the robustness analysis the derivative block s in the upper path (equal to $j\omega$) is incorporated into $M(j\omega)$.

The procedure to create a phase-margin block diagram is analogous to that for a time delay; we simply realize that the phase lag introduced by the Padè approximation is a function of frequency. So, to incorporate a pure phase lag that is independent of frequency, we need a frequency dependent time delay $exp[-\tau(\omega)s]$, where $\tau(\omega)s = j\phi$. This results in the block diagram in Fig. 2-9.

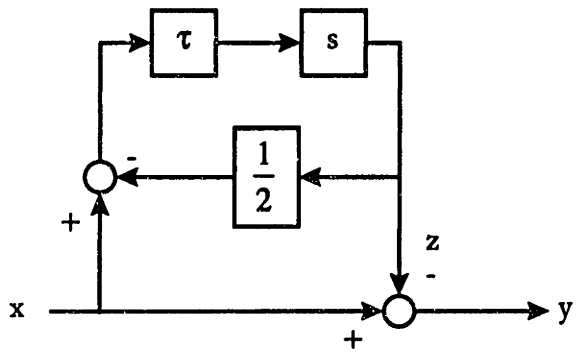

Fig. 2-8 First order Padè rearranged to isolate τ.

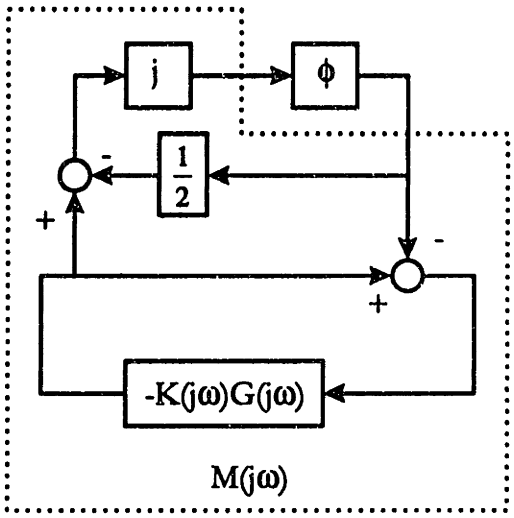

Fig. 2-9 Robustness problem for phase margin.

2.6.3 Higher-order approximation of phase shift

In many practical applications, a first order Padè approximation may not adequately describe the delay or phase uncertainty. For instance, in cases where more than 180 deg of phase lag is introduced by a time delay in the frequency range of interest, the first order Padè approximation will not be adequate, because the maximum phase lag it can introduce is 180

deg. Fig. 2-10 compares the phase of a pure delay ($e^{-i\omega\tau}$) to the phases of a first and second order Padè approximation of a time delay. From the figure it is evident that a first order Padè approximation becomes inadequate at frequencies higher than 10 rad/sec when a delay of 0.1 sec is considered.

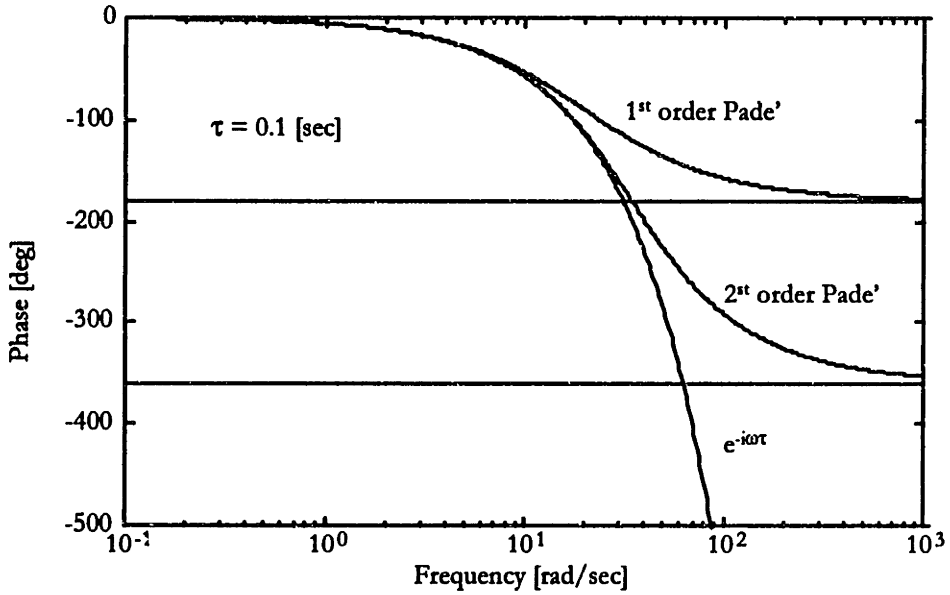

Fig. 2-10 First and second order Padè approximations of a time delay.

The two plots in Fig. 2-11 make more clear the error introduced by a first and second order Padè approximation, and can help in the decision on which approximation to adopt. The x-axis represents the amount of delay that we want to consider and the y-axis is the maximum delay error introduced by the two approximations. In these plots we have assumed that the maximum frequency of interest is 15 rad/sec This is a reasonable assumption for many aerospace applications. Plot (b) shows the actual error in seconds and plot (a) shows the percentage of the error with respect to the delay approximated. The advantage in the use of a second order Padè is evident, the maximum percentage error introduced is about 38% for a delay of 0.1 sec.

The problem is then to translate a second order (or even higher) Padè approximation into a real μ problem.

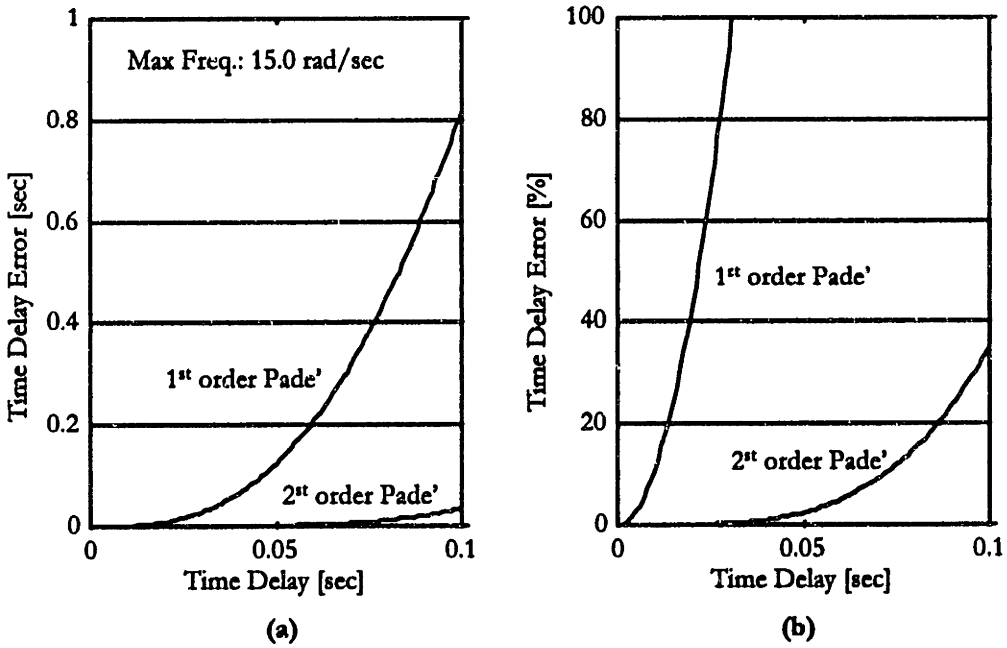

Fig. 2-11 Error in time delay introduced by a first and second order Padè

We will show that this can be efficiently accomplished using an approach that is similar to the one described earlier. For example, for a second order Padè we have

$$e^{-\tau s} \cong \frac{1-(\tau/2)s+(\tau^2/12)s^2}{1+(\tau/2)s+(\tau^2/12)s^2} = 1+\frac{k_1\tau s}{\tau s-a_1}+\frac{k_1^*\tau s}{\tau s-a_1^*}$$

where

$$k_1 = i\frac{6}{\sqrt{3}} \qquad a_1 = -3+i\sqrt{3}$$

In this case the phase uncertainty in the robustness problem takes the form of a pair of repeated real uncertainties. The block diagram that describes the second-order Padè phase uncertainty is shown in Fig. 2-12.

The matrices T and Q are defined in the following way. Let x and y be the input and the output of the second order Padè,

$$y = \left[1+\frac{k_1\tau s}{\tau s-a_1}+\frac{k_1^*\tau s}{\tau s-a_1^*}\right]x$$

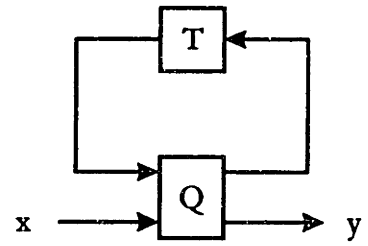

Fig. 2-12 Second order Padè phase uncertainty.

Now we can define the following variables:

$$u_1 = \frac{k_1 \tau s}{\tau s - a_1} x \qquad u_2 = \frac{k_1^* \tau s}{\tau s - a_1^*} x$$

With some simple algebra operation we can rearrange the above equations as follows

$$u_1(\tau s - a_1) = k_1 \tau s x \qquad \Rightarrow \qquad u_1 = \tau s \left(\frac{1}{a_1} u_1 - \frac{k_1}{a_1} x \right)$$

At this point we can define an auxiliary variable v_1

$$v_1 = \frac{1}{a_1} u_1 - \frac{k_1}{a_1} x$$

The same operation can also be done on u_2, defining an auxiliary variable v_2. Finally we can write

$$\begin{bmatrix} v_1 \\ v_2 \\ y \end{bmatrix} = \begin{bmatrix} 1/a_1 & 0 & -k_1/a_1 \\ 0 & 1/a_1^* & -k_1^*/a_1^* \\ 1 & 1 & 1 \end{bmatrix} \begin{bmatrix} u_1 \\ u_2 \\ x \end{bmatrix} \qquad \begin{bmatrix} u_1 \\ u_2 \end{bmatrix} = \begin{bmatrix} \tau s & 0 \\ 0 & \tau s \end{bmatrix} \begin{bmatrix} v_1 \\ v_2 \end{bmatrix}$$

From the last equation it follows immediately the definition of the matrices T and Q and the block diagram of Fig. 2-12.

$$T = \begin{bmatrix} j\phi & 0 \\ 0 & j\phi \end{bmatrix} \qquad Q = \begin{bmatrix} 1/a_1 & 0 & -k_1/a_1 \\ 0 & 1/a_1^* & -k_1^*/a_1^* \\ 1 & 1 & 1 \end{bmatrix}$$

The block diagram of Fig. 2-13 is in the form of a standard repeated real stability robustness problem. As before, we have converted from delay to phase uncertainty by letting $\tau s = j\phi$ and incorporating j into $M(j\omega)$.

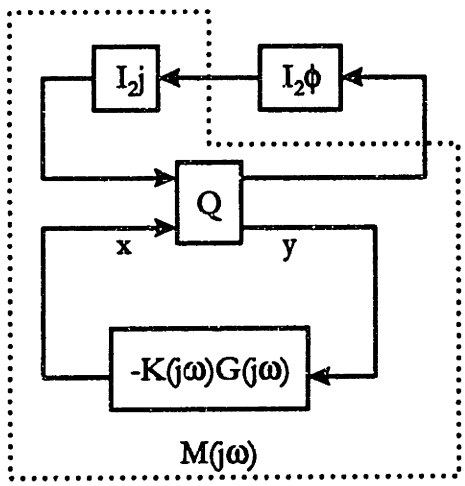

Fig. 2-13 Standard repeated-real stability robustness problem.

2.6.4 Correction of the Padè approximation phase error

The phase margins calculated with the procedure described in the previous paragraphs can be optimistic due to the phase error introduced by the Padè approximation. Depending on the frequency and the size of the delay this error can lead to phase margins that are larger than in reality. Fig. 2-11 shows the errors introduced by the first and second order Padè approximations; if we are interested in frequencies up to 15 rad/sec the first order Padè approximation can easily double the expected phase margin.

Fortunately a simple expedient can help us to solve this problem and get a more accurate solution. Let us assume that τ_c and ω_c are the time delay and the corresponding frequency obtained via the real uncertainty robustness test. τ_c and ω_c result in a unity magnitude number in the complex plane that puts the system at the verge of instability. Assuming that a first order Padè approximation was used, this complex number is defined by:

$$\alpha + j\beta = \frac{2 - j\omega_c\tau_c}{2 + j\omega_c\tau_c} \qquad |\alpha + j\beta| = 1$$

The phase of this complex number is the correct phase margin of the system, i.e. the amount of phase lag that we have to add in order to destabilize the plant. The correct phase margin is then defined as:

$$\phi_{corr} = phase\left(\frac{2 - j\omega_c\tau_c}{2 + j\omega_c\tau_c}\right)$$

From this phase margin we can then calculate a more precise time delay as:

$$\tau_{corr} = \frac{\phi_{corr}}{\omega_c}$$

In practice once we have calculated the approximated phase margin we need only to calculate the phase of the Padè approximation for the particular destabilizing τ_c. It is clear that this is only valid at the particular frequency ω_c where the phase margin is occurring. In the following example we will show the importance of this corrective procedure.

2.6.5 Numerical Example

This section illustrates the use of the first and second order Padè approximation in the calculation of the phase margin. Consider a system with the following loop gain function:

$$G(s) = \frac{90(s+1)(s^2+2s+44)}{s^2(s+2s+82)(s^2+2s+101)}$$

The Nyquist plot of Fig. 2-14 shows that this system has three crossover frequencies with three phase margins 37.9677° at 0.7784 rad/sec, 84.6331 at 9.2997 rad/sec, and 25.9080 at 9.9951 rad/sec.

As already mentioned, the first order Padè approximation describes the phase margin as a single real uncertainty in the standard robustness problem. In the case of a single uncertainty it is possible to solve directly for the destabilizing perturbation at each frequency.

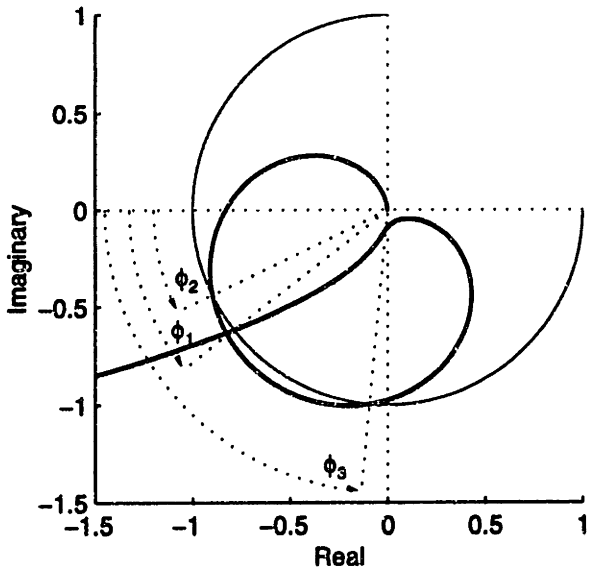

Fig. 2-14 Nyquist diagram of the system in the example.

With some simple algebra it can be found that the destabilizing perturbation is given by:

$$\varphi(\omega) = 2j\frac{1-M(j\omega)}{1+M(j\omega)}$$

In the last equation unity negative feedback has been considered. The phase margin is calculated at the plant input. At each frequency we need to check if the destabilizing perturbation is real or complex; if the perturbation is real then it represents the phase margin of the system at that frequency. Fig. 2-15 is a plot of the destabilizing perturbation at each frequency when a first order Padè is used to approximate the delay. The dashed line represents the imaginary part and the solid line the real part of the destabilizing perturbation; as expected the perturbation becomes real at the three frequencies corresponding to the phase margins. In a similar way it is possible to solve for the destabilizing perturbation when a second order Padè approximation is considered. In this case we need to find the largest positive eigenvalue of a 2x2 matrix. For brevity we will not describe the algebra for the second order Padè.

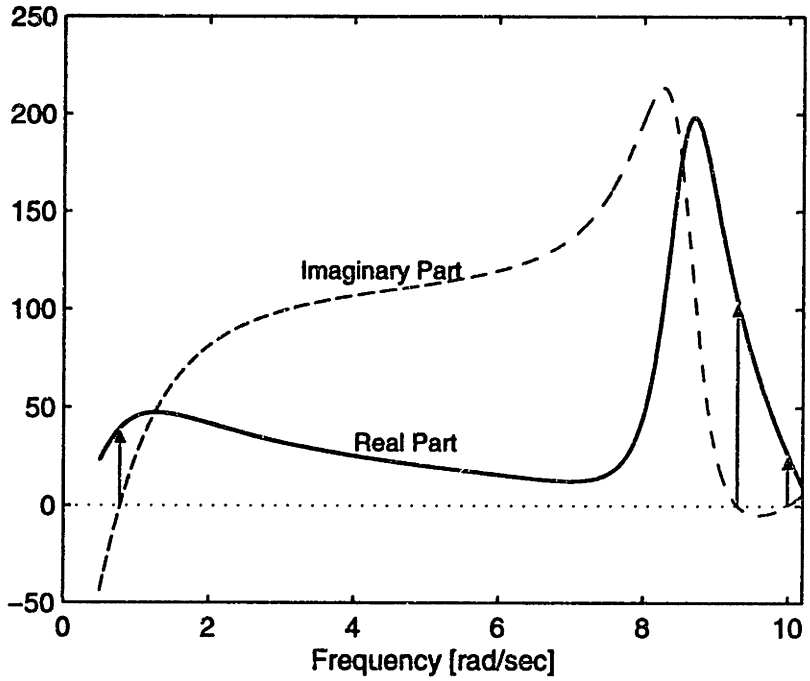

Fig. 2-15 Real and imaginary part of the destabilizing perturbation.

A summary of the results obtained is given in Tab. 2-4. Both the first and second order Padè approximations give optimistic solutions, in the sense that the predicted phase margins are larger than the actual ones. In order to obtain a more precise estimate of the phase margin we can use the procedure described in the previous section. If we add to the calculated phase margins the error introduce by the approximations, we obtain the values ϕ_{corr} listed in Tab. 2-4. After the correction has been made both the first and second order Padè give almost perfect estimates of the three phase margins.

Method	ω_c [rad/sec]	ϕ [deg]	τ [sec]	ϕ_{corr} [deg]	τ_{corr} [sec]
Exact	0.778	37.9677	0.8513	-	-
1st Order	0.778	39.4233	0.8839	37.9698	0.8513
2nd Order	0.778	37.9797	0.8515	37.9698	0.8513
Exact	9.299	84.6331	0.1588	-	-
1st Order	9.299	104.3569	0.1959	84.6474	0.1589
2nd Order	9.299	85.1498	0.1598	84.6474	0.1589
Exact	9.995	25.9080	0.0452	-	-
1st Order	9.995	26.3702	0.0460	25.9189	0.0453
2nd Order	9.995	25.9204	0.0453	25.9189	0.0453

Tab. 2-4 First and Second Order Padè Phase Margins

In this introductory example we have shown how the first and second order Padè can be used to recast the phase margin calculation in the more general standard robustness framework. The phase correction procedure is also an effective way to recuperate the error introduced by the delay approximation.

Once gain and phase perturbations can be incorporated into a system block diagram and manipulated into the standard Δ-block form, one can simultaneously look at guaranteed gain and phase margin variations for multiloop systems using real μ. By separating gain and phase into separate real perturbations, several advantages over complex uncertainties are realized. First, one can scale gain and phase separately to reflect the relative importance and magnitude of each. Also, using the algorithm described in the previous paragraph, it is possible to consider only gain and phase variations in directions that are considered important. For instance, if one is primarily interested in the effects of phase lag, then phase lead perturbations can be excluded from the μ-search. Another advantage of the block structures presented here is that time-delay robustness and delay margin can now also be analyzed directly and in a non conservative manner. Finally, specific robustness questions can be answered directly in terms of standard engineering measures; this is the topic of the following chapter.

2.7 Reference

Ref.2-1 J. C. Doyle, "Analysis of Feedback Systems with Structured Uncertainties", *IEE Proceedings on Control Theory and Applications*, Vol. 129, Pt. D, No. 6, 1982, pp.242-250.

Ref.2-2 M. G. Safonov, "Stability Margins of Diagonally Perutrbed Multivariable Feedback Systems", *IEE Proceedings on Control Theory and Applications*, Vol. 129, Pt. D, No. 6, 1982, pp.251-256.

Ref.2-3 J. C. Doyle, "Structured Uncertainty in Control System Design", *Proceedings of the 24th IEEE Conference on Decision and Control*, (Ft. Lauderdale, FL), Inst. of Electrical and Electronics Engineers, New York, 1985, pp. 260-265.

Ref.2-4 M. Athans and M. G. Safanov, "A Multiloop Generalization of the Circle Criterion for Stability Margin Analysis", *IEEE Transactions on Automatic Control*, AC-26(2), April 1981, pp. 415-422.

Ref.2-5 Young P. M., and Doyle J. C., "Computation of μ with Real and Complex Uncertainties," *Proceedings of the 29th IEEE Conference on Decision and Control*, (Honolulu, HI), Inst. of Electrical and Electronics Engineers, New York, 1990, pp.1230-1235.

Ref.2-6 M. K. H. Fan and A. L. Tits, "Characterization and Efficient Computation of the Structured Singular Value", *IEEE Transactions on Automatic Control*, Vol. AC-31, No. 8, 1986, pp. 734-743.

Ref.2-7 Fan M. H., Tits A. L., Doyle J. C., "Robustness in the Presence of Mixed Parametric Uncertainty and Unmodelled Dynamics", *IEEE Transactions on Automatic Control*, Vol. AC-36, No.1, 1991, pp. 25-38.

Ref.2-8 Young P. M., Newlin M. P., Doyle J. C., "Mu Analysis with Real Parametric Uncertainty", ", *Proceedings of the 30th IEEE Conference on Decision and Control* (Brighton, England, UK) Inst. of Electrical and Electronics Engineers, New York, 1991, pp.1251-1256.

Ref.2-9 Young P. M., Newlin M. P., Doyle J. C., "Practical Computation of the Mixed m Problem", *Proceedings of the American Control Conference*, 1992, pp. 2190-2194.

Ref.2-10 Fan M. K. H., and Tits A. L., "Characterization and Efficient Computation of the Structured Singular Value," *IEEE Transaction on Automatic Control*, Vol. AC-31, No.8, 1986, pp. 734-743.

Ref.2-11 R. R .E. De Gaston and M. Safonov, "Exact Calculation of the Multiloop Stability Margin", IEEE Transactions on Automatic Control, Vol. 33, No. 2, 1988, pp.156-171.

Ref.2-12 C. Beck, and J. Doyle, "Mixed μ Upper Bound Computation". *Proceedings of the 31st Conference on Decision and Control*, Tucson, Arizona, December 1992, pp. 3187-3192.

Ref.2-13 A. Sideris and R.S. Sanchez Peña, "Fast computation of the Multivariable Stability Margin for Real Interrelated Uncertain Parameter", *Proceedings of the American Control Conference* (Atlanta, GA), Inst. of Electrical and Electronics Engineers, New York, 1938, pp. 1483-1488.

Ref.2-14 R.S. Sanchez Peña and A. Sideris, "A General Program to Compute the Multivariable Stability Margin for Systems with Parametric Uncertainty", *Proceedings of the American Control Conference* (Atlanta, GA), Inst. of Electrical and Electronics Engineers, New York, 1988, pp. 317-322.

Ref.2-15 R. L. Dailey, "A New Algorithm for the Real Structured Singular Value", *Proceedings of the American Control Conference* (San Diego, CA), Inst. of Electrical and Electronics Engineers, New York, 1990, pp. 3036-3040.

Ref.2-16 M. Fu and N. E. Barabanov, "Improved Upper Bounds of the Structured Singular Value", *Proceedings of the 34th Conference on Decision & Control*, New Orleans, LA, December 1995, pp. 3115-3120.

Ref.2-17 A. Packard and J. Doyle, "The Complex Structured Singular Value", *Automatica*, Vol. 29, No. 1, 1993, pp.71-109.

Ref.2-18 P. Miotto and J. D. Paduano, "Application of Real Structured Singular Values to Flight Control Law Validation", *Journal of Guidance, Control, and Dynamics*, Volume 19, Number 6, Nov.-Dec. 1996, pp.1239-1245.

Ref.2-19 G. Balas, J. C. Doyle, K. Glover, A. Packard, and R. Smith, "μ-Analysis and Synthesis Toolbox", MuSyn, Inc. Minneapolis, MN, 1991.

This page intentionally left blank.

Chapter 3

Flight Control Law Validation: The Real-μ Application

3.1 Introduction

The motivation for the analytical discussion just completed is the need for methods of flight control law validation. The following section presents flight control law validation issues raised at NASA Dryden, and recasts these problems in the real-μ analysis framework. We are going to present three distinct problems that use the procedures just introduced. The first is an application of the weighting procedure to determine the relative importance of several aerodynamic parameters to the robustness of the X-31 lateral-directional control system. The second example shows how to calculate a robustly guaranteed phase margin in the face of uncertainties in the aerodynamic parameters. The concept will be illustrated using the X-31 Quasi-tailless experiment. The last application describes how robustness measures can be implemented during flight test.

3.2 The X-31A Quasi-tailless flight test

The X-31A Quasi-tailless flight test will be used as a motivating example for the use of the robustness tools presented in the previous chapter.

The X-31A aircraft was built by Rockwell International and Deutsche Aerospace in order to demonstrate enhanced fighter maneuverability by using thrust vectoring to fly beyond stall limits. The X-31A was equipped with a thrust vectoring control system which was able to provide pitch and yaw moments by deflecting the thrust vector. A simple mechanism with three paddles placed symmetrically around the exhaust nozzle was used to deflect the engine plume (see Fig. 3-1). The X-31 program has shown that enhanced fighter maneuverability can be successfully obtained using thrust vectoring.

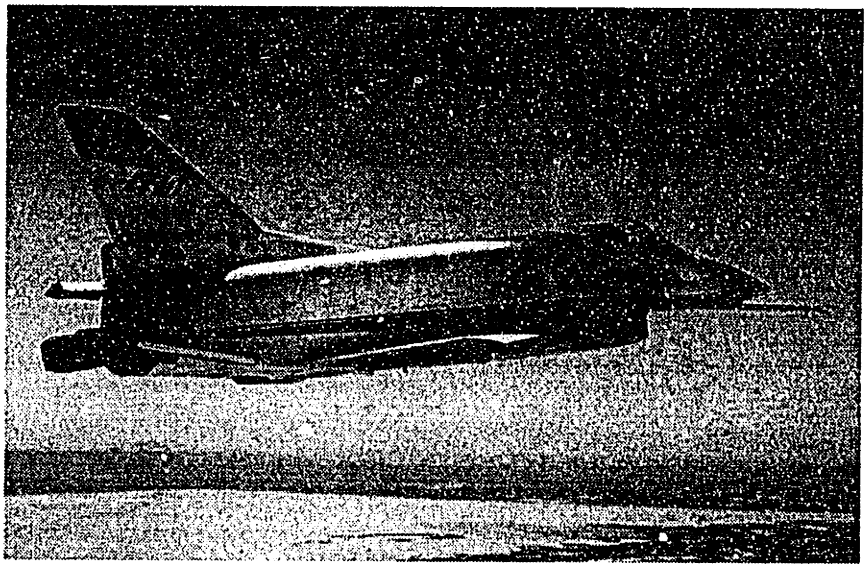

Fig. 3-1 The X-31A experimental aircraft.

The importance of the X-31A Flight Control Law (FCL) is that it represents one of the first application of a Linear Quadratic Regulator to flight control system. A good description of the control law is given by Beh and Hofinger in Ref.3-1. We will give only a brief description of the control law.

The basic structure of the X-31A FCL is shown in Fig. 3-2. The flight control law is based on three major units: the feedback LQR gains (K_{LQR}), the feed-forward input function (K_{Fu}), and the feed-forward output function (K_{Fy}).

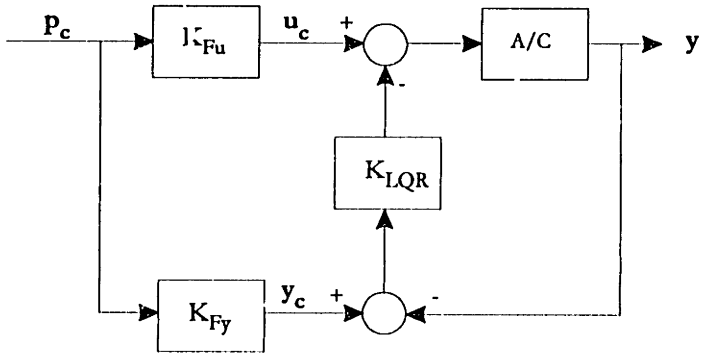

Fig. 3-2 The basic structure of the X-31A FCL.

The feed-forward input function K_{Fu} calculates the steady state surface deflections necessary to trim the aircraft in accordance to the pilot command input vector p_C. At the

same time the function K_{Fy} calculates the steady state output vector based on the pilot input command. This structure is necessary to implement the Linear Quadratic Regulator in the form of a Linear Quadratic Servo. All the state feedback signals need to be calculated from the pilot input in order to generate the required error signal. The error signal is then passed through the K_{LQR} gains. K_{Fy} and K_{Fu} are nonlinear functions of the aircraft flight condition and describe the inverse steady state model of the aircraft. The K_{LQR} gains are scheduled against Mach number, altitude, and angle of attack. A *Simulink* version of the X-31 FCL is shown in Fig. 3-3.

A recent flight program at NASA Dryden Flight Research Center was the X-31 Quasi-tailless flight test, in which the rudder channel control augmentation system was redesigned in order to simulate the removal of the tail. In practice the LQR gains of the rudder channel were changed in order to destabilize the aircraft and to place the closed loop poles of the lateral directional axis in a location similar to that of a reduced tail aircraft. Many remarks can be made about the methodology used to simulate a reduced tail aircraft, but in general we can say that this was an effective and practical method to verify the capacity of the thrust-vectoring system to stabilize a tailless aircraft.

The quasitailless configuration is a conservative and safe approach to testing the performance without the tail. It is safe because the tail can be brought back in place at any time, by switching back to the nominal flight control law. It is conservative because one can phase out the tail incrementally, using changes in the control laws instead of hardware, and fly the aircraft with, for instance, 25, 50, 75, or 100% of the tail removed.

The concept behind the Quasi-Tailless experiment is to simulate a tailless aircraft using the rudder and the differential flap to cancel the stabilizing effect of the vertical tail. No stabilizing command is then given to the rudder. Assuming that a linearized model for the tailless aircraft has been obtained from wind tunnel test, we can write:

$$\dot{x} = A_{TL}x + B_{TL}u_{TL}$$

Where the subscript TL stands for tailless. The state vector is $x = [p \quad r \quad \beta \quad \varphi]^T$ and the tailless controls are $u_{TL} = [\delta_{DF} \quad 0 \quad \delta_{TV}]^T$. In order to replicate the tailless dynamics using

the rudder and the differential flaps a destabilizing feedback controller was implemented. The X-31A dynamics can be written as:

$$\dot{x} = Ax + Bu_{TL} + Bu_{DS}$$

where the subscript DS identify the destabilizing input. A static feedback controller that replicates the dynamics of the tailless X-31A can be defined in the following way:

$$u_{DS} = K_{DS}x \qquad \Rightarrow \qquad \dot{x}=(A+BK_{DS})x + Bu_{TL}$$

and

$$(A+BK_{DS}) = A_{TL} \qquad \Rightarrow \qquad K_{DS} = (B^T B)^{-1} B^T (A_{TL} - A)$$

The matrix K_{DS} is represented by the blocks *DES_P*, *DES_R*, and *DES_B* in Fig. 3-3. From the figure it is possible to see that the destabilizing command of the rudder is also sent to the thrust vectoring with its sign changed. This command is also scaled by the ratio of control effectiveness. In this way the thrust vectoring is used to overcome the destabilizing effect of the rudder. A whole family of tailless dynamics, corresponding to different levels of tail removal, were calculated using wind tunnel data. This was an effective and simple way to simulate different levels of tail reduction. The Quasi-tailless flight test was accomplished in a large flight envelope covering both supersonic and subsonic speed. A simulated approach to a carrier and a ground attack profile were successfully flown (see Ref.3-2).

In this chapter we are going to present three different stability robustness tests that can be used to validate the X-31A FCL in the Quasi-Tailless configuration. The tests are based on a linearized model of the aircraft dynamics and were performed at a single flight point.

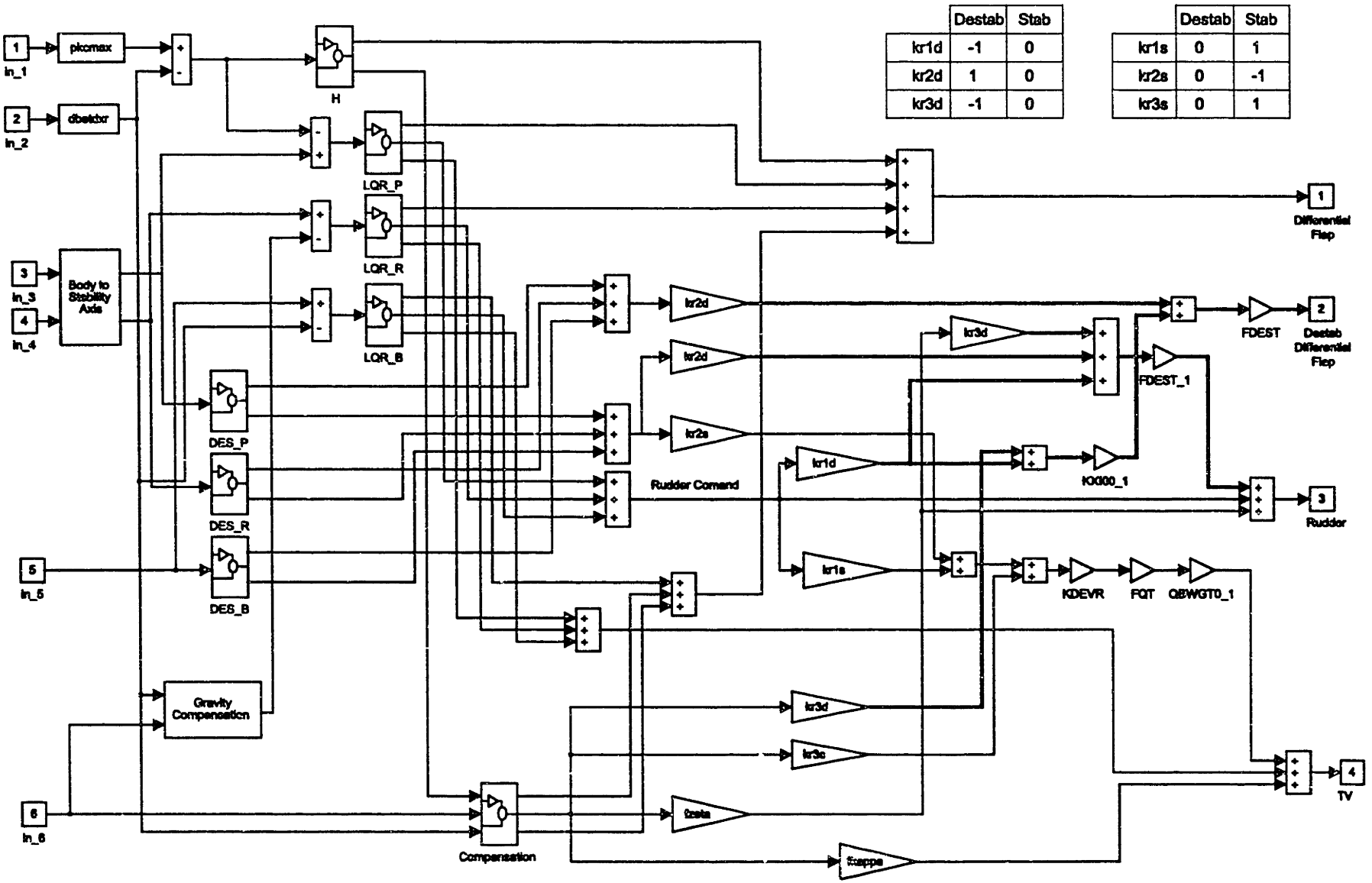

Fig. 3-3 X-31A Lateral Directional Flight Control Law for Quasi-tailless flight test.

The model employed represents the decoupled lateral dynamics of the aircraft linearized at Mach 0.6 and altitude 20,000 ft in straight level flight. The fourth order rigid airframe dynamics include three stable modes: a second order Dutch roll mode, a first order spiral mode, and a first order roll mode. The state vector is $x=[p \quad r \quad \beta \quad \varphi]^T$ and the tailless controls are $u_{TL}=[\delta_{DF} \quad \delta_R \quad \delta_{TV}]^T$. All the angles are measured in degrees. The state space matrices that describe the linear mode are:

$$\left[\begin{array}{c:c} A & B \\ \hdashline C & D \end{array}\right] = \left[\begin{array}{cccc:ccc} -1.9708 & 1.1512 & -29.9509 & 0 & -90.0515 & 12.0536 & 0.4005 \\ -0.0157 & -0.3857 & 3.3499 & 0 & -3.6307 & -3.7732 & -2.2436 \\ 0.1262 & -0.9888 & -0.1871 & 0.0512 & 0.0565 & 0.0401 & 0.0154 \\ 1.0000 & 0.1251 & 0 & 0 & 0 & 0 & 0 \\ \hdashline 1.0000 & 0 & 0 & 0 & 0 & 0 & 0 \\ 0 & 1.0000 & 0 & 0 & 0 & 0 & 0 \\ 0 & 0 & 1.0000 & 0 & 0 & 0 & 0 \\ 0 & 0 & 0 & 1.0000 & 0 & 0 & 0 \end{array}\right]$$

The angle of attack at this flight condition is α = 6.9566 deg. The robustness analysis was done using a *Simulink* block diagram of the linearized lateral directional dynamics. Fig. 3-4 is an example of the *Simulink* block diagrams utilized for the analysis, showing the main blocks that comprise the simulator. Linear models are implemented to simulate the actuators and the sensors.

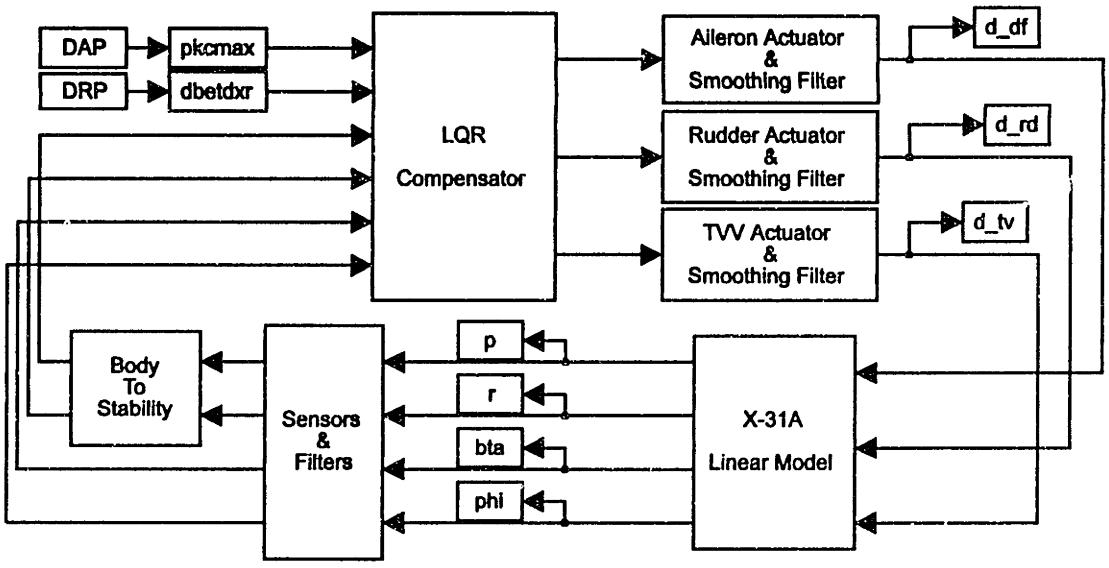

Fig. 3-4 X-31A *Simulink* block diagram of the closed loop system.

The LQR compensator block diagram is shown in Fig. 3-5. It is possible to identify the set of LQR gains and the redistribution of the thrust vectoring command to the other surface. The thrust vectoring is used only when the aerodynamic surfaces are not capable of delivering the required moment.

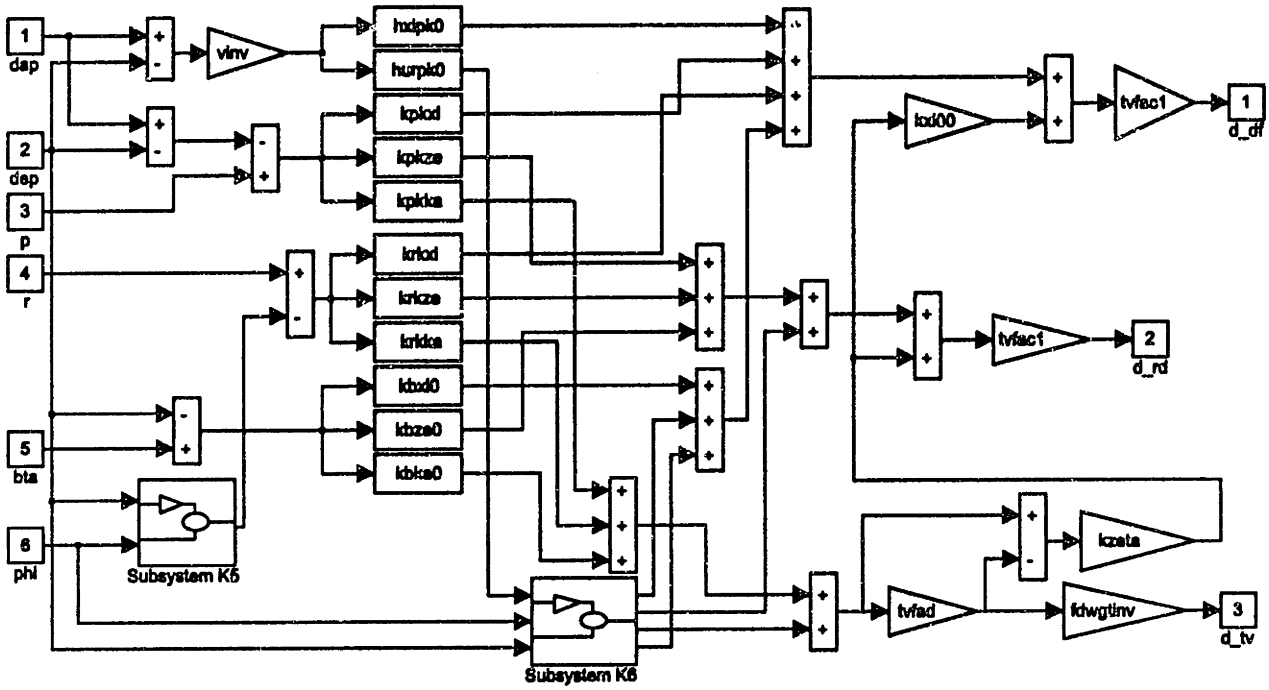

Fig. 3-5 X-31A Lateral-Directional LQR compensator.

This ends the description of the model utilized for the robustness test. In the next section we describe how to incorporate flying qualities requirements into a robustness test. In many practical situations a mere stability robustness test is not sufficient; we need instead to guaranteed acceptable performance levels. Detailed flying qualities requirements for both the longitudinal and lateral dynamics have been developed in the past; we will show how to incorporate these requirement into our robustness measures.

3.3 Lateral Directional Flying Qualities Requirements

When analyzing the robustness of a flight control system it is important to incorporate the requirements for flying and handling qualities. Lateral directional flying

qualities are partially specified based on closed loop pole locations, and these specifications form boundaries which can easily be incorporated into the robustness analysis.

The requirements that we will consider are those of a fighter (Class IV) in flight Category A. Our robustness analysis will reflect the desire to maintain level 2 flying qualities., in the face of variations in the stability derivatives of the aircraft. The specifications are:

- Spiral mode: min time to double 8 sec (real pole to the left of 0.0866)
- Dutch mode: min $\zeta_d = 0.02$;
  min $\zeta_d \omega_d = 0.05$;
  min $\omega_{nd} = 0.4$;
- Roll mode: max roll time constant 1.4 sec (real pole to the left of 0.7143)

Standard analysis indicates that the two modes that most greatly affect the robustness of the X-31 in the lateral directional axes are, in order of importance, the spiral mode and the Dutch roll mode. For this reason we incorporate only the requirements of this two modes. During the stability test we need to find the condition at which the spiral mode moves to the right of 0.0866 and the Dutch roll mode moves to the right of a line passing through zero at an angle of 91.2 deg or inside a circle centered at the origin of radius ω_{nd}. These requirements can be incorporated in our robustness analysis by simply calculating $\det(I-\Delta M(s))$, from the definition of μ, along the following contour in the s-plane.

$$s=\begin{cases} 0.0866 & \text{for} \quad \beta=0 \\ -\left(\omega_n^2-\beta^2\right)^{1/2}+j\beta & \text{for} \quad \beta\in[0,\ \sigma] \\ -\dfrac{1}{\tan\left(\cos^{-1}(\zeta_d)\right)}\beta+j\beta & \text{for} \quad \beta\in(\sigma,\infty) \end{cases} \qquad \sigma=\pi-\cos^{-1}(\zeta_d)$$

From the above equations it appears that the requirement for the Dutch roll mode is not as stringent as the one on the spiral mode; the un-perturbed closed loop pole is far from the required boundary. We can thus expect it not to be critical in our multivariable robustness analysis. On the other hand, the requirement on the spiral mode is very important to the analysis because the nominal closed loop pole of the spiral mode is slightly unstable.

Normally this condition would violate the assumptions of our robustness analysis framework, which require that the poles of the nominal system be to the left of the $j\omega$-axis, along which one normally computes μ. But because the handling quality requirements allow the spiral mode to be unstable, we can simply indent the contour a finite amount at $\omega = 0$, so that there are no nominal poles to the right of the contour along which we compute μ. The contour used in our μ analysis is shown in Fig. 3-6.

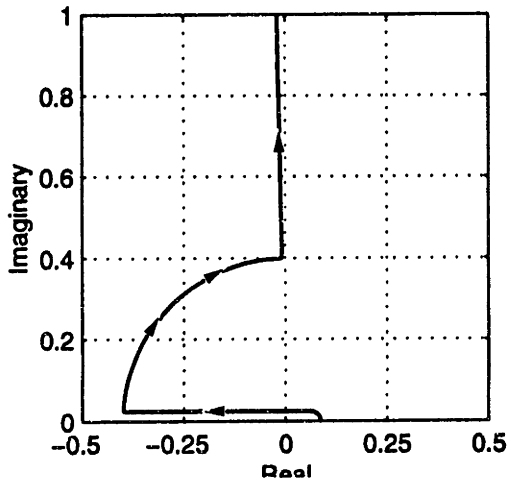

Fig. 3-6 s-plane contour for real-μ calculation.

This approach must be treated with caution; in general a perturbation Δ might cause the spiral mode to split with the roll damping mode a give rise to a complex conjugate pair — the contour chosen would then be invalid. In this example, the perturbations required to change the spiral mode dynamics to this extent are far outside the range of interest, and the analysis gives meaningful results.

In the next two sections we will apply this approach to two different situations. In the first example the robustness test is conducted on a set of uncertain aerodynamic parameters and the spiral mode is identified as the critical mode for stability. In the second example a robustly guaranteed phase margin in the thrust vectoring is calculated; in this case the Dutch roll mode is the mode violating the stability boundaries

3.4 Iterative Weighting to Isolate Important Lateral-Directional Aerodynamic Parameters of the X-31

In this example we use iterative weighting to determine the relative importance of several lateral-directional aerodynamic parameters to the robustness of a linearized X-31 lateral-directional control system. The analysis is performed at a Mach number of 0.6, an altitude of 20,000 ft., and a 50% Quasi-Tailless configuration.

In Tab. 3-1 are listed the elements of the A matrix that have been chosen as uncertain. Each element can be related to two aerodynamic derivatives; the first element in parenthesis is the aerodynamic derivative that most strongly affects the corresponding element in A.

Element	Aerodynamic Derivatives	Nominal Value
A(1,1)	$f(C_{L_p}, C_{N_p})$	-1.9708
A(1,2)	$f(C_{L_r}, C_{N_r})$	1.1512
A(1,3)	$f(C_{L_\beta}, C_{N_\beta})$	-29.9509
A(2,2)	$f(C_{N_r}, C_{L_r})$	-0.3857
A(2,3)	$f(C_{N_\beta}, C_{L_\beta})$	3.3499
A(3,3)	$f(C_{Y_\beta})$	-0.1871

Tab. 3-1 Uncertain elements in the A matrix and their aerodynamic dependence

Once the uncertain elements in the state space model are selected, we need to formulate the problem in the classical robustness framework. Morton and McAfoos in Ref.3-3 proposed a method to isolate the uncertain elements in the matrices of a state space models in a real uncertainty Δ-block. As an alternative to their approach, we can use a more intuitive and flexible method using *Simulink*. The state space model is described in a *Simulink* block diagram with each matrix element expressed as an individual gain. In Fig. 3-7 and Fig. 3-8 are shown the block diagram of the aircraft state space model with uncertain elements in the A matrix. It is clear that a similar procedure can be used to insert uncertainties in the other matrices of the model.

The state space model defined in Fig. 3-7 can then be inserted in the block diagram of Fig. 3-4 and the standard robustness problem can be formulated.

The next step is to define a weighting matrix that can give information about the relative importance of each element to the robustness measure. One way of doing this is to weight each element $A(i,j)$ with its own absolute nominal value multiplied by a scaling factor:

$$W(k) = \left|A_{NOM}(i,j)\right| \frac{w_k}{100}$$

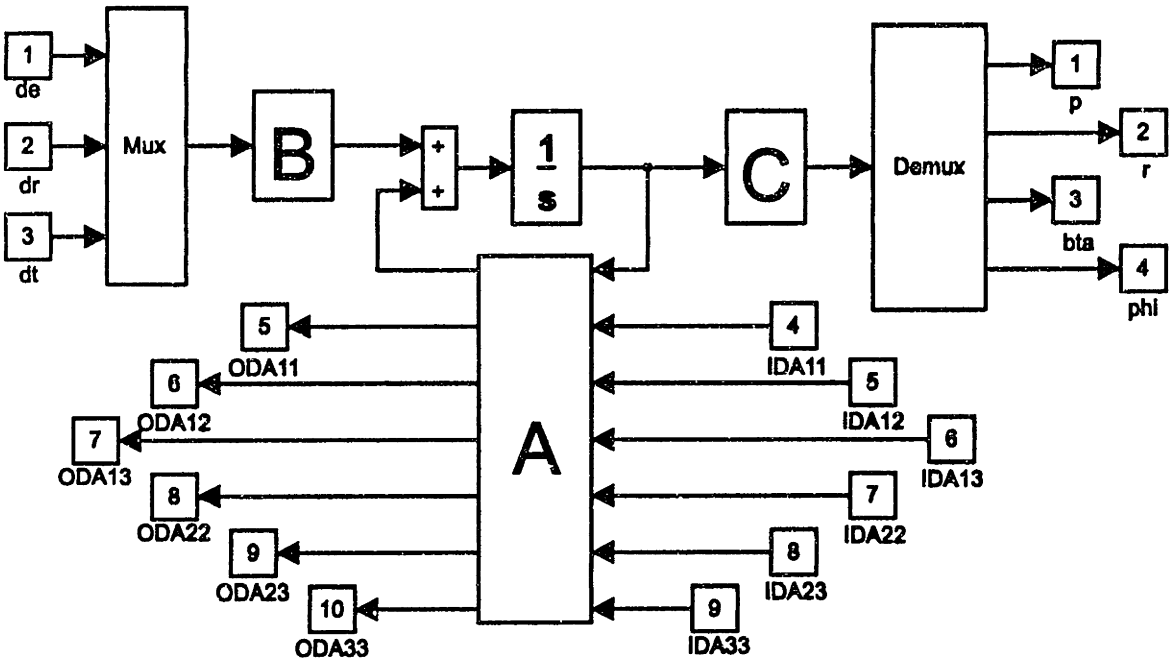

Fig. 3-7 State-space model with uncertainty in the A Matrix: *Simulink* block diagram.

The factor w_k represents the percentage variation from the nominal value. At each iteration stability will be guaranteed for variations of each element within:

$$A(i,j) \in \left|A_{NOM}(i,j)\right| \frac{w_k}{100} \frac{1}{\mu}$$

In the last equation μ is the maximum real structured singular value calculated with this set of weightings. Applying the iterative scaling procedure described in Chapter 2 it is possible to identify the elements that are most important for stability.

The initial scaling is chosen so that 100% variations in each element are given equal weighting; then the weighting procedure described in Chapter 2 is applied. In Tab. 3-2 are listed the combined percent uncertainty that are admissible simultaneously in each of the matrix elements.

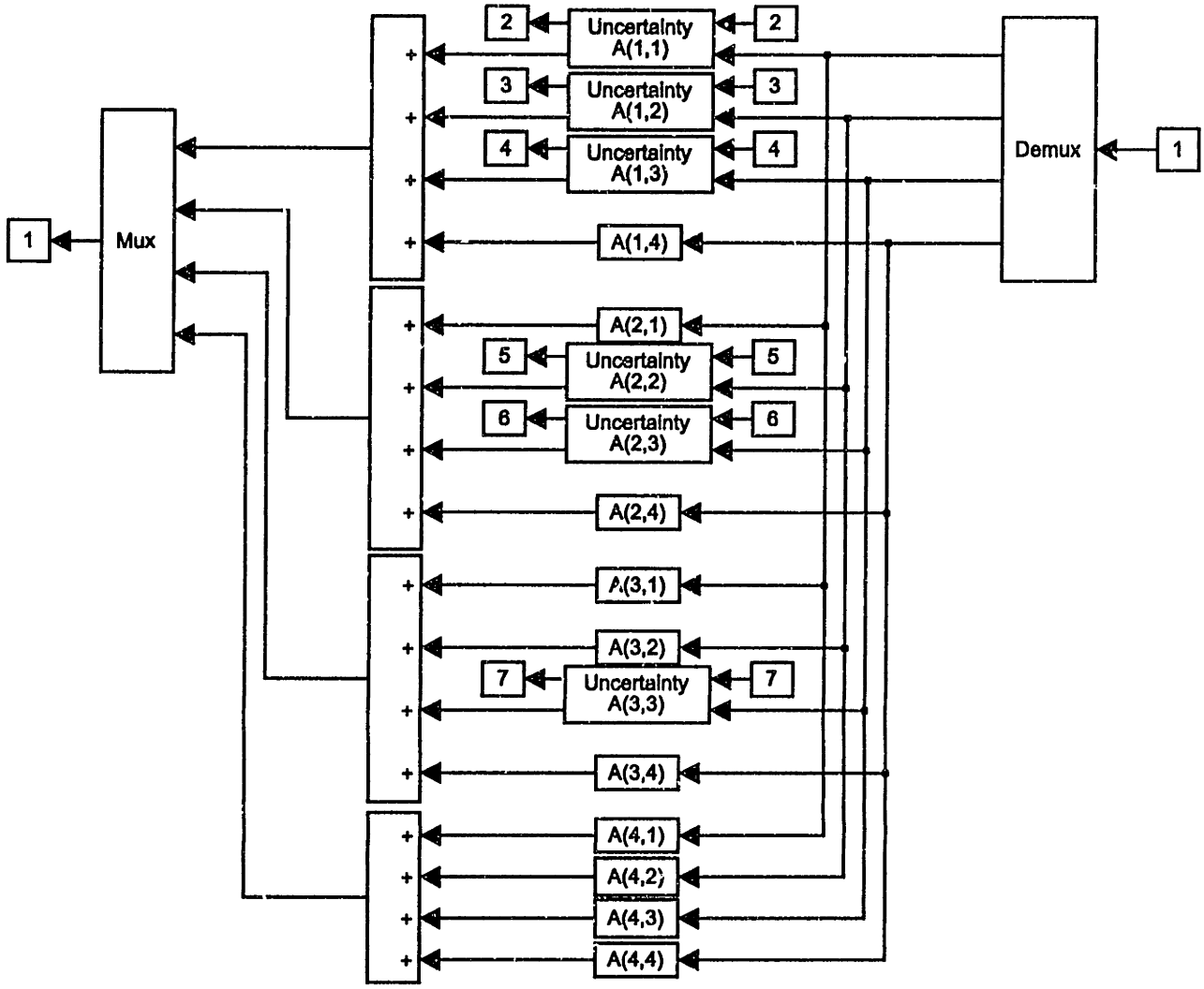

Fig. 3-8 A matrix with uncertain elements: *Simulink* block diagram.

In Tab. 3-2, note that the initial weighting allows equal magnitude percentage perturbations in all the elements. Also note that each solution of the weighted real μ problem (each row) carries a flag (denoted by a star in Tab. 3-2) indicating the element or the elements of the Δ-block that are responsible for the actual bound. The subsequent solution (next row) is computed with the starred elements of the previous solution reweighted as shown on the

top of the row. The weighting on the starred elements is reduced by 0.1 while the weighting on the non starred elements is increased by the same quantity. The allowable perturbation on the starred elements is thus reduced, allowing the less important parameters to vary over larger percentages.

Iteration	$\Delta A(1,1)$	$\Delta A(1,2)$	$\Delta A(1,3)$	$\Delta A(2,2)$	$\Delta A(2,3)$	$\Delta A(3,3)$
1	w = 1.0 43.08°[b]	w = 1.0 43.08	w = 1.0 43.08°	w = 1.0 43.08	w = 1.0 43.08	w = 1.0 43.08
2	w = 0.9 39.87°	w = 1.1 48.74	w = 0.9 39.87°	w = 1.1 48.74	w = 1.1 48.74	w = 1.1 48.74
3	w = 0.8 36.49°	w = 1.2 54.73	w = 0.8 36.49°	w = 1.2 54.73	w = 1.2 54.73	w = 1.2 54.73
4	w = 0.7 32.92°	w = 1.3 61.14	w = 0.7 32.92°	w = 1.3 61.14	w = 1.3 61.14	w = 1.3 61.14
5	w = 0.6 29.14°	w = 1.4 68.00	w = 0.6 29.14°	w = 1.4 68.00	w = 1.4 68.00	w = 1.4 68.00
6	w = 0.5 25.13°	w = 1.5 75.38	w = 0.5 25.13°	w = 1.5 75.38	w = 1.5 75.38	w = 1.5 75.38

a Each row defines a stable hypercube of perturbations associated with the weighting (w) on top; the union of these hypercubes is also guaranteed stable.

b Stars indicate the edge of the hypercube of perturbations that is striking the true stability boundary.

Tab. 3-2 Percent of allowable variations in the aerodynamic elements of the X-31 lateral directional control system (0% Quasi-Tailless)

After only six iterations on weightings, the algorithm concludes that the two most important elements (in terms of the multivariable stability of the overall system) are the *A(1,1)* and *A(1,3)* elements. From the last iteration we can see that if these elements are known within 25% accuracy, then all the other elements need to be known only with an accuracy of 75%. In this application the worst case perturbation vector, calculated with Dailey's algorithm, always had the same two elements equal to its norm; for this reason at each iteration we were scaling down two elements, *A(1,1)* and *A(1,3)*, and up all the other elements. The elements of the worst case perturbation vector calculated from the *Matlab* lower bound are instead identical; therefore this vector cannot be used to identify the elements that dominate the robustness measure. The μ upper and lower bounds calculated at each iteration are shown in Tab. 3-3. The unscaled worst case perturbation vectors (real element variations) are show in Tab. 3- 4.

Iteration number	1	2	3	4	5	6
Upper bound (μ-tool)	2.3211	2.2572	2.1923	2.1262	2.0587	1.9898
Lower bound (μ-tool)	2.3210	2.2571	2.1922	2.1260	2.0586	1.9898
New Lower bound	2.3210	2.2571	2.1922	2.1260	2.0586	1.9898

Tab. 3-3 Real μ upper and lower bounds.

Iteration	ΔA(1,1)	ΔA(1,2)	ΔA(1,3)	ΔA(2,2)	ΔA(2,3)	ΔA(3,3)
1	0.8491	0.4960	12.9044	-0.1662	-1.4433	0.0806
2	0.7858	0.5610	11.9427	-0.1880	-1.6326	0.0912
3	0.7192	0.6302	10.9302	-0.2111	-1.8338	0.1024
4	0.6489	0.7039	9.8614	-0.2359	-2.0484	0.1144
5	0.5744	0.7829	8.7294	-0.2623	-2.2782	0.1272
6	0.4952	0.8679	7.5262	-0.2908	-2.5254	0.1410

Tab. 3- 4 Worst case perturbation vectors

Physically the elements *A(1,1)* and *A(1,3)* correspond to the aerodynamic coefficients C_{Lp} and $C_{L\beta}$, both of which have a strong influence on the spiral instability of the aircraft. Throughout the analysis, the frequency corresponding to the maximum μ was always the zero frequency. This frequency corresponds to a real pole, the spiral mode, violating the stability requirement. Tab. 3-5 shows the location of the closed loop poles when the worst case perturbation was applied to the system. The last row of the table indicates the location of the poles at the nominal conditions. It is always the spiral mode that reaches its performance limit, the Dutch roll mode on the contrary remains well within its acceptable limits. In Fig. 3-9 are shown the locations of the closed loop poles in the worst case scenario.

Iteration	Spiral mode	Dutch roll mode	Roll subsidence
1	0.0872	-4.9537±1.7008I	-2.2427
2	0.0871	-4.9809±1.6239I	-2.2468
3	0.0870	-5.0097±1.5401I	-2.2442
4	0.0869	-5.0398±1.4478I	-2.2339
5	0.0868	-5.0706±1.3447I	-2.2153
6	0.0867	-5.1010±1.2270i	-2.1874
Unperturbed Locations	0.0286	-2.9948±2.7080	-3.9056

Tab. 3-5 Close loop pole location at the worst perturbation

Another important characteristic of real μ that becomes evident in this example is the discontinuous nature of this robustness measure. The value of μ is discontinuous at the zero frequency, where it reaches its maximum. This example shows the importance of checking the zero frequency, to see if there is any real pole that crosses the $j\omega$ axis at zero. In general there can also be other frequencies where μ is discontinuous and takes values that are higher than expected.

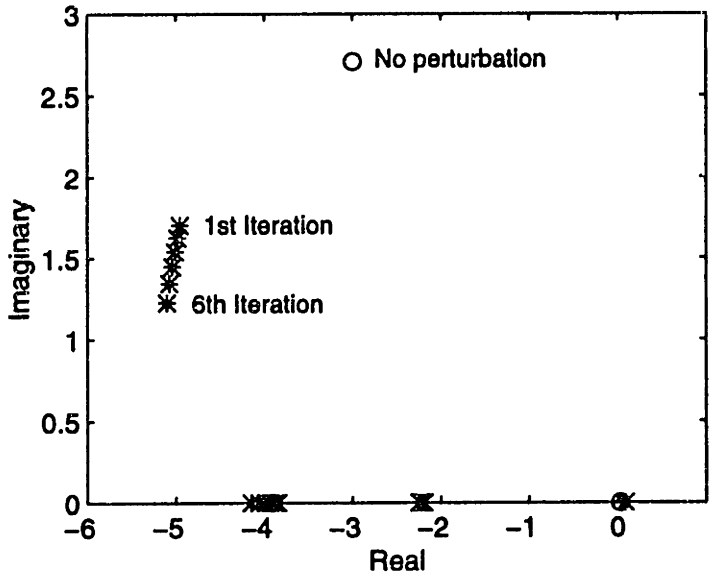

Fig. 3-9 Worst case perturbation root locus.

In Fig. 3-10, Fig. 3-11, and Fig. 3-12 are shown the μ plot corresponding to three different iterations. In the upper left corner is shown the value of μ at the zero frequency. In the same figures are shown the upper and lower bound calculated with *Matlab* and our new algorithm. We can see that there is a prefect match between the two lower bounds when *Matlab* is able to converge to a solution.

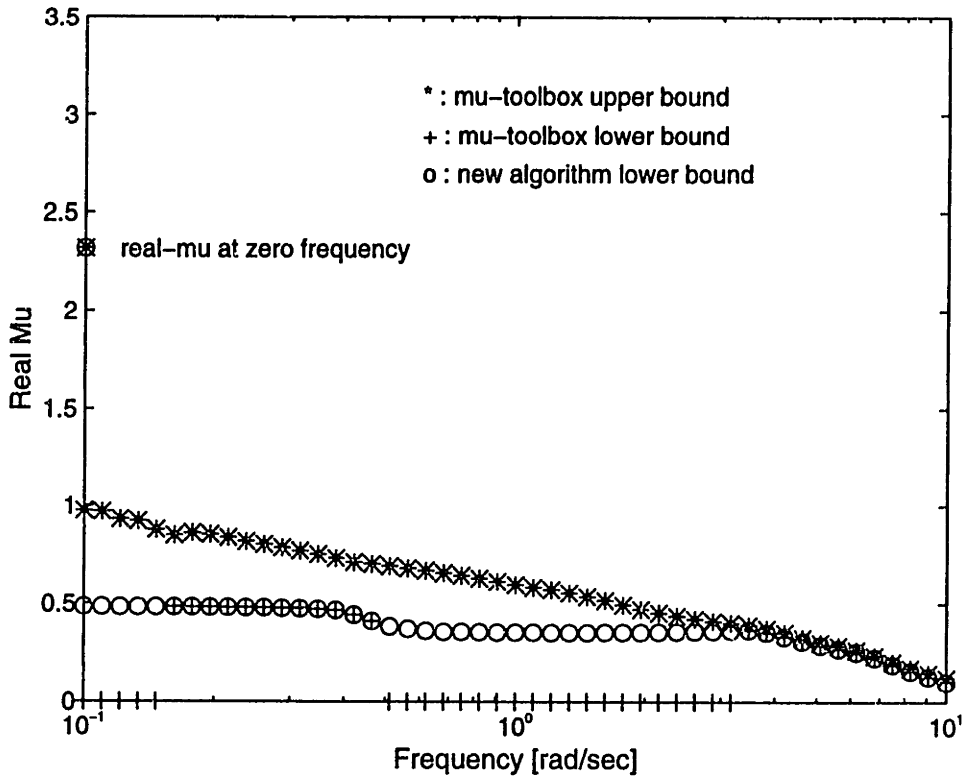

Fig. 3-10 Iteration 1: real μ upper and lower bounds.

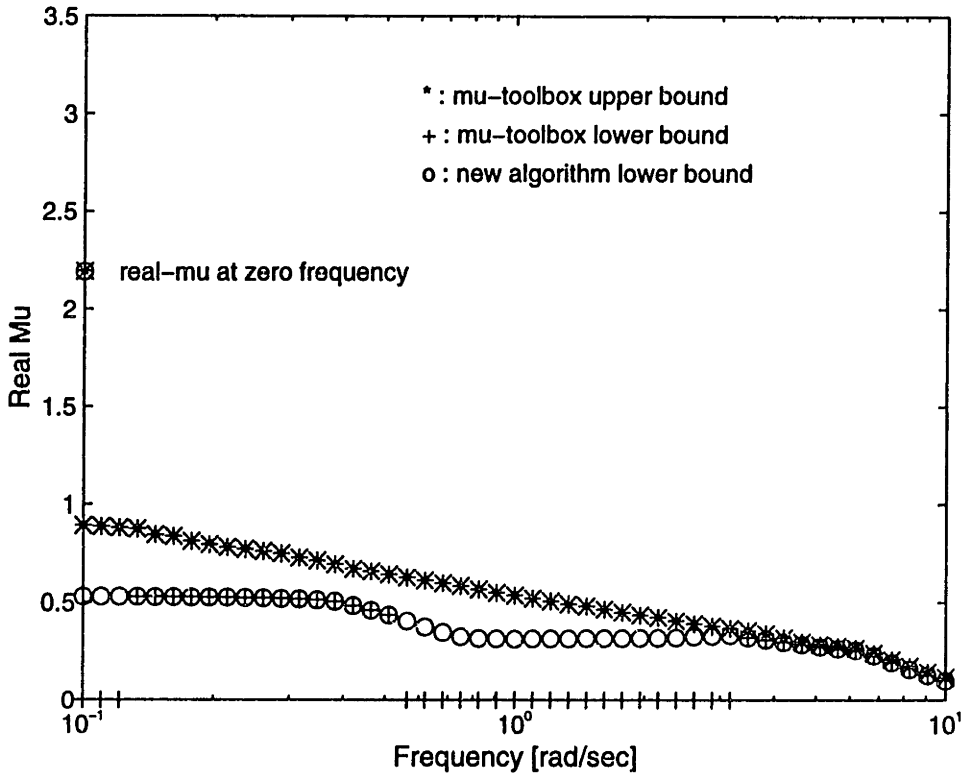

Fig. 3-11 Iteration 3: real μ upper and lower bounds.

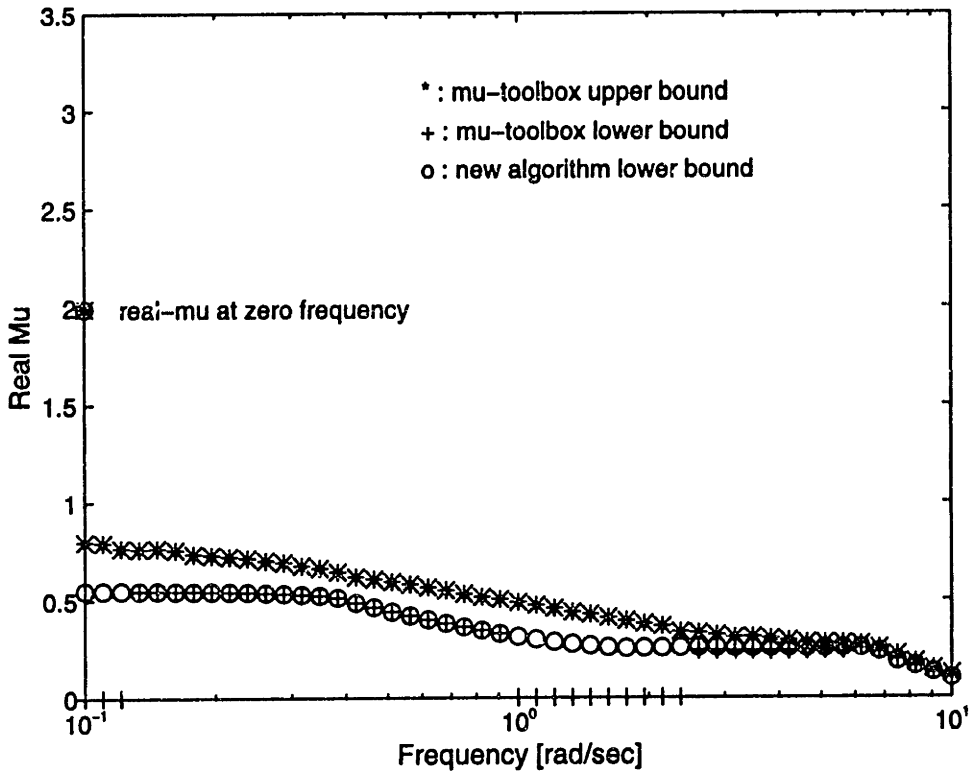

Fig. 3-12 Iteration 6: real μ upper and lower bounds.

3.5 Quasitailless X-31: Robustly guaranteed Phase Margins

In this section we utilize the phase-margin block structure introduced in Chapter 2 and present the concept of a robustly guaranteed margin, which is simply a phase margin or gain margin that is guaranteed to hold in the face of other plant parameters variations. Once again the X-31 Quasi-Tailless flight test is used to illustrate this concept.

The aerodynamic derivatives of the X-31 will change significantly in the tailless configuration. The derivatives that will change the most, and are thus subjected to the highest uncertainty, are those related to the size of the tail and those related to the lateral-directional control power of thrust vectoring: $C_{L\beta}$, $C_{N\beta}$, C_{Nr}, $C_{L\delta_{TV}}$, and $C_{N\delta_{TV}}$. These derivatives, in turn, factor almost directly into the state-space system matrix elements *A(1,3)*, *A(2,3)*, *A(2,2)*, *B(1,3)*, and *B(2,3)*.

Using the weighting procedure described in Chapter 2 and looking at single-input/single-output (SISO) and multi-input/multi-output (MIMO) gain and phase margins, we have identified the phase margin in the thrust vectoring channel as the most direct measure of directional stability in the quasitailless configuration (reduced rudder authority increases the importance of thrust vectoring for stability). The question that we pose is the following: What is the phase margin in the TV channel for different percent uncertainties in the most important aerodynamic derivatives? In other words, what phase margin can we guarantee in the presence of 30, 40, and 50% uncertainty in the derivatives listed earlier?

Fig. 3-13 shows the *Simulink* block diagram utilized for this example. The uncertainties in the state space model are incorporated into the robustness problem using a *Simulink* expansion of the linear models (as discussed in section 3.4). The five uncertainties in the plant, and the phase uncertainty in the thrust vectoring channel are apparent in this figure. A first order Padè approximation was used to calculate the phase margin.

Fig. 3-14 shows the SISO and MIMO (i.e. *robust*) phase margins in the TV channel as functions of the percent tail reduction. The solid thick line represents the SISO phase margin in the case that there are no uncertainties in the aerodynamic parameters. As expected, the SISO phase margin is always higher than the MIMO phase margin. With 10% aerodynamic uncertainty we have an average reduction of the phase margin of about 2 degrees, with 20% uncertainty the reduction is 4 degrees, with 30% it is 8 degrees, and with 40% it is 11 degrees. Under the SISO line lies also the line corresponding to a 1% uncertainty, with such a small uncertainty it is not possible to distinguish the two curves. Considering that the SISO phase margin was calculated not using the real-μ algorithm, this confirms the precision of the algorithm that we used for the robustness analysis.

The conclusions one reaches from this plot is as follows: if a 45 degree phase margin is required for flight safety at this flight condition, the SISO phase margins suggest that one can fly up to about 73% quasi-tailless. On the other hand, the MIMO robust phase margin indicates that, with 20% uncertainty in the uncertain elements, one should not fly above 59% tailless. With 30% and 40% percent uncertainty in the aerodynamic parameters, one is confident to fly only up to 48% and 40% quasi-tailless respectively. These results corroborate

results at NASA Dryden obtained through more conventional engineering analysis of the quasi-tailless configuration. Precision approach tasks were successfully flown with quasi-tailless settings of 40 and 50 percent. During these flight the pilots didn't feel changes in the flying qualities caused by the quasi-tailless mode.

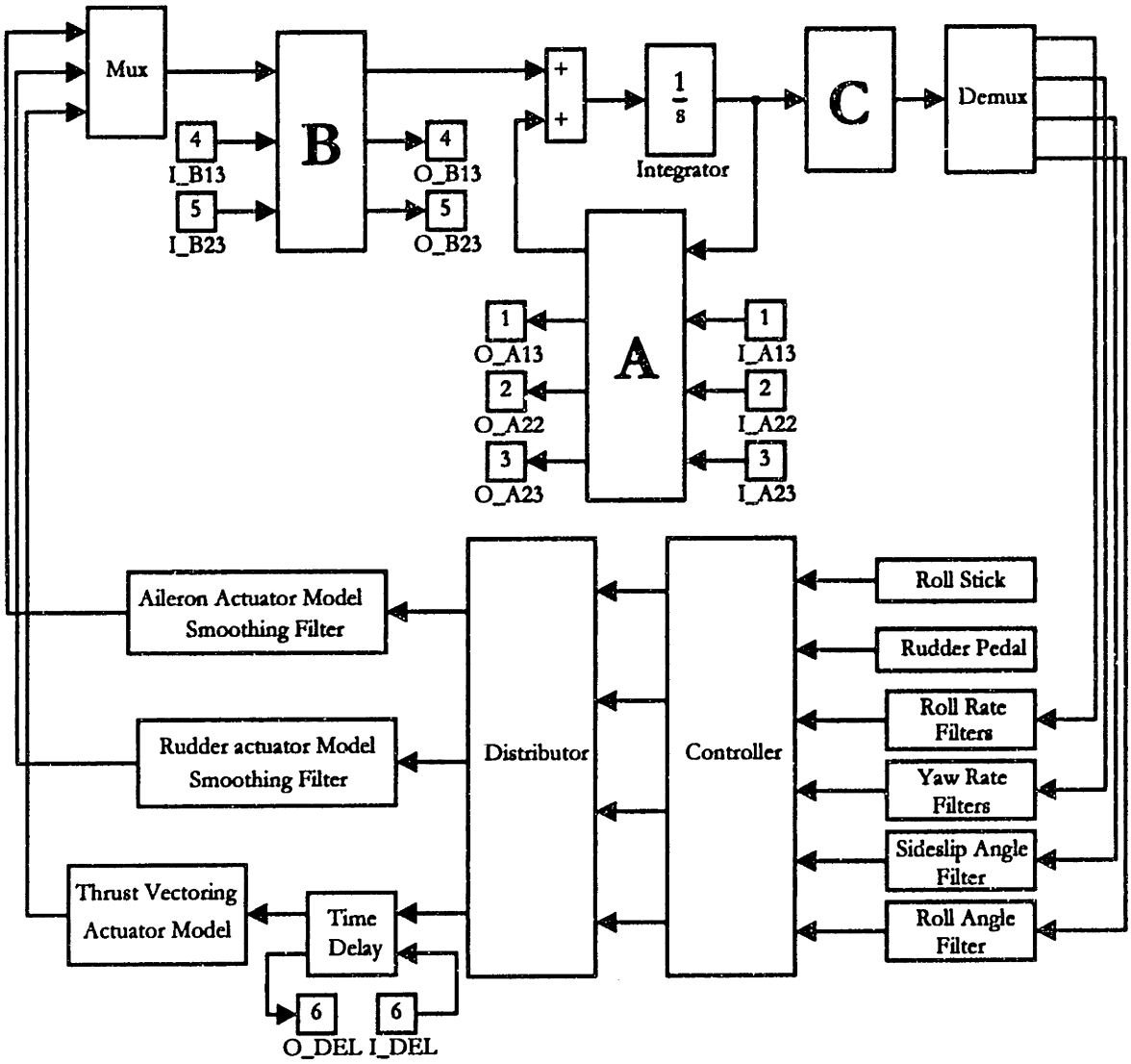

Fig. 3-13 X-31 Lateral Directional Closed Loop System for the robustly guaranteed phase margins - *Simulink* block diagram.

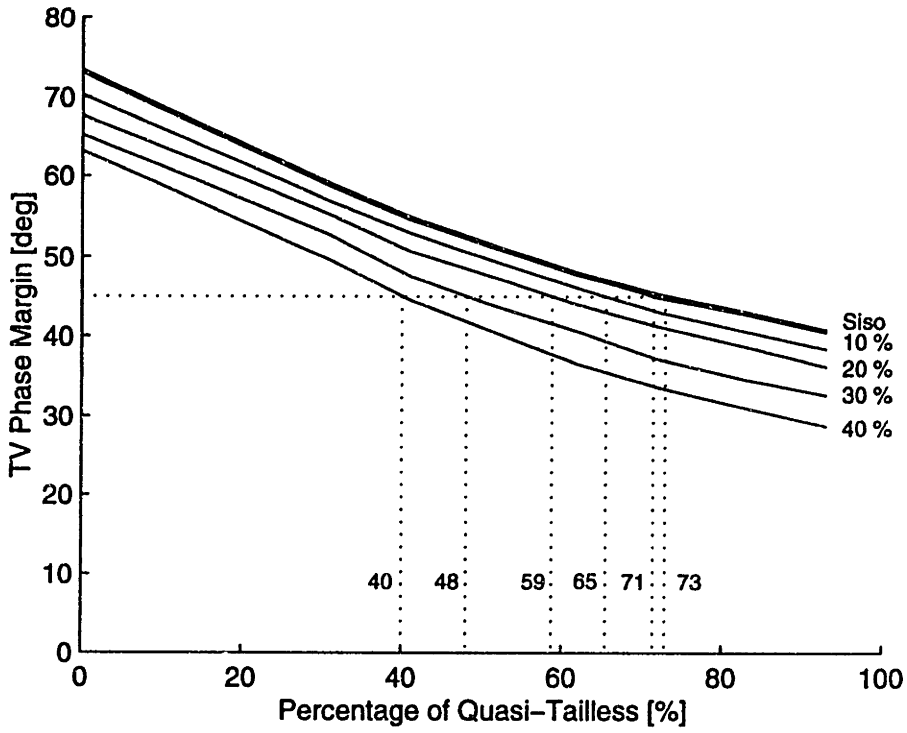

Fig. 3-14 Robustly guaranteed phase margin in thrust vectoring channel for various levels of uncertainty in a set of five aerodynamic coefficients.

Fig. 3-15 and Fig. 3-16 show the real μ plots for 30% uncertainty level at the 52% and 72% tailless condition. The two solid lines are the *Matlab* μ upper bound and the lower bound calculated with the new algorithm. The dots represent the *Matlab* lower bound. On the left is also shown the value of μ at zero frequency; in this case the spiral mode is not critical and the value of μ at zero frequency is not the maximum μ. The maximum μ is always reached at a frequency between 4 and 6 rad/sec, corresponding to the Dutch roll mode violating the performance boundaries in the s-plane. In the previous example, when only aerodynamic uncertainties were considered, the Dutch roll mode was not critical for stability. In this case instead the addition of a phase uncertainty makes the Dutch roll the critical mode for stability. The locations of the closed loop poles when the worst case perturbation is applied are shown in Tab. 3-6. These values correspond to 30% uncertainty in the model. We can see that the spiral mode is almost unchanged from its nominal (0.0286) and actually becomes more stable. The Dutch roll mode is almost on the performance boundary. From the real-μ plots we can see that there is some uncertainty in the frequency where μ is

maximum; this affects the calculation of the maximum time delay and the exact location of the closed loop poles.

In order to find the robustly guaranteed phase margin, an iterative weighting procedure, that finds the weightings for which μ is equal to one, was implemented. In all the cases we found that the size of the stable hypercube was set by the phase margin in the thrust vectoring channel, so the value of the weighting on the phase uncertainty when μ is equal to one is exactly our phase margin (before correction). Indicating with W_ϕ the weighting on the phase uncertainty, the weighting for the next iteration was defined as:

$$W_\phi(New) = \frac{W_\phi}{\mu}$$

Using this iterative scheme the algorithm was converging to $\mu = 1$ after about 10 iterations (using W = 90 deg at the first iteration).

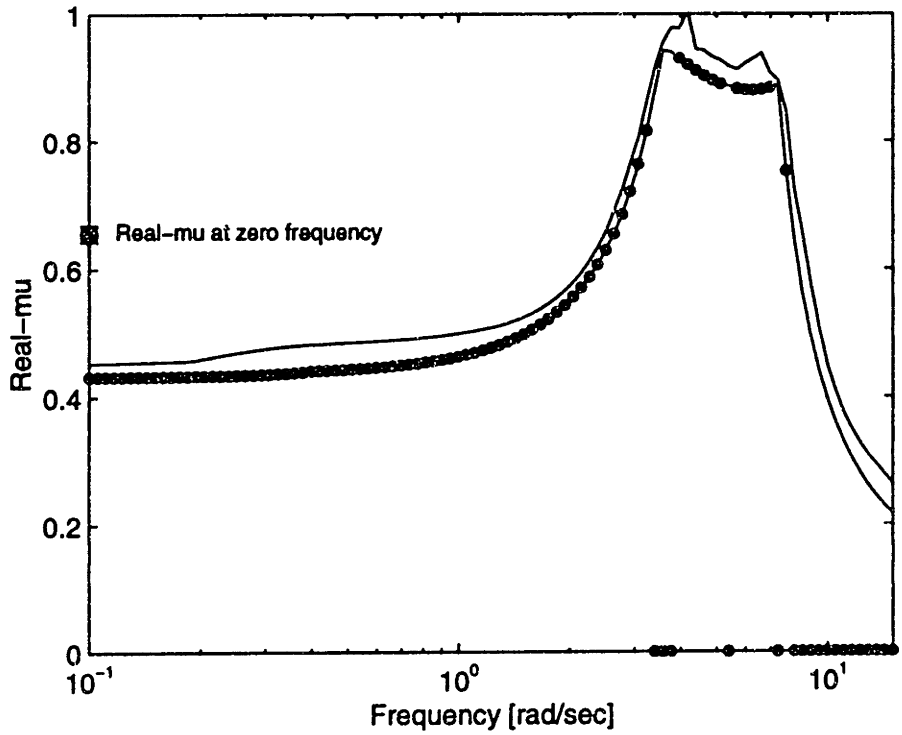

Fig. 3-15 μ upper and lower bounds at 30% uncertainty level and 41% Quasi-Tailless. Dots represent the *Matlab* real-μ lower bound.

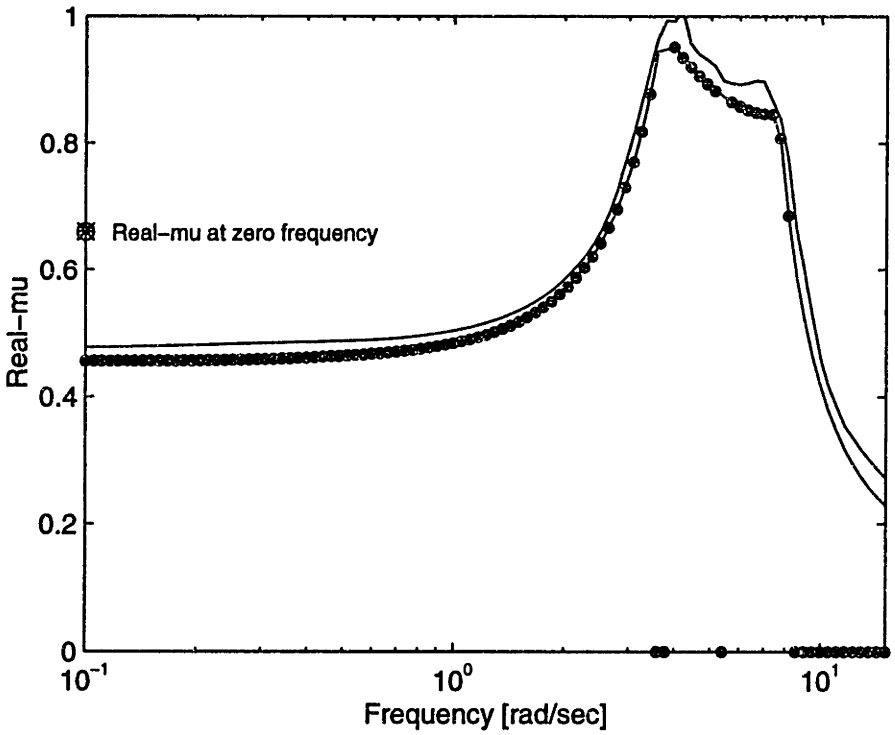

Fig. 3-16 μ upper and lower bounds at 30% uncertainty level and 62% Quasi-Tailless. Dots represent the *Matlab* real-μ lower bound.

Tailless %	Spiral mode	Dutch roll mode	Roll subsidence
0	0.0191	-0.4672±i6.5822	-1.3168
31	0.0192	-0.2402±i4.1611	-3.1413
41	0.0190	-0.2781±i4.1589I	-3.5584
52	0.0190	-0.2520±i4.1330	-3.7644
62	0.0189	-0.2633±i4.1243	-3.8570
72	0.0189	-0.2608±i4.1137	-3.8978
83	0.0187	-0.3014±i4.1132	-3.9215
93	0.0186	-0.3707±i4.3218	-3.9339

Tab. 3-6 Close loop pole location at the worst perturbation

The last consideration that we want to make from this example is about the discontinuous nature of real μ. Fig. 3-17 shows the plots of the μ lower bounds for different levels of uncertainty in the model. If there is no uncertainty, real-μ is discontinuous and μ is real only at the exact frequency where the phase margin is located. As the uncertainty level in the other parameters is increased, μ becomes real in a larger and larger portion of the

frequency axis. With small levels if uncertainty the calculation of a good phase margin can be critical, in order to have a good estimate we need to have a very fine frequency grid at least in the region where μ is maximum. If the grid is not fine enough there is the risk of considering a value of μ that is much lower than in reality or in some cases we can completely miss the peak and calculate the maximum μ at the peak occurring in some other frequency region.

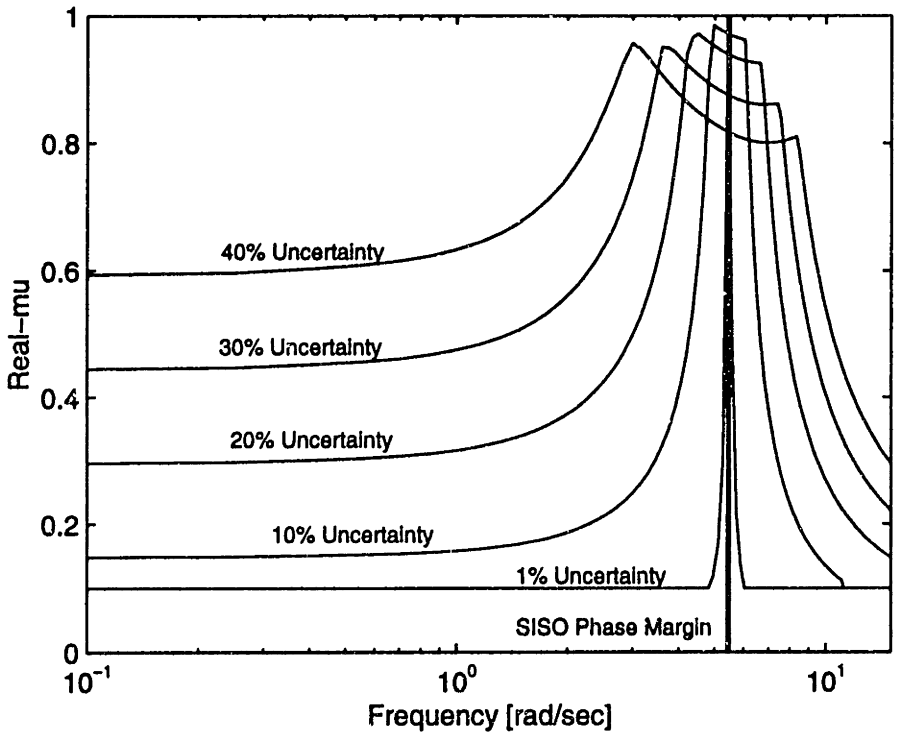

Fig. 3-17 Real-μ lower bound for different values of the uncertainty level. These values are calculated for 62% Quasi-Tailless.

3.6 Implementation of Robustness Measures During Flight Test

Having discussed a technique for analyzing the generalized robustness problem, and given methods to apply the procedure to answer specific questions, we turn now to the problem of implementing multivariable robustness measures during flight test. We address two issues in this context. The first is the question of how to incorporate experimental data into the problem; here we treat only uncertainties that can be reflected external to the measured plant dynamics. The second issue is what specifically to display in the control room to provide easily interpreted information to the flight test engineers. In this case we need to keep in mind that we have a limited time for computations.

The question of what to include in the delta-block structure is also of interest; for our example we choose simultaneous gain and phase margins at the plant input simply because single-loop gain and phase margins are common practice at NASA Dryden. Thus multivariable margins provide a smooth transition from currently used measures of system robustness.

The procedure shown here is a relatively straight-forward extension of the technique implemented by Burken, who applied complex structured singular values to open-loop transfer functions measured in flight. Procedures for determining open-loop transfer functions in flight are also described by Burken (Ref.3-4), and will not be repeated here. It suffices to give a brief description of the motivation and background of the problem.

During an envelope-expansion type flight test, a central goal is to determine whether the behavior of the system is enough like that predicted to allow the next flight condition to be confidently flown. One technique currently used at NASA Dryden to assess how well the overall system is behaving, is in-flight phase and gain margin determination. Using either injected signals or pilot inputs, the system's open loop transfer function is deduced using spectral analysis techniques. During flight the aircraft operates in closed loop as shown in Fig. 3-18. A frequency sweep signal is inserted directly on the control surfaces and is

represented in this case by $r(t)$. During closed loop testing the open loop plant transfer function $G(j\omega)$ is determined from the equation:

$$G(j\omega) = Y(j\omega) * \left(I + X(j\omega)\right)^{-1}$$

The matrix $Y(j\omega)$ is the cross spectral spectral density function of the signals $r(t)$ and $y(t)$, while $X(j\omega)$ is the cross spectral spectral density function of $r(t)$ and $x(t)$.

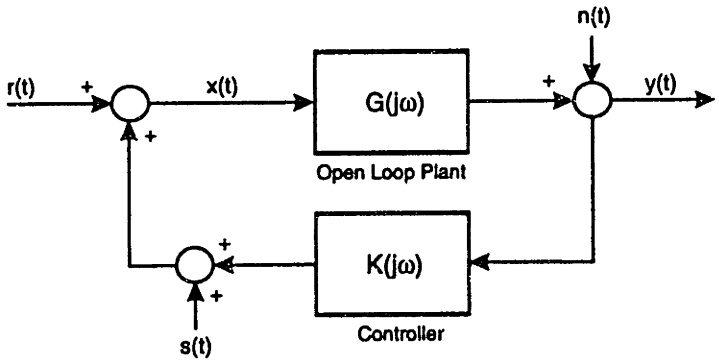

Fig. 3-18 A closed loop system.

Direct estimation of $G(j\omega)$ based upon $x(t)$ and $y(t)$ gives biased results and unfeasible frequency response. A detailed explanation on non-parametric system identification in the case of closed loop systems can be found in Ref.3-5 and Ref.3-6.

The experimental transfer function $G(j\omega)$ is next used to determine the actual gain and phase margins of the control system. As systems become more complicated and multivariable, it is of interest to generalize this procedure to a multivariable robustness evaluation procedure. Robustness can be defined in the general framework described above, but one must work out how to incorporate experimental data into the analysis procedure.

The plant transfer function is represented by the frequency domain transfer function $G(j\omega)$, and the controller by the transfer function $K(j\omega)$. We will assume that the controller transfer function is perfectly known and that an estimate of the plant transfer function has been obtained during flight. Fig. 3-19 shows the interconnection of the resulting stability robustness problem.

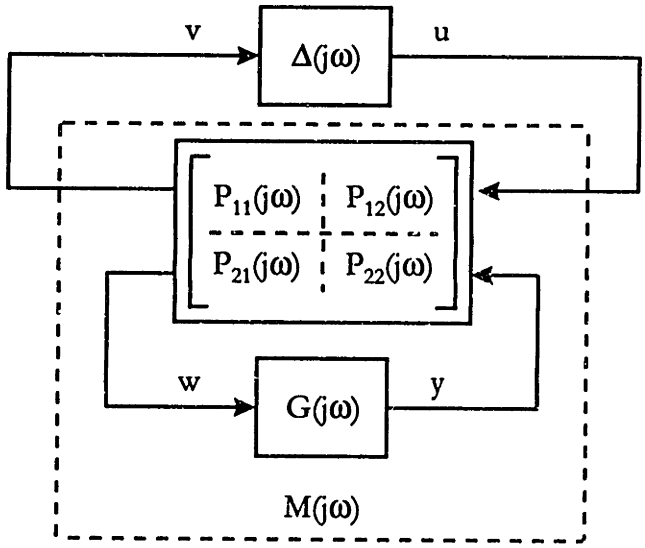

Fig. 3-19 Stability robustness problem for an experimental plant transfer function.

We have the following relations:

$$\begin{bmatrix} v \\ w \end{bmatrix} = \begin{bmatrix} P_{11} & P_{12} \\ P_{21} & P_{22} \end{bmatrix} \begin{bmatrix} u \\ y \end{bmatrix}$$

and the transfer function from u to v can be expressed as:

$$M = P_{11} + P_{12}G\left(I - P_{22}G\right)^{-1}P_{21}$$

In this representation the P matrix represent the part of the transfer function M that is perfectly known, (i.e. a manipulated version of the controller K), while G is the estimated transfer function of the aircraft plus actuators and sensors (from measurable inputs to measurable outputs). Using this equation, one can translate $G(j\omega)$ into $M(j\omega)$ which is the matrix transfer function required for robustness analysis. Once this experimental $M(j\omega)$ is found, all the analytical procedures described in the previous chapter can be applied.

The *Simulink* block diagram of the linearized X-31A lateral-directional flight control system is presented in Fig. 3-20. We have inserted gain and phase uncertainties at the plant input, but any other set of uncertainties in the control system is possible; uncertain delays, phases, and gains can be placed anywhere in the *Simulink* block diagram. We are again

analyzing the quasi-tailless configuration: thus we are interested in determining from flight data the robustness of the aileron and thrust vectoring channels.

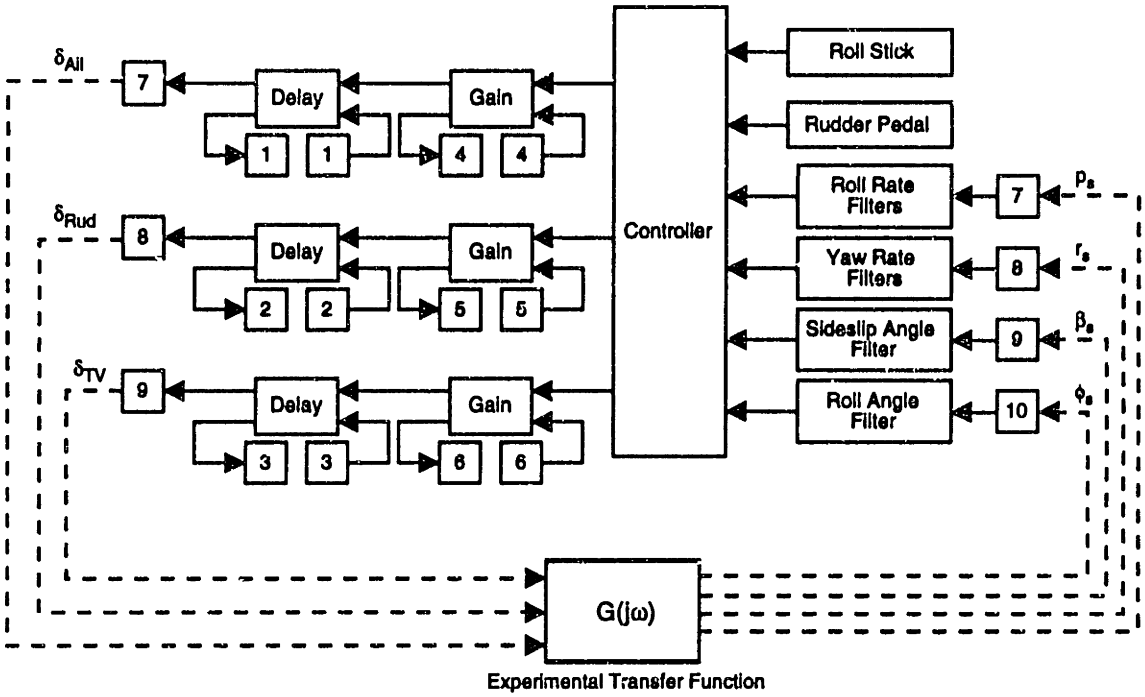

Fig. 3-20 *Simulink* block diagram for experimental multivariable phase and gain margins.

The requirements for gain and phase margin are shown in Tab. 3-7. The gain and phase margin on the rudder channel have been intentionally reduced because this is the channel used to destabilize the aircraft and simulate the tailless condition. The other values are reasonable combined multivariable gain and phase margins based on simulation studies.

	Aileron	Rudder	TV
Delta Gain	0.5	0.1	0.5
Delta Phase [deg]	20	5	20

Tab. 3-7 Gain and Phase margin requirements for in-flight robustness analysis

The question is now: are the above values of gain and phase margin simultaneously guaranteed in a given actual flight condition? Gain and phase margins at a given point are just one of many aspects that must be verified before moving to the next flight point in a flight

envelope expansion. Thus it is important to have a near real time measure that can be quickly interpreted.

A simple way to check robustness is through a properly weighted μ-plot. If we choose the weighting such that $\|\Delta\| = 1$ corresponds to the gain and phase boundaries shown above, then we know that stability is guaranteed within the given uncertainty level if the real-μ plot is less than one. Fig. 3-21 shows the plot of the upper and lower bound of real-μ calculated using an 'experimental' $G(j\omega)$ from a nonlinear simulation, implemented in the framework described above. Frequency sweeps on each control surface were injected in the nonlinear simulator to simulate an in-flight system identification. The data were collected and an 'experimental' transfer function was calculated. Note that either the lower bound or the upper bound provide an excellent measure of the actual proximity of the system to the minimum robustness level set by the weighting, and that the flight test engineer need only check the proximity of the plot to 1 to get a quick picture of the robustness situation.

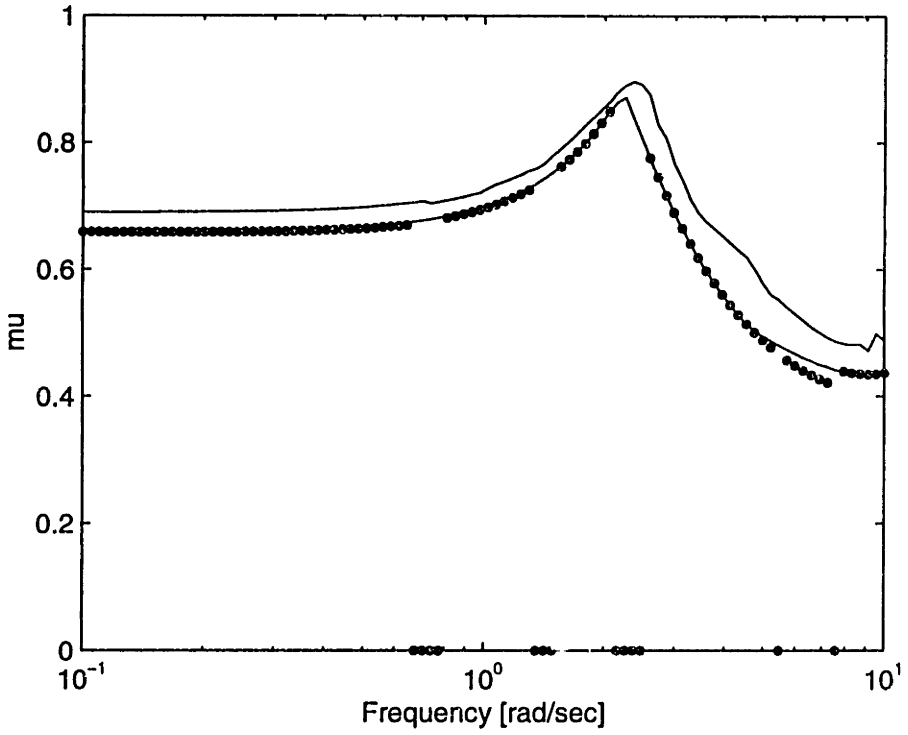

Fig. 3-21 Experimental Robustness Evaluation. Real-μ upper and lower bounds.

From the μ-plot we can see that μ is less than 1. This means that the requested gain and phase margins are fulfilled in this flight condition, even in the worst case scenario. We can see that μ has its peak at about 2.4 rad/sec which corresponds to an underdamped Dutch roll mode crossing the $j\omega$ axis. The worst case perturbation vector calculated by the new lower bound is shown in Tab. 3-8. This vector indicates that the worst scenario corresponds to the largest delay and gain reduction in the thrust vectoring channel, the maximum anticipation and amplification of the rudder channel. Note that the rudder channel is the destabilizing channel. The same conclusion can be reached by simple physical considerations: delay and reduce the stabilizing control and anticipate and emphasize the destabilizing signal. The phase in the thrust vectoring channel, as already emphasized in the previous example, is the element playing the most important role in the stability of the system.

Φ_{AIL}	Φ_{RUD}	Φ_{TV}*	G_{AIL}	G_{RUD}	G_{TV}
1.1025	-5.7566	22.7424	0.5761	0.1152	-0.5761

Tab. 3-8 Worst Case Perturbation Vector. Positive phase indicates a lag. The starred element is the one fixing the maximum μ.

This kind of analysis can be easily implemented in a flight test program. Therefore we believe that such techniques can give immediate information about the robustness of the flight control system. An in-flight robustness test can greatly help the flight test engineer in the decision to move to the next point in a flight envelope expansion.

3.7 Reference

Ref.3-1 H. Beh and G. Hofinger, "X-31A Control Law Design", *Technology for Highly Maneuverable Aircraft*, AGARD CP-548, Mar. 1994, pp. 13-1/13-9.

Ref.3-2 J. Bosworth and P. Stolicker, "The X-31A Quasi-Tailless Flight Test Results", NASA Technical Paper 3624, June 1996.

Ref.3-3 B. Morton and F. McAfoos, "A μ test for robustness analysis of a real parameter variation problem", *Proc. American Control Conference*, 1985, pp. 135-138, Boston.

Ref.3-4 J. Burken, "Flight-Determined Stability Analysis of Multiple-Input-Multiple-Output Control Systems", NASA TM-4416, November 1992.

Ref.3-5 P. Wellstead, "Non-Parametric Methods of System Identification", Automatica, Vol.17, No. 1, pp. 55-69, 1981.

Ref.3-6 A Pototzky, C. Wieseman., S. Hoadley, and V. Mukhopadhyay, "Development and Testing of Methodology for Evaluating the Performance of Multi-Input/Multi-Output Digital Control Systems", NASA Technical Memorandum 102704, August 1990.

Chapter 4

Synthesis of Fixed Structure Control Laws

4.1 Introduction

The design of flight control laws for modern high performance aircraft involves many steps which have not been traditionally addressed by control theory. In this chapter and in the next one we describe how some of these steps can be treated in the context of modern control theory. The specific areas that we will address are:

1) modifying existing control structures in the face of changes in the plant to assure a certain level of stability and performance;

2) incorporation of handling qualities criteria in the control design process;

3) automatic gain scheduling.

We will briefly motivate these goals before introducing our approach.

In developing a complex engineering system, one of the many assets that can be drawn upon is past experience. Practical flight control systems are typically modifications of previous control structures, modified for the specific aircraft to be controlled. Simple control augmentation schemes designed via ad hoc methods to perform various flight tasks have been successfully implemented in all different types of aircraft, to the satisfaction of both the pilot and the control engineer.

Until recently so called classical flight control design techniques have been disregarded in modern control theory as non-suitable for high performance aircraft. On the other hand little practical application has been made so far of these modern control techniques in aerospace applications. Modern flight control laws are radically different from their classical counterparts, and they often are viewed with skepticism by the aerospace industry.

There are several reasons that contribute to this lack of faith in modern control theory, but the most important are associated with hardware issues and complexity. Hardware issues are generally related to the speed of the processors that are flight qualified for military aircraft and also to the memory available on the on board computer. More precisely, we can talk about the limited CPU time and memory assigned to the control law. In modern aircraft the flight control computer performs many tasks and only one is the flight control augmentation system. Fairly complicated control laws including high order compensators with large computations require an unacceptable amount of CPU time. There are several programs — the EH101 helicopter was one case in which the author was directly involved — in which complicated control laws had to be simplified in the course of program to correct robustness problems caused by the large delays introduced by the control law. Furthermore, to achieve acceptable performance throughout the flight envelope, the flight control system needs to have some scheduling, switching, and/or blending scheme. It is not conceivable even in modern control theory to design a time invariant controller capable of providing the requested robustness and performance levels over the entire flight envelope.

To the author's knowledge the most 'modern' flight control system employed so far was the one implemented on the X-31 high maneuverability demonstrator, where an LQR design was used (see Ref.3-1). The designers of the X-31 flight control law admitted that several adjustments to the calculated feedback gains had to be made in order for the control law to be scheduled throughout the flight envelope. Because of the large changes in aircraft dynamics as the aircraft traverses the flight envelope, the scheduling of LQR gains presented serious practical issues. Similar, if not more serious, difficulties would arise from scheduling of high order H_∞ controllers (Ref.5-3). The issues of complexity and scheduling are addressed by the fixed order gain scheduled H_∞ controllers (Linear Parameter Varying controllers) presented in the next chapter.

At this point it is clear why methods which allow a proven control structure to be optimized for a new plant are valuable. Further, if flight test indicates that a control system has inadequacies due to errors in the aero model, it is of interest to make simple changes to the existing control system, which has already undergone extensive development and

validation. Although outside our current scope, reconfiguring the control law of an aircraft depending on its mission or its weight is also important as is reconfiguration of the control law in the face of damages in the control system. The capability to easily design simple control laws that take into account different types of damages, and subsequently store them in the flight control computer can be of great value. It will become apparent how this would be done with the method described here.

Another issue that must be addressed by flight controls is handling qualities. Experience exists to help the designer choose feedback signals, weight stick inputs, and provide 'force-feel' feedback to the pilot — all with the goal to improve the pilots' ability to complete the mission in concert with the aircraft. Methods also exist to analyze the handling qualities of a control system and its ability to perform satisfactory for different pilots (high/low gain, high/low frequency pilots), and much effort has been expended in improving this analysis (Ref.4-7, Ref.4-8, Ref.4-9, Ref.4-11, and Ref.4-16). Less work has been done on explicitly including handling qualities in the design optimization step. If one proposes to automate the modification of gains in an existing flight control structure, maintaining or improving handling qualities is a central problem.

Finally, the flight control design (or modification) process must result in a control law which is valid over a wide range of operating conditions, which cause variations in the plant dynamics that are invariably represented using tabulated empirical coefficients. Design has been quite successfully accomplished in the past using linear control law design at fixed operating points, followed by gain scheduling within the context of a fixed control structure. Much of the complexity of modern control systems lies in the details of scheduling and blending of various feedback gains and filters, to cope with the disparate requirements of landing, up-and-away flight, acquisition, tracking, etc..

The approach presented is designed to retain these interconnections, blends, gain schedules, and stick shaping filters, because they represent the accumulated knowledge of many years of practical design experience, and because it is costly to re-code these when problems are found late in development. Thus we are going to work on existing control laws making only specific changes to improve the design and the handling qualities of the aircraft,

which is more desirable than creating costly major architectural changes and often re-introduce a high level of uncertainty. We will focus on optimizing the gain tables and other numerical particulars of the control law, which are simple to change and do not require revalidation of the software. We will also incorporate handling quality requirements in the optimization and perform the optimization over a range of operating conditions, so that a gain schedule results.

The rest of the thesis is organized as follows. In this chapter we describe the fixed structure control problem and present two algorithms that can be used to find a solution, the first algorithm uses Linear Matrix Inequalities (LMI) and the second a standard Newton search. We then show how a handling quality metric, based on the Neal-Smith criteria, can be included in the cost functional and become part of the design process. Finally, with a realistic example regarding the refueling of the F-18 HARV, we will show how the design procedure can be used in practice.

The next chapter is dedicated to the gain scheduling of fixed structure controllers. As an example, some of the gains of the longitudinal and lateral CAS of the F-18 HARV were redesigned in order to improve performance and handling qualities. The design includes a large portion of the subsonic part of the flight envelope. Finally, we show the results of a series of tests performed in the fixed base flight simulator at NASA Dryden. A refueling task was performed by several pilots in the F-18 HARV simulator with the new gain scheduling, the old control law, and the standard F-18. Comparisons between the three configurations are presented.

4.2 The Fixed Structure Control Problem

The fixed structure control problem can be stated in the following way:

given a certain controller structure and a set of free parameters within that structure, find the set of free parameters that minimize a given cost function.

One of the first algorithms proposed for the optimization of controller parameters within a fixed structure was proposed by Edmunds in 1979 (see Ref.4-4). He describes a

method for designing linear multivariable control schemes which have a closed loop frequency response as close as possible, in a least square sense, to a desired response. The main limitation of the algorithm is that it assumes that only the coefficients of the C and D matrices of a given controller can be adjusted. In other words, given a controller $K(s) = N(s)/d(s)$, only the coefficients of the matrix of polynomials $N(s)$ can be optimized while the common denominator $d(s)$ is assumed fixed.

Another important method for the optimization of controller parameters is the one that goes under the name of Multi-Objective OPptimization. The method was proposed by Kreisselmeier and Steinhauser in Ref.4-1 and Ref.4-2 and is implemented in the Multi Objective Programming System (MOPS, Institut fur Dynamik der Flugsysteme at DLR). The design problem is translated into a set of performance objectives that form a vector of objective functions. The performance index vector can contain a variety of requirements such as closed-loop pole locations, closed-loop frequency responses, and closed loop time domain properties. Hyde in Ref.4-3 used MOPS as a benchmark against which to compare an H_∞ design to various fixed structure compensators. Hyde's conclusion was that the tradeoff between performance and controller complexity for the H_∞ design is not easy and that model reduction techniques cannot be applied if gain scheduling is used. For this reason he suggests using an H_∞ design to set the achievable performance for the plant, then performing a multi objective optimization on a fixed structure controller, and finally comparing with the H_∞ design. In practice his conclusion is that the H_∞ design approach is not feasible for application where the complexity must be kept low.

The approach that we present is in the family of the Multi-Objective optimization. The framework that we use is based on block perturbations and norm-based objectives. It has proven to be an excellent way to develop generalized solutions to the problem.

Our problem is characterized in Fig. 4-1. A linear controller $K_N(s)$ contains key gains and time constants that need to be adjusted. We isolate these key parameters and break the controller into a fixed part $K(s)$ and a variable part described by a diagonal matrix ΔK,

$\Delta K \in R^{m \times m}$, where m is the number of parameters that characterize the controller. Depending on the structure of the controller ΔK can also contain *repeated real* elements.

The transfer function $P_A(s)$ of Fig. 4-1 includes the plant augmented with the fixed part of the controller. It can also include weightings and target dynamics, as we will discuss later. The augmented plant is described by the following equations:

$$\begin{aligned} \dot{x}(t) &= Ax(t) + B_1 w(t) + B_2 n(t) \\ z(t) &= C_1 x(t) + D_{11} w(t) + D_{12} n(t) \\ y(t) &= C_2 x(t) + D_{21} w(t) + D_{22} n(t) \end{aligned} \qquad [4\text{-}1]$$

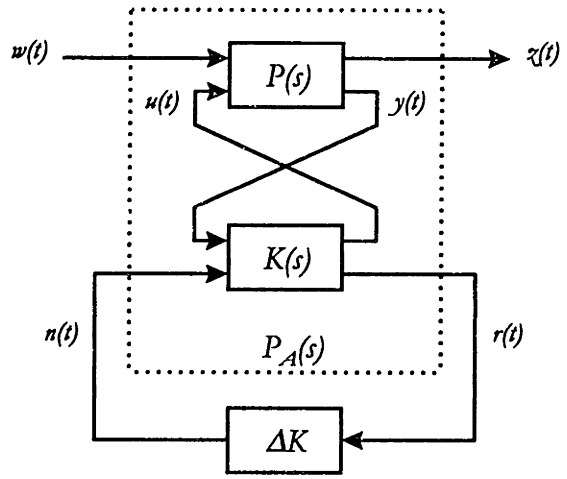

Fig. 4-1 The Fixed Structure Control Problem

The fixed structure control problem is then stated in the following way:

> *find a diagonal internally stabilizing controller* ΔK, $\Delta K \in R^{m \times m}$, *such that n-norm* $\|T_{zw}(s)\|_n$ *is less than* γ, *where* γ *is some prescribed performance level. If such a controller exists we will call it a* γ *suboptimal controller.*

Depending on the norm that we minimize, this will be an H_∞ or an H_2 control problem.

The performance objective can be defined in the classical form of an H_∞ optimization problem using a set of weighting functions $W_i(s)$, $i = 1 \ldots n$, acting on specific transfer functions of the closed loop plant. This weighting function can be specified for example to

obtain good disturbance rejection, good tracking, and robustness to unstructured multiplicative output perturbation. Alternatively in order to achieve our desired goals we can introduce a 'model matching' structure to compute $\|T_{zw}(s)\|_\infty$. Fig. 4-2 shows how this is done. If we minimize the norm of the transfer function from w to z then the closed loop of the plant $P(s)$, the fixed part of the controller, and the diagonal matrix ΔK will be as close as possible to the target plant $P_T(s)$ in terms of the chosen norm. The weighting function $W(s)$, shown in the figure, can be used to emphasize the frequency region where model matching is more important.

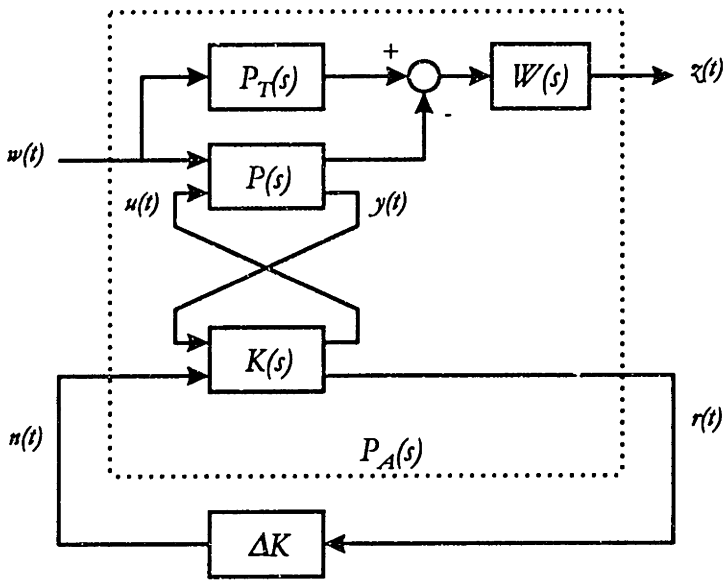

Fig. 4-2 The H_∞ model matching problem

The reference model $P_T(s)$ has the ideal time domain response characteristics, which the closed loop system is desired to follow. The target plant, $P_T(s)$, can be defined in many different ways depending on the nature of the problem.

4.2.1 Multi-objective optimization

In many practical situations it is highly desirable to add to the norm-based cost functional one or more additional terms that take into account other desired characteristics of the closed loop system. We can constrain some poles to lie within a certain region of the s-

plane, or constrain the shape of time domain response. In our example, we found it useful to add a term describing the distance between the current Neal-Smith plot from the desired Neal-Smith plot.

4.2.1.1 The Neal-Smith Criterion as a design objective function

Several methods exist to analyze handling qualities, methods based on pole-zero specification, frequency response specification, and/or time-response specifications. The Neal-Smith criterion is one of the most common and well known ways to analyze the handling quality of a closed loop aircraft (Ref.4-16 and Ref.4-9). The Neal-Smith criteria was specifically designed for good closed loop tracking performance. The criterion is formulated by modeling the pilot-airplane control loop as a unity feedback system with a pilot model of an assumed form in the forward loop. The pitch attitude control loop is modeled as in Fig. 4-3

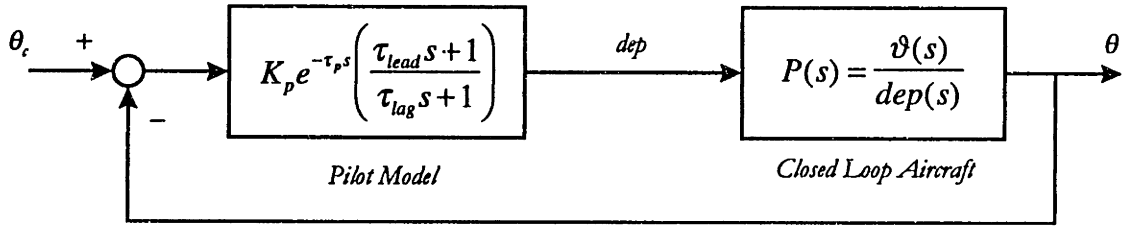

Fig. 4-3 Pilot-Aircraft Closed Loop System for Neal-Smith Criterion

The pilot is modeled as a pure delay plus a phase advance. The criterion is based on the hypothesis that if good closed loop dynamics are achieved with a simple pilot model then real pilot will also be able to attain good performance. The criterion assumes the pilot to impose a standard of task performance or degree of aggressiveness in closing the loop. This performance standard is measured in the frequency domain by the closed loop bandwidth frequency ω_b. The bandwidth requirement is task-dependent and determined from correlation of available pilot ratings and comments. For a given value of time delay (τ_p is in general within 0.2 and 0.3 sec), the pilot model parameters are adjusted to optimize the overall closed loop performance in attaining the specified bandwidth. It is assumed that the human pilot adjusts the lead, lag, and gain (τ_{lead}, τ_{lag}, and K_p in Fig. 4-3) so that the droop and

peak magnification of the closed loop frequency response are minimized, as shown in Fig. 4-4. The droop is calculated as the distance between the actual droop and an assigned one; a droop of -3dB is often defined and the pilot parameters are adjusted in order to obtain such a droop.

Flying qualities are evaluated by plotting the measured values of pilot compensation and maximum closed loop resonance on the Neal-Smith parameter plane against the flying qualities boundaries. Fig. 4-5 shows the Neal-Smith plot for the F/A-18 flying at an altitude of 20,000 ft and Mach 0.6. We can see that for a task bandwidth within 2.5 and 3.0 a solid level 1 flying quality is expected. The flying qualities then rapidly degrade for tasks with higher bandwidths.

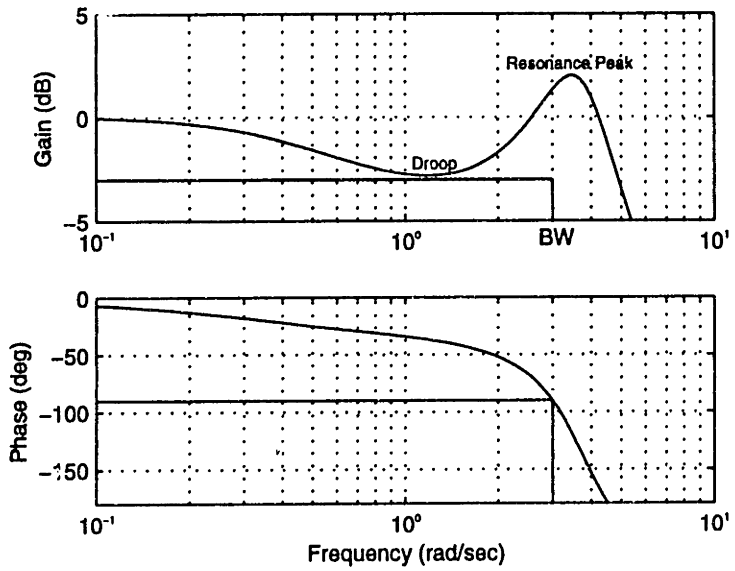

Fig. 4-4 Neal-Smith Criterion Parameters, Bandwidth = 3.0 rad/sec
F/A-18, H = 20,000 ft, Mach = 0.5

From Fig. 4-5 it is clear that a good flight control system is one capable of keeping the Neal-Smith plot within the level 1 region for the largest bandwidth possible. Sharp increases in the resonance peak as a function of the bandwidth must thus be avoided.

Our approach will be to minimize the H_∞ norm of the transfer function T_{zw} of Fig. 4-2, while making the Neal-Smith plot as close as possible to the target plant.

The cost that we wish to minimize is thus:

$$J = \left\| T_{zw} \right\|_{\infty} + J_{HQ} \qquad [4\text{-}2]$$

where:

$$J_{HQ} = \frac{1}{5}\sum_{i=1}^{5}\sqrt{(P_i - P_{ti})^2 + (R_i + R_{ti})^2} \qquad [4\text{-}3]$$

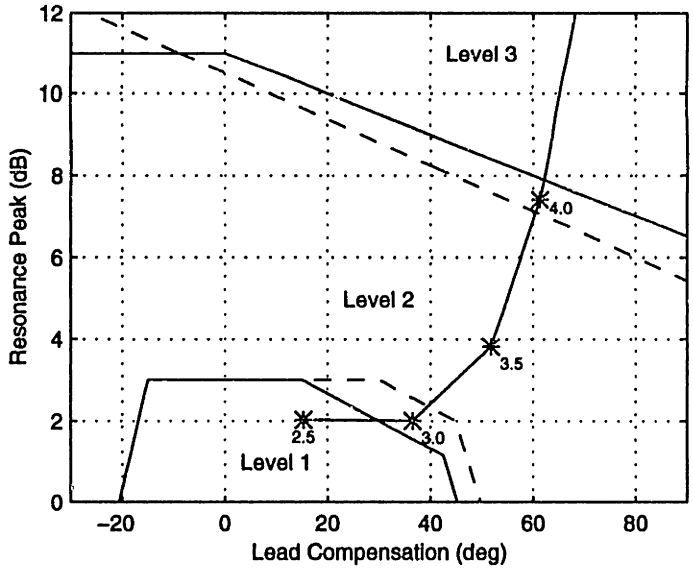

Fig. 4-5 Neal-Smith Plot for different bandwidths
F/A-18, H = 20,000 ft, Mach = 0.5

The handling quality metric in equation 4-3 represents the average distance between the target and the actual Neal-Smith plot calculated at the following five values of the task bandwidth: 2.5, 3.0, 3.5, 4.0, and 4.5 rad/sec. P_i is the pilot lead compensation in *rad* and R_i is the resonance peak calculated from the Neal-Smith criteria at the bandwidths B_i. The subscript t indicates that the variable refers to the target plant.

Fig. 4-6 shows how the handling quality metric based on the Neal-Smith plot is defined. There are several reasons why it is useful to add a term related to this handling quality metric to a norm based cost. First, J_{HQ} provides the solution a certain level of robustness against differences in the pilot bandwidth. If we are able to confine the Neal-Smith plot in the Level 1 one region for bandwidths between 2.5 and 3.5 (see Fig. 4-6) then

we can expect good handling quality for pilots with different characteristics. Additionally, this handling quality metric will help the optimization routine to find a feasible solution when the H_∞ optimization alone is not able to reach a physically realistic solution. This is needed because when the target and the actual plant are too far apart and the controller parameters are not able to match the target plant, a pure H_∞ objective function can give rise to a solution that is optimal in terms of the H_∞ norm, but which has an undesirable shape. In this situation the J_{HQ} cost drives the optimization to a more realistic solution. In many situations we also found that the handling quality metric speeds up the convergence of the optimization algorithm.

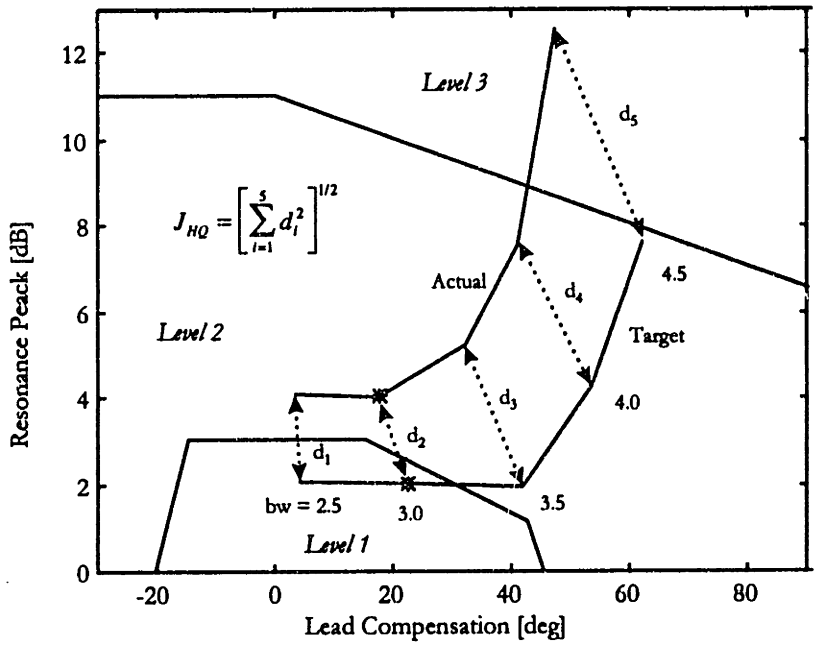

Fig. 4-6 Handling quality metric definition

4.3 Flying Qualities Requirement Definitions

In this section we will give a brief description of some terms used in the assessment of an aircraft flying qualities.

The flying qualities requirements depend on the type of the aircraft. For this reason the aircraft have been divided in four different classes. Class I includes small and light

aircraft, Class II aircraft of medium weight and normal maneuverability, Class III large and heavy aircraft with normal maneuverability, and Class IV high maneuverability aircraft. In our work we will always refer to Class IV aircraft.

Another important factor that distinguishes the handling qualities requirements is the task or flight phase. The aircraft missions are divided in three different classes, in Tab. 4-1 are shown the three different flight phases.

Flight Phase	Description
Phase A	Non terminal phases of flight involving rapid maneuvering, precision tracking, or precise control of the flight path. Included in phase A are: • CO: air-to-air combat; • GA: ground attack; • WD: weapon delivery; • RR: air-to-air refueling acting as a receiver; • TF: terrain following; • RC: reconnaissance; • FF: close formation flying; • AB: aerobatics.
Phase B	Non terminal phases of flight usually accomplished by gradual maneuvers which do not require precise tracking. Included in phase B are: • CL: climbing; • CR: cruising; • D: descending; • AD: aerial delivery; • RT: air-to-air refueling in which the aircraft acts as a tanker.
Phase C	Terminal flight phases requiring accurate flight path control. Included in phase C are: • TO: take-off; • L: landing • PA: powered approach.

Tab. 4-1 Flight Phases Classification

The easy with which a mission can be completed is classified in three different levels. These levels define the level of acceptability of a control system.

Level	Characteristics
1	The flying qualities are adequate for the particular flight phase being considered.
2	The flying qualities are adequate for the particular phase being considered, but there is either some loss in the effectiveness of the mission, or there is a corresponding increase in the workload imposed upon the pilot to achieve the mission or both.
3	The flying qualities are such that the aircraft can be controlled, but either the effectiveness of the mission is gravely impaired, or the total workload imposed upon the pilot to accomplish the mission is so great that it approaches the limit of his capacity.

Tab. 4-2 Flying Level Classification

The level of acceptability is then related to the pilot rating scale using the so called Cooper-Harper (CH) rating chart (Tab. 4-3) . The Cooper Harper rating was first presented in 1969 (Ref.4-14) and has since become the most accepted scale to describe the pilot's rating. The CH scale is directly linked to the three levels of acceptability and is then used to define the flying level of the aircraft. The CH rating is determined by the pilots responses to a simple set of questions.

This completes the description of our approach to the stated problem. Several comments are in order before we describe the technical details and results. First, we have adopted a modern framework, which allows additional robustness and performance considerations to be included. In other words, it allows us to tap into the large body of knowledge that has been built up around this framework in recent years. In particular, this formulation can be modified to a Linear Parameter Varying (LPV) control problem, which will allow gain scheduling to be addressed. No consideration has yet been given to computational complexity; rather we have formulated a practical problem in the context of current methods. We will see shortly how this approach leads to a non-convex optimization problem.

Level	Pilot Rating	Aircraft Characteristics	Pilot's required operation
1	1	Excellent: High desirable	Pilot compensation is not a factor for desired performance
	2	Good: Negligible deficiencies	Pilot compensation is not a factor for desired performance
	3	Fair: Some mildly unpleasant deficiencies	Minimal pilot compensation needed for desired performance
2	4	Minor but annoying deficiencies	Desired performance needs moderate pilot compensations
	5	Moderately objectionable deficiencies	Adequate performance needs considerable pilot compensation
	6	Very objectionable but tolerable deficiencies	Adequate performance needs extensive pilot compensation
3	7	Major deficiencies	Adequate performance cannot be achieved without maximum pilot compensation. Controllability not in question
	8	Major deficiencies	Considerable pilot compensation is required for control
	9	Major deficiencies	Intense pilot concentration needed to retain control
3	10	Major deficiencies	Control is lost during some part of required operation

Tab. 4-3 Cooper-Harper Rating Chart

4.4 Algorithms for Solution of Fixed Structure Optimization

A closed form solution to the fixed structure control problem does not exist. Fortunately fast computation and efficient numerical algorithms are widely available, and sufficient to solve our problem. We will present two algorithms: one based on an LMI formulation of the control problem and the other on Newton's method. Other algorithms, such as genetic algorithms or neural networks, could be used; in general it is good practice to solve non-convex problems using different methods to help insure the optimality of the solution.

4.4.1 LMI Solution of the Fixed Structure Control Problem

The LMI solution of the fixed structure control problem is based on two important lemmas: The Bounded Real Lemma and The Maximum H_2 Norm Lemma. These two

lemmas can be used to formulate the fixed structure control problem as a bilinear matrix inequality.

With some simple matrix algebra we can define the closed loop transfer function of the system described in equation 4-1 as follows

$$\dot{x}(t) = A_{CL}x(t) + B_{CL}w(t)$$
$$z(t) = C_{CL}x(t) + D_{CL}w(t)$$

With the assumption that the feedthrough term $D_{22} = 0$, we have:

$$A_{CL} = A + \sum_{i=1}^{q} F_i k_i \qquad \mathrm{B_{CL}} = B_1 + \sum_{i=1}^{q} G_i k_i$$
$$C_{CL} = C_1 + \sum_{i=1}^{q} H_i k_i \qquad \mathrm{D_{CL}} = D_{11} + \sum_{i=1}^{q} N_i k_i \qquad [4\text{-}4]$$

where:

$$F_i = \left[i^{th} \text{ column of } B_2\right] * \left[i^{th} \text{ row of } C_2\right]$$

$$G_i = \left[i^{th} \text{ column of } B_2\right] * \left[i^{th} \text{ row of } \mathrm{D_{21}}\right]$$

$$H_i = \left[i^{th} \text{ column of } \mathrm{D_{12}}\right] * \left[i^{th} \text{ row of } \mathrm{C_2}\right]$$

$$N_i = \left[i^{th} \text{ column of } \mathrm{D_{12}}\right] * \left[i^{th} \text{ row of } \mathrm{D_{21}}\right]$$

and

$$\Delta K = diag\left(k_1, k_2, k_3, \ldots, k_q\right)$$

In this way we have expressed the closed loop state space matrices as linear function of the controller parameters k_i that we need to identify.

4.4.1.1 The H_∞ Fixed Structure Control Problem

The solution of the H_∞ fixed structure control problem via LMIs is based on the Bounded Real Lemma, which states that, for an LTI system given by:

$$\begin{aligned}\dot{\underline{x}}(t) &= A\underline{x}(t) + B\underline{u}(t)\\ \underline{y}(t) &= C\underline{x}(t) + D\underline{u}(t)\end{aligned} \qquad [4\text{-}5]$$

the H_∞ norm of the transfer function from u to y, is less than γ if and only if there exists a semi positive definite matrix P, $P \geq 0$, such that:

$$\begin{bmatrix} A^T P + PA & PB \\ B^T P & -\gamma^2 I \end{bmatrix} + \begin{bmatrix} C^T \\ D^T \end{bmatrix} \begin{bmatrix} C & D \end{bmatrix} \leq 0 \qquad [4\text{-}6]$$

The importance of this lemma is that it transforms the H_∞ control problem into a finite dimensional matrix inequality. If we substitute the closed loop state space model of equation 4-4 in equation 4-6, we get:

$$\begin{bmatrix} \left(A^T + \sum_{i=1}^{q} F_i^T k_i\right)P + P\left(A + \sum_{i=1}^{q} F_i k_i\right) & P\left(B_1 + \sum_{i=1}^{q} G_i k_i\right) & C_1^T + \sum_{i=1}^{q} H_i^T k_i \\ \left(B_1^T + \sum_{i=1}^{q} G_i^T k_i\right)P & -\gamma I & D_{11}^T + \sum_{i=1}^{q} N_i^T k_i \\ C_1 + \sum_{i=1}^{q} H_i k_i & D_{11} + \sum_{i=1}^{q} N_i k_i & -\gamma I \end{bmatrix} < 0 \qquad [4\text{-}7]$$

The variables in the matrix inequality of equation 4-7 are the positive definite matrix P and the controller coefficients k_i. Unfortunately equation 4-7 is nonlinear in the variables P and k_i, so we have a non-convex problem with no simple solution. For a given controller ΔK the matrix inequality is affine in γ and P and defines a convex set in P; efficient interior points methods from convex optimization are now available to compute the smallest feasible γ and the associated positive definite matrix P (this is the analysis problem). On the other hand, for a given matrix P the matrix inequality is affine in γ and the controller parameters k_i; once again we can use interior point methods to find the smallest feasible γ and the associated controller ΔK. The idea is then to find an optimal solution solving iteratively two linear matrix inequalities: the first in γ and P for a given ΔK, and the second in γ and ΔK for a given P. We have the following two step procedure:

First LMI given a controller ΔK^* we can find the minimum γ for which there exist a positive definite matrix P that verifies equation 4-7;

Second LMI given a positive definite matrix P^*, solution of the first LMI, find the minimum γ and the associated controller ΔK for which equation 4-7 is satisfied.

The algorithm is visualized in Fig. 4-7.

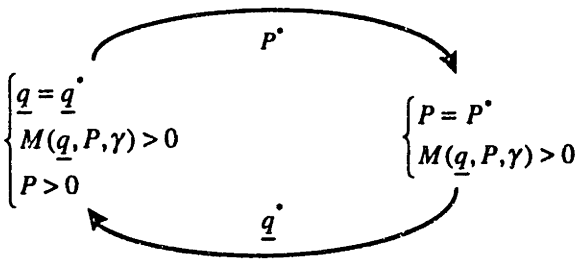

Fig. 4-7 Iteration between Linear Matrix Inequalities ($\underline{q}$ is a vector containing the controller parameters k_i)

In order to start the algorithm we need to have an initial stabilizing controller. In most practical situations with fixed structure controllers this is not a problem. The algorithm guarantees that the value of γ will not increase between iterations, but there is no guarantee that a global minimum will be found. The first LMI also assures that the closed loop system will be stable.

It is worth mentioning that it is not necessary to express the closed loop matrices as described in equation 4-4 to set up the LMI problem. The matrix ΔK can simply be kept in its diagonal form. This formulation, however, becomes convenient when we solve the fixed structure *gain scheduling* problem in Chapter 5.

Once the LMI problem has been formulated then there are several software packages that solve linear matrix inequalities. In our examples we used the LMI Matlab toolbox (Ref.4-17).

4.4.1.2 The H_2 Fixed Structure Control Problem

The LMI can also be set up for the case when an H_2 norm is used instead of an H_∞ norm. In this case the property we rely on is that the H_2 norm of the transfer function from u to y in equation 4-5, is less than γ if and only if $D = 0$ and:

$$Trace\left(CPC^T\right) \leq \gamma^2 \qquad [4\text{-}8]$$

subject to

$$\begin{bmatrix} A^T P + PA & PB \\ B^T P & -I \end{bmatrix} \leq 0 \qquad [4\text{-}9]$$
$$P > 0$$

Again the norm criterion has been transformed into a finite dimensional linear matrix inequality. Using the closed loop state space model of equation 4-4 and the maximum H_2 norm lemma, our H_2 Fixed Structure Control Problem can be stated in the following way:

$$\textit{minimize} \quad \text{Trace}\left[\left(C_1 + \sum_{i=1}^{q} H_i k_i\right) P \left(C_i^T + \sum_{i=1}^{q} H_i^T k_i\right)\right] \qquad [4\text{-}10]$$

subject to

$$\begin{bmatrix} \left(A^T + \sum_{i=1}^{q} F_i^T k_i\right) P + P\left(A + \sum_{i=1}^{q} F_i^T k_i\right) & P\left(B_1 + \sum_{i=1}^{q} G_i k_i\right) \\ \left(B_1^T + \sum_{i=1}^{q} G_i^T k_i\right) P & -I \end{bmatrix} < 0 \qquad P > 0 \qquad [4\text{-}11]$$

Ref.4-6 gives a detailed description of the problem and a complete historical reference (Ref.4-6 page 141 and 78).

Again we do not have a convex problem, and we define a two step procedure and iterate between two LMIs. Given an initial controller we can find the positive definite matrix P that minimizes the trace in equation 4-10 and satisfies the inequalities of equation 4-11. We can then use this matrix P and solve for a new controller that minimizes the trace in equation 4-10 and satisfies the inequalities of equation 4-11. Using this iterative scheme until a minimum of the H_2 norm is reached or the maximum number of iterations is exceeded, it is

possible to find a controller that locally minimizes the H_2 norm of the transfer function from w to z, but there is no guarantee that a global minimum will be found.

4.5 Newton Search Solution of the Fixed Structure Control Problem

Besides the LMI approach, both the H_2 and H_∞ fixed structure control problem can be efficiently solved using a search procedure. The method we selected is the Quasi-Newton method that uses the BFGS formula to update the Hessian (see Ref.4-18, Ref.4-19, Ref.4-20, and Ref.4-21). An algorithm that implements this technique is available in Matlab and it is straightforward to implement the fixed structure control minimization problem (Ref.4-22).

The main advantage of the Quasi-Newton method with respect to the LMI solution is the speed of convergence. The reduction in the cost obtained at each iteration between the two LMIs is always very small; in order to solve a problem involving 5 controller parameters and 14 states, we found that ~1000 iterations are required, requiring 10 hours on a workstation. The Newton method was able to find a solution in less than one our. For problems involving a small number of states (up top 10) the LMI solution demonstrated to be reliable and fast.

Another advantage of the Newton search method is that it allows us to augment the cost with additional terms to account for other important performance specifications, such as the handling qualities cost described in the previous section. In the LMI framework it is more difficult, if not impossible, to add additional elements to the cost, because in this case additional terms in the cost must always be added as LMI constraints.

4.6 Single Flight Point Design Example

Let us take for example the task of in-flight refueling of the F/A-18 HARV. Although this task is often performed on the standard F/A-18, the F/A-18 HARV has some characteristics that make this task challenging.

This design example is for a linearization of the F-18 HARV at Mach 0.6 and altitude 20,000 ft for the in-flight refueling task. This is an example where the fixed structure control law design can really improve the performance of the aircraft. We will show that with only small adjustments in the controller gains it is possible to recover the performance of the standard F-18, in spite of the large difference in dynamics of the HARV.

Refueling is a critical flight control task because precision tracking is necessary. Fig. 4-8 shows the F-18 HARV being refueled by a KC-135 tanker (November 1995). In order to refuel successfully and with a reasonable pilot work load, Level 1 flying qualities (Cooper Harper rating from 1 to 3) are required. Refueling of the F-18 HARV was performed at NASA Dryden by two pilots during two different flights, twice per flight. Both pilots found the task amazingly difficult and their CH rating was 8 or 9.

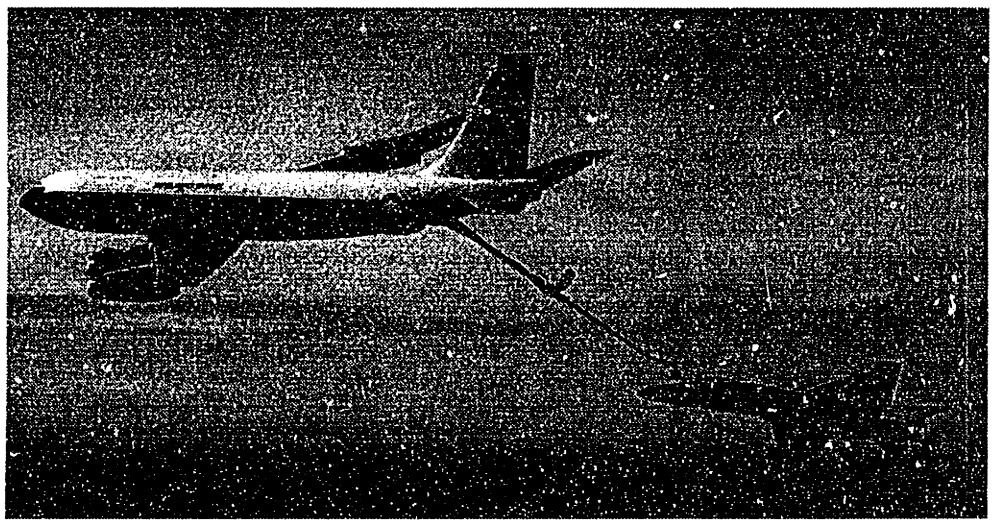

Fig. 4-8 F-18 HARV refueling by a KC-135 tanker

We report some of the comments given during flight to show the level of frustration of the pilots during the various refueling attempts. The comments of the first pilot are:

⇒ *this is ridiculous*

⇒ *I have to use very low gain, you really have to go open hand with it*

⇒ *There is a zone, about five feet from the tank, where I cannot settle the airplane down*

⇒ *Surely amazing*

⇒ *I can't make any fine correction*

⇒ *The problem is I have huge time delays*

⇒ *I cannot make the smallest correction*

⇒ *Once I get there I cannot fly formation*

⇒ *There is no doubt about it, it is rough*

⇒ *It is amazing we haven't got it done yet*

⇒ *To use this task as an H/Q experiment it is better you get an airplane you can fly*

⇒ *I cannot believe this*

While those of the second pilot were:

⇒ *A little bit more sluggish than a standard F-18*

⇒ *There is a longitudinal motion going on here*

⇒ *Mostly I'm getting a longitudinal pitch motion attitude*

⇒ *You can see the airplane really lope longitudinally more than anything else*

⇒ *The airplane tends to get this rather low to medium frequency longitudinal movement going if you try to make any fine correction to stay behind the basket. Need to use a kind of open handed technique and it seems to stay out.*

The first pilot has been characterized by NASA Dryden engineers as a high gain high frequency pilot while the second is generally seen as a lower gain lower frequency pilot. From the video of the task it is possible to see that the first pilot had a harder time performing the task. There is an interesting comment in the flight engineering summary that says:

> *With the aircraft being sluggish in the longitudinal stick direction, it was discovered that the pilot gains to control the longitudinal axis were much less than anticipated.*

It is clear that it was much harder for the first pilot to adapt his "aggressive" flying style to such a low gain and low frequency task. On the contrary, the task was easier for the second pilot. The different flying style of the two pilots is confirmed by the power spectral density of their stick input during refueling. Fig. 4-9 shows the average power spectral densities of the longitudinal stick input for the two pilots.

The first pilot put most of his energy around 3 rad/sec and above while the second most of the time worked around 2.5 rad/sec. The different levels of the PSDs confirm that the first is a high gain high frequency pilot while the second one is a low gain pilot.

Despite the differing pilot styles their general comments about the refueling task on the F-18 HARV were unanimous, their Cooper-Harper rating was 8 or 9. From the flight data and the video it is evident that a strong tendency to PIO exists and that the pilot work load is quite high. The same maneuver is performed regularly on a standard F-18 and does not present the same problem. The control law in both cases is the same; the difference lies primarily in the mass and inertia characteristics. The moment of inertia around the y-body axis is almost doubled in the HARV as opposed to the F-18 SRA, due to the weight of the thrust vectoring assembly, spin chute, and associated ballast in the nose (see Tab. 4-4). It is thus not surprising that the aircraft has poor performance in certain (surprisingly very limited) regions of the flight envelope.

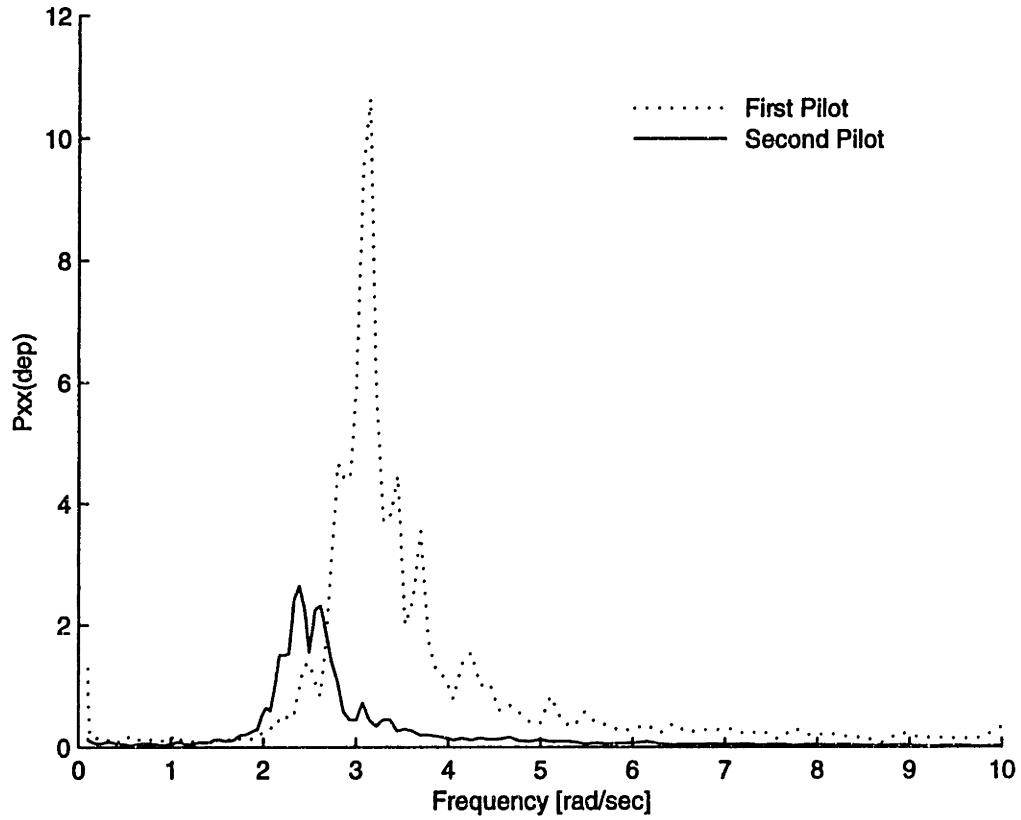

Fig. 4-9 Comparison between the PSD of the stick input of the two pilots

The approach taken here is to make the longitudinal transfer function of the F-18 HARV as similar as possible to that of the F-18 SRA. Our goal, then, is to re-optimize the gains of this control system to recover the input-output characteristics and handling qualities of the original F-18. The desired input-output characteristics will be defined as a 'target plant', and the handling qualities will be based on the Neal-Smith criterion.

F-18 HARV		F-18 SRA	
Total Mass	1142.48 slugs	Total Mass	988.01 slugs
CG Percent Chord	22.88 %	CG Percent Chord	21.50 %
CG Buttline	0.0 in	CG Buttline	0.0 in
CG Waterline	102.96 in	CG Waterline	103.47 in
Moment of Inertia Ix	23466.9 slug*ft^2	Moment of Inertia Ix	17178.3 slug*ft^2
Moment of Inertia Iy	181600.7 slug*ft^2	Moment of Inertia Iy	119208.2 slug*ft^2
Moment of Inertia Iz	196669.8 slug*ft^2	Moment of Inertia Iz	132354.5 slug*ft^2
Product of Inertia Ixz	-1741.85 slug*ft^2	Product of Inertia Ixz	-2148.64 slug*ft^2

Tab. 4-4 F-18 HARV vs F-18 SRA Mass and Inertia Characteristics

4.6.1 Handling Qualities Analysis From Flight Data

In section 4.2.1.1 we introduced the Neal-Smith criterion as a method by which to assess the handling quality of an aircraft. It is of interest to compare the comments recorded from the pilots during the refueling task with the Neal-Smith criteria.

During refueling both pilots spent a long time maneuvering at Mach 0.55 and altitude 20,000 ft. From the flight data it is possible to find the closed loop transfer function of the aircraft (airframe plus control law) from the longitudinal stick to pitch rate or pitch attitude angle. Even though this transfer function is obtained from closed loop data (the pilot is closing the loop) the effect of the disturbances and sensor noise can be neglected. The same calculation was performed using simulation data and the closed loop transfer function obtained from closed loop data and open loop data were almost identical.

Fig. 4-10 and Fig. 4-11 show the transfer functions from longitudinal stick to pitch rate obtained using the data from the flight example of the F/A-18 HARV. The thick solid lines represent the average transfer function obtained from 7 refueling maneuvers performed at almost the same Mach number and altitude. The thin lines are the transfer function

obtained from the data of flight 300 and 366 respectively. The last plot of each figure represents the power spectral density of the longitudinal stick input. The average transfer function is obtained using the coherence at each frequency as a weighting factor. In both figures it is possible to see that the coherence is very high in the frequency range where most of the input energy is exercised.

The next step is to apply the Neal-Smith criteria to the average longitudinal transfer function.

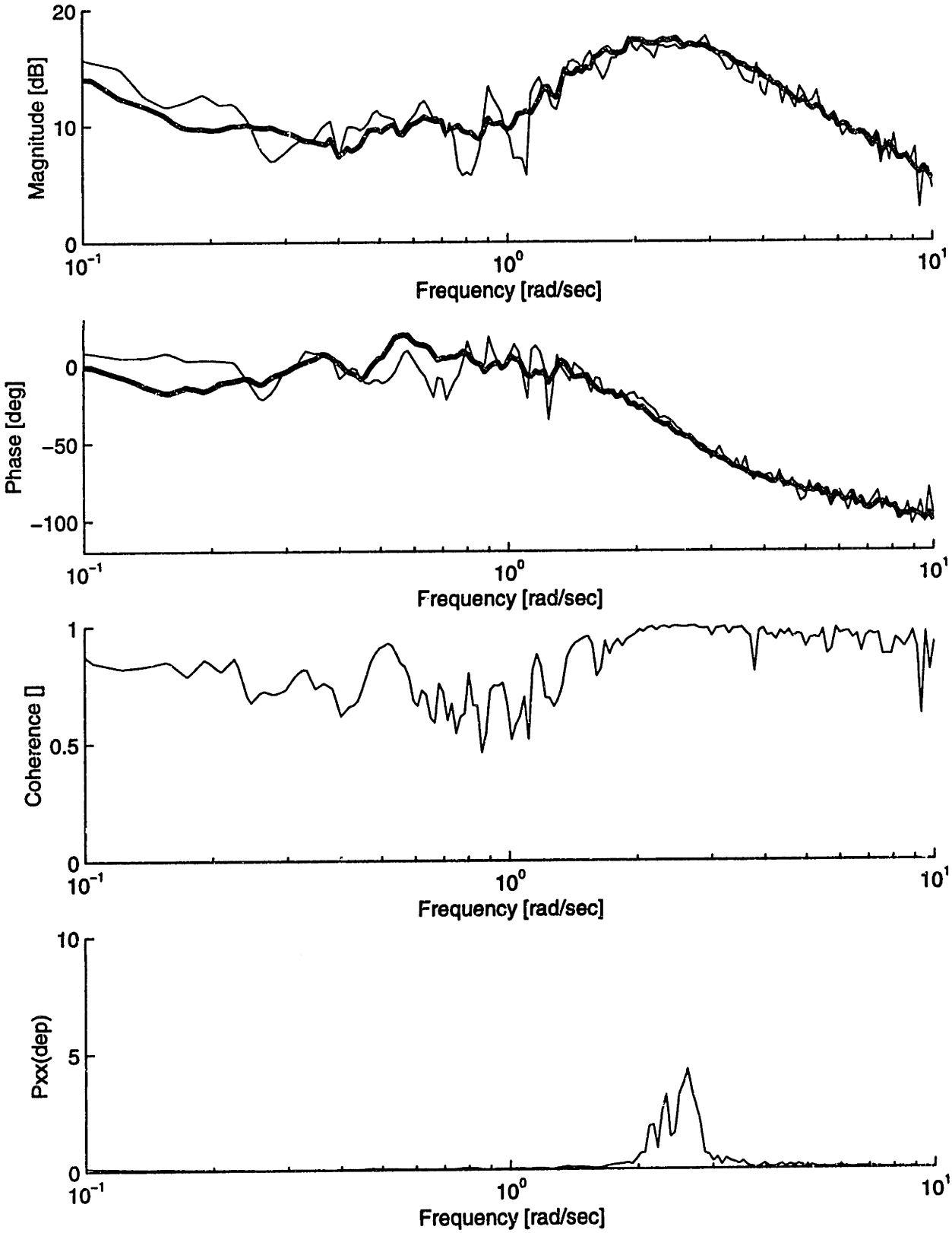

Thick Line: Average Transfer Function
Thin Line: Plots obtained from the data of flight 300 only.

Fig. 4-10 Flight 300 - q/dep Transfer Function - First Refueling Maneuver

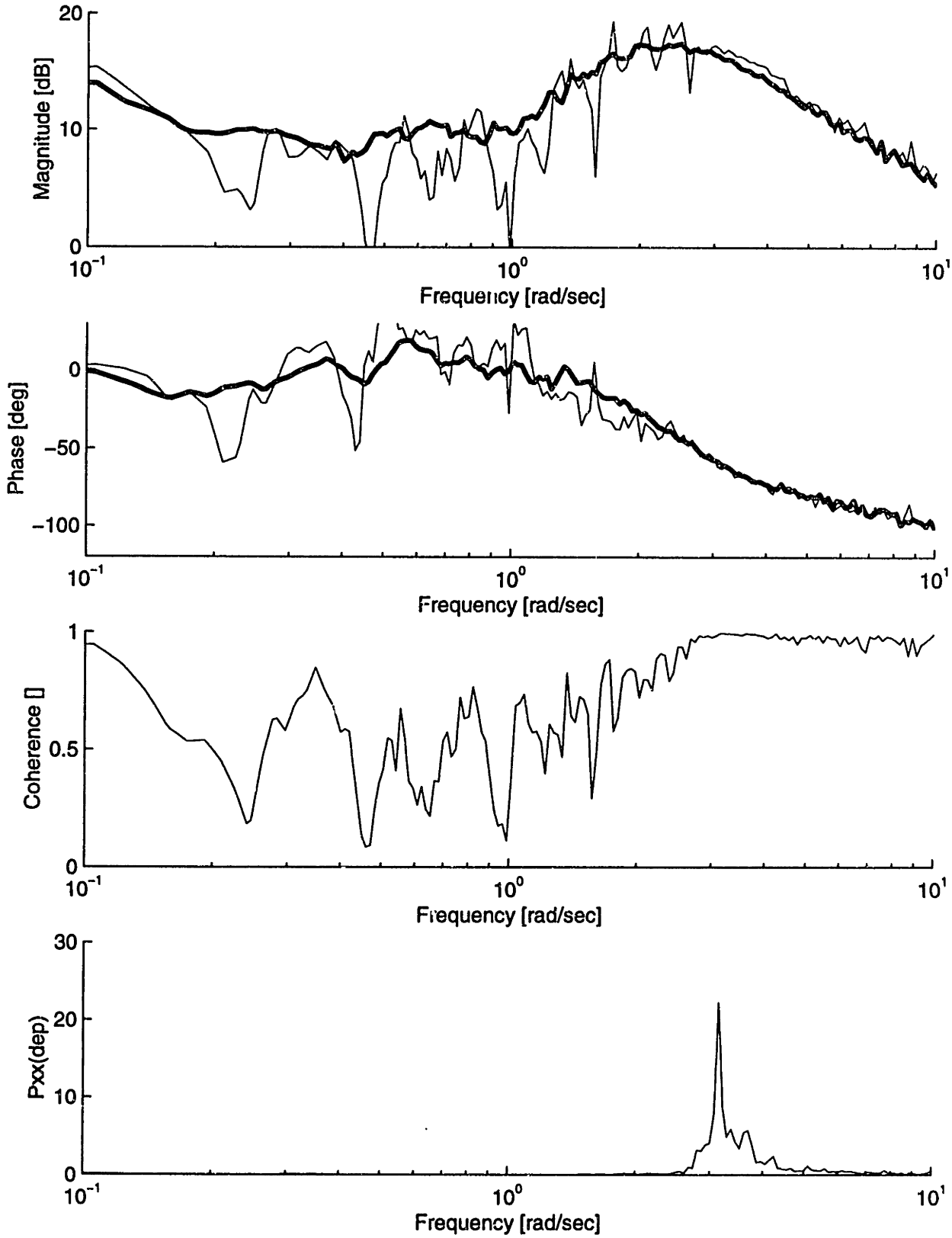

Thick Line: Average Transfer Function
Thin Line: Plots obtained from the data of flight 366 only.

Fig. 4-11 Flight 366 - q/dep Transfer Function - First Refueling Maneuver

Fig. 4-12 shows the average transfer function and its smoothed version. In Fig. 4-13 the Neal-Smith carpet plot calculated from this experimental transfer function is shown. For a bandwidth of 3 rad/sec the plot shows marginal level 2 flying qualities. The performances rapidly degrade with an increase in the task bandwidth and at 3.5 rad/sec level 3 HQ are predicted. The Neal-Smith plot confirms the Cooper-Harper rating given by the two pilots. Considering that the refueling task (when the aircraft is acting as a receiver) is classified as flight phase A and level 1 handling qualities are required, we can see that the F-18 HARV longitudinal response is not adequate for this task. As mentioned by both pilots, the best strategy is to fly almost open handed. The pilots in general refer to fly open handed when they have to be very gentle on the stick using it as minimum as possible.

In order to compare the fixed base flight simulator with the real flight, the q/dep transfer function was also estimated using the data from the flight simulator. A series of longitudinal pulses of different amplitude and length were injected by the pilot. This maneuver was repeated by six pilots and an average transfer function was calculated from this data. The longitudinal frequency response and the associated Neal-Smith carpet plot are shown in Fig. 4-14 and Fig. 4-15.

Unfortunately the transfer function obtained from flight data does not match the one calculated from the simulation data. A comparison of the two transfer functions (TF) is shown in Fig. 4-16. The solid line TF is obtained from flight data and the dashed TF from simulation data. The bandwidth of the two transfer functions is very similar, about 6 rad/sec (calculated as the frequency were the phase is equal to -90 deg). The phases are almost identical but the magnitudes are different. The problem is that the flight data TF presents a large droop that we don't have in the simulation data TF. The Neal-Smith carpet plot obtained from the simulated data is not as bad as the one calculated from flight data. At 3 rad/sec we are in Level 2 condition and the HQs rapidly degrade with higher frequency tasks. We don't have particular reasons to justify the different behavior of the fixed base simulator from the flight; one thing that we can mention is that the coherence of the flight data is quite small in the region were the large droop is shown, for this reason we are not very confident in the transfer function obtained in this frequency region.

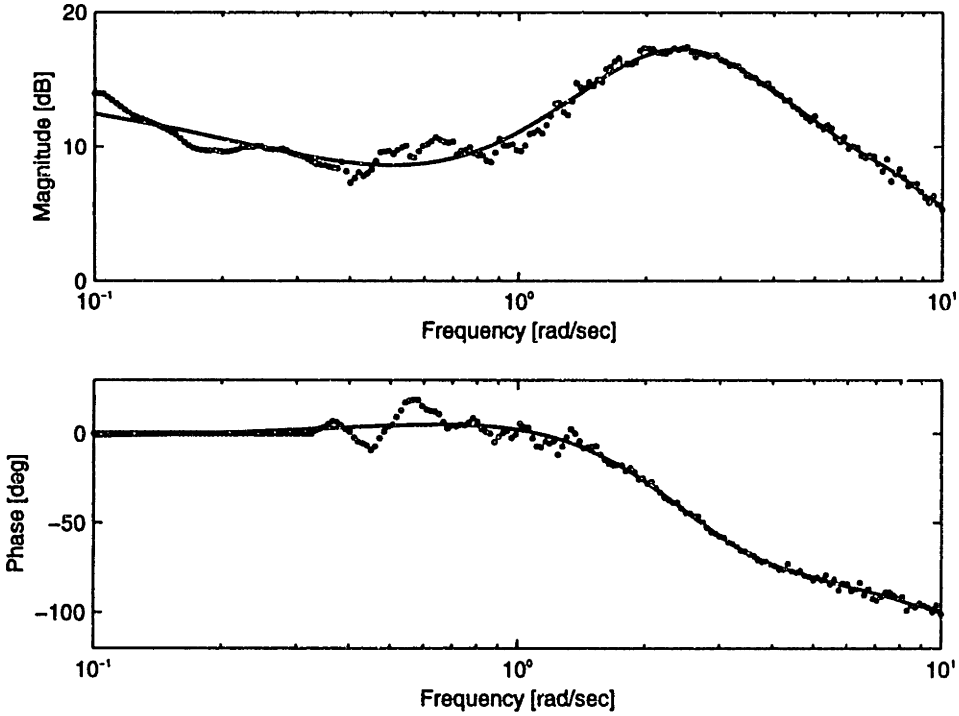

Fig. 4-12 F-18 HARV: Transfer Function q/dep estimated from Refueling Flight Data

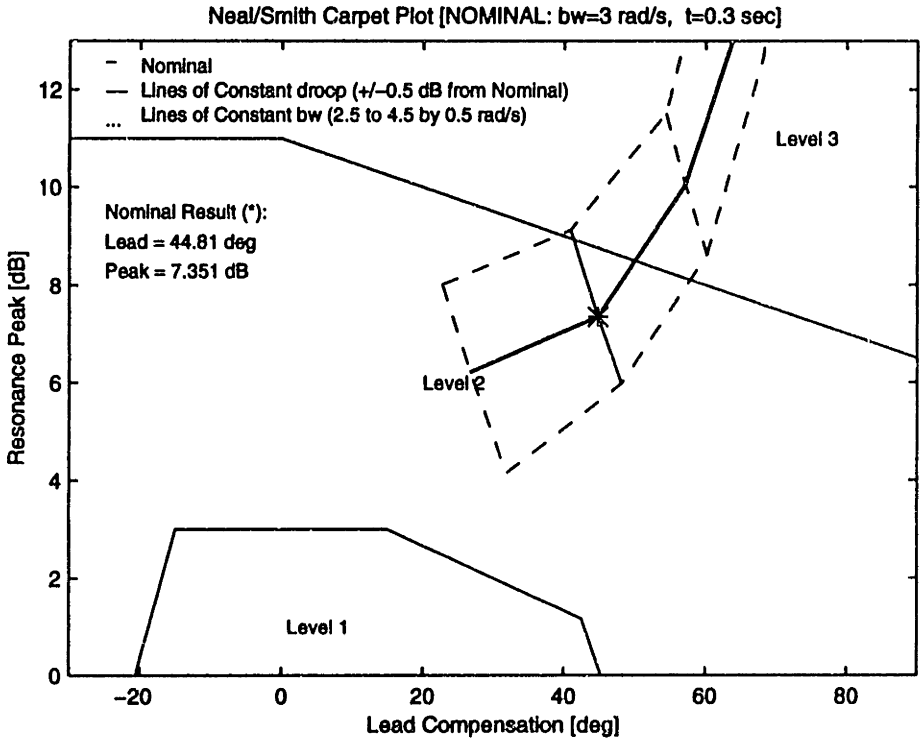

Fig. 4-13 F-18 HARV: Neal-Smith Carpet Plot calculated from the smoothed experimental transfer function

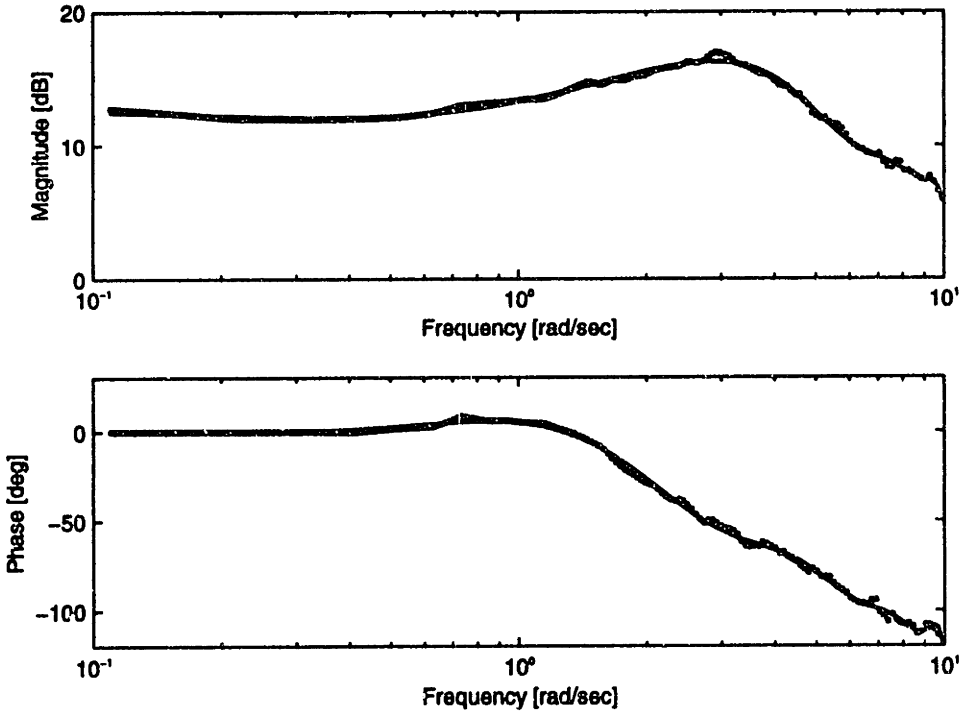

Fig. 4-14 F-18 HARV: Transfer Function q/dep estimated from PMP Simulation Data

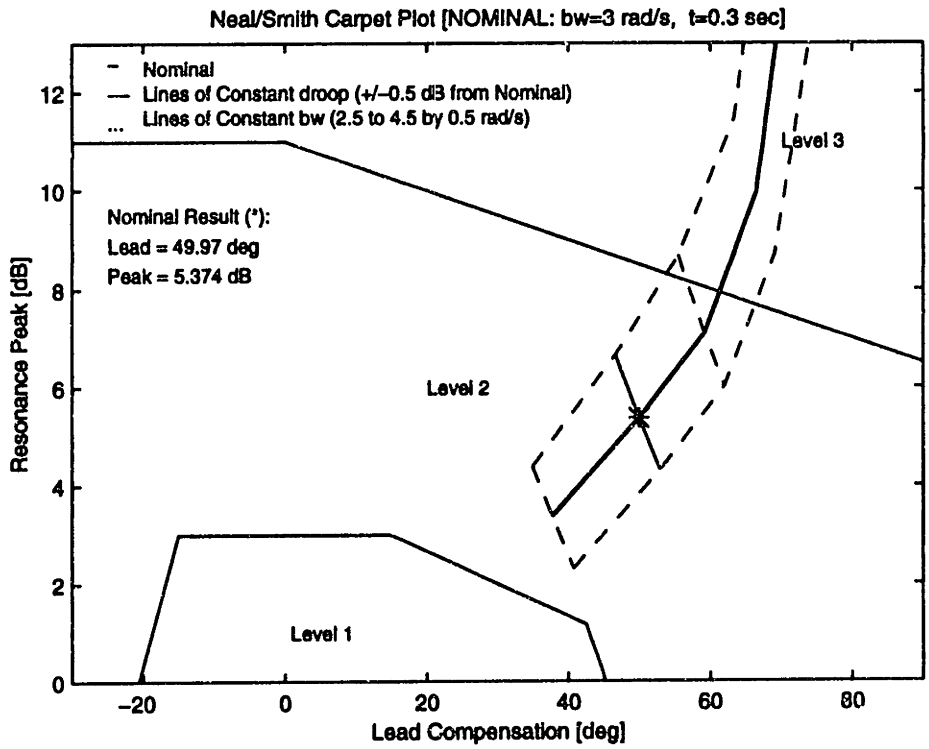

Fig. 4-15 F-18 HARV: Neal-Smith Carpet Plot Calculated from the Simulation Data

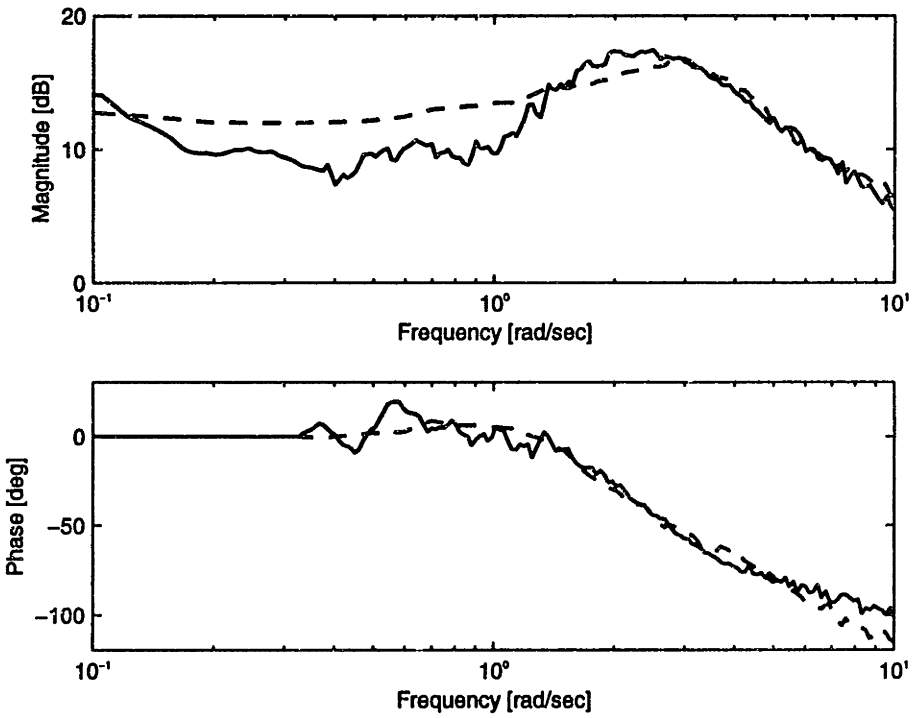

Solid: Experimental Data
Dashed: Simulation Data

Fig. 4-16 Comparison between the transfer functions obtained from flight data and simulation data

So far we have analyzed the flight data and shown that the Neal-Smith criterion was able to predict the poor behavior of the F-18 HARV during refueling. The next step in the design of fixed structure controllers is the definition of a target plant, this will be discussed in the next section.

4.6.2 Definition of the Target Plant

One of the most important tasks in the design of fixed structure controllers is the selection of the target plant. The approach taken here is to make the F-18 HARV longitudinal dynamics look like the ones of the F-18 SRA. Our target plant will have the pitch response of the F-18 SRA at 20,000 ft and Mach 0.6. Our choice is based on the assumption that refueling is judged to be level 1 on the standard F-18 and that the F-18 SRA is a standard F-18 in all important aspects.

The longitudinal target plant is defined as the transfer function from the pilot stick input (*dep*) to the pitch rate (q). We are going to present two target plants that differ only in

their order. A full order target plant that includes all the longitudinal states plus a complete model of the longitudinal CAS, and low order target plant that uses the short period approximation of the longitudinal motion and only the integrator states of the CAS.

The low order model is used when solving the fixed structure control problem via LMIs. In this case we need to keep our model as simple as possible because the LMI algorithm encounters convergence problems when the system has a large number of states. The total number of states is the sum of the target states and the plant states an this defines the size of the Lyapunov matrix P. If P is too large, solutions cannot always be found for the two Linear Matrix Inequalities that are defined in section 4.4.1.1.

The high order model, on the other hand, is used when the optimization problem is solved with the Newton search. In this case a full order model can be used and a more precise solution can be found.

The low order target transfer function is:

$$G_{TAR}(s) = \frac{31.5638\ (s+1.6921)\ (s+0.7653)}{(s+2.3956 \pm 2.5849i)\ (s+0.8254)}$$

The high order transfer function in terms of poles, zeros, and gain is:

Poles	Zeros
-61.6501 +/- 84.8776I	-5.6374 +/- 82.7068I
-14.2553 +/- 31.1079I	-24.2142
-21.8051	-6.2880
-5.5266	-2.6788
-4.2952	-1.6921
-2.2043 +/- 2.6588i *	-0.9364 +/- 0.5412I *
-0.9096 +/- 0.5227i	-0.0120 *
-0.0113 *	0 *
0.0027 *	
Gain = -6.2824e+004	

Tab. 4-5 High order target plant transfer function. Starred elements indicate poles and zeros of the plant.

Note that in the high order target plant the phugoid poles have degenerated in two real poles, one of which is slightly unstable but within the limit of level 1 flying qualities. The phugoid poles are almost canceled by the zeros and thus don't play an important role in the pitch-rate response.

4.6.3 The Interconnection Structure For the Model Matching Problem

Once the target plant has been defined the next step is to create the interconnection structure that describes the model matching problem and select what gains and/or time constants need to be redesigned. It is very important to select the parameters in the control law that are important and necessary to achieve the desired target transfer function. Recall that we will be solving a non convex optimization problem and that the algorithms may not converge if too many variables are selected. It is critical at this point to have a good knowledge of the plant and of the role that each element in the control law has in the closed loop system response characteristics. Fortunately, classical controls are developed from exactly this perspective, so this is a reasonable requirement.

We select three gains: the pitch stick proportional gain, the n_z proportional gain, and the pitch rate proportional gain. The nominal values of those gains at Mach 0.6 and altitude 20,000 ft are shown in Tab. 4-6.

Variable	Description	Nominal Value
PK15	Pitch stick proportional gain. Adjusts the DC gain of the transfer function.	0.3823
PK16	Normal acceleration, n_z, proportional gain. Acts on the frequency ω_n of the short period mode.	1.3380
PK18	Pitch rate proportional gain. Changes the damping of the short period mode.	0.3801

Tab. 4-6 Longitudinal CAS variables selected for design

A root locus that shows the effects of the feedback gains, PK16 and PK18, is shown in Fig. 4-17. It is possible to see that the normal acceleration proportional gain (PK16) acts on the natural frequency of the short period mode leaving the damping almost constant, while the pitch rate proportional gain (PK18) changes the damping keeping unaltered the

natural frequency. These three gains give us enough degrees of freedom to reach a good matching with the target transfer function.

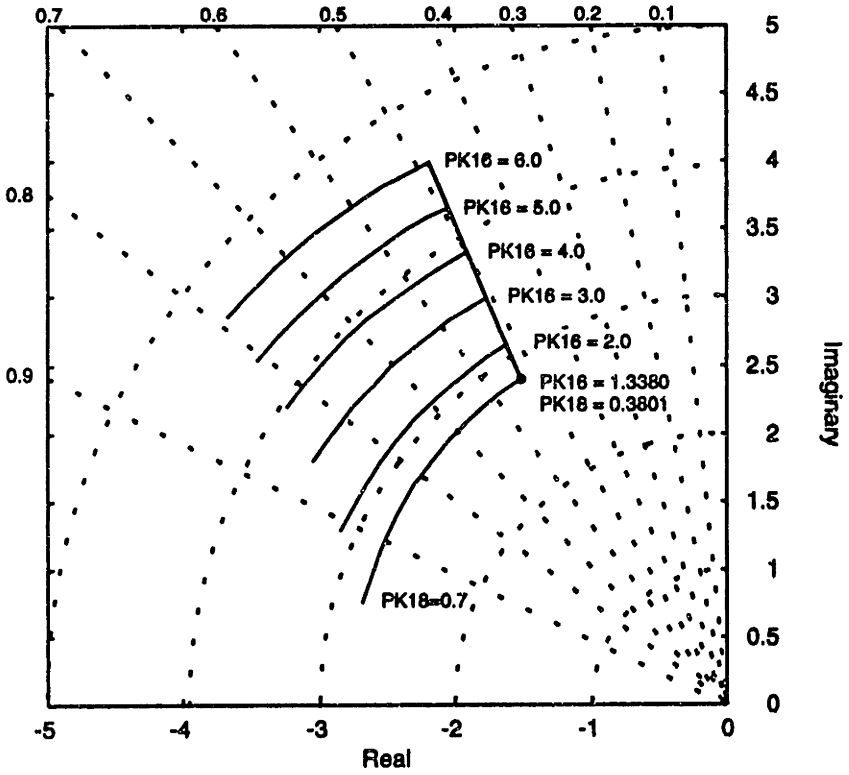

Fig. 4-17 Short Period Mode Root Locus as a function of the gains PK16 and PK18

In order to create the interconnection for the model following problem a block diagram description of the system can be of great help. We have presented the numerical values only for the low order system. The block diagram of the longitudinal dynamics of the F-18 HARV opened at the three controller gains is shown in Fig. 4-18.

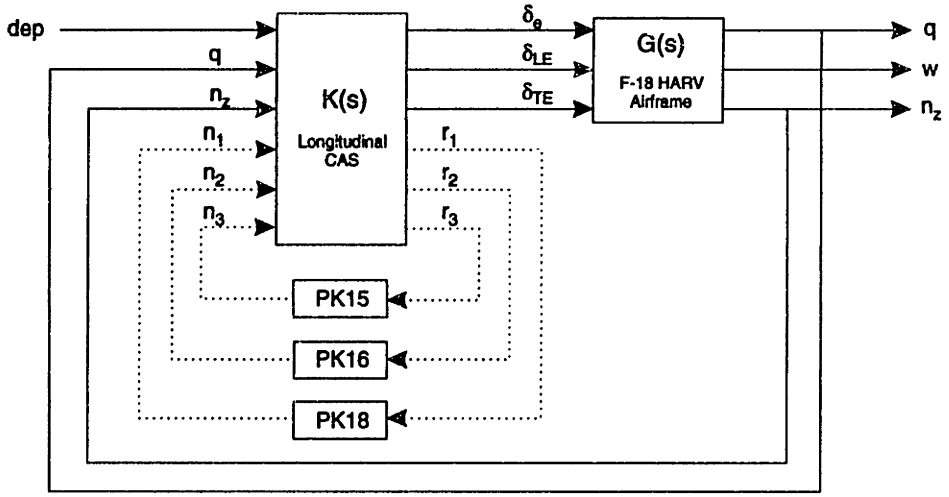

Fig. 4-18 F-18 HARV Closed Loop Longitudinal Dynamics With Controller opened at the proportional gains

The transfer function, *P(s)*, has the following form

$$\dot{x} = Ax + B_{11}dep + B_{12}n$$
$$q = C_{11}x + D_{11}dep + D_{12}n$$
$$r = C_{21}x + D_{21}dep + D_{22}n$$

where n and r are the output and the input to the ΔK block. The matrices of the linear model are shown in Tab. 4-7.

$$A = \begin{bmatrix} -0.2780 & -0.0062 & -0.1208 \\ 617.3039 & -0.7056 & -1.3543 \\ 14.5292 & 0.0592 & 0.1137 \end{bmatrix} \quad B_{11} = \begin{bmatrix} 0.0063 \\ 0.0708 \\ -4.6196 \end{bmatrix} \quad B_{12} = \begin{bmatrix} 0.1208 & -0.1208 & -0.1208 \\ 1.3543 & -1.3543 & -1.3543 \\ -0.1137 & 0.1137 & 0.1137 \end{bmatrix}$$

$$C_{11} = \begin{bmatrix} 57.2958 & 0 & 0 \end{bmatrix} \qquad D_{11} = [0] \qquad D_{12} = \begin{bmatrix} 0 & 0 & 0 \end{bmatrix}$$

$$C_{21} = \begin{bmatrix} 0 & 0 & 0 \\ 0.1061 & 0.0220 & 0.0421 \\ 57.2958 & 0 & 0 \end{bmatrix} \quad D_{21} = \begin{bmatrix} 7.0070 \\ -0.0022 \\ 0 \end{bmatrix} \quad D_{22} = \begin{bmatrix} 0 & 0 & 0 \\ 0 & 0 & 0 \\ 0 & 0 & 0 \end{bmatrix}$$

Tab. 4-7 State Space Matrices of the F-18 HARV with the Controller opened at the proportional gains

At this point we are ready to form the interconnection structure for the model matching, by simply placing the target plant in parallel to the F-18 HARV block diagram and

calculating the difference between closed loop and desired pitch rate. This simple structure is shown in Fig. 4-19.

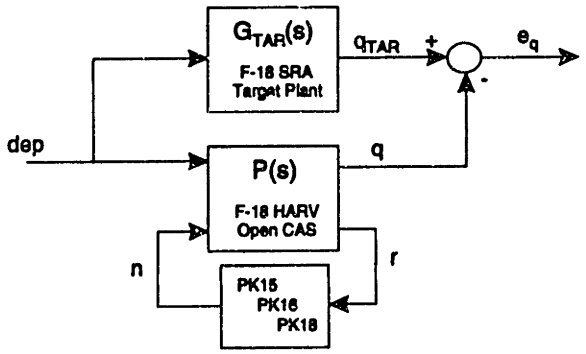

Fig. 4-19 The structure of the model following problem

The linear model of the model matching problem can be easily obtained from the state space models of the target plant and the F-18 HARV opened at the controller gains.

$$A = \begin{bmatrix} A & 0 \\ 0 & A_{TAR} \end{bmatrix} \qquad B = \begin{bmatrix} B_{11} & B_{12} \\ B_{TAR} & 0 \end{bmatrix}$$

$$C = \begin{bmatrix} C_{11} & -C_{TAR} \\ C_{21} & 0 \end{bmatrix} \qquad D = \begin{bmatrix} D_{11} - D_{TAR} & D_{12} \\ D_{21} & D_{22} \end{bmatrix}$$

The problem is now to find the set of gains PK15, PK16, and PK18 which minimizes the infinity norm of the transfer function from *dep* to e_q, where e_q is the difference between the target and actual pitch rate.

4.6.4 Results

The optimization problem was solved using the LMI algorithm described in paragraph 4.4.1.1 and the Newton search procedure outlined in paragraph 4.5. The design was performed on both the low order model and the full order model.

The actual gains of the longitudinal CAS were used as the starting point of the LMI procedure. Fig. 4-20 shows the values of the gains as we iterate between the two LMIs. We can see that after 30 iterations the gains stabilize around their final value. The H_∞ norm of

the pitch error (γ) is shown in the last plot of Fig. 4-20. In the same plot the dotted lines show the values of the gains and of the H_∞ norm obtained using a Newton search. We can see that the end values are very close, the difference being related to the precision with which we calculate the H_∞ norm.

In order to show that a minimum was really reached, Fig. 4-21 shows the contour plots of constants norms and the path followed by the two gains, PK16 and PK18, during the LMI iteration. The steep increase in the norm divides the plane into stable and unstable regions. It is well known that the H_∞ norm goes to infinity when the plant become unstable. For values of gains to the left of the boundary the system is unstable while for values to the right it is stable. This kind of plot is very useful to check the solution: we can clearly see that in terms of PK16 and PK18 the solutions corresponds to a global minimum. Similar plots for different combinations of the gains showed that the solution is in fact a global minimum for the three gains.

Variable	Initial Value	LMI Solution	Newton Solution
PK15	0.3823	0.6596	0.6663
PK16	1.3380	2.6025	2.5594
PK18	0.3801	0.6222	0.6283
H_∞ norm (γ)	3.2379	0.1915	0.1857

Tab. 4-8 Longitudinal CAS: initial and final gains

Fig. 4-22 compares the Bode diagrams of the F-18 HARV with the nominal gains and the new gains, to that of the target transfer function. As expected the F-18 HARV with the new gains is very close to the target plant; the system now has a larger bandwidth and is more damped.

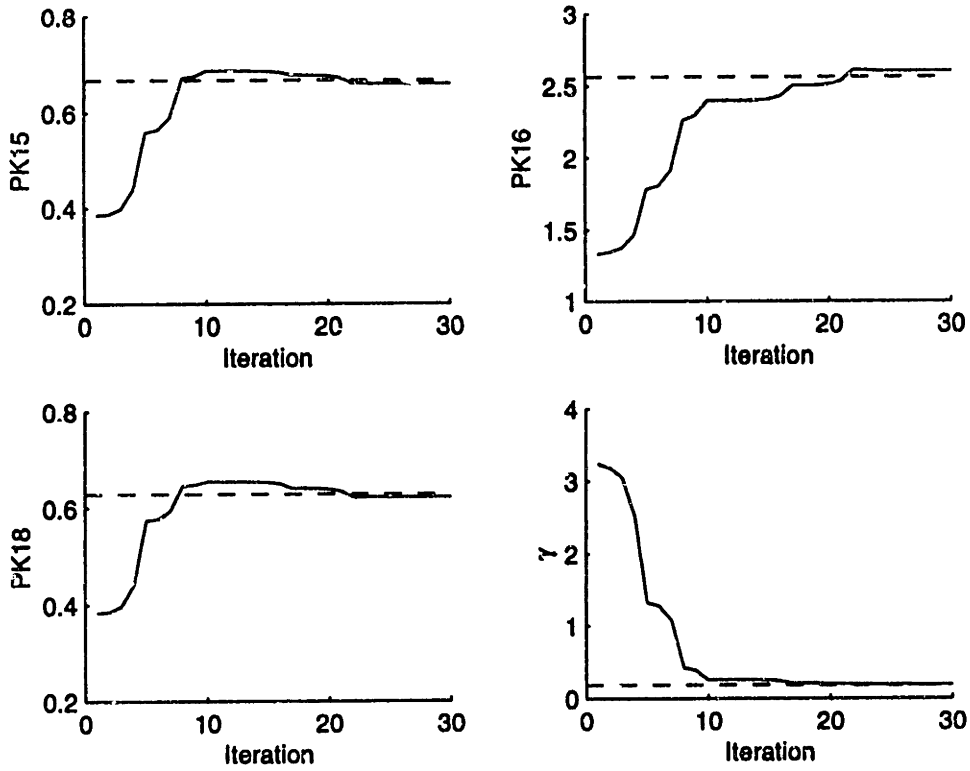

Solid Line: LMI iterations

Dashed Line: Solution found at the end of Newton search

Fig. 4-20 Convergence of the CAS Variables during the LMI optimization

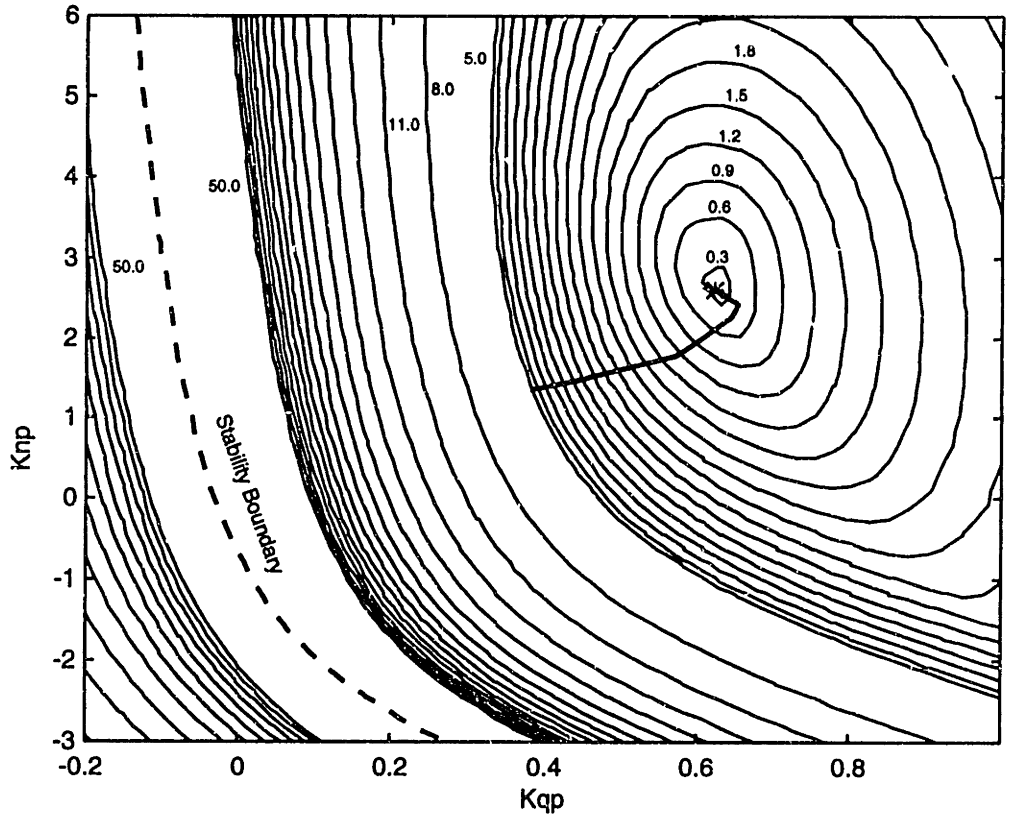

Fig. 4-21 Path along which the minimum is reached using LMIs

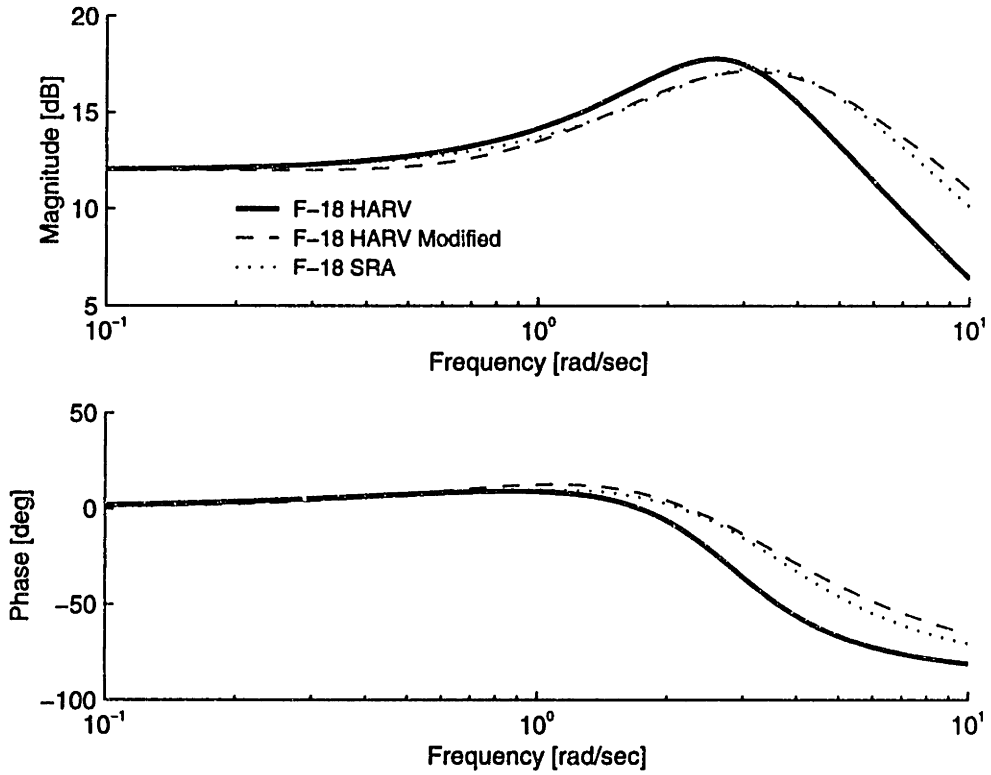

Fig. 4-22 F-18 HARV Modified, Target, and Standard Bode Diagrams

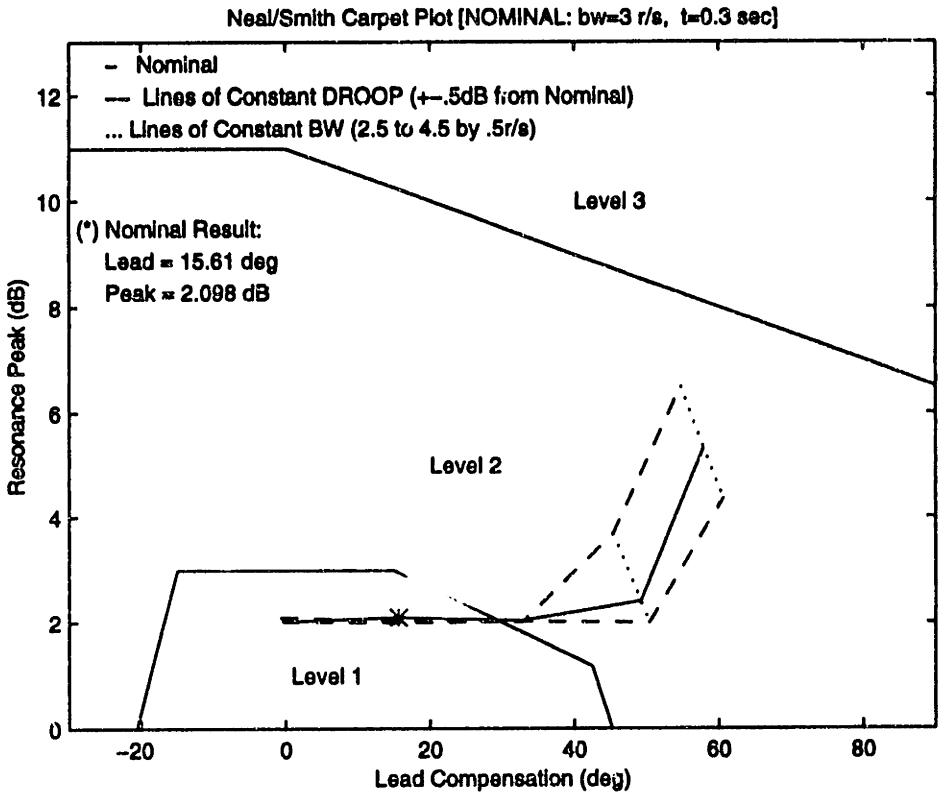

Fig. 4-23 Neal-Smith Carpet Plot of the F-18 HARV with the new gains

The Neal-Smith Carpet plot of Fig. 4-23 shows that the airplane with the new set of gains has reached a solid level 1 flying qualities for a 3 rad/sec task bandwidth.

The design was also performed on the full order model. In this case the LMI algorithm was unable to converge to a solution. The Newton optimization gave γ_{min} = 0.2756, which indicates that a good match with the target plant was obtained.

Fig. 4-9 shows the proportional gains of the new controller.

Variable	Newton Solution Full Order
PK15	0.6100
PK16	2.3097
PK18	0.5831
H_∞ norm (γ)	0.2756

The linearized model included the five states of the rigid body longitudinal dynamics, three second order models for the actuator dynamics, and a fourth order CAS.

Tab. 4-9 Longitudinal CAS: high order system H_∞ design

The Bode diagrams of the target plant, the F-18 HARV, and the F-18 HARV with the new gains are shown in Fig. 4-25. As in the previous case there is a good matching between the target plant and the HARV with the new gain. Also the Neal-Smith plot of Fig. 4-26 shows that level 1 handling qualities are achieved for 3 rad/sec task bandwidth. The introduction of the linearized actuators model made the system more sensitive to the task bandwidth.

An H_2 design was also completed on the high order system. In this case instead of minimizing the H_∞ norm of the error, we minimized the H_2 norm of the difference between the target transfer function and the F-18 HARV transfer function. The gains are very similar to the ones obtained in the H_∞ design. The results are summarized in the following table:

Variable	Newton Solution Full Order - H_2	Newton Solution Full Order - H_∞
PK15	0.5974	0.6100
PK16	2.4150	2.3097
PK18	0.5633	0.5831
H_2 norm (γ)	0.2919	0.2756

Tab. 4-10 Longitudinal CAS: high order system H_2 design

Finally the algorithms were tested adding two more gains to the design problem. The pitch rate integral gain (PK21) and the normal acceleration integral gain (PK19) were added to the ΔK block of Fig. 4-19. The design was performed on the low order model. The LMI algorithm didn't have any convergence problem and starting from the nominal gains it reduced the cost function down to 0.1653. This value is a little lower than the minimum cost obtained when three gains were redesigned (see Tab. 4-8). On the contrary the Newton search presented serious convergence problems; after several attempt a final of cost of 0.1639 was reached and an optimal solution was found. Tab. 4-11 shows the proportional and integral gains obtained at the end of the 5 gains design. The two gains that play the most important role are the pitch stick proportional gain (PK15) and the pitch rate proportional gain (PK18). Both algorithms converge to the same values for PK15 and PK18. The other three gains are instead a little different at the end of the two optimization algorithms even if

the final norm is almost the same. This indicated that the final value of the H_∞ norm does not change significantly with small changes in one of these three gains.

Variable	Initial Value	LMI Solution	Newton Solution
PK15	0.3823	0.6683	0.6646
PK16	1.3380	2.2488	2.1034
PK18	0.3801	0.6182	0.6144
PK19	1.3380	1.0195	0.9217
PK21	0.2486	0.3190	0.3496
H_∞ norm (γ)	3.2379	0.1653	0.1639

Tab. 4-11 Longitudinal CAS: Five Gains Design

Fig. 4-24 shows the convergence of the gains to their optimal value when the LMI algorithm is used. After about 100 iterations the cost has almost reached its minimum value and the gains are stabilized at their final value.

4.6.5 Time Domain Nonlinear Simulations

The new set of gains obtained by the high order system design were implemented in a full nonlinear simulator. A brief overview of the F-18 nonlinear simulator is given in Appendix A. For a more complete description of the simulator refer to Ref.4-5.

The higher gains represent the major concern in the new design. In the case of large pilot inputs we can expect to saturate the stabilator which can induce rate-limited PIOs. For this reason large pilots inputs were used and the commands of the new control law were compared with those of the old one. In general the difference in the surfaces activity was not large enough to create a real concern.

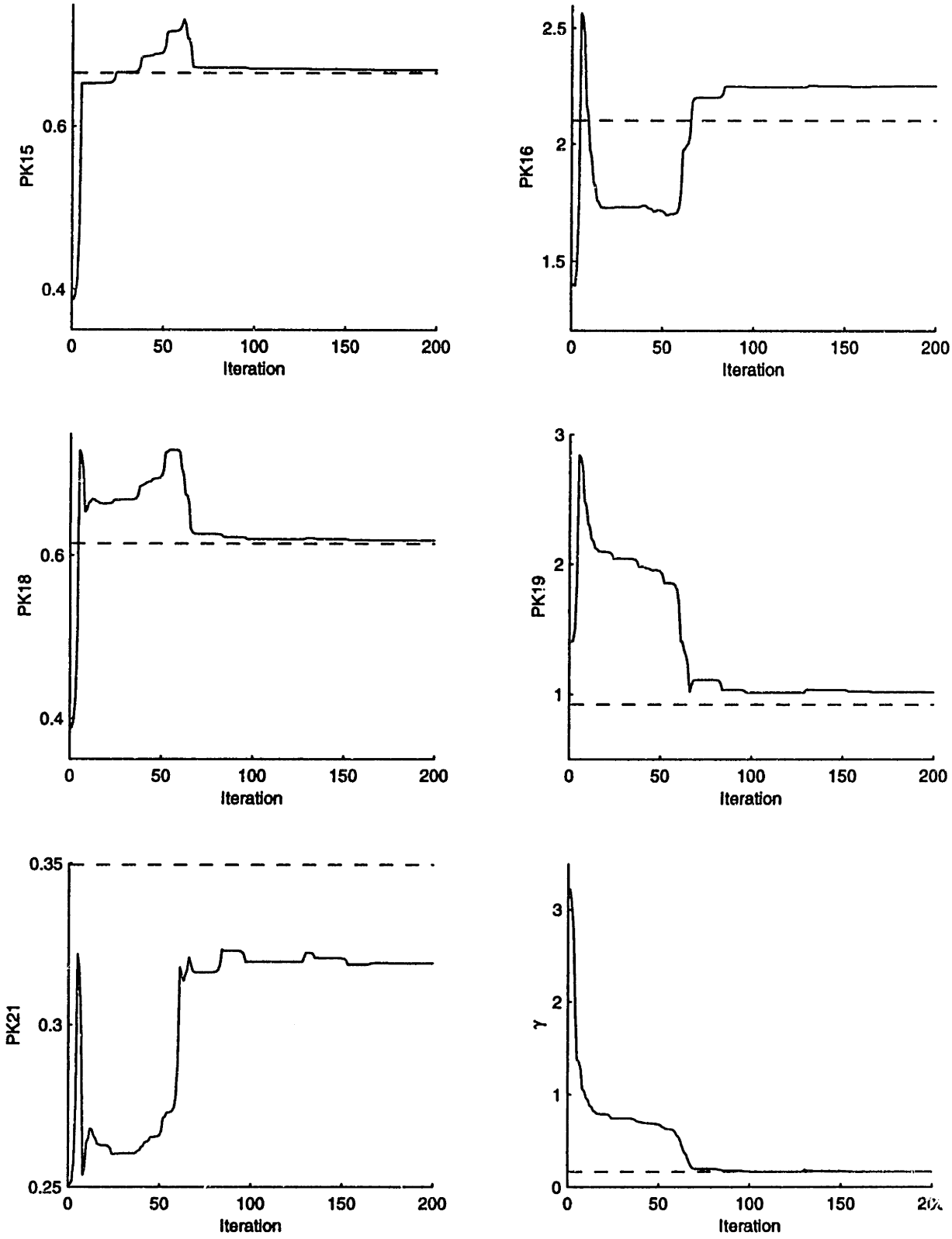

Fig. 4-24 Convergence of the CAS Variables during the LMI optimization

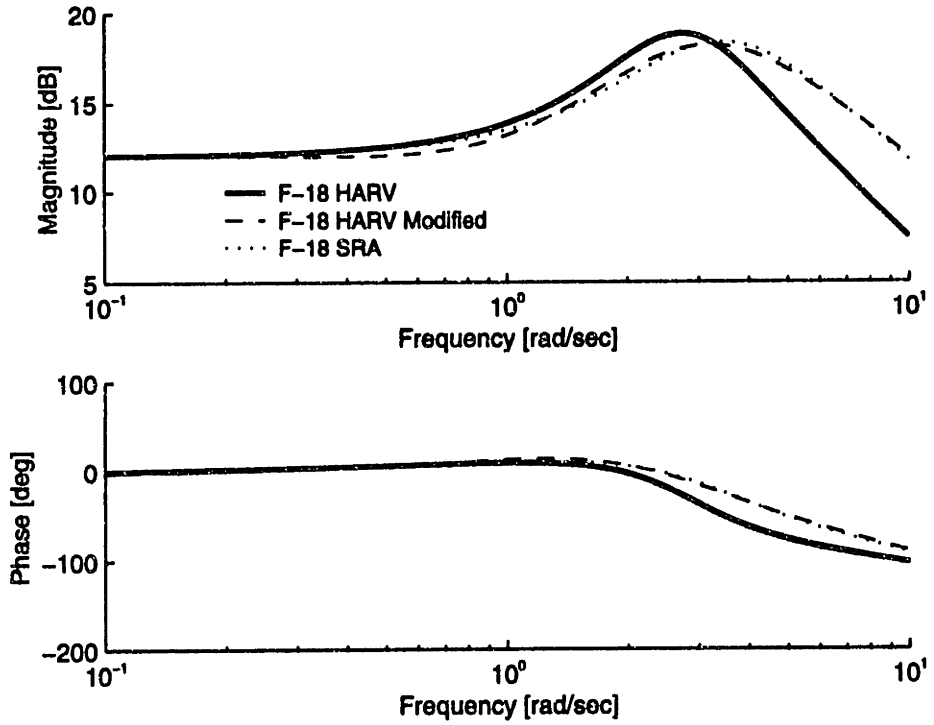

Fig. 4-25 High order System: Modified, Standard, and Target Bode Diagrams

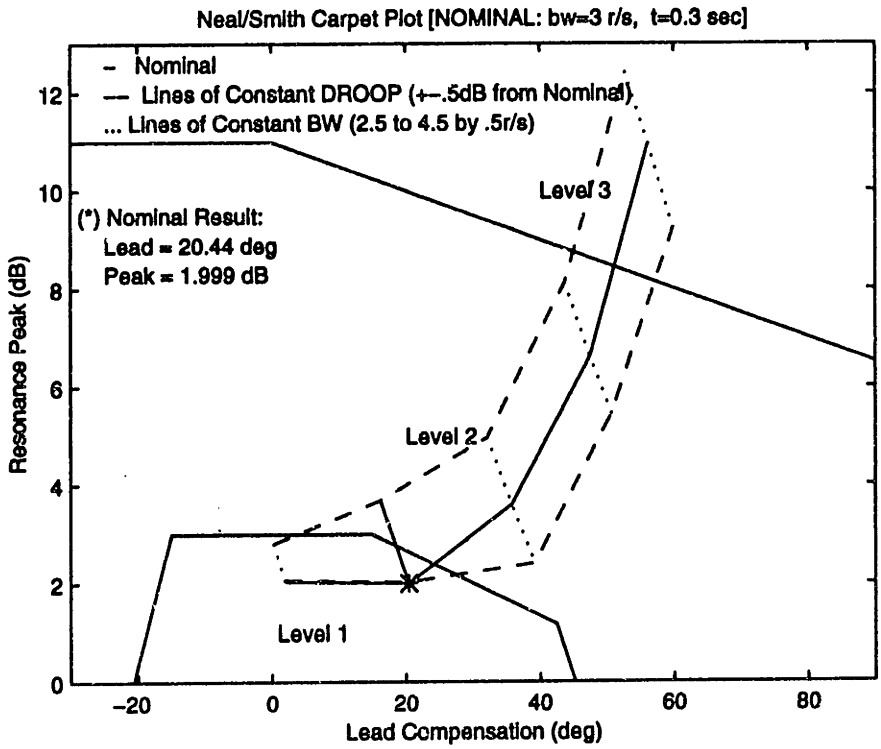

Fig. 4-26 Neal-Smith Carpet Plot of the High Order F-18 HARV with New Gains

Pulses of different amplitudes, doublets, and ramps were used to show the performance of the new CAS. The response of the F-18 SRA, the F-18 HARV, and the F-18 HARV with the modified gains to pitch stick pulses are shown in Fig. 4-27, and Fig. 4-29. The differences in the trim values of the pitch attitude and angle of attack reflect the differences in the mass and inertia characteristics of the F-18 HARV with respect to the F-18 SRA. Looking at the time domain traces, we see how the modified control law has a response very similar to the F-18 SRA. The response of the HARV with the unmodified control law is slower with a longer longitudinal oscillatory motion. The modification to the control law corrects this aspect almost perfectly. The peak time and the rise time (measured as the time to go from 10% to 90% of the peak overshoot) of the F-18 HARV modified are almost identical to those of the F-18 SRA, the standard F-18 HARV as expected presents a slower response. The beneficial effects of the new gains are less important for large stick inputs. In this case the stabilator reaches its rate limit and also the modified gains are unable to speed up the response of the F-18 HARV. This is evident in the time history of the pitch rate shown in Fig. 4-29.

The stabilator deflection and rate time histories for both the control law are plotted in Fig. 4-28 and Fig. 4-30. As we already mentioned, the main concern is rate saturation due to higher gains. From those plots we can see that the modified CAS makes a stronger use of the horizontal tail but the rate saturation level is still very similar to the standard CAS.

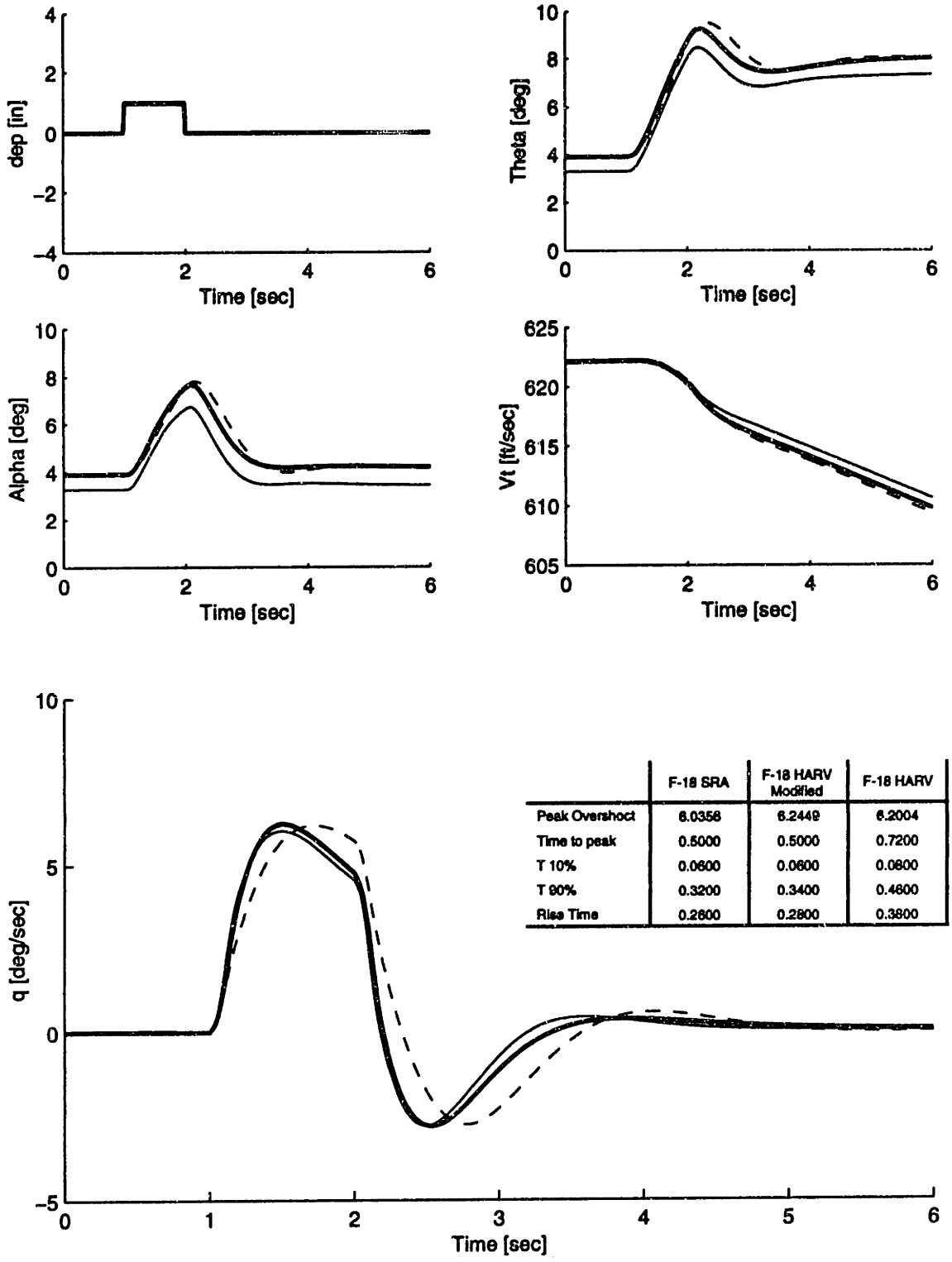

	F-18 SRA	F-18 HARV Modified	F-18 HARV
Peak Overshoot	6.0358	6.2449	6.2004
Time to peak	0.5000	0.5000	0.7200
T 10%	0.0600	0.0600	0.0600
T 90%	0.3200	0.3400	0.4600
Rise Time	0.2600	0.2800	0.3800

Fig. 4-27 Time domain response to a 1 inch pitch stick impulse: longitudinal states

Thick Solid Line: F18 HARV Modified
Thin Solid Line : F-18 SRA
Dashed Line: F-18 HARV

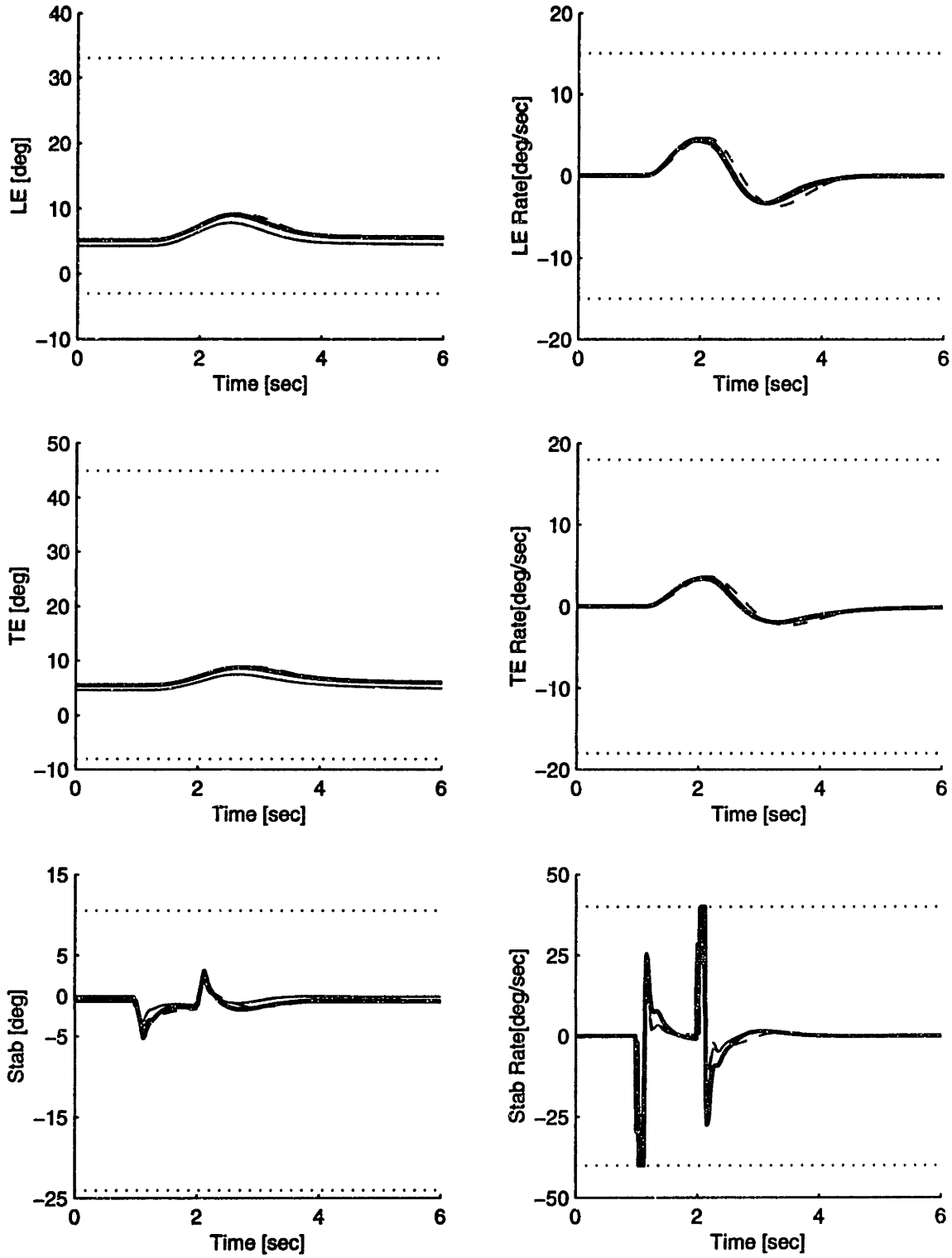

Fig. 4-28 Time domain response to a 1 inch pitch stick impulse: controls

Thick Solid Line: F18 HARV Modified
Thin Solid Line : F-18 SRA
Dashed Line: F-18 HARV

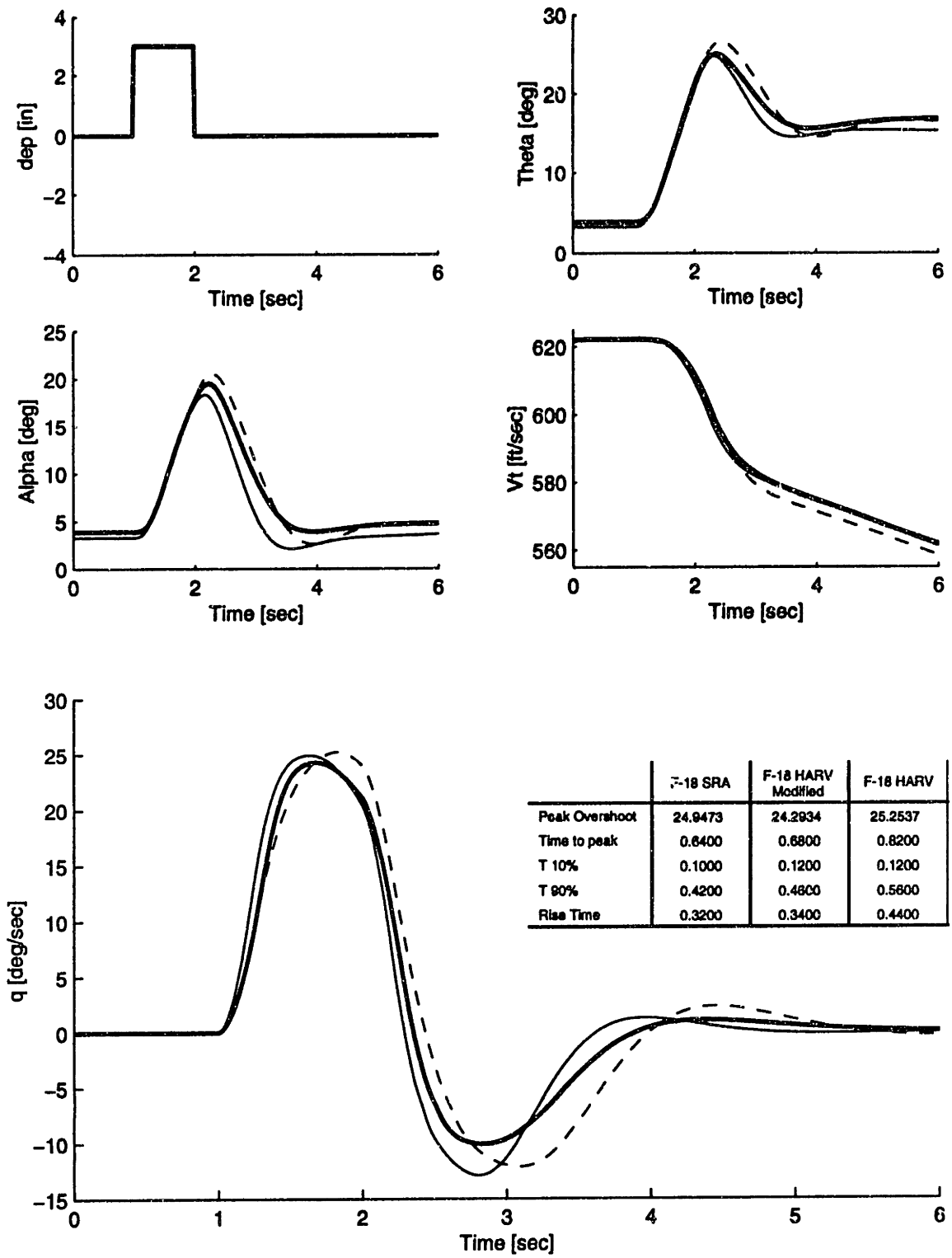

	F-18 SRA	F-18 HARV Modified	F-18 HARV
Peak Overshoot	24.9473	24.2934	25.2537
Time to peak	0.6400	0.6800	0.8200
T 10%	0.1000	0.1200	0.1200
T 90%	0.4200	0.4800	0.5600
Rise Time	0.3200	0.3400	0.4400

Fig. 4-29 Time domain response to a 3 inch pitch stick impulse: longitudinal states

Thick Solid Line: F18 HARV Modified
Thin Solid Line : F-18 SRA
Dashed Line: F-18 HARV

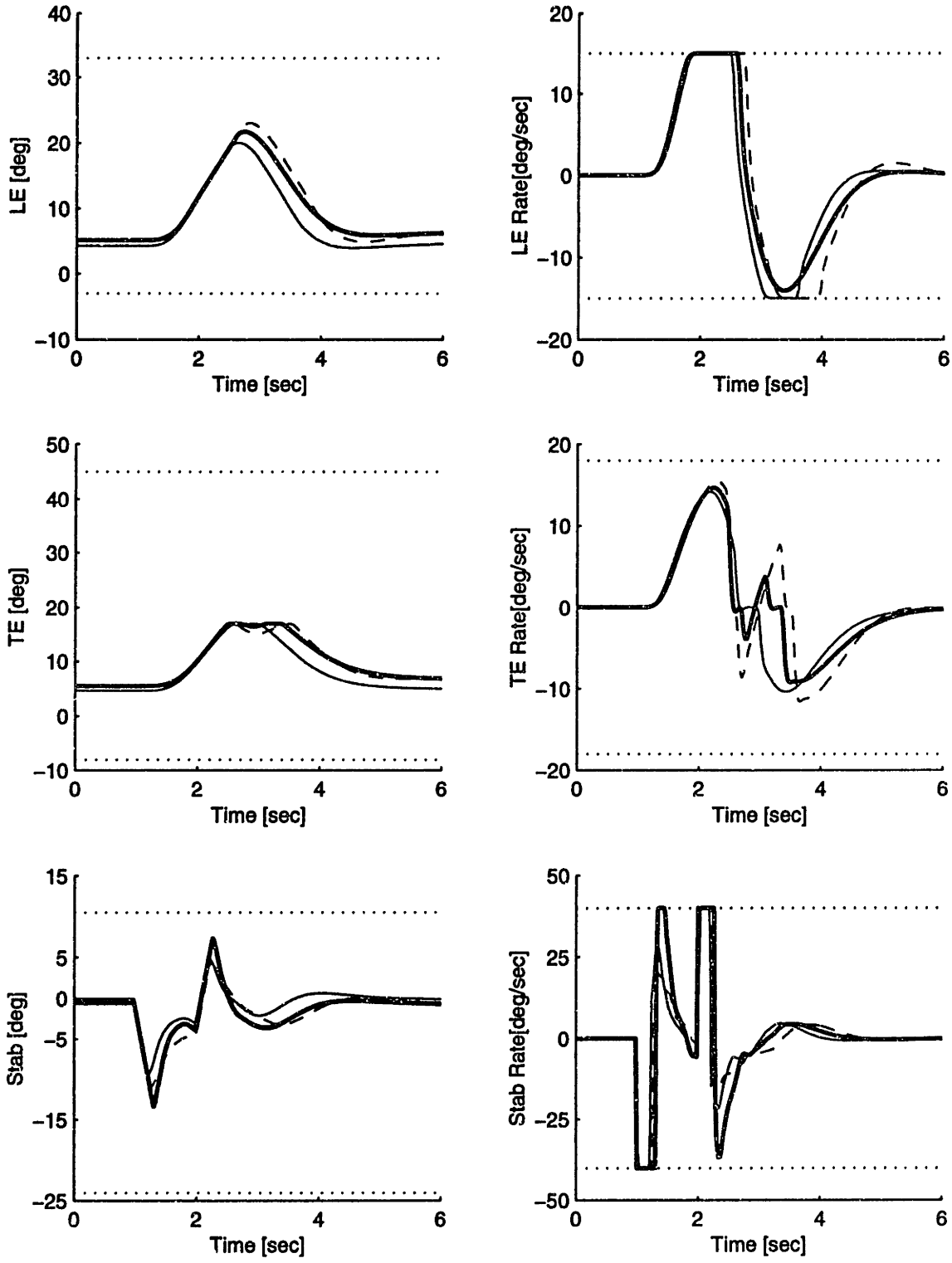

Fig. 4-30 Time domain response to a 3 inch pitch stick impulse: controls

Thick Solid Line: F18 HARV Modified
Thin Solid Line : F-18 SRA
Dashed Line: F-18 HARV

4.7 References

Ref.4-1 G. Kreisselmeier and R. Steinhauser, "Systematic Control Design by Optimizing a Vector Peformance Index", *Proceedings of IFAC Symposium on Computer Aided Design of Control Systems*, Zurich, 1979, pp.113-117.

Ref.4-2 G. Kreisselmeier and R. Steinhauser, "Application of Vector Performance Optimization to a Robust Control Loop Design for a Fighter Aircraft", *International Journal of Control*, 1983, Vol. 37, No. 2, pp. 251-284.

Ref.4-3 R. A. Hyde, "H_∞ Aerospace Control Design", Springer-Verlag, 1995, pp. 103-119.

Ref.4-4 J. M. Edmunds, "Control system design and analysis using closed-loop Nyquist and Bode arrays", *International Journal of Control*, 1979, Vol. 30, No. 5, pp. 773-802.

Ref.4-5 P. Miotto and J. D. Paduano, 'Nonlinear F-18 HARV Simulator for Matlab and Simulink', Massachussetts Institute of Technology, ICE Lab, Internal Note, January 1997.

Ref.4-6 S. Boyd, L. El Ghaoui, E. Feron, and V. Balakrishnan, "Linear Matrix Inequalities in System and Control Theory", *SIAM Studies in Applied Mathematics*, 1994.

Ref.4-7 "Military Specification, Flying Qualities of Piloted Airplanes", MIL-F-8785C, August 1980.

Ref.4-8 "Military Standard, Flying Qualities of Piloted Vehicles", MIL-STD-1797A, January 1990.

Ref.4-9 R.E. Bailey and R.E. Smith, Analysis of Augmented Aircraft Flying Qualities Through Application of the Neal-Smith Criterion, *AIAA Guidance and Control Conference*, Albumquerque, New Mexico, 1981.

Ref.4-10 J.T. Bosworth and T.H. Cox, "A design procedure for Handling Qualities Optimization of the X-29A Aircraft", NASA Technical Memorandum 4142, 1989.

Ref.4-11 D. J. Wilson, J. E. Buckley, and D. R. Riley, "Unified Flying Qualities Criteria For Longitudinal Tracking", *AIAA Atmospheric Flight Mechanics Conference*, Portland, Oregon, August 1990, pp. 64-74.

Ref.4-12 J. C. Gibson, "Piloted Handling Qualities Design Criteria for High Order Flight Control Systems", *AGARD FMP Conference*, Forth Worth, Texas, April 1982.

Ref.4-13 K. R. Boff and J. E. Lincoln, "Engineering Data Compendium: Human Perception and Performance", AAMRL, Wright-Patterson AFB, OH, 1988, pp. 1644-1645.

Ref.4-14 G. E. Cooper and R. P. Harper, "The use of pilot rating in the evaluation of aircraft handling qualities", NASA-TN-D-5153, Moffet Filed Ca, Ames Research Center NASA, 1969.

Ref.4-15 J. D. McDonnel, "Pilot rating techniques for the estimation and evaluation of handling qualities", AFFDL-TR-68-76, Wright-Patterson AFB, OH, Air Force Flight Dynamics Laboratory, 1968.

Ref.4-16 T. P. Neal and R. E. Smith, "An In-Flight Investigation to Develop Control System Design Criteria for Fighter Airplanes", AFFDL-TR-70-74, June 1970.

Ref.4-17 P. Gahinet, A. Nemirovski, A. J. Laub, and M. Chilali, "LMI Control Toolbox", The MathWorks Inc., 1995.

Ref.4-18 C. G. Broyden, "The Convergence of a Class of Double-rank Minimization Algorithms", *J. Inst. Maths. Applics.*, Vol. 6, pp.76-90, 1970.

Ref.4-19 R. Fletcher, "A New Aopproach to Variable Metric Algorithms", *Computer Joirnal*, V0l. 13m pp. 317-322, 1970.

Ref.4-20 D. Golfarb, "A Family of Variable Metric UpdatesDerived by Variational Means", *Mathematics of Computing*, Vol. 24, pp. 23-26, 1970.

Ref.4-21 D. F. Shanno, "Conditioning of Quasi-Newton Methods for Function Minimization", Mathematics of Computing, Vol.24, p. 23-26, 1970

Ref.4-22 A. Grace, "Optimization Toolbox", The MathWorks Inc., October 1994.

Chapter 5

Gain Scheduling of Fixed Structure Controllers

5.1 Introduction

In the previous chapter, we formulated the fixed-structure control problem in a framework consistent with modern control theory. The goal was to allow commonly encountered flight-control redesign problems to be addressed in the context of currently available computational techniques and theories. In particularly, we showed how to formulate an H_∞ model-matching optimization, and append this optimization with a measure of Neal-Smith handling qualities performance, to improve the refueling handling qualities of the F/A-18 HARV.

The development was purposely set up to allow the additional issue of gain scheduling to be addressed. This is the main topic of this chapter. Control law design must be carried out at a large number of flight points to create a realistic flight control system. Typically this is done using separate point designs, tied together through interpolations and blends. It is our purpose here to automate this procedure by first defining the *form* of the gain schedule, and then determining the coefficients in the gain schedule via optimization. By utilizing recent theoretical developments for linear parameter varying (LPV) systems, we are able to insure that the optimization yields stabilizing controllers.

This chapter is organized much like the previous one. We start by introducing the Linear Parameter Varying control theory and we relate it to the gain scheduling of fixed structure controllers. We then describe a motivating example, based again on the F/A-18 HARV Control Augmentation System. We show the practical use of the method by designing a new gain scheduling that covers a large portion of the flight envelope. Finaliy we show the results of a series of tests performed on a fixed based flight simulator at NASA

Dryden. In particular we analyze the refueling task performed on the simulator by several pilots and we show the improvements obtained with the new gain schedule.

5.2 LPV Systems and Gain Scheduling of Fixed Structure Controllers

Recent years have seen a growing interest in the use of LPV-based methods to design controllers that work over a wide operating range of the plant. Conceptually there is a strong relation between classical gain scheduling and LPV control theory. In both cases there is an attempt to schedule the controller against the key nonlinear parameters that affect the plant behavior. The classical gain scheduling technique is primarily a manual procedure in which the control engineer builds up his control law piece by piece, considering one operating point at a time and closing one loop at a time. In contrast, the LPV technique treats the design of a full-envelope dynamic controller; the gain schedule is determined as part of the procedure. The design via LPV comes with guaranteed robustness and performance, and in general LPV theory has reached a high level of maturity and theoretical elegance. The main disadvantage of this and other modern control techniques is that it is difficult to introduce additional constraints (such as a fixed controller structure) or to adapt existing design criteria (such as handling qualities). Thus years of experience and testing are ignored if the mathematical framework is adopted unaltered.

Our goal is to combine the advantages of fixed structure classical gain scheduling and LPV control theory. The possibility to retain the guaranteed robustness and performance of an LPV design provides classical gain scheduling with the algorithmic approach and theoretical foundation that has long been considered missing. We start by describing LPV systems, then we show how the problem of gain scheduling of fixed structure controllers can be viewed as an LPV control problem.

5.2.1 LPV Systems

In this section we introduce the Linear Parameter Varying control problem and a set of definitions that will be used throughout this chapter.

Definition 5-1 (Parameter Variation Set) *Given a compact subset* $\Theta \subset R^s$, *the parameter variation set* $\mathcal{F}_\Theta$ *denotes the set of all continuous functions mapping* R^+ *(time) into* Θ.

Definition 5-2 (Linear Parameter Varying (LPV) System) *Assume that the following are given: a compact set* $\Theta \subset R^s$, *and the continuous functions* $A : R^s \to R^{n\times n}$, $B : R^s \to R^{n\times n_u}$, $C : R^s \to R^{n_y\times n}$, *and* $D : R^s \to R^{n_y\times n_u}$. *These represent an* n^{th} *order linear parametrically varying (LPV) system whose dynamics evolve as*

$$\begin{bmatrix}\dot{x}(t)\\ y(t)\end{bmatrix}=\begin{bmatrix}A[\theta(t)] & B[\theta(t)]\\ C[\theta(t)] & D[\theta(t)]\end{bmatrix}\begin{bmatrix}x(t)\\ u(t)\end{bmatrix} \qquad [5\text{-}1]$$

where $\theta \in \mathcal{F}_\Theta$

These two definitions fully characterize LPV systems. In other words LPV systems are linear systems where the state-space matrices A, B, C, and D are explicit functions of a time varying parameter θ (θ can also be a vector). LPV systems can represent different situations depending on the definition of θ. They can represent linear system subject to uncertainties (in this case θ is a vector of time varying uncertainties), or a family of linear systems derived from the linearization of a nonlinear plant (in this case θ represents measurable parameters that capture the nonlinear behavior of the system). In this work we will consider the second definition of LPV systems.

An LPV description of a system can be obtained directly from the nonlinear equations of motion (as an example see the LPV control design for pitch axis auto-pilot Ref.5-4) or via interpolation of linear models obtained at various points of the operating envelope (see the linear parameter-varying control of a ducted fan engine Ref.5-5 or the linear parameter-varying control design of a pressurized water reactor Ref.5-6). In this example we will use an interpolation of linear models to define our LPV system.

The next definition that we give is that of quadratic stability of an LPV system. Suppose that we are given Θ and the continuous matrix function $A : R^s \to R^{n\times n}$. Consider the undriven LPV system

$$\dot{x}(t) = A[\theta(t)]\dot{x}(t) \qquad [5\text{-}2]$$

where $\theta \in \mathscr{F}_\Theta$. Define the scalar valued function $V: R^n \to R$ as $V(x) = x^T P x$, where $P = P^T > 0$. For any $\theta \in \mathscr{F}_\Theta$, along trajectories of equation 5-2, the time derivative of $V(x)$ is given by

$$\frac{d}{dt}V[x(t)] = x^T(t)\left[A^T[\theta(t)]P + PA[\theta(t)]\right]x(t) \qquad [5\text{-}3]$$

Definition 5-3 (Quadratic Stability of LPV Systems) *The function A is quadratically stable over Θ if there exists a $P \in R^{n\times n}$, $P = P^T > 0$, such that for all $\theta \in \Theta$*

$$A^T[\theta(t)]P + PA[\theta(t)] < 0 \qquad [5\text{-}4]$$

We now define the induced L_2 - norm of a quadratically stable LPV system.

Definition 5-4 (L_2 - norm of a qudratically stable LPV system) *Given a quadratically stable LPV system, for zero initial conditions, the induced L_2 - norm is defined as*

$$\left\|G_{\mathscr{F}_\Theta}\right\| := \sup_{\theta\in\mathscr{F}_\Theta}\sup_{\substack{\|u\|_2\neq 0\\ u\in L_2}}\frac{\|y\|_2}{\|u\|_2} \qquad [5\text{-}5]$$

We now can define the main analysis lemma in the solution of the quadratic LPV $\gamma-$ performance problem.

Lemma 5-5 (LPV $\gamma-$performance problem) *Given an LPV system, as in definition 5-2, and a scalar $\gamma > 0$. If there exists a $P \in R^{n\times n}$, $P = P^T > 0$, such that for all $\theta \in \Theta$,*

$$\begin{bmatrix} A^T[\theta(t)]P + PA[\theta(t)] & PB[\theta(t)] & C^T[\theta(t)] \\ B^T[\theta(t)]P & -\gamma I & D^T[\theta(t)] \\ C[\theta(t)] & D[\theta(t)] & -\gamma I \end{bmatrix} < 0 \qquad [5\text{-}6]$$

then:

1) *the function A is quadratically stable over* Θ;

2) *there exists a* $\beta < \gamma$ *such that* $\left\| G_{\mathscr{F}_\Theta} \right\| \le \beta$.

Proof: see Ref.5-1.

Note that if instead of an LPV system we have an LTI system, then Lemma 5-5 is equivalent to A being stable and the H_∞ norm from u to y being less than γ.

Once the LPV system analysis has been established, the next step in LPV theory is a performance-oriented, parametrically dependent, output feedback synthesis problem. Packard in Ref.5-1 calls this problem the *quadratic LPV* γ*-performance problem.*

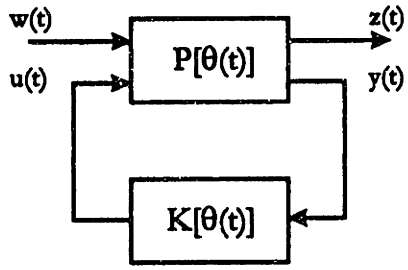

Fig. 5-1 The H_∞ synthesis structure for LPV systems

The problem is to derive a controller $K[\theta(t)]$ (see Ref.5-1) that minimize the induced L_2 - norm from w to z. Let the open loop LPV system $P[\theta(t)]$ be defined as:

$$\begin{bmatrix} \dot{x}(t) \\ z(t) \\ y(t) \end{bmatrix} = \begin{bmatrix} A[\theta(t)] & B_1[\theta(t)] & B_2[\theta(t)] \\ C_1[\theta(t)] & D_{11}[\theta(t)] & D_{12}[\theta(t)] \\ C_2[\theta(t)] & D_{21}[\theta(t)] & D_{22}[\theta(t)] \end{bmatrix} \begin{bmatrix} x(t) \\ w(t) \\ u(t) \end{bmatrix} \qquad [5\text{-}7]$$

where $\theta \in \Theta$.

In the context of LPV theory the linear feedback controller is defined as follows. Given a nonnegative integer m, and continuous functions $A_K : R^s \to R^{m \times m}$, $B_K : R^s \to R^{m \times n_y}$, $C_K : R^s \to R^{n_u \times m}$, and $D_K : R^s \to R^{n_u \times n_y}$, the linear controller can be written as

$$\begin{bmatrix} \dot{x}_k(t) \\ u(t) \end{bmatrix} = \begin{bmatrix} A_K[\theta(t)] & B_K[\theta(t)] \\ C_K[\theta(t)] & D_K[\theta(t)] \end{bmatrix} \begin{bmatrix} x_k(t) \\ y(t) \end{bmatrix} \qquad [5\text{-}8]$$

where $\theta \in \Theta$.

With simple linear algebra it is then possible to calculate the state space model of the closed loop system in Fig. 5-1.

$$\begin{bmatrix} \dot{x}_{cl}(t) \\ z(t) \end{bmatrix} = \begin{bmatrix} A_{cl}[\theta(t)] & B_{cl}[\theta(t)] \\ C_{cl}[\theta(t)] & D_{cl}[\theta(t)] \end{bmatrix} \begin{bmatrix} x_{cl}(t) \\ w(t) \end{bmatrix} \qquad [5\text{-}9]$$

Where $x_{cl}^T = \begin{bmatrix} x^T & x_k^T \end{bmatrix}$ and

$$A_{cl} = \begin{bmatrix} A + B_2(I - D_K D_{22})^{-1} D_K C_2 & B_2(I - D_K D_{22})^{-1} C_K \\ B_K C_2 + B_K D_{22}(I - D_K D_{22})^{-1} D_K C_2 & A_K + B_K D_{22}(I - D_K D_{22})^{-1} C_K \end{bmatrix}$$

$$B_{cl} = \begin{bmatrix} B_1 + B_2(I - D_K D_{22})^{-1} D_K D_{21} \\ B_K D_{21} + B_K D_{22}(I - D_K D_{22})^{-1} D_K D_{21} \end{bmatrix}$$

$$C_{cl} = \begin{bmatrix} C_1 + D_{12}(I - D_K D_{22})^{-1} D_K C_2 & D_{12}(I - D_K D_{22})^{-1} C_K \end{bmatrix}$$

$$D_{cl} = \begin{bmatrix} D_{11} + D_{12}(I - D_K D_{22})^{-1} D_K D_{21} \end{bmatrix}$$

(In these equations we dropped the dependence of matrices on $\theta(t)$ for brevity.)

Using Lemma 5-5 we can say the *quadratic LPV γ-performance problem* is solvable if there exists a controller [5-8] and a positive definite matrix $P \in R^{n \times n}$, $P = P^T > 0$, such that for all $\theta \in \Theta$

$$\begin{bmatrix} A_{cl}^T[\theta(t)]P + PA_{cl}[\theta(t)] & PB_{cl}[\theta(t)] & C_{cl}^T[\theta(t)] \\ B_{cl}^T[\theta(t)]P & -\gamma I & D_{cl}^T[\theta(t)] \\ C_{cl}[\theta(t)] & D_{cl}[\theta(t)] & -\gamma I \end{bmatrix} < 0 \qquad [5\text{-}10]$$

The condition defined by the Matrix Inequality in equation 5-10 can be converted to a Riccati inequality using Schur complements

$$A_{cl}^T P + PA_{cl}^T + \frac{C^T C}{\gamma^2} + \left(PB + \frac{C^T D}{\gamma^2} \right) \left(I - \frac{D^T D}{\gamma^2} \right) \left(B^T P + \frac{D^T C}{\gamma^2} \right) < 0 \qquad [5\text{-}11]$$

Where again for simplicity we have dropped the dependence on $\theta(t)$.

We will not present the solutions to the quadratic LPV γ-performance problem, readers that are interested in a detailed description of the synthesis problem can find it in Ref.5-1, Ref.5-2, and Ref.5-3. In Ref.5-9 the authors present the LPV control design for pitch axis missile autopilot. In this case, due to the nonlinear dependence of the equation of motion on the scheduling parameters, the synthesis problem is solved gridding the bi-dimensional parameter space. In Ref.5-8 the same problem is solved using a self-scheduled H_∞ control. In this example the authors assume that the state space matrices $A(\theta)$, $B(\theta)$, $C(\theta)$, and $D(\theta)$ depend affinely on θ and that the time varying parameter θ varies in a polytope Θ. The synthesis problem results in the design of LPV polytopic controllers.

In the next section we will show how the analysis of gain scheduled fixed structure controllers can be recast to that of LPV systems.

5.2.2 Gain Scheduling of Fixed Structure Controllers: LPV formulation

In this section we will formalize the gain scheduling fixed structure control problem using the LPV formulation.

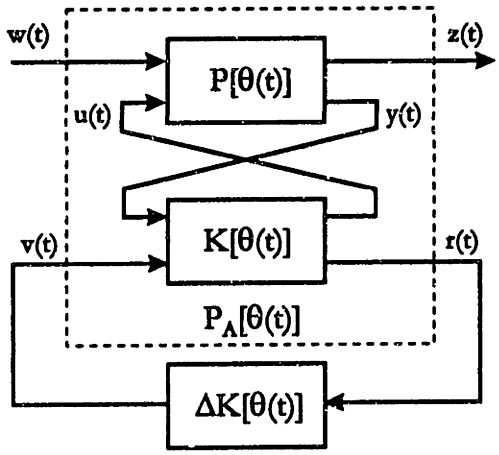

Fig. 5-2 Fixed Structure LPV Control Problem

Fig. 5-2 shows the block diagram that describes the *LPV* formulation of the fixed structure control problem. The transfer function $P[\theta(t)]$ has the same role as that of Fig. 5-1; it includes the plant and the weighting functions. The transfer function $K[\theta(t)]$ represents the fixed part of the controller (fixed in the sense that the design procedure will not try to

modify it) while $\Delta K[\theta(t)]$ is a diagonal matrix formed with the parameters of the controller that we want to redesign.

The plant $P[\theta(t)]$ in Fig. 5-2 is described by equation 5-7 while the fixed part of the controller is described by the following LPV system:

$$\begin{bmatrix} \dot{x}_k(t) \\ u(t) \\ r(t) \end{bmatrix} = \begin{bmatrix} A_k[\theta(t)] & B_{k1}[\theta(t)] & B_{k2}[\theta(t)] \\ C_{k1}[\theta(t)] & D_{k11}[\theta(t)] & D_{k12}[\theta(t)] \\ C_{k1}[\theta(t)] & D_{k21}[\theta(t)] & D_{k22}[\theta(t)] \end{bmatrix} \begin{bmatrix} x_k(t) \\ y(t) \\ v(t) \end{bmatrix} \quad [5\text{-}12]$$

The plant and the fixed part of the controller can be merged as an augmented plant $P_A[\theta(t)]$. The augmented plant is described by the usual state space model

$$\begin{bmatrix} \dot{x}_A(t) \\ z(t) \\ r(t) \end{bmatrix} = \begin{bmatrix} A_A[\theta(t)] & B_{A1}[\theta(t)] & B_{k2}[\theta(t)] \\ C_{A1}[\theta(t)] & D_{A11}[\theta(t)] & D_{A12}[\theta(t)] \\ C_{A1}[\theta(t)] & D_{A21}[\theta(t)] & D_{A22}[\theta(t)] \end{bmatrix} \begin{bmatrix} x_A(t) \\ w(t) \\ v(t) \end{bmatrix} \quad [5\text{-}13]$$

The block $\Delta K[\theta(t)]$ in Fig. 5-2 has the form:

$$\Delta K[\theta(t)] = diag\begin{bmatrix} k_1(\theta) & k_2(\theta) & \dots & k_m(\theta) \end{bmatrix} \quad [5\text{-}14]$$

where $k_i(\theta) \in R^1$ and $\theta \in \Theta$. In other words $\Delta K[\theta(t)]$ is a diagonal matrix whose elements are explicit functions of the time-varying parameter θ.

Analogous to section 5.2.1 we can now calculate the closed loop system of Fig. 5-2 as

$$\begin{bmatrix} \dot{x}_{cl}(t) \\ z(t) \end{bmatrix} = \begin{bmatrix} A_{cl}[\theta(t)] & B_{cl}[\theta(t)] \\ C_{cl}[\theta(t)] & D_{cl}[\theta(t)] \end{bmatrix} \begin{bmatrix} x_{cl}(t) \\ w(t) \end{bmatrix} \quad [5\text{-}15]$$

Where $x_{cl} = x_A$, and

$$A_{cl} = \begin{bmatrix} A_A + B_{A2}\Delta K(I - D_{A22}\Delta K)^{-1} C_{A2} \end{bmatrix} \quad [5\text{-}16]$$

$$B_{cl} = \begin{bmatrix} B_{A1} + B_{A2}\Delta K(I - D_{A22}\Delta K)^{-1} D_{A21} \end{bmatrix} \quad [5\text{-}17]$$

$$C_{cl} = \begin{bmatrix} C_{A1} + D_{A12}\Delta K(I - D_{A22}\Delta K)^{-1} C_{A2} \end{bmatrix} \quad [5\text{-}18]$$

$$D_{cl} = \left[D_{A11} + D_{A12}\Delta K (I - D_{A22}\Delta K)^{-1} D_{A21} \right] \qquad [5\text{-}19]$$

At this point we are ready to state the *quadratic LPV γ-performance problem* in the case of fixed structure controller. Using Lemma 5-5 we can say that *the quadratic fixed structure LPV γ-performance problem* is solvable if there exists a matrix $\Delta K[\theta(t)]$, equation 5-14, and a positive definite matrix $P \in R^{n \times n}$, $P = P^T > 0$, such that for all $\theta \in \Theta$

$$\begin{bmatrix} A_{cl}^T[\theta(t)]P + PA_{cl}[\theta(t)] & PB_{cl}[\theta(t)] & C_{cl}^T[\theta(t)] \\ B_{cl}^T[\theta(t)]P & -\gamma I & D_{cl}^T[\theta(t)] \\ C_{cl}[\theta(t)] & D_{cl}[\theta(t)] & -\gamma I \end{bmatrix} < 0 \qquad [5\text{-}20]$$

The last equation can also be put in the form of a Riccati inequality. It is clear at this point the analogy between the gain scheduling of fixed structure controller and the H_∞ LPV control problem. The synthesis of gain scheduled fixed structure controllers is discussed in the following section.

5.2.3 Synthesis of Gain Scheduled Fixed Structure Controllers

So far we haven't make any assumption about the dependence of ΔK on the scheduling parameters θ. In order to define a synthesis procedure that automatically takes into account gain scheduling, the dependence of the control parameters k_i on the time varying vector θ must be an integral part of the optimal control problem (see for example Ref.5-7). Assuming for example a linear relation we have:

$$k_i(\underline{\theta}) = a_{i0} + \sum_{j=1}^{n} \theta_j a_{ij} \qquad i = 1 \ldots m, \qquad [5\text{-}21]$$

where the coefficients a_{ij} determine the variable gain control law over the operating range spanned by θ. We can also consider more general nonlinear relationships between the control variables and the time varying parameters θ. For each controller parameter k_i we can define p_i nonlinear functions $F_i(\theta)$ and determine the coefficients a_{ij} in the following way:

$$k_i(\underline{\theta}) = \sum_{j=1}^{p_i} F_j(\underline{\theta}) a_{ij} \qquad i = 1 \ldots m. \qquad [5\text{-}22]$$

The total number of coefficients that need to be calculate in this case is:

$$r = \sum_{i=1}^{m} p_i \qquad [5\text{-}23]$$

Using equation 5-22 it is possible to rewrite the block $\Delta K[\theta(t)]$ in equation 5-14 as a linear function of the a_{ij} coefficients that we need to determine.

$$\Delta K[\underline{\theta}(t)] = \sum_{i=1}^{r} T_i[\underline{\theta}(t)] b_i \qquad [5\text{-}24]$$

In the above expression the vector $\underline{b}$ contains the stacked-up coefficients a_{ij} of equation 5-22. The synthesis problem now reduces to finding the coefficients b_i that verify equation 5-20. As already discussed in section 4.4, this is a non-convex problem and a closed form solution does not exists. In the next two sections we present two possible solutions of the synthesis problem. The first method is based on LMIs and the second on Newton search.

5.2.3.1 Controller Synthesis via LMI

The linear dependence of $\Delta K[\theta(t)]$ on the coefficients b_i (equation 5-24) allows us to set up an iterative procedure similar to that discussed in section 4.4. From equation 5-24 and equation 5-13 it is possible to derive the closed loop state space model:

$$\dot{\underline{x}}(t) = A_{CL}[\underline{\theta}(t)]\underline{x}(t) + B_{CL}[\underline{\theta}(t)]\underline{w}(t)$$
$$\underline{z}(t) = C_{CL}[\underline{\theta}(t)]\underline{x}(t) + D_{CL}[\underline{\theta}(t)]\underline{w}(t)$$

With the assumption that the feedthrough term $D_{A22} = 0$ in equations 5-16 ... 5-19, we have:

$$A_{CL}[\underline{\theta}(t)] = A_A[\underline{\theta}(t)] + \sum_{i=1}^{r} \left(B_{A2}[\underline{\theta}(t)] T_i[\underline{\theta}(t)] C_{A2}[\underline{\theta}(t)] \right) b_i$$

$$\mathrm{B}_{\mathrm{CL}}[\underline{\theta}(t)] = B_{A1}[\underline{\theta}(t)] + \sum_{i=1}^{r} \left(B_{A2}[\underline{\theta}(t)] T_i[\underline{\theta}(t)] D_{A21}[\underline{\theta}(t)] \right) b_i$$

$$C_{CL}[\underline{\theta}(t)] = C_{A1}[\underline{\theta}(t)] + \sum_{i=1}^{r}\left(D_{A12}[\underline{\theta}(t)]T_i[\underline{\theta}(t)]C_{A2}[\underline{\theta}(t)]\right)b_i$$

$$\mathrm{D}_{CL}[\underline{\theta}(t)] = D_{A11}[\underline{\theta}(t)] + \sum_{i=1}^{r}\left(D_{A12}[\underline{\theta}(t)]T_i[\underline{\theta}(t)]D_{A21}[\underline{\theta}(t)]\right)b_i$$

This expression is similar to equation 4-4. The matrices F_i, G_i, H_i, and N_i of equation 4-4 are now functions of θ and are defined as follows:

$$F_i[\underline{\theta}(t)] = B_{A2}[\underline{\theta}(t)]T_i[\underline{\theta}(t)]C_{A2}[\underline{\theta}(t)]$$

$$G_i[\underline{\theta}(t)] = B_{A2}[\underline{\theta}(t)]T_i[\underline{\theta}(t)]D_{A21}[\underline{\theta}(t)]$$

$$H_i[\underline{\theta}(t)] = D_{A12}[\underline{\theta}(t)]T_i[\underline{\theta}(t)]C_{A2}[\underline{\theta}(t)]$$

$$N_i[\underline{\theta}(t)] = D_{A12}[\underline{\theta}(t)]T_i[\underline{\theta}(t)]D_{A21}[\underline{\theta}(t)]$$

In this way we have expressed the closed loop state space matrices as linear function of the controller parameters b_i that we need to identify. Using lemma 5-5 we can say that the H_∞ norm of the transfer function from w to z, is less than γ if and only if there exists a $P \geq 0$ such that:

$$\begin{bmatrix} \left(A_A^T[\theta] + \sum_{i=1}^{q} F_i^T[\theta]k_i\right)P + P\left(A_A[\theta] + \sum_{i=1}^{q} F_i[\theta]k_i\right) & P\left(B_{A1}[\theta] + \sum_{i=1}^{q} G_i[\theta]k_i\right) & C_{A11}^T[\theta] + \sum_{i=1}^{q} H_i^T[\theta]k_i \\ \left(B_{A1}^T[\theta] + \sum_{i=1}^{q} G_i^T[\theta]k_i\right)P & -\gamma I & D_{A11}^T[\theta] + \sum_{i=1}^{q} N_i^T[\theta]k_i \\ C_{A1}[\theta] + \sum_{i=1}^{q} H_i[\theta]k_i & D_{A11}[\theta] + \sum_{i=1}^{q} N_i[\theta]k_i & -\gamma I \end{bmatrix} < 0 \quad [5\text{-}25]$$

Since this Matrix Inequality depends continuously on θ, in order to find a solution we must resort to gridding the parameter set Θ and define a matrix inequality at each point of the grid. In this way we define a system of matrix inequalities that is not linear in b_i and P; to find a solution we must set up a two step iterative procedure. This procedure is completely analogous to that discussed in section 4.4, so it will not be repeated here.

5.2.3.2 Controller Synthesis via Newton search

Newton's method can also be used to find a solution to the synthesis problem. In this case it is not necessary to express $\Delta K[\theta(t)]$ as a linear function of the gain scheduling parameters b_i. We can rely directly on the closed loop state space model of equation 5-15 through 5-19 calculated at each point of the grid. If Θ_g is the finite subset of Θ formed with all the point in the grid, then the induced L_2 - norm (or H_∞ norm) over this subset can be defined as

$$\left\|G_{zw}(P_A,\Delta K)\right\|_\infty = \sup_{\theta\in\Theta_g}\sup_{\substack{w\in L_2\\ \|w\|_2\neq 0}}\frac{\|z\|_2}{\|w\|_2} = \sup_{\theta\in\Theta_g}\left(\bar{\sigma}[G_{zw}(P_A(\theta),\Delta K(\theta),j\omega)]\right) \qquad [5\text{-}26]$$

Several methods are available to calculate this norm; we can use the LMI of equation 5-20 and reduce γ until this LMI is unfeasible, we can reduce γ in the Riccati inequality of equation 5-11 until the Riccati equation has no solution, or form the Hamiltonian matrix and reduce γ until M has an eigenvalue on the imaginary axis , or simply pick the maximum of the maximum singular values calculated at each point of the grid (Ref. 4-6). In our applications we used the Hamiltonian matrix and the maximum singular value methods. We didn't find significant difference between the two methods. If the frequency region, where the maximum singular value occurs, is well known then the singular value method is faster in finding the the induced L_2 - norm over the subset.

Using any of these methods, a function that calculates the H_∞ norm on the finite grid can then be implemented in *Matlab*. Once the H_∞ norm is computed, numerical partial derivatives are taken, and a standard descent is conducted. The algorithm can be stopped when the norm is below a certain value or when a minimum is reached. If it is possible to find a solution to this problem, we will call it a "γ-suboptimal fixed structure controller".

The Newton search has presented several advantage over the LMI algorithm. The convergence is definitely faster and the H_∞ cost can easily be augmented with other terms that take into account frequency and/or time domain constraints, and handling qualities. The addition of a handling quality metric to the cost functional, discussed in section 4.2.1 , can

directly be applied to the fixed structure gain scheduling problem. In the next section we will describe how the model following problem and the handling quality metric, used for the single flight point design in chapter 4, can be used in the gain scheduling of fixed structure controllers.

5.3 Multi-Objective optimization in the gain scheduling problem

The use of the Newton search to find a solution to the fixed structure LPV problem, described in the previous section, allows us to introduce a term that takes into account handling quality requirements, in addition to the pure H_∞ cost in equation 5-26.

This cruitical feature will be described through the F/A-18 design example. The cost functional that will be used includes two parts: the first is the H_∞ norm of the difference between the target plant and the actual one and the second is a measure of the distance between the Neal-Smith carpet plot of the target and the actual plant. The cost functional is then given by:

$$J(\theta) = \left\| T_{zw}(\theta) \right\|_\infty + \frac{1}{5}\sum_{i=1}^{5}\sqrt{\left(P_i(\theta) - P_{it}(\theta)\right)^2 + \left(R_i(\theta) - R_{it}(\theta)\right)^2} \qquad \theta \in \Theta \qquad [5\text{-}27]$$

Where the range of variation of θ, Θ, is defined by the flight envelope, and the index i is for the various bandwidths at which the Neal-Smith Criterion is evaluated. This handling quality metric is the same as the one described in paragraph 4.2.1.1, the only difference being that it now depends on the flight condition θ.

The target plant and the desired handling qualities at each of the flight points will be those of a standard F/A-18. It is important to point out that now the desired performance changes throughout the flight envelope. It is clear that we cannot expect to have the same target transfer function in different flight regimes. The transfer function $T_{zw}(\theta)$ defines a model matching problem for each flight point in the flight envelope.

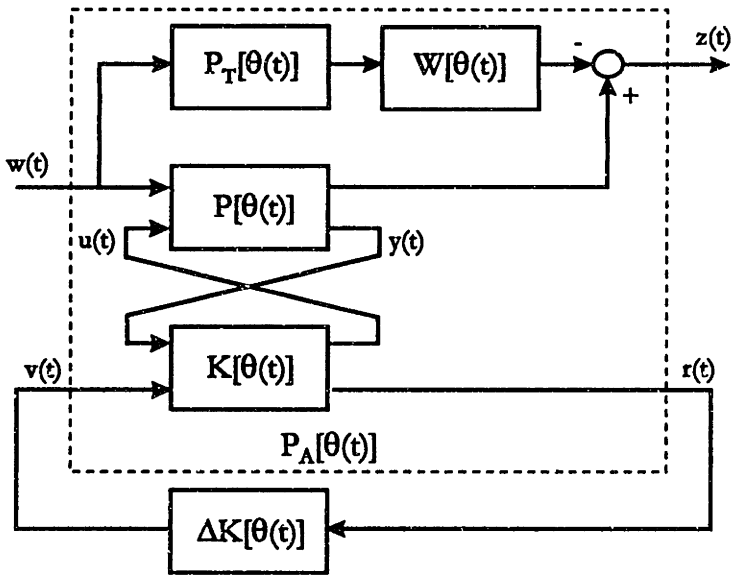

Fig. 5-3 The H_∞ model matching problem

The block diagram of the model matching problem that we are going to address is shown in Fig. 5-3. As in the single point design, $K(\theta)$ contains the fixed part of the control system, while $\Delta K(\theta)$ contains a diagonal matrix of gains to be adjusted. $P_T[\theta(t)]$ is the target plant its definition and dependence on the flight envelope is discussed in section 5.4.2.

5.4 Gain Scheduling in the F/A-18 HARV

We take as our example a typical flight test situation at NASA Dryden. The F/A-18 HARV was built as a full-scale development vehicle, to study thrust vectoring and high angle of attack fighters. Because of the additional inertia of the thrust vectoring paddles, the spin chute, emergency systems, and ballast, the HARV has significantly different dynamics than the original F/A-18. For this reason, and because the HARV flies at significantly different flight conditions (high alpha) than the F/A-18, new control laws were developed. This new control laws were also designed to include the thrust vectoring system in the flight control system. We will present an alternate approach to designing these flight control laws, based on redesign of the original control laws to recover the input-output and handling qualities properties of the F/A-18.

To implement the control laws actually used on the HARV, the flight control system was adapted from the existing flight control system by adding a reconfigurable research flight control system (RFCS). The RFCS provided the capability to examine multiple control law designs and their variants without compromising the safety of the pilot or aircraft. This computer was designed to provide Class B (mission critical but not safety critical) control environment that, by definition, ensured safe reversion back to the F/A-18 configuration if a failure was detected or if the pilot desired to return to the original flight control system. During normal flight operations, (i.e. when thrust vectoring is not specifically being tested) the standard practice was to reconfigure the control system back to the original flight control system, or reversion mode.

We mention these operational details to emphasize two points: first, in reversion mode (and also during refueling) the original F/A-18 control laws were used, which resulted in degradation of handling qualities. The changes to the gain tables we will suggest are aimed at improving these handling qualities. The second point that we derive from this example is that new control laws are rarely flown without extensive validation, and even in the case of Class B validated HARV control laws, a reversion mode was required to maintain safety. The modifications to the man-rated F/A-18 control laws that we will develop here could be validated at much lower cost than a complete redesign of the control system, because no new flight code is required.

Based on this discussion the objective is to redefine the gain schedule of the F/A-18 control laws. Our purpose will be to recover the performance of the F/A-18 on the HARV over a wide flight envelope.

5.4.1 Definition of the Flight Envelope

The flight regime that we will consider is shown in Tab. 5-1 and Fig. 5-4. Although this flight regime does not cover the entire flight envelope, it is a regime in which the dynamics of the aircraft change so significantly that gain scheduling is necessary to maintain the same level of performance at different altitudes and Mach numbers.

Flight Point	Altitude [ft]	Mach	Dynamic Pressure [psf]	Static Pressure [psf]	Flight Point	Altitude [ft]	Mach	Dynamic Pressure [psf]	Static Pressure [psf]
1	10,000	0.40	169.70	1461.6	16	25000	0.40	91.82	792.3
2	10,000	0.50	271.13	1465.4	17	25000	0.50	146.71	793.0
3	10,000	0.60	401.14	1464.4	18	25000	0.60	217.06	793.9
4	10,000	0.70	563.63	1466.4	19	25000	0.70	304.99	795.1
5	10,000	0.80	763.45	1468.9	20	25000	0.80	413.11	796.6
6	15,000	0.40	139.50	1202.0	21	30000	0.40	73.46	634.8
7	15,000	0.50	222.87	1203.1	22	30000	0.50	117.38	635.1
8	15,000	0.60	329.74	1204.4	23	30000	0.60	173.66	635.8
9	15,000	0.70	463.30	1206.0	24	30000	0.70	244.01	636.8
10	15,000	0.80	627.56	1208.2	25	30000	0.80	330.51	638.2
11	20,000	0.40	113.51	978.6	26	35000	0.40	58.32	505.0
12	20,000	0.50	181.35	979.5	27	35000	0.50	93.18	504.8
13	20,000	0.60	268.31	980.6	28	35000	0.60	137.87	505.4
14	20,000	0.70	377.00	982.0	29	35000	0.70	193.72	506.3
15	20,000	0.80	510.65	983.8	30	35000	0.80	262.40	507.4

Tab. 5-1 Flight points aero data

In this example the six flight points in the lower right corner of the flight envelope (below the line) were removed from the synthesis problem. Both the dynamic and the static pressure are very low in this flight regime and the longitudinal transfer function of the HARV is very different from that of the F/A-18. To include these points, additional degrees of freedom would be required in the gain scheduling definition. Alternatively, and perhaps preferably, we would define a new 'gain region' which handles the low dynamic pressure part of the envelope. In this way we reduce the gain scheduling problem to choosing several broad classes in which automatic gain scheduling is performed.

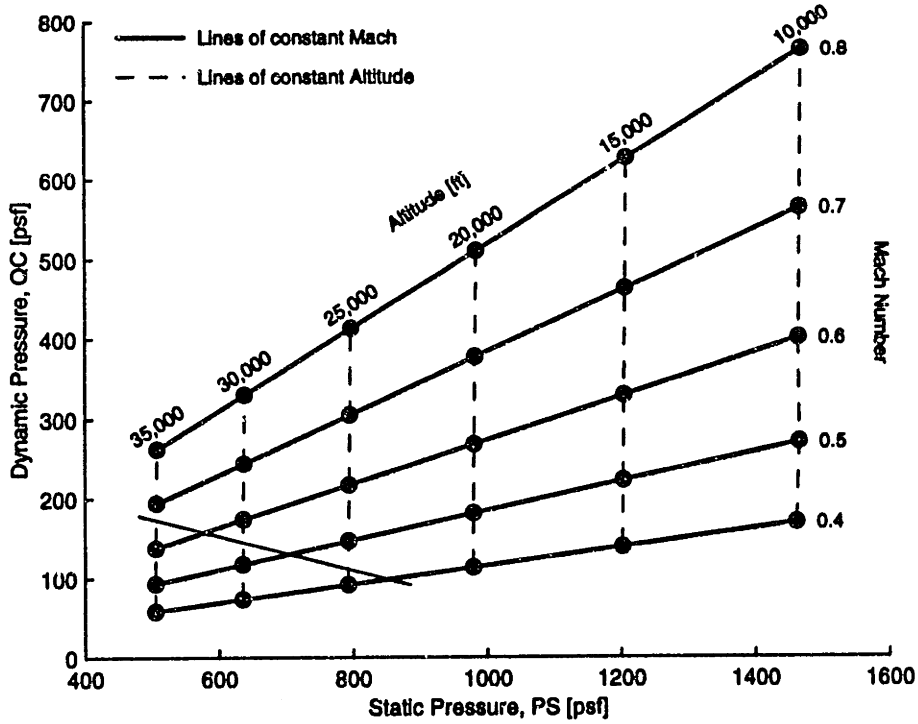

Fig. 5-4 Flight Envelope

Fig. 5-5 and Fig. 5-6 show the locations of the closed loop poles of the Short Period and Dutch Roll modes for Mach numbers between 0.4 and 0.8 at an altitude of 20,000 ft. Two things are apparent in these figures. The first is that the dynamics of the aircraft change dramatically in this region of the flight envelope. The second is the large difference between the dynamics of the HARV and those of a standard F/A-18. The circles (o) and plus signs (+) represent the closed loop poles of the HARV and the F/A-18 respectively. We can see that there are significant differences in the damping and the natural frequency. The short period mode of the F/A-18 HARV has lower frequency and lower damping at each flight point. While the damping of the standard F/A-18 is around 0.6, that of the HARV is between 0.4 and 0.5. The differences in the Dutch Roll mode are similar; the HARV has lower frequency and lower damping.

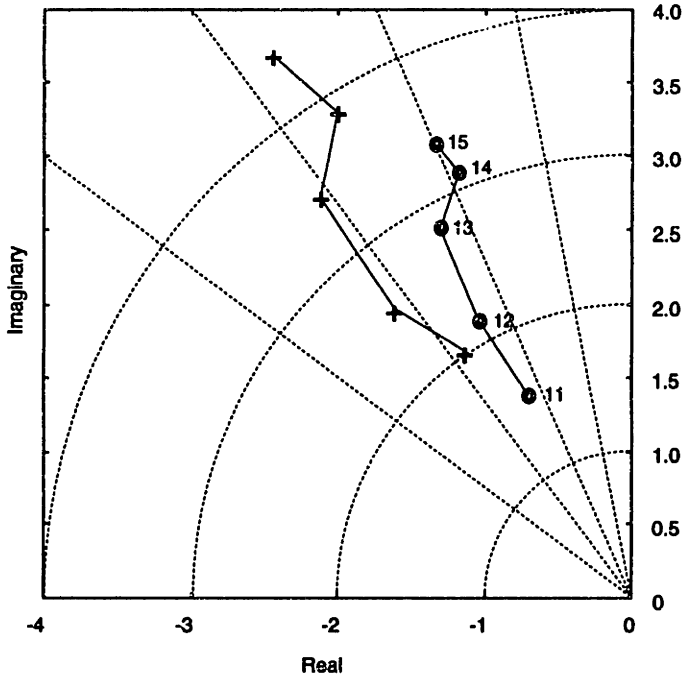

Flight Point	F/A-18 ω_n	F/A-18 ζ	HARV ω_n	HARV ζ
11	2.0114	0.5589	1.5404	0.4551
12	2.5481	0.6341	2.1555	0.4802
13	3.4593	0.6155	2.8374	0.4566
14	3.8518	0.5177	3.1149	0.3785
15	4.4006	0.5530	3.3585	0.3982

Fig. 5-5 Short period mode pole locations

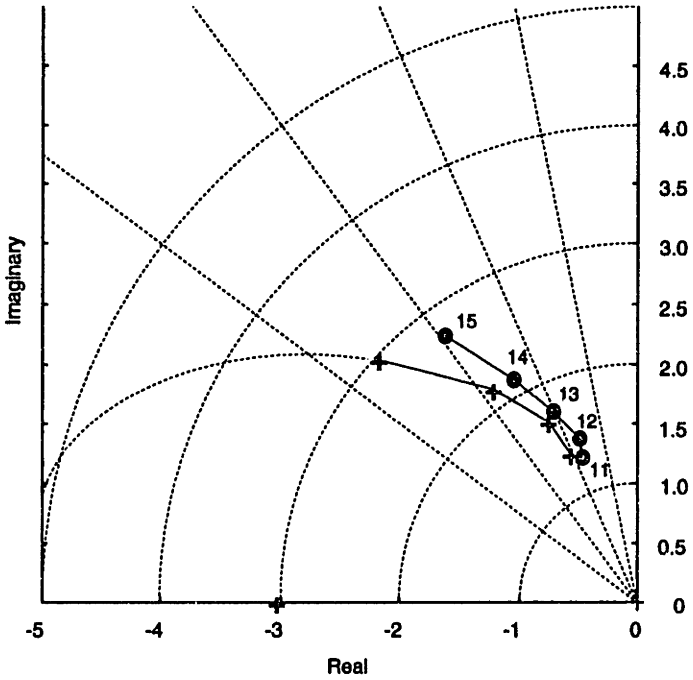

Flight Point	F/A-18 ω_n	F/A-18 ζ	HARV ω_n	HARV ζ
11	1.3810	0.4060	1.3051	0.3542
12	1.6980	0.4378	1.4671	0.3433
13	2.1598	0.5606	1.7562	0.4079
14	2.9737	0.7294	2.1404	0.4906
15	1.000	3.0228*	2.7616	0.5889

* The Dutch Roll poles split into 2 real stable poles at this flight point.

Fig. 5-6 Dutch roll mode pole locations

5.4.2 Preparation of linear models at the grid points

In this section we describe how the linearized models of all the elements forming the model matching problem of Fig. 5-3 were calculated. All the models were obtained via linearization of *Simulink* block diagrams.

Once the flight envelope has been define, the next step is to linearize the nonlinear model of the aircraft at each flight point. This task can be easily performed using the F/A-18 nonlinear simulator for *Matlab* and *Simulink* described in Appendix A. The procedure outlined in section A-1.10 was used to calculate the linearized models of the F/A-18 HARV and of the standard F/A-18. The linearized models of the F/A-18 HARV define the block $P[\theta(t)]$ of Fig. 5-3.

In order to form the block structure for the model matching problem, we need also to linearize the CAS opened at the gains that we want to reschedule. Fig. 5-7, Fig. 5-8, and Fig. 5-9 show the *Simulink* block diagrams of the CAS broken at the scheduling gains. This "open loop" CAS corresponds to what we defined as the fixed part of the controller. As for the plant, the CAS linearized models must be calculated at each flight point. The linearization of the control augmentation system must be done with a certain caution; dead-bands need to be eliminated and, if using the *Matlab* function *linmod*, the levels of the perturbations must be tuned in accordance to the sizes of the inputs. The models of the "open loop" CAS form the block $K[\theta(t)]$ of Fig. 5-3.

A linearized model of the standard F/A-18 CAS can be calculated just using the fixed part of the controller, $K[\theta(t)]$, and introducing the nominal gains as $\Delta K[\theta(t)]$. The linearized F/A-18, augmented with this CAS defines the target plant at each flight point (the block $P_T[\theta(t)]$ of Fig. 5-3). The target plant for the longitudinal axis is the SISO transfer function from pitch stick to pitch rate, while the target plant in the lateral/directional axis is the MIMO transfer function from the roll stick and pedal inputs to the roll rate and yaw rate outputs.

In this section we have defined all the blocks forming the model matching problem over the flight envelope shown in Fig. 5-4. In the following section we describe which gains were selected for gain scheduling, as well as the form of the various scheduling functions.

5.4.3 Definition of the gains to reschedule

The longitudinal CAS gains that we will redesign are: the pitch stick proportional gain, the n_z proportional gain and the pitch rate proportional gain. Fig. 5-7 shows the *Simulink* block diagram of the longitudinal CAS. As we already mentioned in chapter 4, the longitudinal CAS is basically a PI controller. The integrator gains do not play a fundamental role in the location of the short period poles and thus we will not redesign the scheduling of those gains. For a description of the gain scheduling refer to Appendix B. The thick solid lines in Fig. B-2, Fig. B-5, and Fig. B-6 represent the gain scheduling of the standard F/A-18 control law. The circles shown in these figures represent the optimum gain when a design at each flight point is performed. In all the three cases the single point designs follow the curvature of the actual gain scheduling; thus, the form of the gain scheduling function was selected to follow that of the actual one. Furthermore, the shape of the actual schedule suggests that the same form can be used for all the three longitudinal gains. The function selected is:

$$K = \begin{cases} X_1 + X_2 * QC + \dfrac{X_3}{QC} + X_4 * PS & \text{QC} \geq \text{QC}_b \\ X_5 + X_6 * PS & \text{QC} < \text{QC}_b \end{cases} \qquad [5\text{-}28]$$

$$QC_b = \frac{-[(X_1 - X_5) + (X_4 - X_6)PS] - \sqrt{[(X_1 - X_5) + (X_4 - X_6)PS]^2 - 4X_2X_3}}{2X_2}$$

In the last equation QC is the dynamic pressure, PS the static pressure, and Xi are the coefficients that must be found. The X_i terms take the place of the a_{ij} coefficients of equation 5-22. The longitudinal gains do not depend on dynamic pressure in the low dynamic pressure region; when QC is less than QC_b. In the optimization we then have to find a total of 18 coefficients, 6 for each gain to be rescheduled.

Fig. 5-8 shows the lateral directional CAS while Fig. 5-9 shows the directional part of the control augmentation system. In this case we will redesign all the available gains with the exception of the Rolling-Surface-to-Rudder-Interconnect (RSRI) gain. This interconnect is used to reduce sideslip and angle of attack excursions during rolling maneuver. The reason why we decided not to redesign the RSRI gain is because this gain is scheduled with angle of attack and air data. This will add an additional term to the scheduling parameters making the problem more difficult. A separate design for this gain can be conducted if large excursions in sideslip appear during roll maneuvers.

In the lateral-directional CAS the gains selected for rescheduling are: lateral stick gain, roll rate feedback gain, lateral acceleration gain, yaw rate feedback gain, and pedal increment gain. Fig. B-8, Fig. B-10, Fig. B-13, Fig. B-14, and Fig. B-16 show the gain scheduling of the actual CAS. In this case the form of the scheduling function has to be different for each gain. As an example Fig. B-8 shows the gain scheduling of the lateral stick gain. The solid thick line is the actual gain schedule and the circles are the optimal gain when a single flight point design is performed. These plots suggest the use of a linear dependence on dynamic pressure in the low dynamic pressure region and a quadratic one in the high dynamic pressure region. The dependence on static pressure will also be linear. Thus the lateral stick gain scheduling function has the following form:

$$K = \begin{cases} X_1 + X_2 * QC + X_3 * QC^2 + X_4 * PS & QC \geq QC_b \\ X_5 + X_6 * QC + X_7 * PS & QC < QC_b \end{cases}$$

$$QC_b = \frac{-(X_2 - X_6) + \sqrt{(X_2 - X_6)^2 - 4X_3(X_1 - X_5) - 4X_3(X_4 - X_7)PS}}{2X_3}$$

In this case there are 7 coefficients that need to be optimized.

Appendix B contains all the other lateral/directional gains. We can see that in some cases the gain scheduling function has a quadratic form, in some others is purely linear, and in one case the gain is constant. A total of 21 coefficients define the new gain scheduling of lateral/directional CAS.

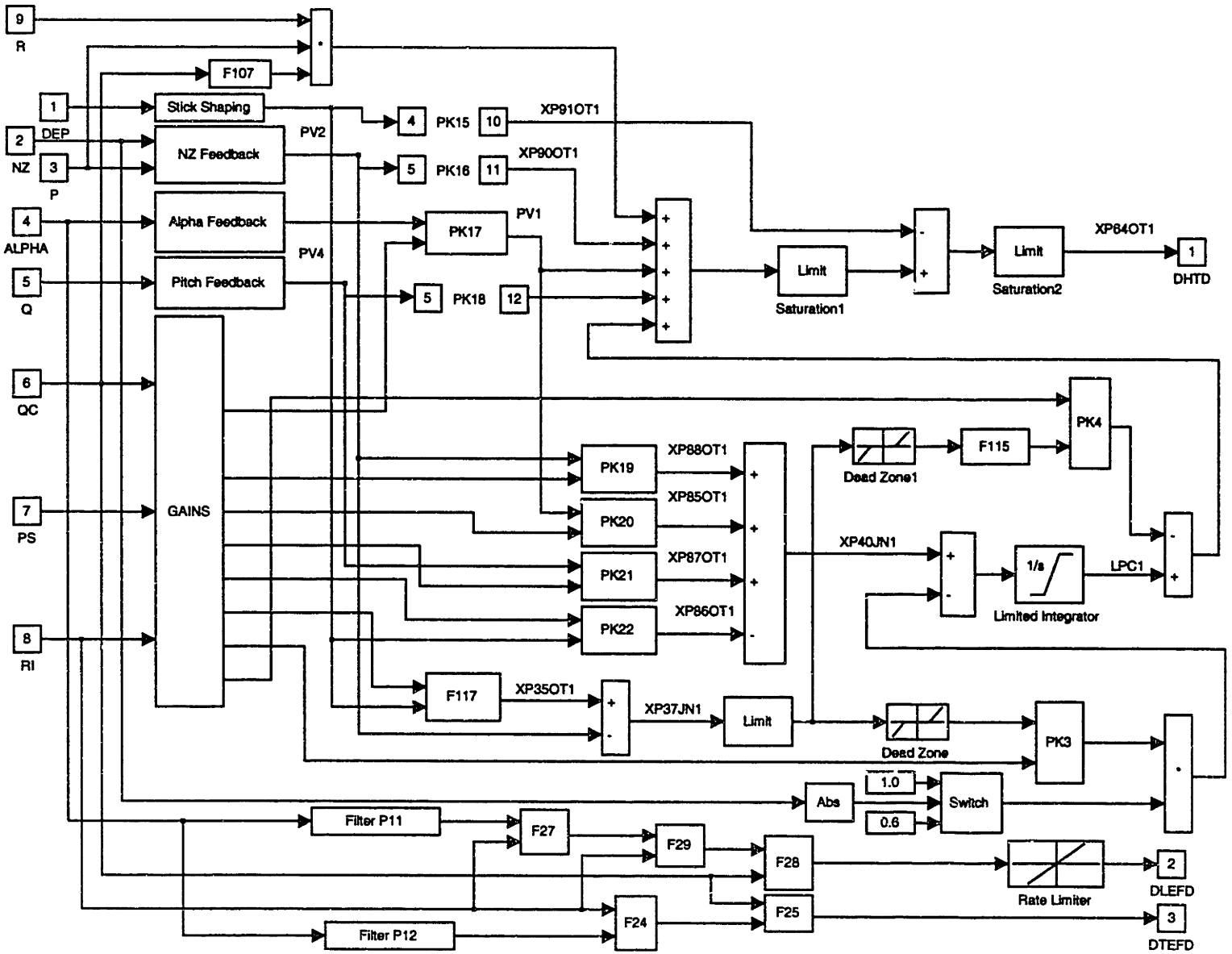

Fig. 5-7 Longitudinal CAS with modified gains

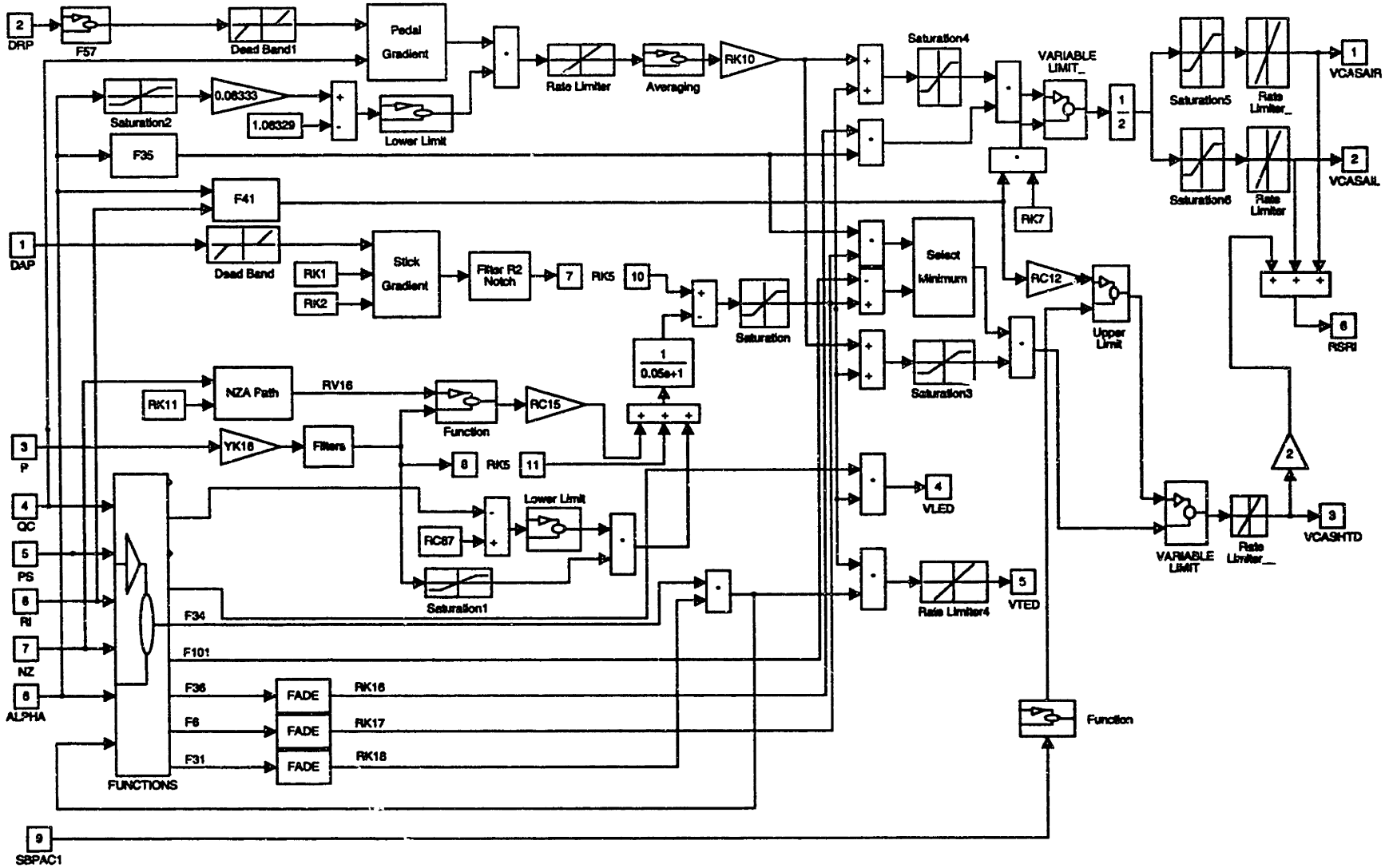

Fig. 5-8 Lateral CAS with modified gains

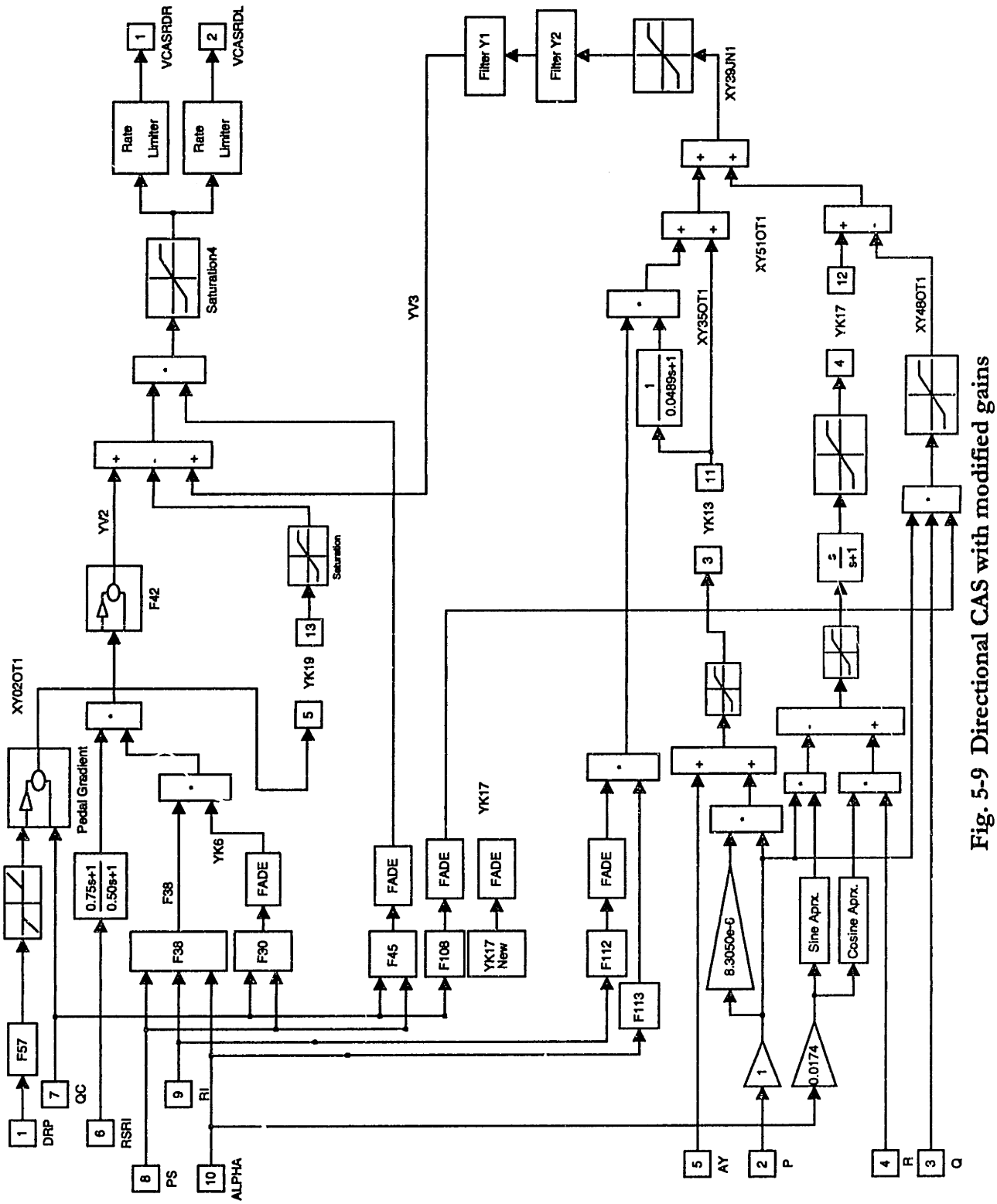

Fig. 5-9 Directional CAS with modified gains

5.4.4 Optimization via Newton Search

The first thing to do in order to start the optimization routine is to define the initial values of the gain scheduling coefficients. The selection of the initial condition is critical to the convergence of the optimization. The number of coefficients that need to be defined is very high and there is the serious risk that the Newton search does not converge or it converges very slowly to some local minimum. One way to define the starting point of the Newton optimization is obtained via a least squares fit of the single flight point design. In other words, first we find the optimum gains at each flight point and then we find the coefficients of the gain scheduling function via a least squares. As an example, consider the gain of equation 5-28. Assume that the optimal longitudinal gains were calculated at each of the 30 flight points. Let K_i^* be the optimal gain at the i^{th} flight point. At each flight point define the following two row vectors:

$$F_{1,i} = \begin{bmatrix} 1 & QC_i & \frac{1}{QC_i} & PS_i \end{bmatrix}$$

$$F_{2,i} = \begin{bmatrix} 1 & PS_i \end{bmatrix}$$

We can then write:

$$K_i^* = a_{1,i} * F_{1,i} * z_1 + a_{2,i} * F_{2,i} * z_2 = \begin{bmatrix} a_{1,i} * F_{1,i} & a_{2,i} * F_{2,i} \end{bmatrix} \begin{bmatrix} z_1 \\ z_2 \end{bmatrix} \qquad [5\text{-}29]$$

where

$$z_1 = \begin{bmatrix} X_1 & X_2 & X_3 & X_4 \end{bmatrix}^T$$
$$z_2 = \begin{bmatrix} X_5 & X_6 \end{bmatrix}^T$$

and

$$\begin{cases} a_{1,i} = 1 \\ a_{2,i} = 0 \end{cases} \quad \text{if } QC_i \geq QC_{b0} \qquad \begin{cases} a_{1,i} = 0 \\ a_{2,i} = 1 \end{cases} \quad \text{if } QC_i < QC_{b0}$$

QC_{b0} is some initial dynamic pressure break point. Equations 5-29 can the be stacked in a matrix form

$$\begin{bmatrix} K_1^* \\ K_2^* \\ \vdots \\ K_{30}^* \end{bmatrix} = \begin{bmatrix} a_{1,1} * F_{1,1} & a_{2,1} * F_{2,1} \\ a_{1,2} * F_{1,2} & a_{2,2} * F_{2,2} \\ \vdots & \vdots \\ a_{1,30} * F_{1,30} & a_{2,30} * F_{2,30} \end{bmatrix} \begin{bmatrix} z_1 \\ z_2 \end{bmatrix} = M * z$$

At this point we can readily calculate the least square solution equation for the gain scheduling variables as:

$$z_{LS} = (M^T M)^{-1} M^T K^* \qquad [5\text{-}30]$$

The coefficients z_{LS} can then be used as the starting point of the optimization code. Repeating the same procedure for all the gains, we can define the starting point of the optimization routine.

The single flight point design not only helps identifying the starting point of the optimization routine but also gives us the minimum cost that can be obtained. The knowledge of the minimum cost that we can reach is of fundamental importance during the optimization; it give us a way to judge our final solution. In our case, it is possible to calculate this minimum by simply evaluating the cost functional at each grid point with the gains derived from the single flight point design. It is clear that the best scheduling function is the one going through the single point design gains. If the final cost is too far from the minimum, probably it means that the form of the scheduling functions that we selected is not right. In the next two sections we summarize the results of the optimization routine.

5.4.4.1 Optimization of the Longitudinal Parameters

The cost functional utilized in the longitudinal CAS design is defined in equation 5-27. It is composed of two parts: the first is the H_∞ norm of the transfer function from the pitch stick input to the difference in the pitch rate of the target plane and the actual one, the second is the HQ metric. Tab. 5-2 summarize the results of the optimization. The first column, γ_0, is the value of the cost when the standard F/A-18 controller is used. The term

γ_{LS} represents the cost when the least square solution is used. γ_{opt} is the value of the cost at which the optimization routine has converged. The last column, γ_{min}, is the absolute minimum that can be reached. From these values we can see how the least square solution already has greatly reduced the cost functional. At the end of the optimization routine the cost was about 32% closer to its absolute minimum (calculated as $(\gamma_{LS}-\gamma_{opt})/(\gamma_{LS}-\gamma_{min})*100$).

γ_0	γ_{LS}	γ_{opt}	γ_{min}
8.6795	1.1121	0.9611	0.6421

Tab. 5-2 Longitudinal Optimization: Minimum Cost Functional

The coefficients of the three longitudinal scheduling functions are listed in appendix B (Fig. B-1, Fig. B-3, and Fig. B-5). These figures also show the *Simulink* block diagrams that implement the new gain schedules.

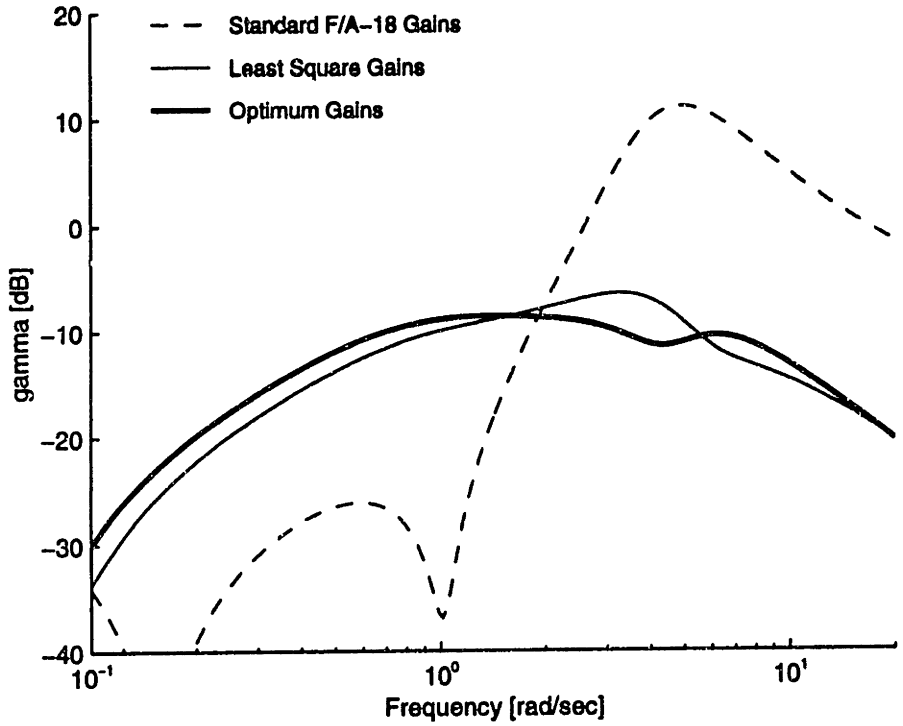

Fig. 5-10 H_∞ part of the cost in the longitudinal model matching problem. Flight condition: Mach 0.7, Altitude 15,000 ft

Fig. 5-10 shows the H_∞ part of the cost as a function of frequency. The flight condition is straight-and-level flight at Mach 0.7 and altitude 15,000 ft. The plots shows a

good match between the HARV with the new gains and the target plant. Fig. 5-11 shows the bode diagrams of the target plant and the three configurations of the F/A-18. The F/A-18 HARV with the new gains now has the same bandwidth as the standard F/A-18. The new gain schedule also increases the damping of the short period mode.

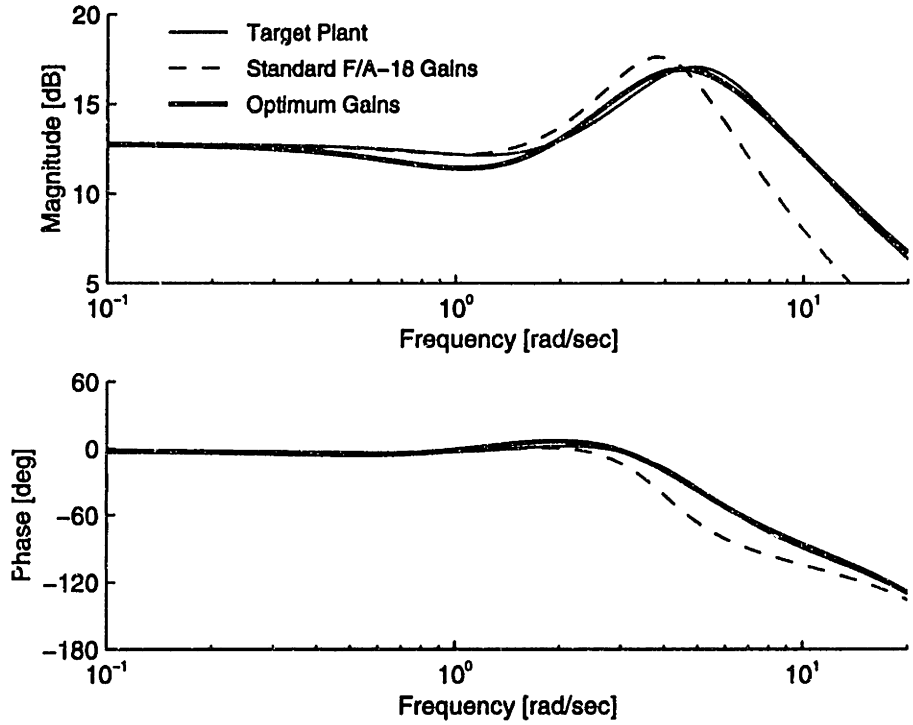

Fig. 5-11 Bode Plot of the target plant and the three F/A-18 configurations.

As already mentioned the handling quality metric forms the second part of the cost functional that is minimized. Fig. 5-12 compares the Neal-Smith Carpet plot of the three aircraft: the F/A-18, the HARV, and the HARV with the new gain schedule. For brevity we show only one flight point. We can clearly see that while the HARV has level 2 flying qualities, while the standard F/A-18 has solid level 1 handling qualities. The second plot refers to the HARV with the new gain scheduling. We can see that the new gain scheduling makes the handling quality of the HARV almost identical to that of the standard F/A-18. This fact is further analyzed in the next section where a detailed study of the refueling task is presented.

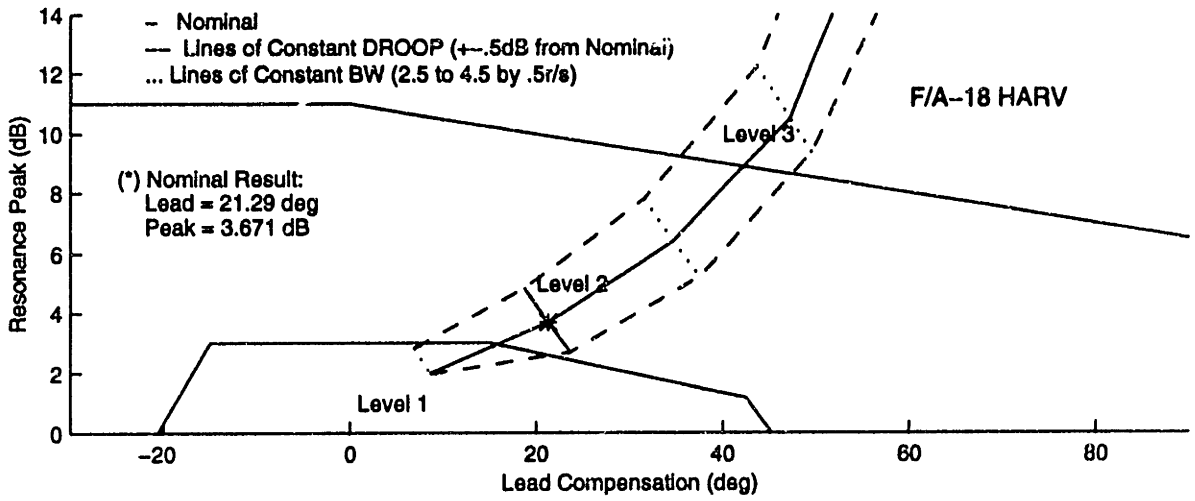

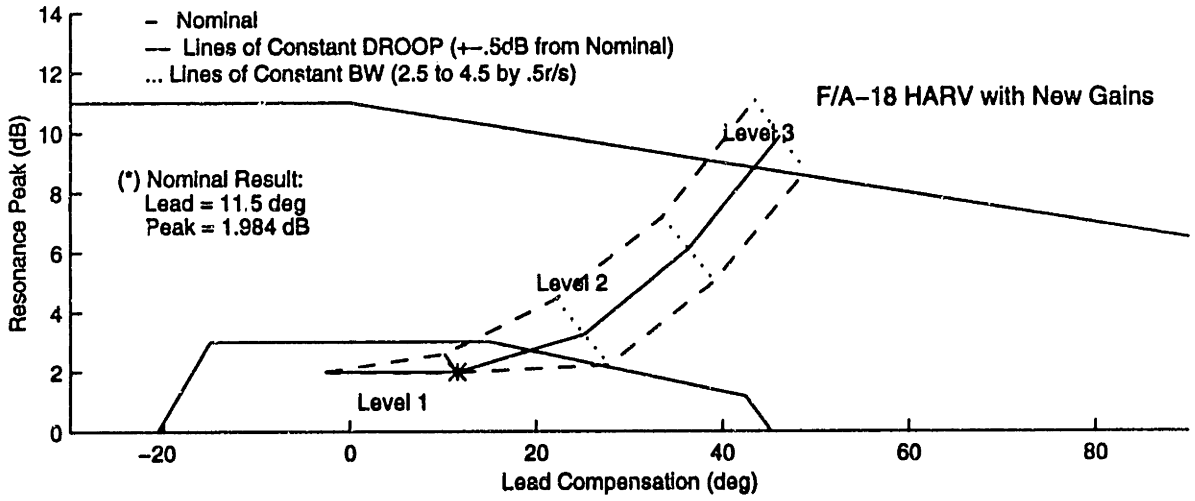

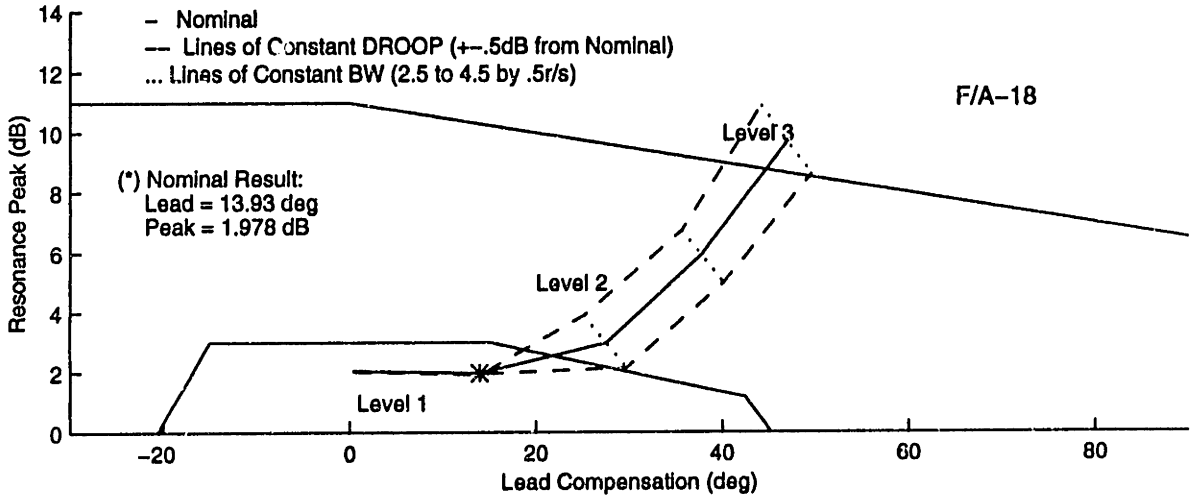

Fig. 5-12 Comparison between the Neal-Smith Carpet Plots of the three F/A-18 Configurations. Flight condition: Mach 0.7, Altitude 15,000 ft

5.4.4.2 Optimization of the Lateral Parameters

Tab. 5-3 summarizes the results of the lateral-directional optimization. The cost functional utilized in this design is the H_∞ norm derived from the model matching problem. No handling quality metric was used in this design. Starting from the least square solution the optimization reduced the cost by about 20%.

γ_0	γ_{LS}	γ_{opt}	γ_{min}
12.8169	3.4013	3.0902	1.9196

Tab. 5-3 Lateral Optimization: Minimum Cost Functional

The optimum coefficients of the scheduling functions are listed in appendix B (Fig. B-7, Fig. B-9, Fig. B-11, Fig. B-12, and Fig. B-15). The main difference between the longitudinal and the lateral design is that in the latter we formulate a two input two output model matching problem.

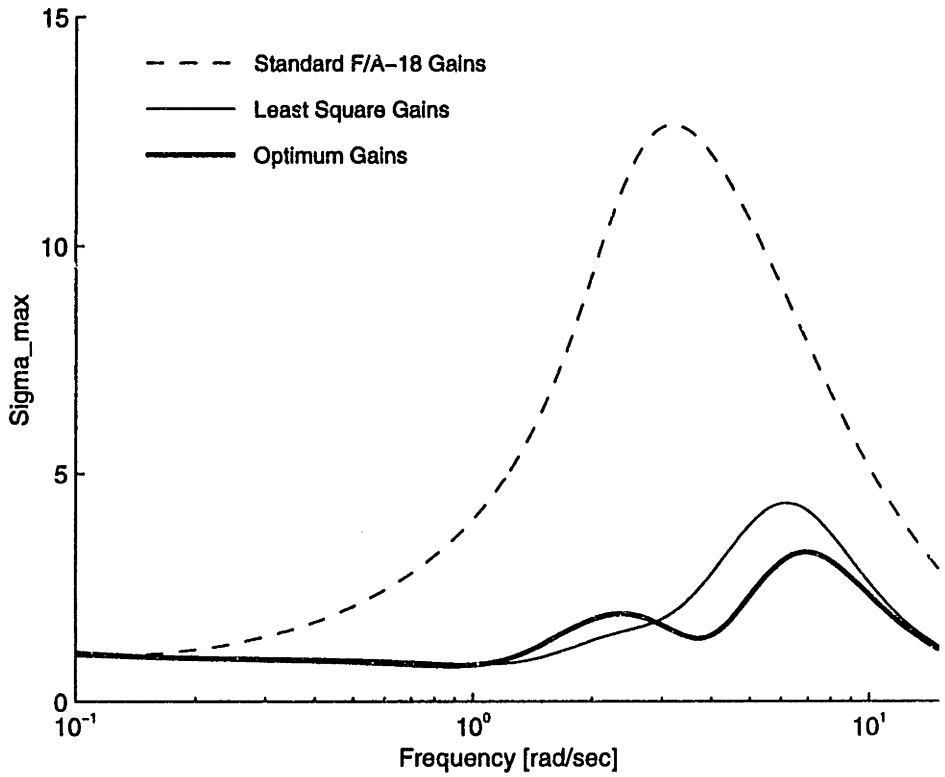

Fig. 5-13 H_∞ cost in the lateral model matching problem. Flight Condition: Mach 0.6, Altitude 10,000 ft

In this case the H_∞ norm, at each flight condition, is equal to the peak of the maximum singular value plot. Fig. 5-13 shows the maximum singular value plot of the closed loop transfer function from w to z (see Fig. 5-3) at Mach 0.6 and altitude 10,000 ft. Notice the large reduction in the peak singular value. Starting from standard F/A-18 gains with an H_∞ norm of about 13, the least square solution reduces the norm down to about 4.5 and the optimization code further reduces the norm to about 3.0. Fig. 5-14 shows the transfer functions of the standard F/A-18 (target plant), of the HARV, and of the HARV with the modified gain. The largest correction occurs on the transfer function from lateral stick to roll rate. In any case all the transfer functions of the HARV with the new gains appear to be fairly close to the target plant. For brevity we will not show similar plots for all the other flight points.

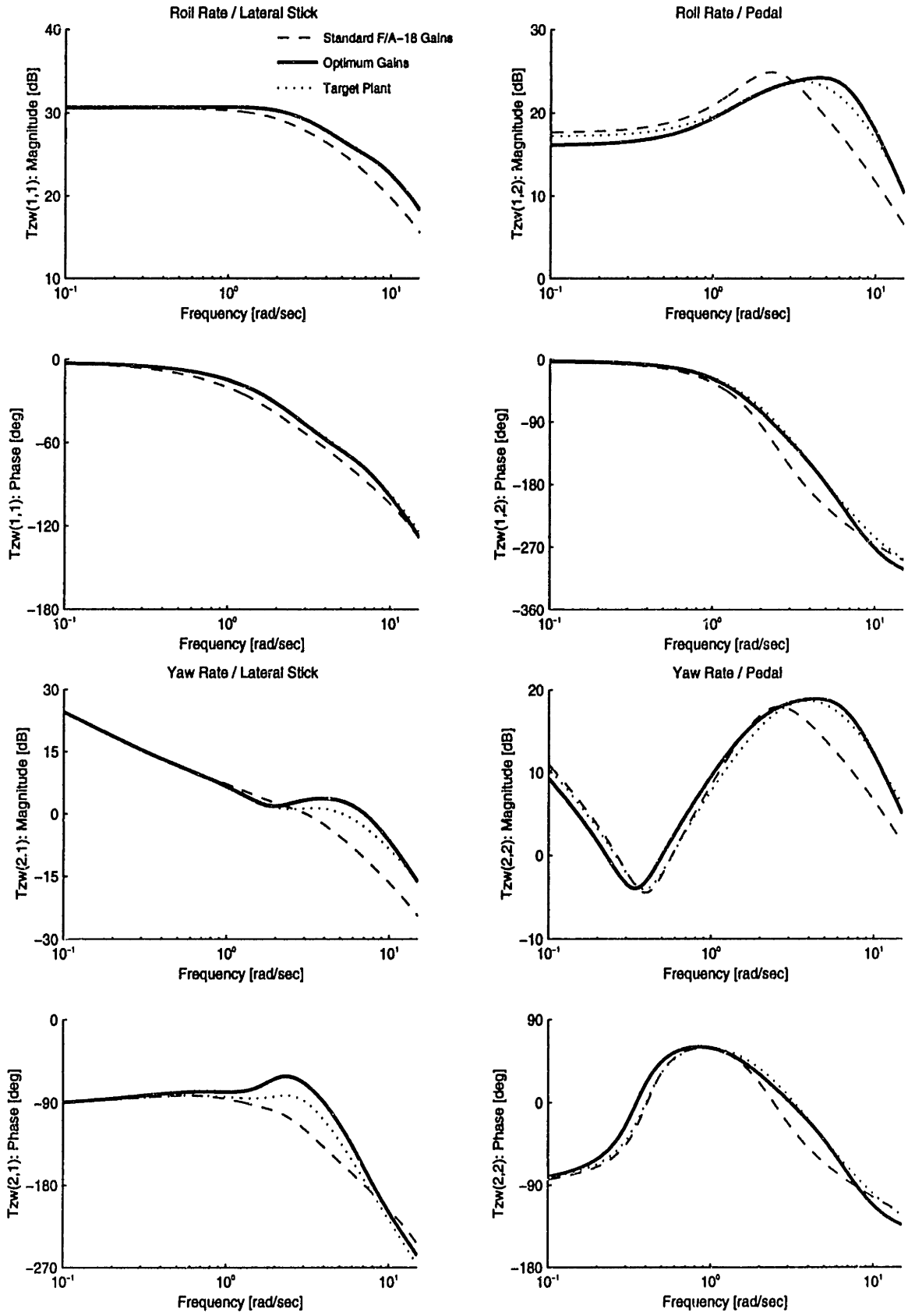

Fig. 5-14 Transfer Functions Comparison. Mach 0.6, Altitude 10,000 ft

5.5 Nonlinear Simulations

Before implementing the new gain schedule on the NASA Dryden fixed base flight simulator, a series of simulations on the *Simulink* nonlinear simulator were performed. The idea behind these "batch" simulations was to verify that the responses of the HARV with the new gain schedule were made closer to those of the F/A-18. Another important aspect was to verify that the new gains didn't cause unacceptable rate saturation in the case of large inputs.

The nonlinear analyses primarily consisted of a series of steps, doublets, and ramps simulated on the batch simulator described in appendix A. These simulations demonstrated the ability of the HARV with the new gain schedule to produce a response consistent with that of the standard F/A-18. It is important to remember that the new gain schedule reproduces the closed loop dynamics of the standard F/A-18, but can do so only to the limits imposed by saturation and rate limit. The response of the HARV to large pilot inputs, which saturates the actuators, will be unaltered by changes in the CAS gains. Once the saturation limits are violated there is nothing we can do changing the characteristics of the CAS.

For brevity we are going to present only the time histories of three tests. In all the figures the thick solid line represents the F/A-18 HARV with the new gain schedule, the dashed line represents the F/A-18 HARV, and the thin solid line represents the F/A-18. The simulation presented were all performed at 20,000 ft and Mach 0.6 (the refueling task flight point).

Fig. 5-15 and Fig. 5-16 shows the response of the airplane to a small step of the longitudinal stick. From the time history of the pitch rate we can see that the modified HARV now has the same rise time as the standard F/A-18. The F/A-18 HARV has a tendency to lag behind and a tendency to oscillate when settling down. Fig. 5-17 and Fig. 5-18 are the response of the aircraft to a large step doublet. The inclination of the HARV to oscillate is now more evident in the pitch rate time history. The HARV definitely has a longer settling time. In this case, the stick input is large causing saturation of the control

surfaces. As already mentioned, when large inputs are involved, the CAS gains don't make any difference. The HARV is heavier and it cannot follow the response of the standard F/A-18. On the other hand, the new gains do benefit the settling part of the response. The new gain schedule makes the HARV more damped with almost the same settling time as the standard F/A-18.

Fig. 5-19 and Fig. 5-20 show the response of the airplanes to a roll reversal maneuver, ($0 \rightarrow +90 \rightarrow 0 \rightarrow -90 \rightarrow 0$). A sequence of 3 inch lateral input of the exact time length, required to achieve the desired bank angles, was applied. Also in this case changes in the CAS gains do not change the overall response of the HARV. There is some difference in the settling time of the heading angle; the HARV has a tendency to oscillate a little longer before settling down. Fig. 5-20 shows that the surfaces are almost always on the rate or saturation limits. From this experiment we see that the saturation of the surfaces does not change significantly when the new gain scheduled is used. This fact is comforting, us because it means that the new gains don't saturate the surfaces more than the standard gains. Extensive simulations with various levels of pilot input show that the new gain schedule makes the response of the HARV almost identical to that of a standard F/A-18. For brevity we don't present the data from these additional simulations.

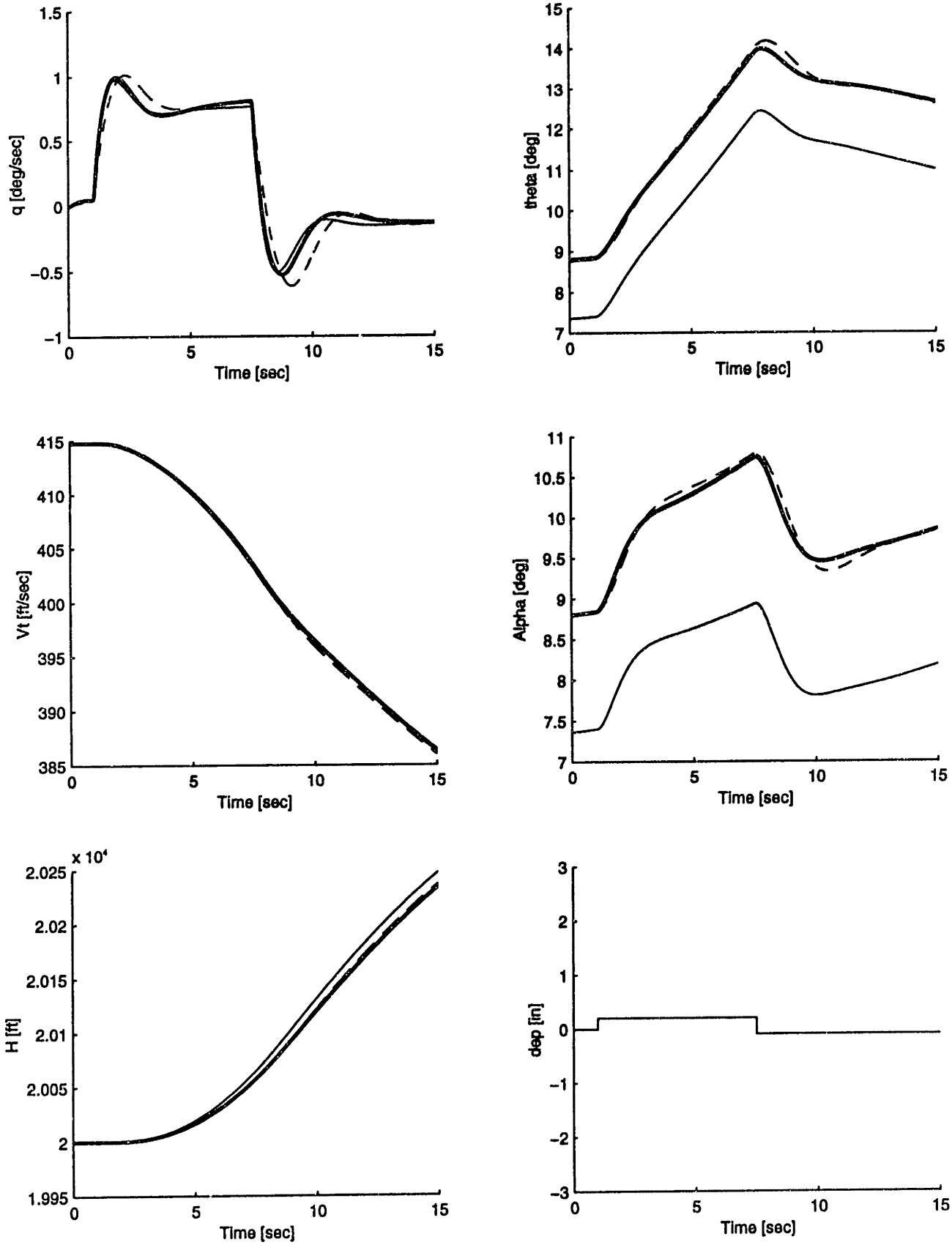

Fig. 5-15 Small step of the longitudinal stick, output variables.

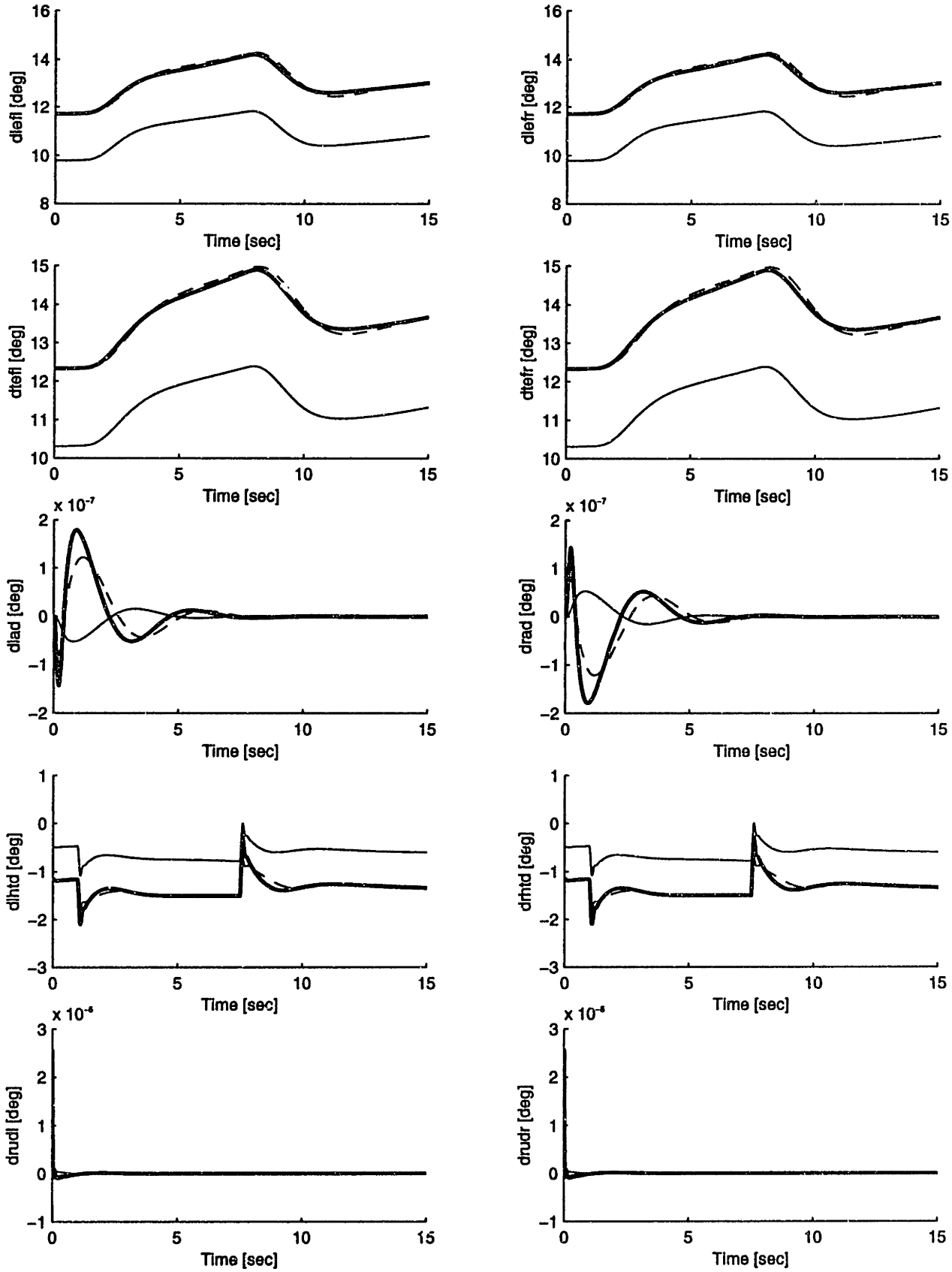

Fig. 5-16 Small step of the longitudinal stick, control variables.

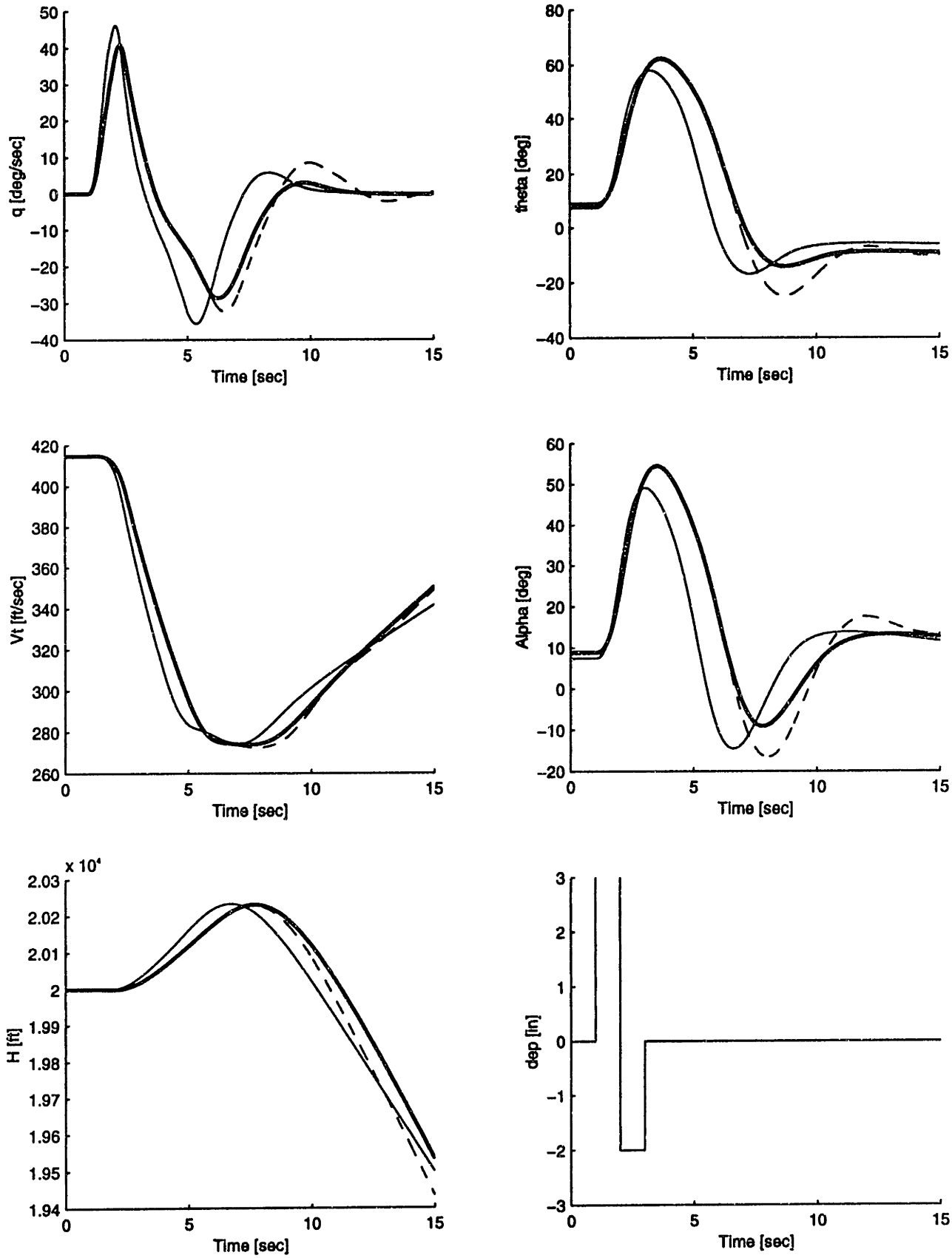

Fig. 5-17 Large longitudinal doublet, output variables.

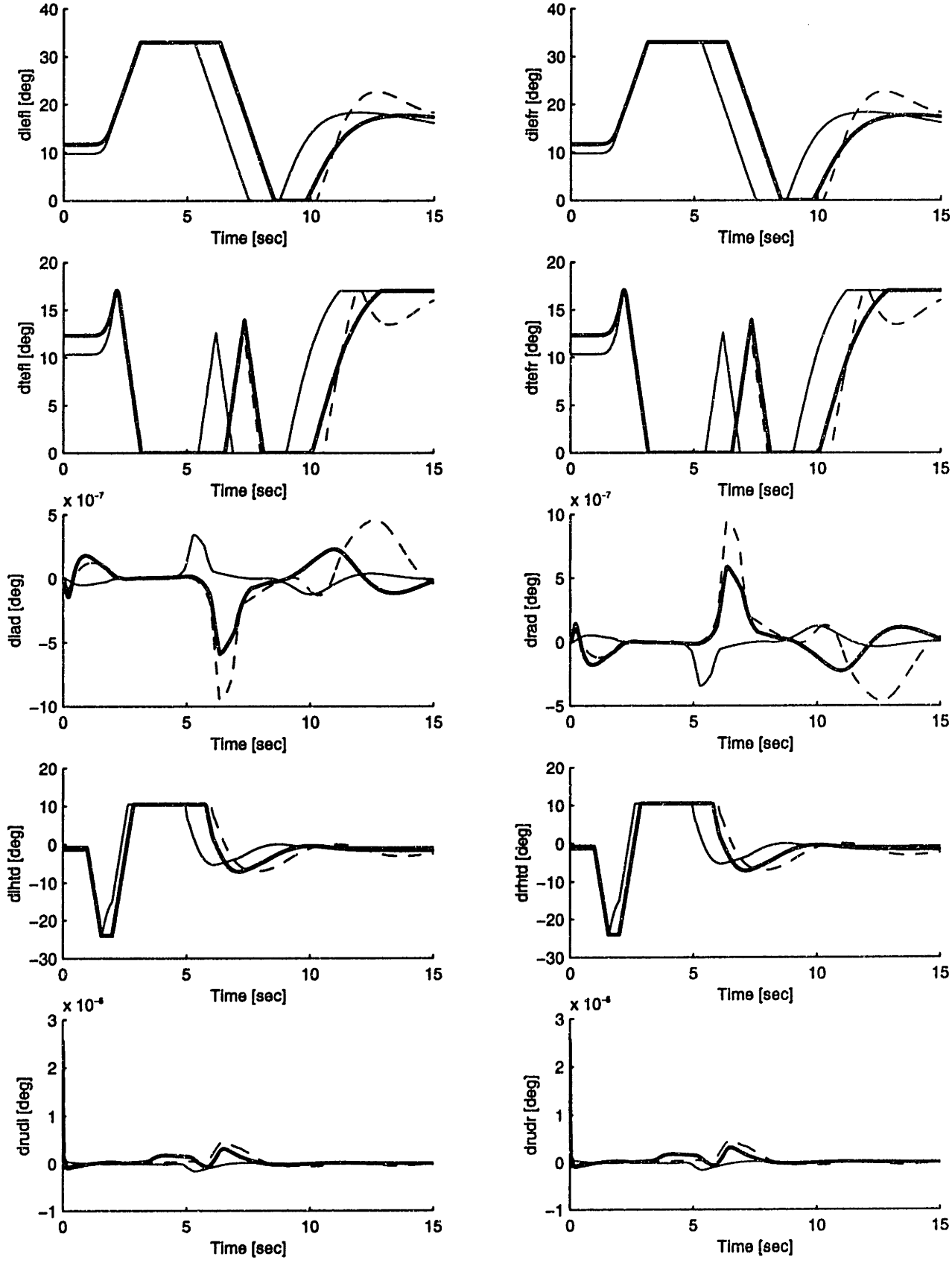

Fig. 5-18 Large longitudinal doublet, control variables.

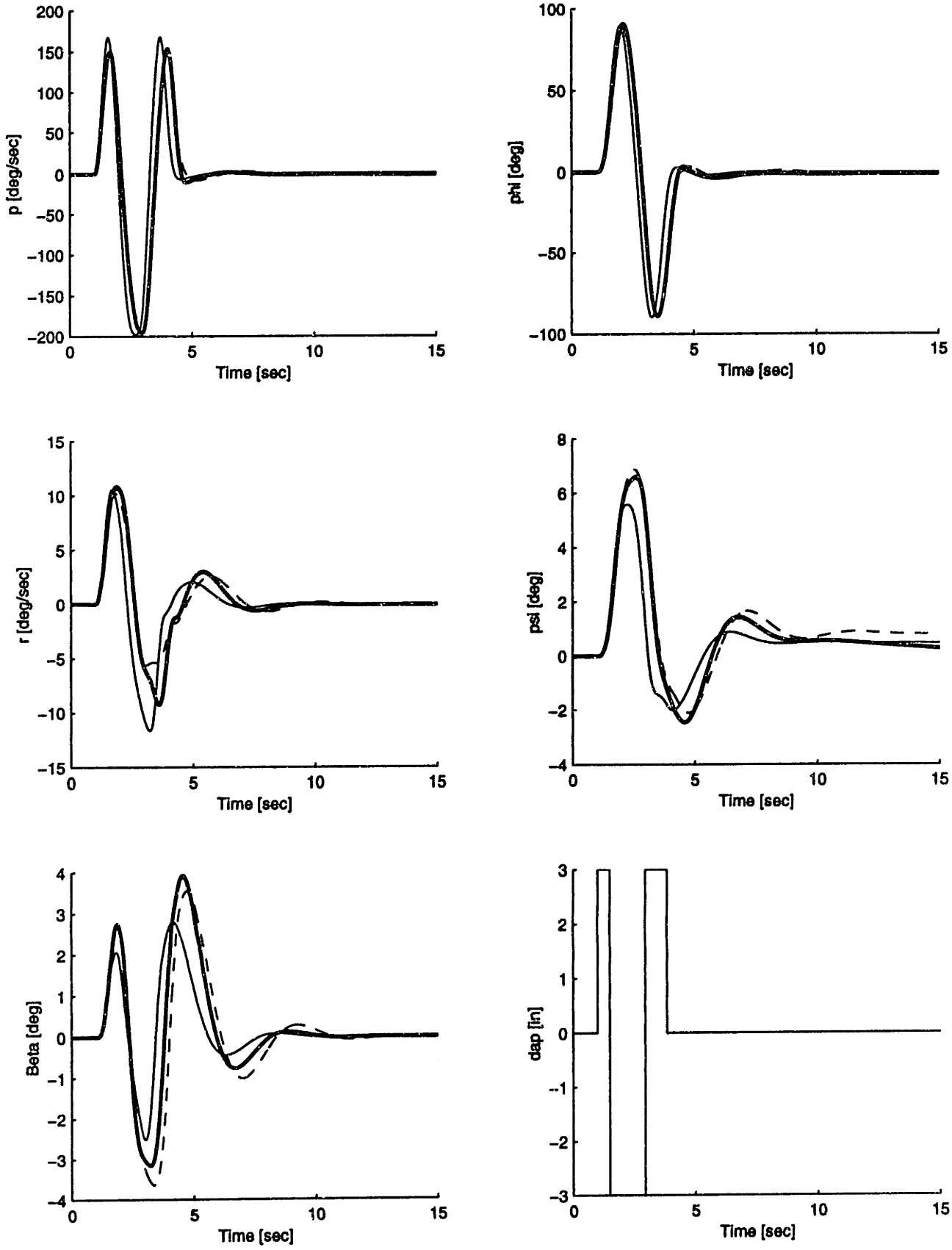

Fig. 5-19 Roll reversal maneuver, output variables.

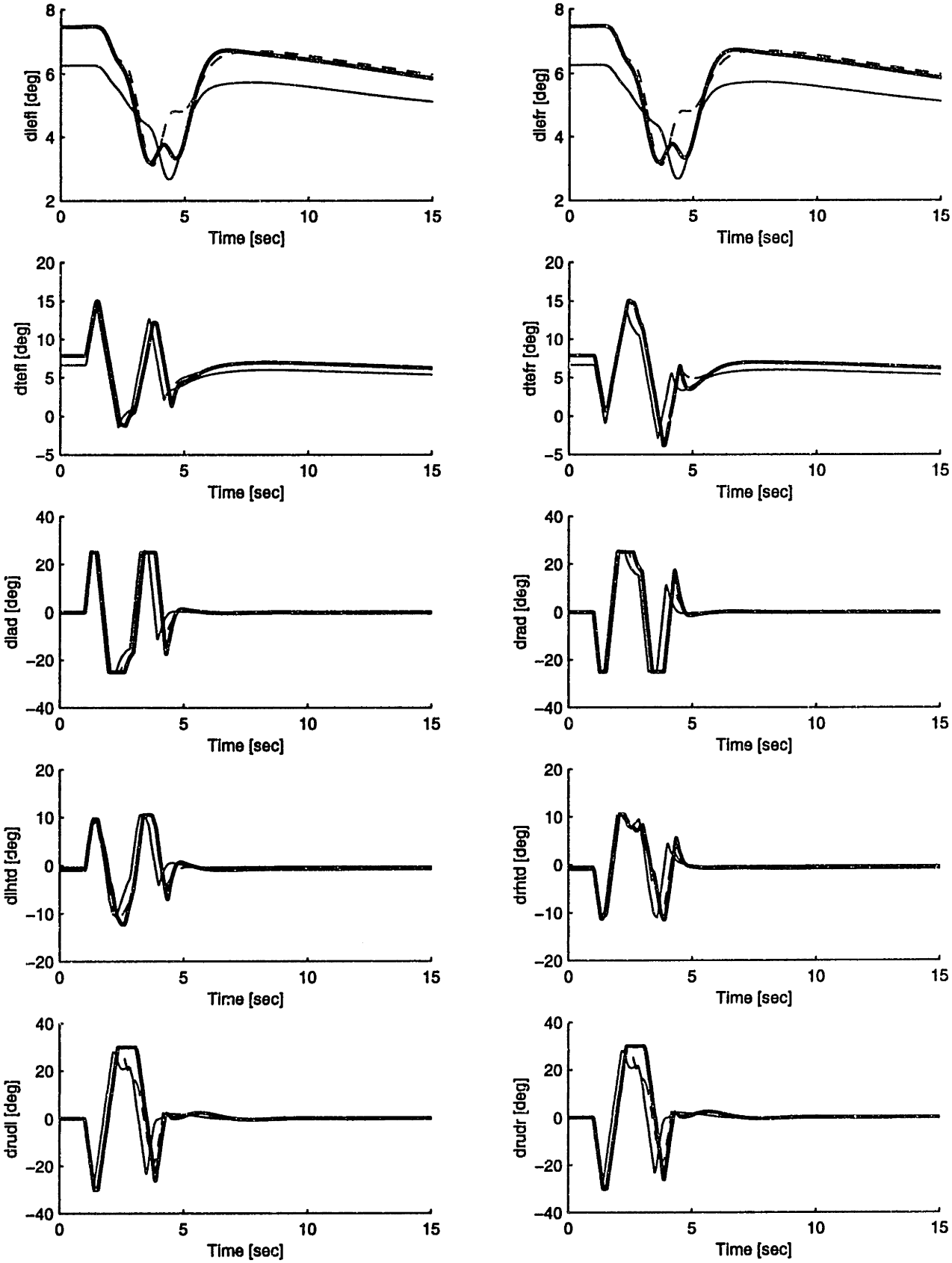

Fig. 5-20 Roll reversal maneuver, control variables.

5.6 Fixed Base Flight Simulator Tests

A six-degree-of-freedom nonlinear simulation incorporated in a fixed-base cockpit mock-up was used to analyze the new gain schedule. The cockpit mock-up incorporated the usual F/A-18 pilot display and controls. A screen projection provided the pilot with a limited view outside the cockpit. The simulation software was adapted to allow automatic switching, from the simulation console, between a standard F/A-18 aircraft, the F/A-18 HARV, and the F/A-18 HARV with the new gain schedule. In order to check one channel at a time it was possible to engage or disengage the new gain schedule on each channel separately. This set-up allowed the sim engineer to change the aircraft configuration without the pilot knowledge.

The simulation also had the capability to project a target aircraft on the screen. Six target aircraft trajectories were flown in advance and recorded. During the recording of the target maneuvers, a standard F/A-18 dynamics were used. Six tasks were performed for the analysis of the new gain schedule: level flight, single pitch pulse, multiple pitch pulses, multiple target acquisitions, refueling task, and descending 2-g turn. Each of these tasks is described below.

The scope of the simulations was to verify the handling qualities of the HARV and the HARV with modified gains, and compare them with those of the standard F/A-18. Before each test, the pilot was allowed to train knowing which aircraft configuration he was flying: the F/A-18, the HARV, and the HARV with new gains. After this training the test was performed and the standard Cooper Harper CH questionnaire was given to the pilot in order to define his CH rating. In addition the pilot was asked which aircraft he thought he was flying. The order of the aircraft the pilot flew was random.

5.6.1 Pilot Tasks

5.6.1.1 Level Flight

The scope of this task was simply to help the pilot familiarize himself with the three aircraft configurations. The target aircraft is in level flight at 20,000 ft and Mach 0.55; the distance from the target is set initially at 1,000 ft. The aircraft starts at the same speed and altitude as the target and the pilot is allowed to perform any maneuvers required for familiarization. Considering that there is not a specific task the pilot is simply asked to give a general opinion about the response of the aircraft to longitudinal and lateral inputs. Some of the pilots, due to the fact that they didn't have a specific task to accomplish, did not give a CHR.

Aircraft Configuration	Pilot A	B	C	D	E	F
F/A-18	--	2	3	1-2	--	--
F/A-18 HARV	--	3	5	2-3	--	--
F/A-18 HARV New	--	2	3	1-2	--	--

Tab. 5-4 CHR for level flight task

Even in this mode the pilots were able to recognize the HARV as an heavier and less responsive aircraft.

5.6.1.2 Single Pulse in the Pitch Axis

The target aircraft was initially in level flight 200 ft in front of the piloted airplane. After five seconds the target started a single pulse in the pitch axis. The pilot was asked to follow the target as closely as possible. Appendix C contains some of the comments recorded after this task. In general the pilots were not able to distinguish between the F/A-18 and the modified HARV. The comments on the HARV were not as good: large overshoot, difficulties in stopping the oscillations, and sluggish longitudinal response were some of the comments common to several pilots. The CH ratings shown in Tab. 5-5 reflect the unsatisfactory response of the HARV.

Aircraft Configuration	Pilot A	B	C	D	E	F
F/A-18	--	2	3	6	2-3	3-4
F/A-18 HARV	--	3	4-5	8	4-5	2-3
F/A-18 HARV New	--	2	3	6	2-3	5-6

Tab. 5-5 CHR for pitch single pulse task

5.6.1.3 Multiple Target Acquisitions

During this task the target aircraft appeared suddenly at different locations on the display. The pilot was asked to acquire the target as fast as possible, maintaining the same distance. Then the target was artificially moved to another location on the screen and a new acquisition was requested.

The scope of this task was to test coupling between the longitudinal and lateral axis during fast tracking. The tests did not revealed any major difference between aircraft. Unfortunately the task was dominated by the difficulty in maintaining a constant distance between the two airplanes. Pilots' CH rating was strongly affected by this fact.

Aircraft Configuration	Pilot A	B	C	D	E	F
F/A-18	--	3	4	--	3	--
F/A-18 HARV	--	4	4	--	5	--
F/A-18 HARV New	--	3	4	--	3-4	--

Tab. 5-6 CHR for Multiple Target Acquisitions

Fig. 5-6 shows the CH rating assigned by the three pilots that performed this task. Two pilots out of three were able to recognize the HARV, assigning a higher CH rating.

5.6.1.4 Multiple Pulses in the Pitch Axis

There are two reasons behind this task. The first is to have a set of data that can be used to calculate an 'experimental' longitudinal transfer function, to utilize in the Neal-Smith HQ criteria. The second is to verify gross tracking in the pitch axis. The target aircraft performed a series of pitch pulses along the longitudinal axis. The overall maneuver lasts 1 minute. The pilot was asked to keep a constant distance of 500 ft and track the target aircraft.

Again the pilots had difficulties distinguishing between the three aircraft. Three pilots were able to identify the HARV but the other three could not see the difference.

Aircraft Configuration	Pilot A	B	C	D	E	F
F/A-18	--	3	3	5	3	--
F/A-18 HARV	--	4	4	4	3	--
F/A-18 HARV New	--	3	3	3	5-6	--

Tab. 5-7 CHR for Pitch Axis Multiple Pulses

Based on the Multiple Target Acquisition and Multiple Pitch Pulse tasks, we conclude that gross tracking is not critical for the HARV, and that the pilots were able to compensate and perform the task on the three aircraft with the same confidence. Although the comments from the pilots did not give a definitive answer about the respective handling quality of the three aircraft, the frequency and Neal-Smith analysis on the data do give important insight into their behavior.

Fig. 5-21 shows the time domain response of one of the tests. It is possible to see that the pilot did not have difficulties remaining 500 ft behind the target. The second plot in Fig. 5-21 compares the actual pitch angle with the target one (solid dashed line); here it is difficult to say that one aircraft was definitely better than the other. This to some extent explains the fact that the CH ratings of the pilots do not always identify the HARV as the worst.

The simulation data were used to calculate an 'experimental' closed loop transfer function. Fig. 5-22 shows the Bode diagram of the transfer function from the stick input to the pitch rate. The frequency domain data clearly shows that the longitudinal response of the F/A-18 HARV with the new gains resembles very closely that of the standard F/A-18.

The Neal-Smith carpet plot calculated using all of the simulation data confirms that the F/A-18 HARV with the new gain schedule is very similar to the F/A-18. Fig. 5-23, Fig. 5-24, and Fig. 5-25 show the NS carpet plot of the three aircraft configurations. The plots show that even the F/A-18 simulator does not meet Level 1 handling quality requirements. This confirms the fact that all the pilots considered the refueling task harder in the simulator than in reality. The NS plots of the F/A-18 and the HARV modified are almost identical; for

a 3 rad/sec task the airplanes are near the boundary between level 1 and level 2. The HQ of the HARV are in the level 2 region and rapidly degrade for tasks with higher bandwidth.

We can conclude that at least in terms of longitudinal transfer function and Neal-Smith HQ criteria, the new gain scheduling corrects the deficiencies of the HARV and make the aircraft very similar to a standard F/A-18.

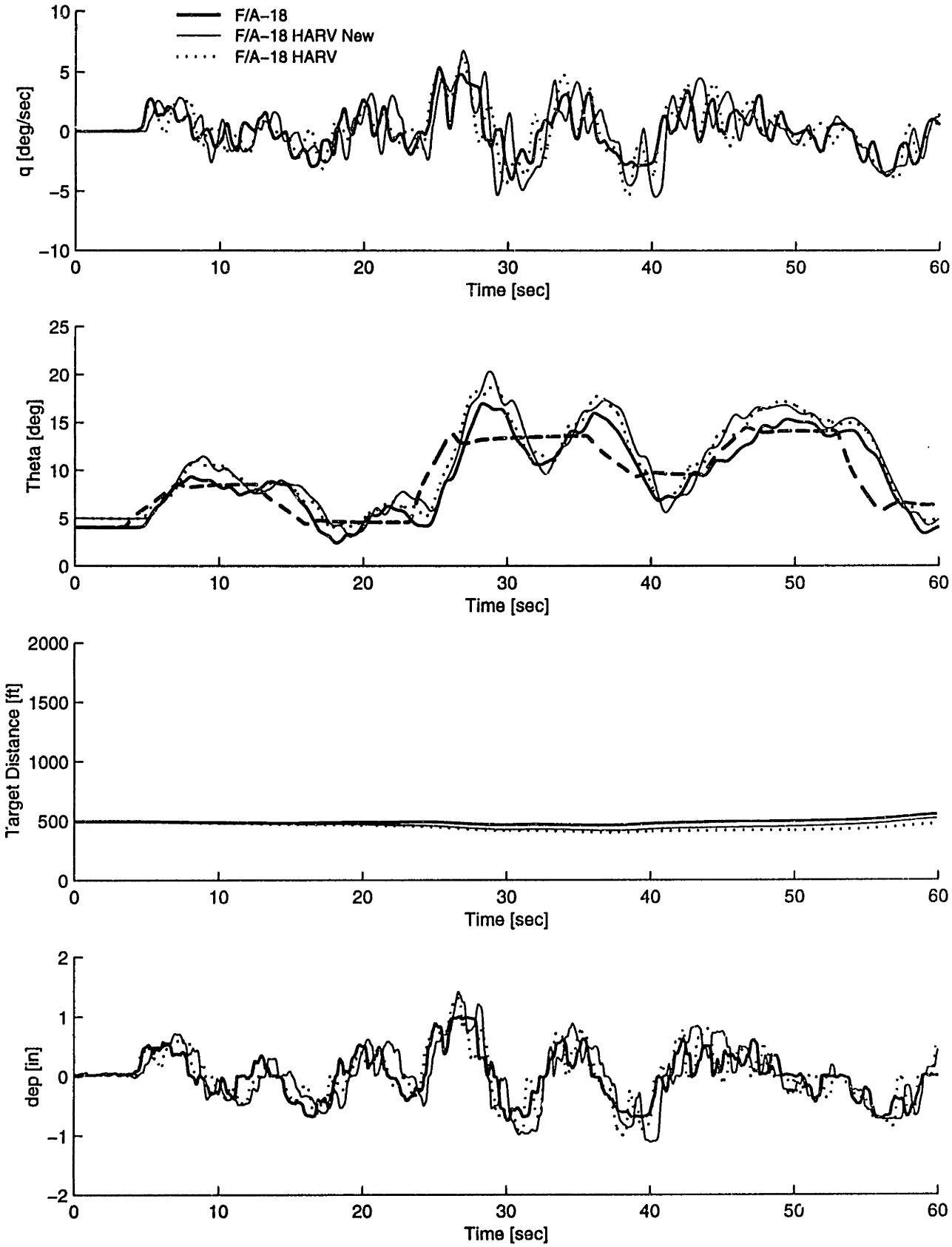

Fig. 5-21 Pilot F: Multiple Pitch Impulse Time Domain Response

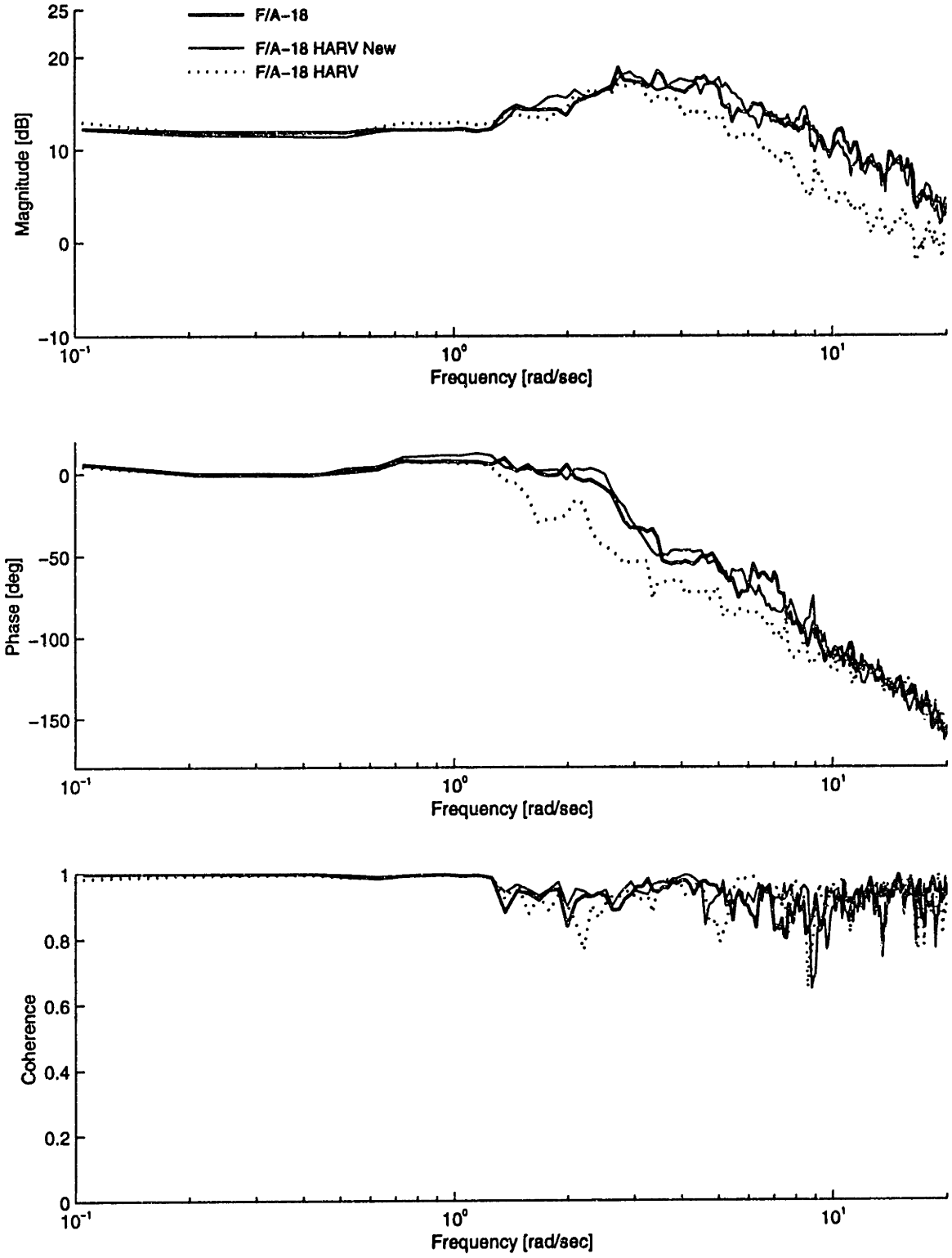

Fig. 5-22 Pilot F: Estimated Closed Loop Transfer Functions

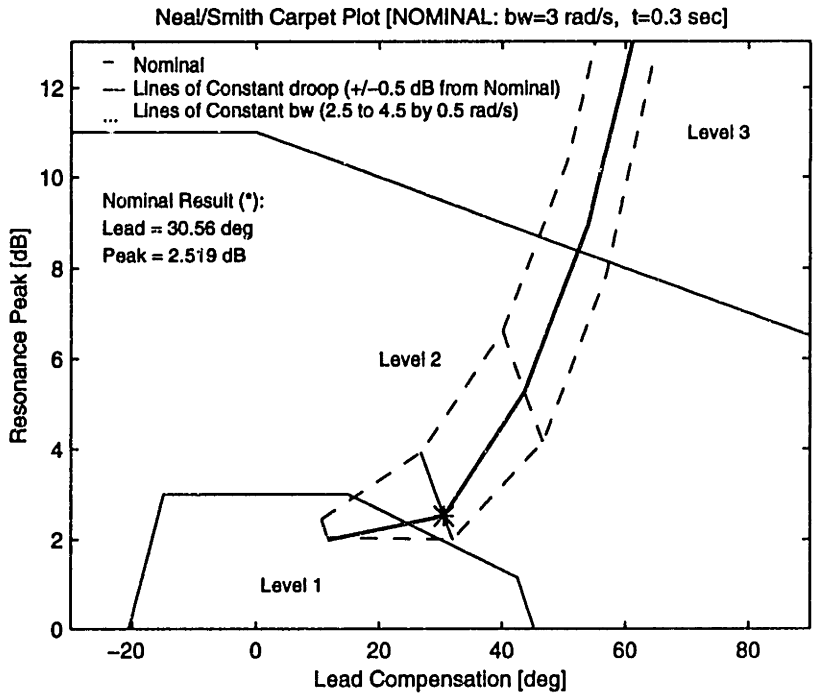

Fig. 5-23 F/A-18: Neal-Smith carpet plot calculated from the smoothed experimental longitudinal transfer function

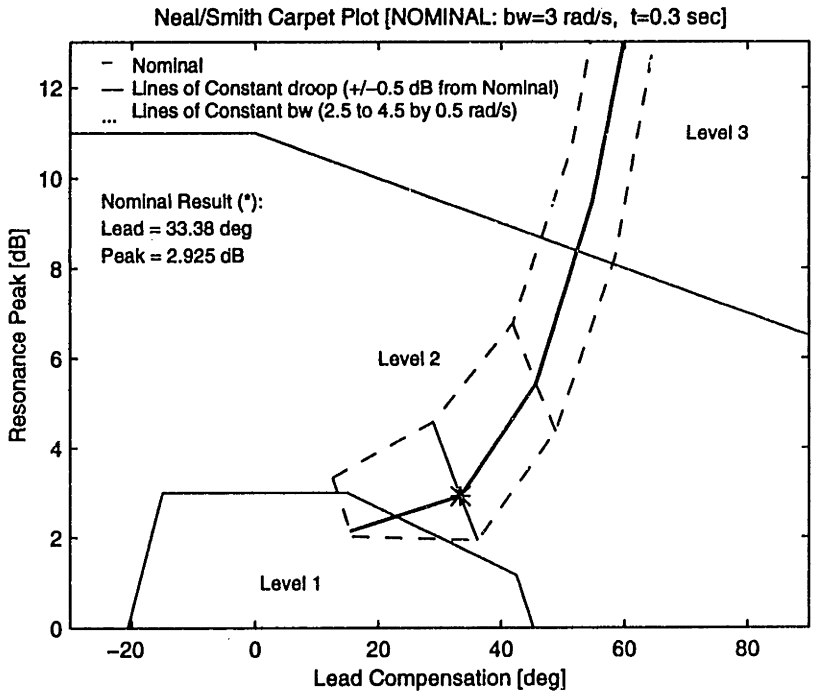

Fig. 5-24 F/A-18 HARV New: Neal-Smith carpet plot calculated from the smoothed experimental longitudinal transfer function

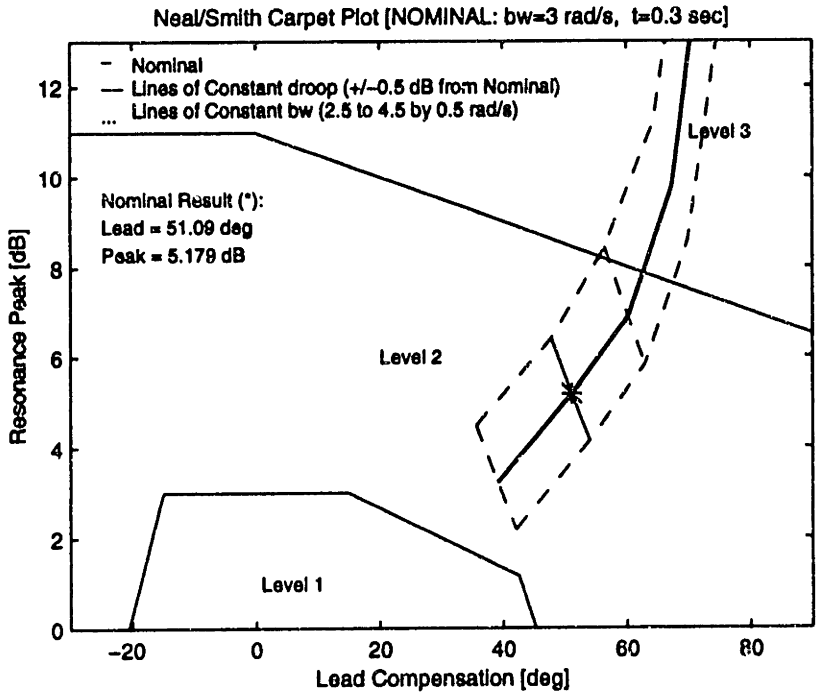

Fig. 5-25 F/A-18 HARV: Neal-Smith carpet plot calculated from the smoothed experimental longitudinal transfer function

5.6.1.5 Refueling Task

The refueling task was performed by four pilots. The target airplane, acting as a tanker, established level flight at 20,000 ft and Mach 0.55. The piloted aircraft was initially flying at the same altitude and Mach number as the tanker, at a distance of 200 ft behind the tanker. The pilot was instructed to reduce his distance from the tanker to about 60 ft and stabilize.

All pilots considered the refueling task in the flight simulator more difficult than in reality. The major problem was the unrealistic behavior of the throttle; this caused the maneuver to be dominated by a fore and aft movement. The aircraft was too responsive to small adjustments in the throttle, an thus it was quite difficult to maintain the aircraft at 60 ft behind the tanker. Furthermore there was a strong coupling between the lateral and longitudinal motion, so that the pilot tended to enter into lateral oscillations.

For this reasons the CH rating given by the pilots was affected by the difficulty in keeping distance within 60~70 ft. Pilot F, who spent the most time testing the refueling task,

considered the task representative of the level of concentration needed during refueling. During the final test he was able to recognize the heavier and more sluggish response of the F/A-18 HARV. Once the gains in the F/A-18 HARV were changed he was unable to distinguish between the HARV and the standard F/A-18. The PIO tendency that characterizes the HARV disappeared almost completely with the new gain schedule. Fig. 5-26 shows the response in the longitudinal axis. After about 60 seconds the pilot closes the distance with the tanker and starts trying to stabilize the aircraft.

Aircraft	Pilot					
Configuration	A	B	C	D	E	F
F/A-18	--	7	5-6	--	3	3
F/A-18 HARV	--	6	5-6	--	3	4
F/A-18 HARV New	--	5	4	--	3	3

Tab. 5-8 CHR for Refueling Task

From the time domain data we can see how difficult the task was, but it is difficult to see the difference between the three aircraft. In order to define the pilot's workload the power spectral density (PSD) of the longitudinal stick input was calculated. Fig. 5-27 shows the longitudinal stick input PSD for each of the four pilots. The area below the PSD measures the mean square value of the process; this is a common measure of the pilot's workload.

Tab. 5-9 shows the mean squared value (msv) of the pilots' longitudinal stick input. Higher msv correspond to higher pilot workloads. We can clearly see that in all cases the pilot workload was higher on the HARV. The workload of the standard F/A-18 is instead very similar to that of the HARV with the new gain schedule.

	Pilot B (1)*	Pilot B (2)**	Pilot C	Pilot E	Pilot F
F/A-18	0.8595	0.3607	1.4710	n.a.	0.3007
F/A-18 HARV	2.5368	0.6065	2.5708	1.8235	0.9330
F/A-18 HARV New	0.5798	0.2634	1.3635	1.3935	0.2286

* First attempt ** Second Attemp t

Tab. 5-9 Longitudinal Stick Input: Mean Square Value

The refueling task can be divided in two phases: acquisition and fine tracking. A more detailed analysis of the pilot work load during this task require separate analyses of these two phases. From Fig. 5-26 we can recognize that the acquisition and stabilization phase ends after about 60 second. For the remaining two minutes the pilot is in the fine tracking phase. Separate power spectral density functions were calculated for each phase. Fig. 5-28 shows the PSD of the pilot input for each aircraft configuration. The first two plots, showing the F/A-18 and the modified HARV, share the same characteristics. The pilot workload is larger in the tracking phase than in the acquisition phase. We can infer that the pilots used the same piloting style on the F/A-18 and the HARV with the modified gains. On the contrary the third plot has completely opposite characteristics, the pilot work load is larger in the acquisition phase than in the tracking phase. This confirms the comments of the pilots' during flight and simulations. In order to successfully perform the refueling on the HARV very low gains must be used. The pilot has to minimize his stick activity in order to avoid PIOs. Thus the bad CH rating is not really related to a higher workload but rather to the fact that a different piloting technique, which is inherently counterintuitive to the pilot, is necessary on the HARV.

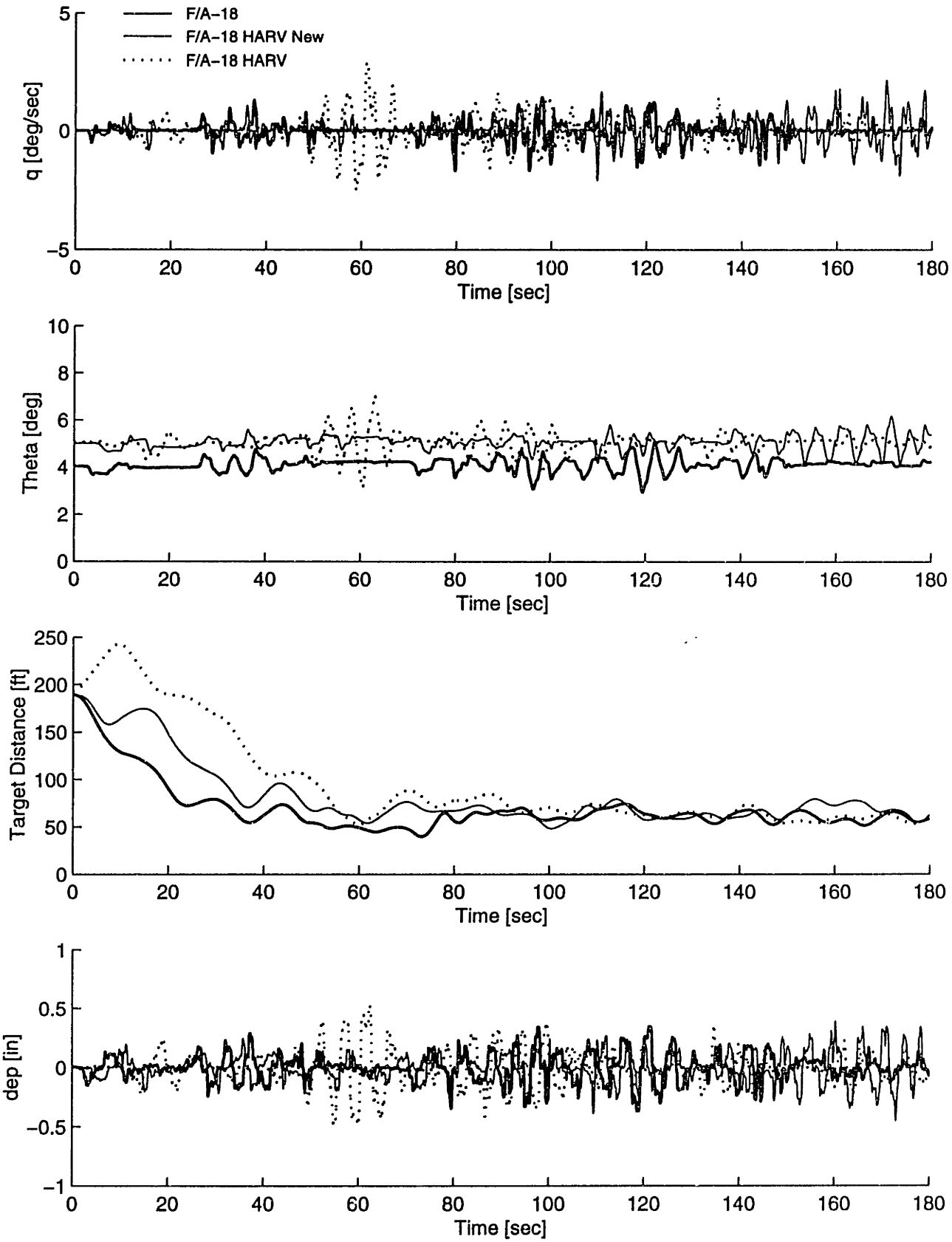

Fig. 5-26 Pilot F: Refueling Task, time domain plot data

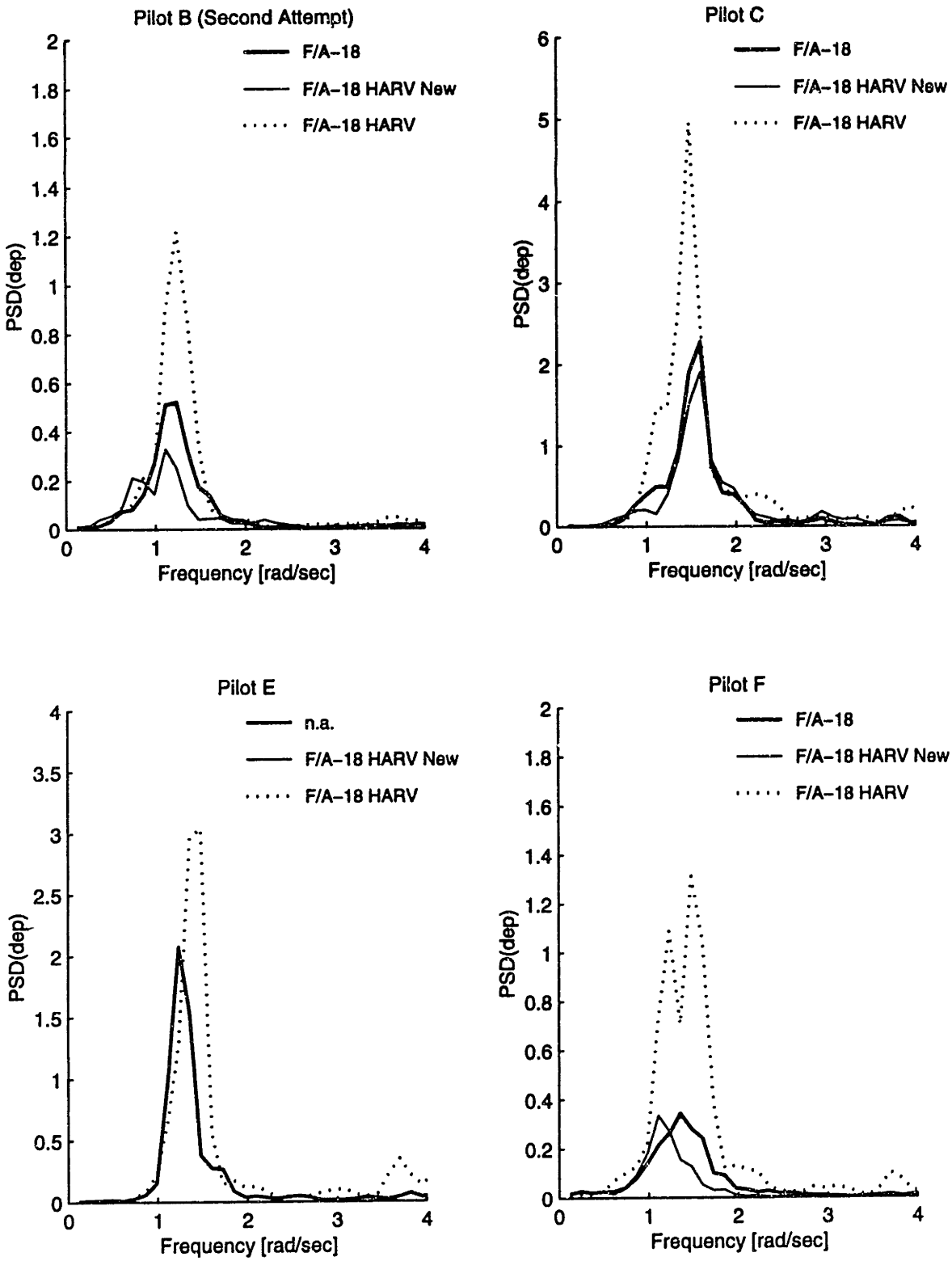

Fig. 5-27 Refueling Task: Power Spectral Density of the Longitudinal Stick Input

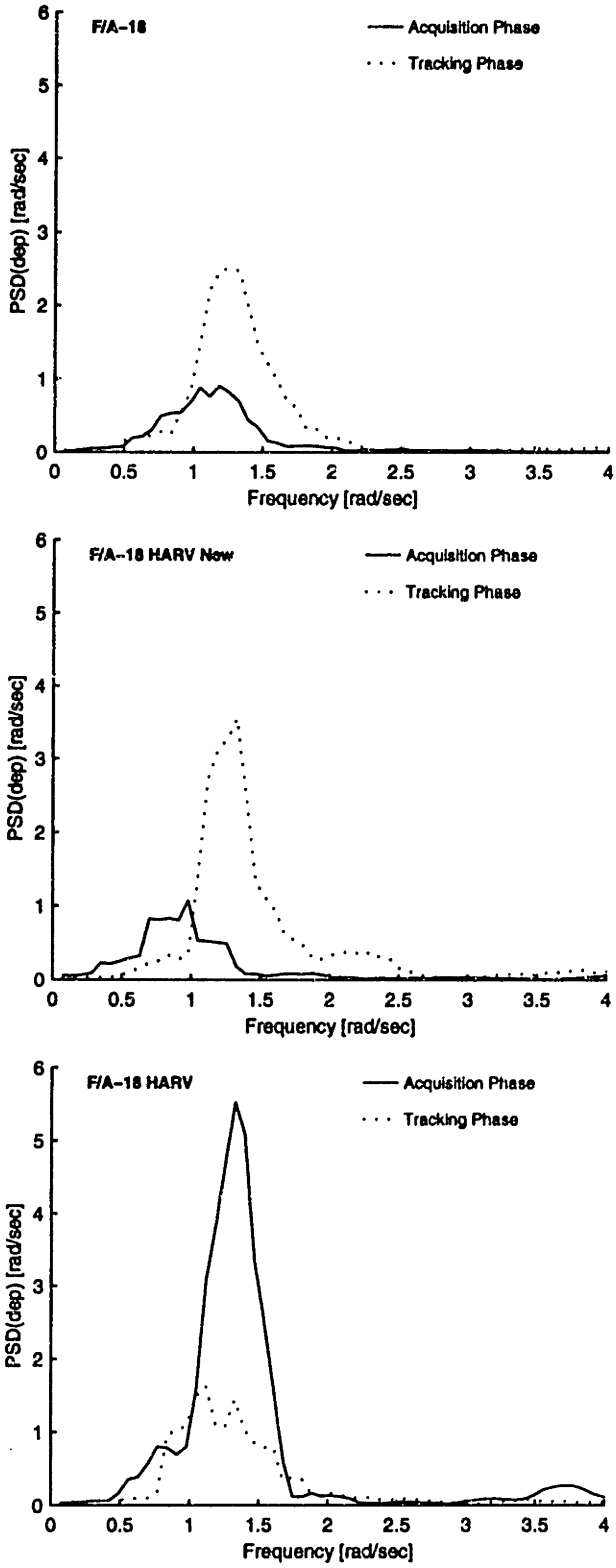

Fig. 5-28 Acquisition and Tracking Phases PSDs

5.6.1.6 Descending 2-g turn

This experiment was conducted to test the gain scheduling activity during an air-to-air fine tracking task. The target aircraft had the dynamics of a standard F/A-18. The maneuver of the target was flown in advance and was designed to be an almost constant 2-g turn descending from 30,000 ft to 20,000. The maneuver starts at Mach 0.4 and ends at Mach 0.8. In Fig. 5-29 is shown the 3-D plot of the target trajectory. The pilot was asked to acquire and track the target maintaining its distance within 2,000 ft.

Three pilots performed this task and they unanimously found the HARV heavier with a tendency to fall behind. The task was rated as 'easy' and the worst CH rating was always assigned to the HARV. The F/A-18 HARV with the new gains always received the same rating as the standard F/A-18.

Fig. 5-30 shows the gain scheduling activity throughout the maneuver. As expected the shape of the modified gains follows that of the standard control law. The F/A-18 HARV with the new gain schedule performed smoothly during the dive, and the pilots did not experience undesired changes in the response of the aircraft.

Aircraft Configuration	Pilot A	B	C	D	E	F
F/A-18	--	2	3	--	3	--
F/A-18 HARV	--	3	3	--	4-5	--
F/A-18 HARV New	--	2	3	--	3	--

Tab. 5-10 CHR for descending 2-g turn maneuver

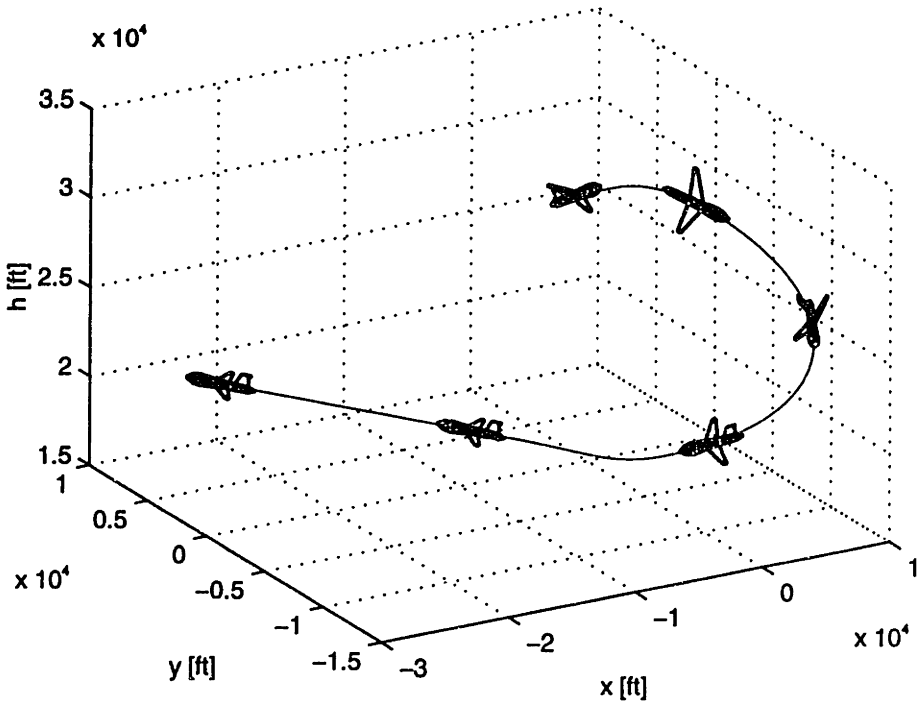

Fig. 5-29 Target trajectory in the spiral 2-g turn

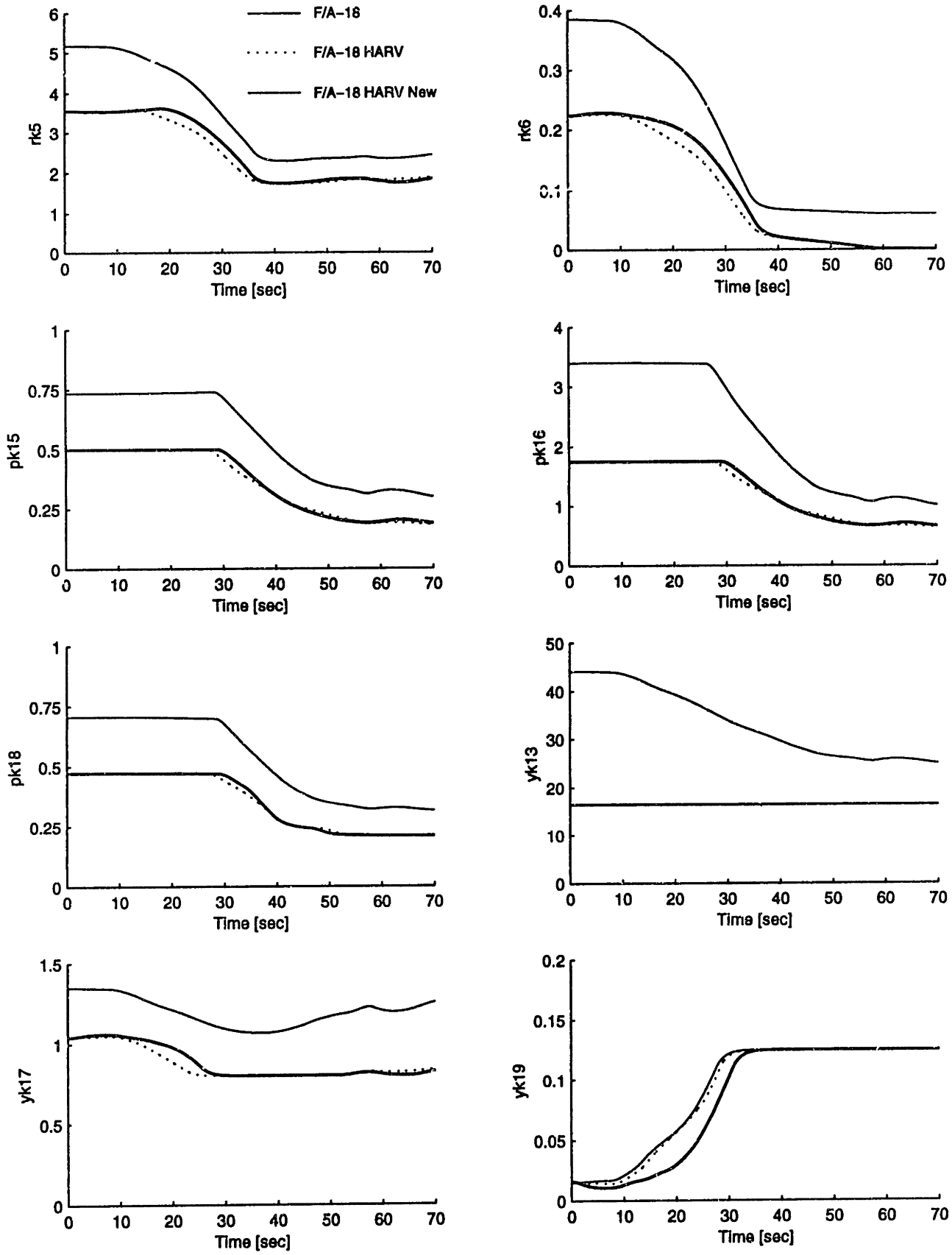

Fig. 5-30 Gain scheduling during the 2-g turn

5.6.2 Summary of the Fixed-Base Flight Simulator Tests

The fixed-base flight simulator validated the purely analytical linear and nonlinear simulation results. The pilot assigned CH ratings and comments further proved the validity of the new gain schedule applied to the HARV.

The refueling task was commented favorably by the pilots. Although it does not replicate in-flight refueling in all its aspects, this task is useful for providing an overall evaluation of aircraft performance in the refueling flight regime. The refueling task can best emphasize differences in the aircraft response that are not revealed by other tracking maneuvers. The task requires a significant amount of simulation time for the pilot to adapt to the fixed-base cockpit environment. The proficiency of the pilots improved significantly during the simulations. Although pilots' comments and CH ratings not always were consistent in identifying the HARV as the most difficult aircraft to fly, the analysis of the simulation data confirmed our expectations. We therefore believe that detailed CH ratings can be obtained only through an extensive simulation program. The CH ratings gathered (appendix C) must be considered in terms of their relative and not absolute values. In so doing we can distinguish a clear pattern in the CH ratings: in each task the average CH rating assigned to the HARV is always higher that the other two. The average CH rating of the HARV modified is instead slightly lower than the standard F/A-18. The reason may be probably attributed to the higher longitudinal stick gain that made the HARV modified a very responsive (may be too responsive) aircraft.

5.7 References

Ref.5-1 G. Becker and A. Packard, "Robust performance of linear parametrically varying systems using parametrically-dependent linear feedback", *Systems & Control Letters*, 23, 1994, pp. 205-215.

Ref.5-2 G. Becker, "A single quadratic Lyapunov function approach to the stabilization and control of parametrically dependent systems", *PhD Thesis*, U.C. Berkeley, December 1993.

Ref.5-3 P. Apkarian and P. Gahinet, "A Convex Characterization of Gain-Scheduled H_∞ Controllers", IEEE Transactions on Automatic Control, Vol. 40, No. 5, May 1995.

Ref.5-4 F. Wu, A. Packard, and G. Balas, "LPV Control Design for Pitch-Axis Missile Autopilots", *Proceedings of the 34th Conference on Decision and Control, New Orleans*, LA, December 1995, 188-193.

Ref.5-5 B. Bodenheimer, P. Bendotti, and M. Kantner, "Linear Parameter Varying Control of a Ducted Fan Engine", *The International Journal of Robust and Nonlinear Control*, January 1995.

Ref.5-6 B. Bodenheimer, and P. Bendotti, "Optimal Linear Parameter Varying Control Design for a Pressurized Water Reactor", *Proceedings of the 34th Conference on Decision & Control*, Vol. 1, December 1995, pp. 182-187.

Ref.5-7 N. Haley, D. Moerder, J. Broussard, and D. Taylor, "A Variable-Gain Output Feedback Control Design Methodology", NASA CR 4226, 1989.

Ref.5-8 P. Apkarian, J. Biannic, and P. Gahinet"Self-Scheduled H_∞ Control of Missile via Linear Matrix Inequalities", *Journal of Guidance, Control, and Dynamics*, Vol. 18, No. 3, May-June 1995.

Ref.5-9 F. Wu, A. Packard, G. Balas, "LPV Control Design for Pitch-Axis Missile Autopilots", *Proceedings of the 34th Conference on Decision & Control*, New Orleans, LA - December 1995.

Ref.5-10 A. Packard, "Gain Scheduling via Linear Fractional Transformations", *Systems & Control Letters*, Vol. 22, 1994, pp. 79-92.

Ref.5-11 D. Guo and W. J. Rugh, "A Stability result for linear parameter varying systems", *Systems & Control Letters*, Vol. 24, 1995, pp. 1-5.

This page intentionally left blank.

Chapter 6

Summary and Conclusions

6.1 Robustness Analysis: Summary

In the first part this thesis we have described a set of developments that allow one to apply recent multivariable robustness analysis measures to flight-test engineering questions. In Chapter 2 a method to calculate the real structured singular value μ, proposed by Dailey, is developed and extended to include repeated real uncertainties. We introduced the idea of iterative weightings as a means to determine which uncertain elements dominate the robustness measure. In addition we showed how to cast phase and delay uncertainty as real structured uncertainties in ways that provide easily interpreted information about flight safety. The discontinuous nature of the real structure singular value μ has been shown with several practical examples. These procedures were applied to some specific control law validation issues raised during the X-31 flight tests. The iterative weighting procedure has been applied to determine the relative importance of several aerodynamic parameters to the robustness of the X-31 lateral-directional control during the Quasi-tailless experiment. The phase-margin block structure was used to present the concept of robustly guaranteed phase margin. In Chapter 3 a methodology to calculate the phase margin that is guaranteed to hold in the face of other plant parameter variations was presented. Finally, we showed how to calculate and present in the control room a measure of multivariable robustness derived during a flight test.

The specific contribution of this thesis are extensions to existing tools to make them useful for robustness analysis in practical flight control applications:

- Dailey's algorithm was extended for repeated real uncertainties;
- An iterative weighting scheme was devised to identify elements critical to robustness;

- Methods to analyze Phase Margin and "Robustly Guaranteed" Phase Margin were introduced;
- The discontinuity of real-μ was analyzed and conditions under which this can occur were elucidated.

6.2 Fixed Structure Gain Scheduling: Summary

Chapter 4 and 5 were dedicated to the important issue of fixed structure control law design. Through a realistic example using the F/A-18 flight control system, we have shown how the problem of fixed-structure gain adjustment can be accomplished using modern methods. The framework of block perturbations and norm-based objectives is an excellent way to develop generalized solutions to the problem. However, this resulting class of design problems is non-convex and therefore requires DK-style iteration on LMIs. The time required by the LMI algorithm to converge grows exponentially with the number of states of the system. The Quasi-Newton approach, however, is found to be an efficient and more versatile way to find a solution for large systems. A mixed cost was introduced which allows Handling Qualities, in terms of the Neal-Smith criterion, to be retained or improved during gain adjustments. The generalized framework for gain adjustment was specifically tailored to allow gain scheduling to be addressed. In Chapter 5 we draw upon the theory of Linear Parameter Varying systems to develop a gain schedule for the F/A-18 HARV. The flight data relative to the refueling of the F/A-18 HARV were analyzed and revealed a degradation in the performance of the standard F/A-18 control law when used on the F/A-18 HARV. The fixed structure LPV technique was applied to redesign the gain scheduling of the CAS in the subsonic portion of the flight envelope. The new gain schedule was successfully tested on the fixed based flight simulator at NASA Dryden. The piloted sim confirmed that the new gain schedule was effective in correcting the problems on the F/A-18 HARV. In general the pilots were not able to distinguish between the standard F/A-18 and the HARV with the new gain schedule.

It is clear from our example that our goal was to rely heavily on existing knowledge concerning the structure of successful control laws, the input-output properties that are important, and the handling qualities criteria that must be met by the final control law. It will also be clear to the knowledgeable reader that many of the performance robustness measures that have been popularized recently can be directly incorporated into the structure developed, without sacrificing the architecture of the flight control system. This highly specialized and mature structure is preserved; as is the simplicity of form of the gain schedule itself.

Again the specific contributions of this thesis are related to bridging the gap between theory and practices:

- The fixed structure control problem was cast as an LPV synthesis problem, and the mathematical properties of this problem were elucidated;
- A new method to introduce Handling Qualities into the optimization process was developed;
- A large-envelope gain scheduling of a real flight control system was designed with this method and tested in a piloted simulator. Thus we have shown constructively and in details how to bridge the gap from theory to practice.

6.3 Conclusions

- **Robustness Analysis:** Clearly, useful analysis can be done using the structured singular value framework. The examples presented here invariably corroborated previous results obtained through conventional means, which require more exhaustive approaches. More work is needed to address the plethora of flight safety, flight dynamics, implementation, and nonlinear issues that arise during flight control law validation, but the framework demonstrated here shows promise due to its versatility and intuitive appeal.
- **Gain Scheduling of Fixed Structure Controllers:** Procedures and guidelines in the design of fixed structure controllers can be extremely valuable in flight control

applications. With respect to the design procedure, we have utilized LPV theory only to the extent that it can be applied in a fixed-structure situation with table look-up plant dynamics. Whenever gridding of the operating points is required, guarantees regarding intermediate points and time variations of θ are lost. Although this limitation may appear severe, in fact it has been imposed on the non-fixed structure applications of LPV that we have found in literature. Two things are gained through utilization of the LPV framework. First the robust control literature of recent years can be made consistent with the practical necessity to gain schedule. Second, automation of the gain scheduling process is made systematic. Such automation allows software reuse, and streamlines development of control laws significantly.

- **Piloted Simulations:** Extremely important results can be obtained from piloted simulations. The refueling task, thanks to its characteristic of fine tracking under stress, is particularly useful in the study of PIO tendency of the aircraft, and in the analysis of the response of the flight control law to pilots with different gains. The analysis of the simulation data and the comments of the pilots closely reflect the conclusions of the Neal-Smith criteria for the longitudinal Handling Quality. The number of redesigns due to unsatisfactory comments from the pilots can be greatly reduced including Handling Quality criteria in the design process.

6.4 Closure

The basic principle which inspired this work in its development becomes an essential point of arrival. As systems grow in complexity the need for specialized control laws becomes increasingly important. The development of unstructured "generic" control methods which are apt to work on a variety of systems, although it represents a significant and interesting challenge, does not reflect the needs of practical engineering. Rather the development of standard architectures, specific to classes of systems, and of automatic methods for parametrized designs is of paramount importance.

This idea is clearly not new. Throughout the DoD there is an increasing interest in the concept of Software Reuse as a means to reduce the life cycle cost of systems. With the increasing importance of software in aerospace applications, the software maintenance takes almost 45% of the total Life-Cycle costs. The Report to Congress on the Software Reuse Initiative (1996-2000) specifically says:

> *Department of Defense (DoD) software costs are expected to grow from about $30 billion in 1990 to $42 billion in 1995 .... effective software reuse would reduce software life-cycle costs and improve the reliability .....*

The minimization of software-specific costs arising during maintenance is critical to the success of a computer system. The activity of redesign and tuning existing control laws from our point of view enters in the category of a maintenance activity. The flight control law, as all the other components of the computer system, must meet specific requirements of maintainability, accessibility, and simplicity. The study presented in this thesis closely follows the philosophy behind the Software Reuse Initiative: the fusion of reuse and its enabling technologies and their unification with software engineering as it becomes a mature engineering discipline. Using standard architectures and parametrized designs to build new application systems will be considered engineering, not merely "reuse".

This page intentionally left blank.

Appendix A

F/A-18 Nonlinear Simulator

A-1 Introduction

The design of modern flight control systems, using the most recent control techniques, is highly related to the availability of a nonlinear flight simulator that is at the same time high fidelity and versatile. In this section we describe a flight simulator for an F/A-18 fighter aircraft that was recently developed at MIT using Matlab and Simulink.

Starting in the late sixties, many simulators have been developed for fighters and large commercial aircraft. They are typically written in Fortran and more recently in C and other high level languages, and their main objectives are fidelity and computational speed. In order to achieve these two goals a price in lack of versatility needs to be paid. It is often difficult or al least not immediate to break the loop at different points, inject signals at particular points of the control law, alter aerodynamic parameters, or calculate transfer functions between specific points of the closed loop system. Flight simulators have been mainly used for pilot training and for flight control law verification and tuning. It is only in recent years that nonlinear simulators have been used as a development tool for flight control law design.

Many software tools for control system design are presently available, two of the most common being *Matrix-X* and *Matlab*. Incorporated in these tools are many functions that can be of great help to control engineers, such as dedicated algorithms for controller analysis and synthesis. These tools in many cases represent the state of the art in control theory. The time required for the design of a new control law or the analysis and tuning of an existing control law can be dramatically reduced with the aid of these software packages.

For this reason we believe that a high fidelity flight simulator, written in one of these high level dedicated packages, is necessary for the design and tuning of modern flight control laws. Using the flight simulator of the F/A-18 that is currently used at NASA Dryden as a

reference model, a new simulator for *Simulink* has been developed. One of the main limitation of *Matlab* is its computational speed. The problem becomes particularly critical when there are hundreds of interpolations that need to be calculate at each frame. In order to speed up the simulation time all the functions which comprise the aircraft model were written in C and integrated into a *Simulink* block diagram. The diagram itself is self explanatory: it is easy to identify each block, its interfaces and its function in the overall system. The input and output variables of each block can be easily recorded during the simulation or plotted in real time at the designer's convenience. Linear models at different flight points can be obtained and new controllers can be easily wrapped around the open loop aircraft model.

Fig. A-1 shows the *Simulink* block diagram of the F/A-18 model with the 701E Control Augmentation System already inserted in the feedback path. In the sequel of this document we will refer to the *Simulink* F/A-18 simulator using the SimSim moniker.

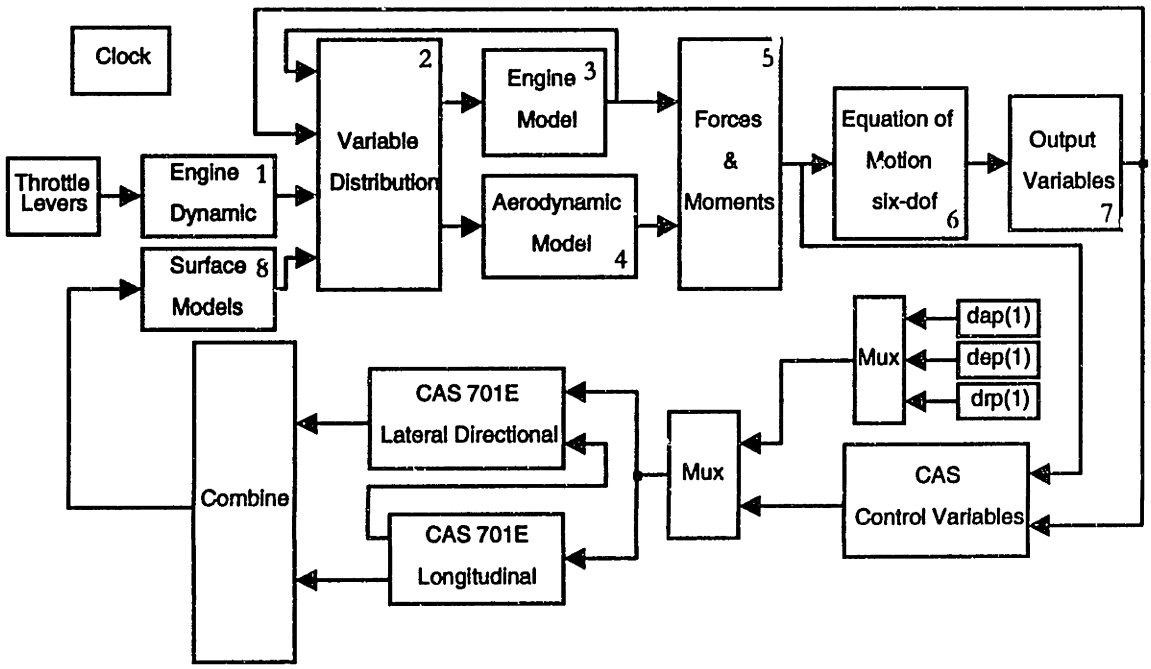

Fig. A-1 SimSim: Simulink block diagram

In the current version of SimSim, a trimming routine is not yet available. In order to trim the aircraft we use the NASA Dryden nonlinear simulator (Release 14). Four hundred trimming points, covering most of the F/A-18 flight envelope, were calculated and stored in files that can easily loaded in the *Matlab* workspace. The user can select the desired flight point from a table of Mach numbers and altitudes. The file associated with this point is then loaded before the simulation is started. A routine that will allow to trim the aircraft at any given initial conditions will be made available by the authors in the near future. Only minor adjustments need to be made to the existing trimming routine in Matlab in order to speed up the trimming process.

In order to show the performance of the simulator for standard simulation tasks, a 30 second maneuver in pitch and roll was performed on three different computers. The results of this test are in Tab. A-1. One important characteristic of SimSim is its transportability between different computers running the same version of Matlab and Simulink. The simulator presented in this document has been developed in *Matlab* Version 4.2c.1 and *Simulink* Version 1.3c. It is important to remember that the simulator is not transportable on older versions of *Simulink*.

Platform	CPU Time
Sparc 5	53.30 [sec]
Sparc 10	51.35 [sec]
Pentium 166 MHz	19.96 [sec]

Tab. A-1 Simulator computation time performance on different platforms

A-2 SimSim Description

The aircraft model has been divided into eight major blocks, each performing one specific function in the overall simulator. The F-18 model top level Simulink blocks are shown in Fig. A-1 and are synthesized in the following table.

N.	Block Name	Block Type	Description
1	Engine Dynamics	C-Function	Integrate second order engine dynamics..
2	Variable Distribution	Simulink Block	Prepare variables for the engine and aerodynamic models.
3	Engine Model	C-Function	Calculate the thrust forces and moments.
4	Aerodynamic Model	C-Function	Calculate aerodynamic forces and moments.
5	Forces & Moments	Simulink Block	Combine the aerodynamic and the thrust forces and moments.
6	Equation of Motion	C-Function	Integrated the 12 first order equation of motion.
7	Output Variables	C-Function	Calculate additional output variables using the state variables.
8	Surface Models	Simulink Block	State space models, rate and position limits for all the aerodynamic surfaces.

Tab. A-2 SimSim top level blocks

In the following sections a brief description of each block and its input and output variables is presented. The Variable Distribution block is not described in a separate paragraph because it performs simple vector manipulations in order to prepare the input for the Engine Model and the Aerodynamic Model. For the same reason the Forces & Moments block is not described, it simply adds the contributions to the total force and moment due to the aerodynamics and the thrust, and prepares the input data for the Equation of Motion block.

As shown above, two types of Simulink blocks are used in the simulator: Simulink Blocks and C-Functions. The Simulink Blocks are simple Simulink diagrams that use the basic built-in functions such as *state space*, *integrator*, *derivative*, *mux*, *demux*, *gain*, *sum*, etc.. The C-Functions are instead dedicated C files that perform computationally intensive operations. For instance the aerodynamic model is composed of more than one hundred interpolation tables; coding this function in *Matlab* would have tremendously increased the computation time and made the simulator unusable.

In order to start the simulation it is necessary to call the matlab m-file **sim_data.m**. It contains all the data necessary to initialize the simulation. Trimming data, aerodynamic data, atmospheric data, and engine data are loaded at the beginning of this file. The file also prepare all the variables that are passed as arguments to the simulink model. After this file is loaded the simulation can be started within matlab or from simulink. In appendix A-7 is given the listing of this file.

A-3 Equation of Motion

In this section the six degrees of freedom equations of motion that describe the nonlinear dynamics of the aircraft are described. The following assumptions are used in the derivation of the equations of motion:

- rigid body;
- flat Earth;
- constant aircraft mass and inertia characteristics.

These are common assumptions for aircraft control law design and flight simulation. Details about the equation of motion can be found in Ref. A-1.

Force Equations

$$\begin{aligned} m\dot{U} &= m(RV - QW) - mg\sin(\theta) + F_x \\ m\dot{V} &= m(-RU + PW) + mg\sin(\phi)\cos(\theta) + F_y \\ m\dot{W} &= m(QU - PV) + mg\cos(\phi)\cos(\theta) + F_z \end{aligned} \qquad \text{[A-1]}$$

Kinematics Equations

$$\begin{aligned} \dot{\phi} &= P + \tan(\theta)(Q\sin(\phi) + R\cos(\phi)) \\ \dot{\theta} &= Q\cos(\phi) - R\sin(\phi) \\ \dot{\psi} &= \frac{Q\sin(\phi) + R\cos(\phi)}{\cos(\theta)} \end{aligned} \qquad \text{[A-2]}$$

Moment Equations

$$\begin{aligned} \dot{P} &= (c_1 R + c_2 P)Q + c_3 L + c_4 N \\ \dot{Q} &= c_5 PR - c_6(P^2 - R^2) + c_7 M \\ \dot{R} &= (c_8 P - c_2 R)Q + c_4 L + c_9 N \end{aligned} \qquad \text{[A-3]}$$

Navigation Equations

$$\begin{aligned} \dot{p}_N &= U\cos(\theta)\cos(\psi) + V(-\cos(\phi)\sin(\psi) + \sin(\phi)\sin(\theta)\cos(\psi)) + W(\sin(\phi)\sin(\psi) + \cos(\phi)\sin(\theta)\cos(\psi)) \\ \dot{p}_E &= U\cos(\theta)\sin(\psi) + V(\cos(\phi)\cos(\psi) + \sin(\phi)\sin(\theta)\sin(\psi)) + W(-\sin(\phi)\cos(\psi) + \cos(\phi)\sin(\theta)\sin(\psi)) \\ \dot{h} &= U\sin(\theta) - V\sin(\phi)\cos(\theta) + W\cos(\phi)\cos(\theta) \end{aligned} \qquad \text{[A-4]}$$

The constants $c_1, \ldots c_9$ are defined as follows [Ref. A-1].

$$c_1 = \Gamma^{-1}\left(J_y - J_z\right)J_z - J_{xz}^2 \qquad c_2 = \Gamma^{-1}\left(J_x - J_y + J_z\right)J_{xz} \qquad c_3 = \Gamma^{-1}J_z$$

$$c_4 = \Gamma^{-1}J_{xz} \qquad c_5 = \frac{J_z - J_x}{J_y} \qquad c_6 = \frac{J_{xz}}{J_y} \qquad \text{[A-5]}$$

$$c_7 = \frac{1}{J_y} \qquad c_8 = \Gamma^{-1}\left(J_x - J_y\right)J_x + J_{xz}^2 \qquad c_9 = \Gamma^{-1}J_x$$

Where:

$$\Gamma = J_x J_z - J_{xz}^2 \qquad \text{[A-6]}$$

The mask of the *Equation of Motions* block is shown in Fig. A-2. Two parameters need to be passed to the mask: the inertia and mass characteristics, and the initial conditions. The vector JJ contains the 9 constants defined in equation A-5, plus two additional terms: the gravity acceleration in ft/sec^2 and the initial mass of the aircraft..

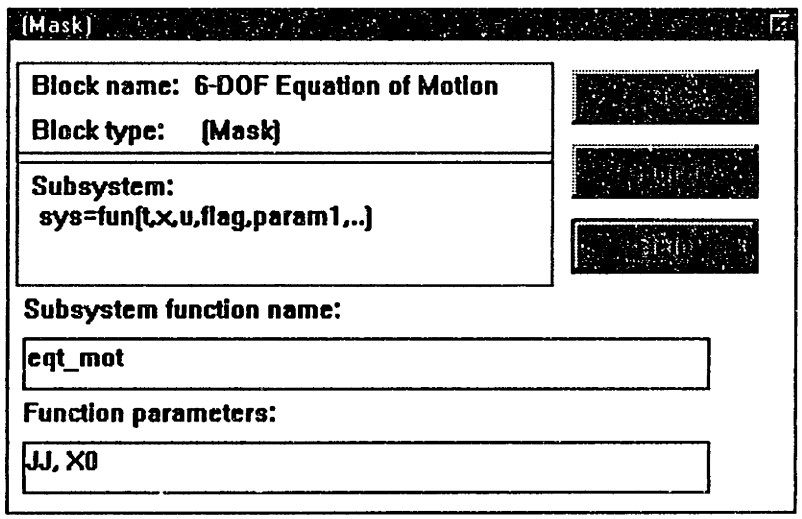

Fig. A-2 Equation of Motion Six-DOF mask

The vector *X0* contains the initial conditions of the 12 rigid body states described in the first order differential equations (equation A-1, A-2, A-3, and A-4).

The **input** to the block are the three forces (F_x, F_y, and F_z) and the three moments (L, M, and N) in the body axis reference frame. The **output** of this block are the twelve states defined in the equation of motion. The 12 first order differential equations are integrated using the method selected by the user in the simulation parameters mask of the Simulink

diagram. In all the simulations presented in the sequel of this document a third order Runge-Kutta method has been used.

Additional terms, representing the angular momentum of spinning rotors, have been omitted in the equation of motions. In the original flight simulator they were taken into account, for the scope of this simulator those terms are negligible.

A-4 Aerodynamic Model

The aerodynamic model implemented in the simulator is a direct derivative of the aerodynamic model used in the NASA Dryden simulator. We are not going to describe the details of the aerodynamic model because it goes beyond the scope of this document. The inputs and the output of this block are shown in the header of the C function in Appendix A-3.

The output vector contains the three aerodynamic forces (FXAR, FYAR, and FZAR) the three aerodynamic moments (MXAR, MYAR, and MZAR), and the six aerodynamic coefficients (CY, CL, CN, CLFT, CM, and CD).

The aerodynamic forces and moments acting on the aircraft are defined in terms of the dimensionless aerodynamic coefficients and are transferred in the body axes reference system. Thus we have:

$$\begin{cases} FXAR = QS * (-CD * \cos(\alpha) + CLFT * \sin(\alpha)) \\ FYAR = QS * CY \\ FZAR = QS * (-CD * \sin(\alpha) - CLFT * \cos(\alpha)) \end{cases} \quad [A\text{-}7]$$

$$\begin{cases} LAR = qbar * S * b * CL + FYAR * deltaz - FZAR * deltay \\ MAR = qbar * S * cbar * CM + FZAR * deltax - FXAR * deltaz \\ NAR = qbar * S * b * CN + FXAR * deltay - FYAR * delatx \end{cases} \quad [A\text{-}8]$$

The aerodynamic model mask is shown in Fig. A-3. Two parameters are requested by this block: geometric data for the aerodynamic model, IA, and thrust vectoring flag, TV_FLAG. The thrust vectoring flag is used to engage the thrust vectoring (TV_FLAG = 1 thrust vectoring on). The vector containing the geometric data is defined in Tab. A-3.

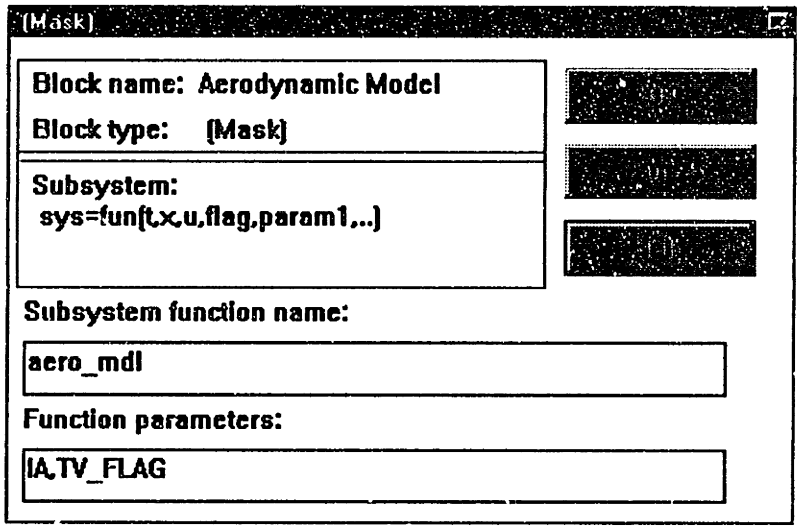

Fig. A-3 Aerodynamic Model Mask

IA	Variable	Description
IA(1)	cbar	Wing mean geometric cord
IA(2)	b	Wing span
IA(3)	mass	Aircraft total mass
IA(4)	deltax	CG shift along the X axis (+forward)
IA(5)	deltay	CG shift along the Y axis (+ right wing)
IA(6)	deltaz	CG shift along the Z axis (+ down)
IA(7)	S	Wing reference area

Tab. A-3 Aerodynamic Mask: function parameters

The aerodynamic forces and moments are then passed to the Forces & Moments block, where they are combined with the forces and moments resulting from the Engine Model to generate the net forces and moments used in the equation of motions.

A-5 Engine Model

The model of the engine was divided in two separate blocks that enter the simulator in two different locations. The first block is the Engine Model and the second block is the Engine Dynamics.

The Engine Model block is the C-Function where the thrust force and moment in body axes are calculated as functions of the Mach number, the altitude, the angle of attack, the throttle position command, and the thrust vectoring angles. This is a feedthrough block, neither discrete nor continuous states are calculated in this block.

Fig. A-4 shows the mask of the engine model. One parameter needs to be passed to this mask.

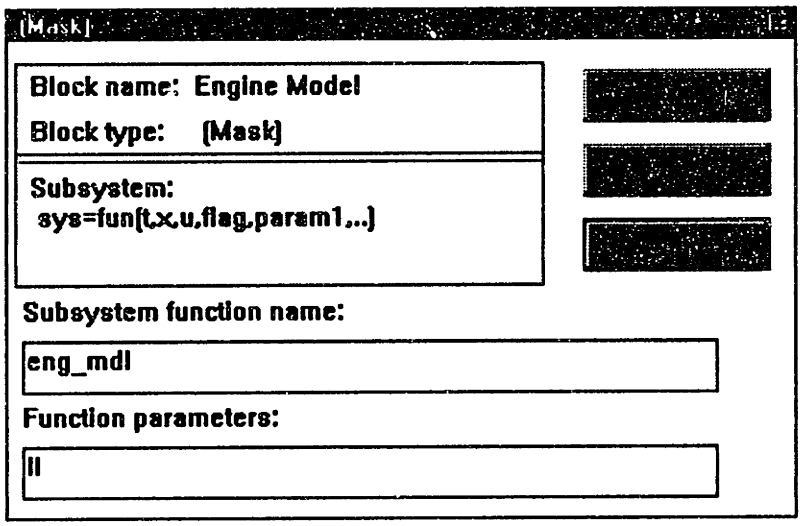

Fig. A-4 Engine Model Mask

The vector *II* is used to pass to the function the geometrical characteristics of the engine. Tab. A-4 describes the entries of the *II* vector.

II	Variable	Description
II(1)	csanxy	Cosine of engine cant
II(2)	snanxy[0]	Sine of left engine cant
II(3)	snanxy[1]	Sine of right engine cant
oII(4)	deltax	CG shift along the X axis (+forward)
II(5)	deltay	CG shift along the Y axis (+ right wing)
II(6)	deltaz	CG shift along the Z axis (+ down)
II(7)	tloc[0]	Point through which left engine thrust passes
II(8)	tloc[1]	Point through which right engine thrust passes

Tab. A-4 Engine Model Mask: Input Vector II

The second function, Engine Dynamics, is used to describe the dynamics of the engine when the throttle command changes with time. This block is formed by a C-Function that implements a simple second order model. In most of the simulations the throttle command remains constant throughout the entire maneuver, for this reason the throttle dynamic block remains unused in most of the cases. A vector with two elements is passed to the mask of the Engine Dynamic block, it contains the initial conditions of the second order system (see Fig. A-5 and Tab. A-5).

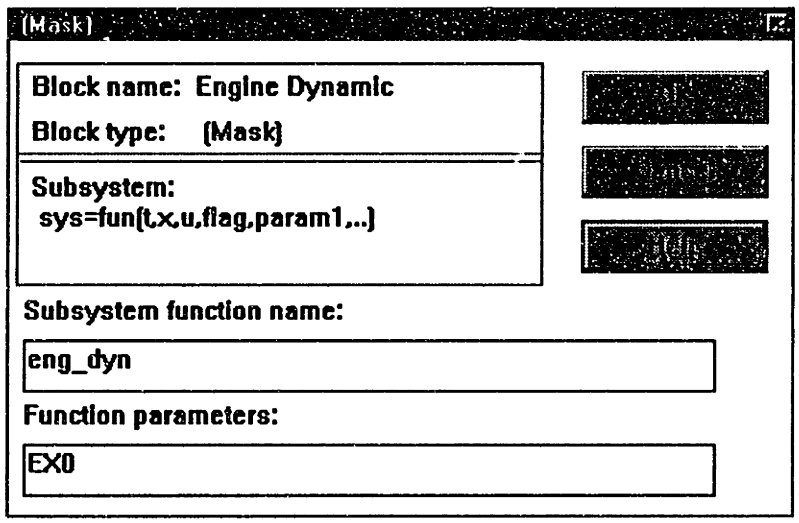

Fig. A-5 Engine Dynamic Mask

II	Variable	Description
EX0(1)	X1(0)	Initial condition
EX0(2)	X2(0)	Initial condition

Tab. A-5 Engine Dynamic Mask: Input Vector EX0

Depending on the actual value of the throttle position, a different time constant and a different level of rate limiting is used.

A-6 Surface Models

In order to model the dynamics of the control surfaces, a set of second and fourth order linear models are implemented in the Surface Models block. The initial conditions of

each state space model are calculated in the initialization routine using the following equation:

$$\underline{x}(0) = -A^{-1}Bu(0) \qquad \text{[A-9]}$$

Where *u(0)* is the initial position of the surface. The state space model describing the dynamics of the surfaces are listed below. With each model is also shown the rate and position limits associated to the particular actuator.

Leading Edge

```
A_LE = [-82.90   26.90;
          0.00  -26.90];
B_LE = [  0.00;
          1.00];
C_LE = [ 82.90    0.00];
D_LE = [  0.00];
Position Limit: +33 + -3 [deg]
Rate Limit: +15 + -15 [deg/sec]
```

Trailing Edge

```
A_TE = 1.0e+03 * [-0.0497  -1.2250;
                    0.0010   0.0000];
B_TE = [  1.00;
          0.00];
C_TE = 1.0e+03 * [ 0.0000   1.2250];
D_TE = [  0.00];
Position Limit: +45 + -8 [deg]
Rate Limit: +18 + -18 [deg/sec]
```

Aileron

```
A_AI = 1.0e+03 * [-0.0885   -5.6250;
                    0.0010    0.0000];
B_AI = [  1.00;
          0.00];
C_AI = 1.0e+03 * [ 0.0000    5.6250];
D_AI = [  0.00];
Position Limit: +45 + -25 [deg]
Rate Limit: +100 + -100 [deg/sec]
```

Horiz. Tail

```
A_LH = [-124.25   -11088.00   -3.58   1069.50;
          1.00        0.00    0.00      0.00;
          0.00        0.00  -29.85  -1325.00;
          0.00        0.00    1.00      0.00];
B_LH = [ 0.1928;  0.0000; 1.0000; 0.0000];
C_LH = [ 0.0000; 11088.0; 0.0000; 0.0000];
D_LH = [ 0.0000];
Position Limit: +10.5 + -24 [deg]
Rate Limit: +40 + -40 [deg/sec]
```

Rudder

```
A_RU = 1.0e+03 * [ -0.099498   -5.19841;
                     0.001000    0.00000];
B_RU = [1.00;
        0.00];
C_RU = 1.0e+03 * [ 0.00  5.19841];
D_RU = [ 0.00];
Position Limit: +30 + -30 [deg]
Rate Limit: +82 + -82 [deg/sec]
```

The positions of the control surfaces are then used in the aerodynamic model to calculate the contribution of each surface to the six dimensionless aerodynamic coefficients.

Fig. A-6 shows the contents of the Surface Models block. It is possible to identify the state space models associated to each surface, the rate limiters and the saturation limits. The **inputs** to the block are the surface commands coming from the Flight Control System while the **outputs** are the actual positions of the surfaces.

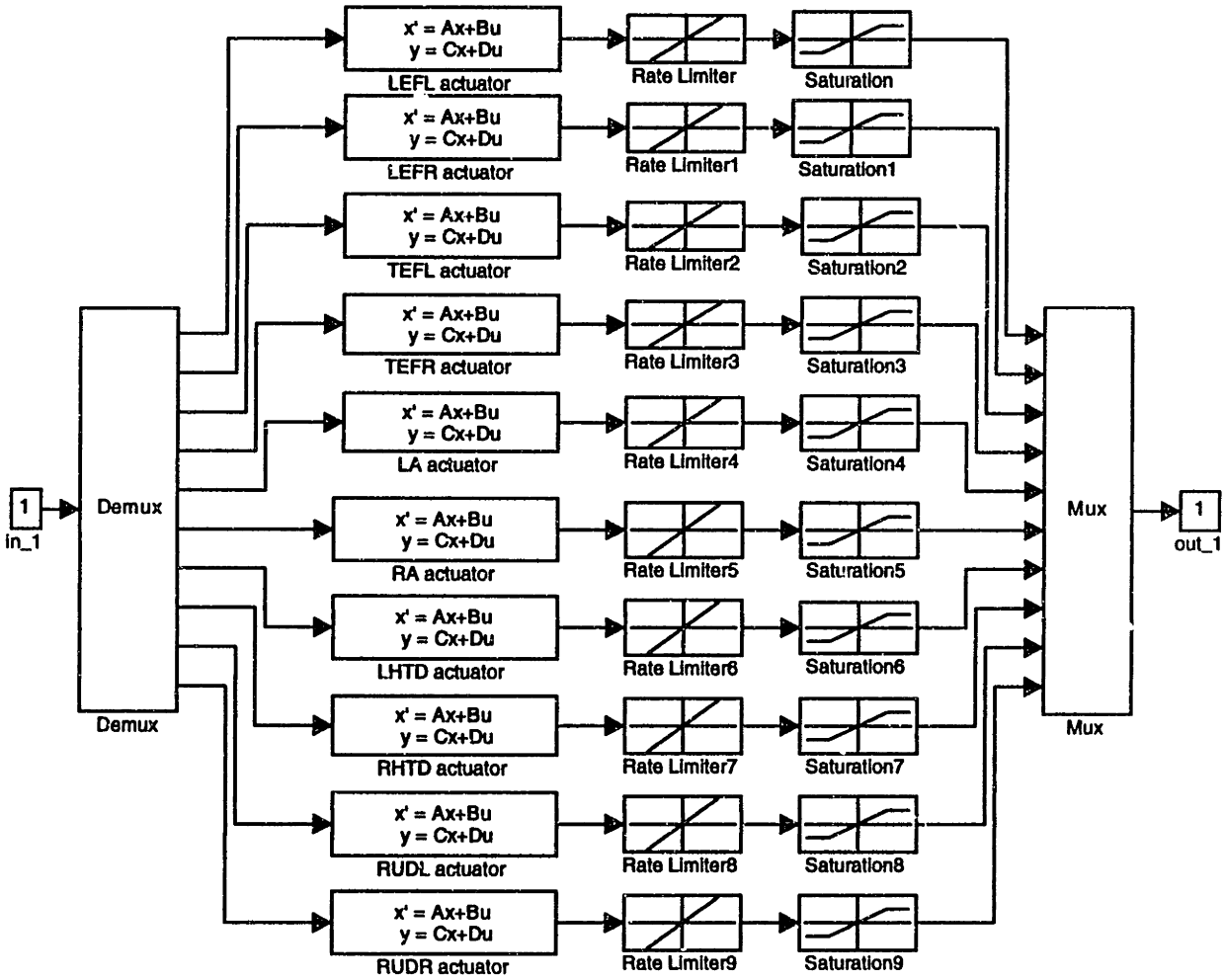

Fig. A-6 Surface Models Simulink Block Diagram

A-7 Additional Output Variables Calculation

In addition to the state variables, a set of additional output variables are calculated at each frame time. This task is performed in the Output block shown in Fig. A-1. No additional parameters need to be passed to the mask of this block. The **inputs** to this

function are the twelve states calculated in the equations of motion block, while the **outputs** are the twelve states and the ten additional variables listed in Tab. A-6. The flight path state variables are calculated from the body state variables as follows:

$$
\begin{aligned}
V &= \left(u^2 + v^2 + w^2\right)^{1/2} \\
\alpha &= \tan^{-1}\left(\frac{w}{u}\right) \\
\beta &= \sin^{-1}\left(\frac{v}{V}\right) \\
\mu &= \tan^{-1}\left(\frac{uv\sin(\vartheta) + (u^2 + w^2)\sin(\varphi)\cos(\vartheta) - vw\cos(\varphi)\cos(\vartheta)}{V(w\sin(\vartheta) + u\cos(\varphi)\cos(\vartheta))}\right) \\
\gamma &= \sin^{-1}\left(\frac{u\sin(\vartheta) - v\sin(\varphi)\cos(\vartheta) - w\cos(\varphi)\cos(\vartheta)}{V}\right)
\end{aligned}
\qquad \text{[A-10]}
$$

In addition to those variables, Mach number, static and dynamic pressure, and two geometric variables used in the aerodynamic model (B2V and C2V) are computed in the output block (see Tab. A-6).

Y	Variable	Description
13	Vt	Total true airspeed [ft/sec]
14	Mach	Mach number
15	alp	Angle of attack [rad]
16	bta	Sideslip angle [rad]
17	qbar	Dynamic pressure [slug/ft/s^2]
18	ps	Static pressure [PSF]
19	B2V	(Wing span)/(2*Vt)
20	C2V	(Mean aerodynamic cord)/(2*Vt)
21	mu	Flight path angle [rad]
22	gma	Angle between flight path and horiz. Plane [rad]

Tab. A-6 Output Function : additional output variables

To calculate the Mach number, the dynamic pressure, and the static pressure a standard atmosphere model is calculated in the Output C-function. The atmosphere model is the same as that implemented by NASA Dryden: a set of look up tables are used to calculate the speed of sound, the air density, the gravity, the ambient static pressure, and the ambient air temperature as a function of the actual altitude.

A-8 Input-Output Variables Summary

In the following tables are listed the input/output variables of each block that comprise the nonlinear simulator.

Block N.1: Engine Dynamics (C-Function)

Input	u[0]: PLAL	Pilot left throttle input	deg
	u[1]: PLAR	Pilot right throttle input	deg
Output	y[0]: pcthlc[0]	Left throttle position command	%
	y[1]: pcthlc[1]	Right throttle position command	%

Block N.2: Variable Distribution (Simulink)

Input Vector 1	Output from "Engine Model" block 3
Input Vector 2	Output from "Output Variables" block 7
Input Vector 3	Output from "Engine Dynamic" block 1
Input Vector 4	Output from "Surface Models" block 8
Output Vector 1	Input vector to "Engine Model" block 3
Output Vector 2	Input vector to "Aerodynamic Model" block 4

Block N.3: Engine Model (C-Function)

Input	u[0]: Mach	Mach number	-
	u[1]: Altitude	Altitude	ft
	u[2]: alpha	Angle of attack	deg
	u[3]: TV_LOSS[0]	Left eng. Thrust loss due to vane defl.	-
	u[4]: TV_LOSS[1]	Right eng. Thrust loss due to vane defl.	-
	u[5]: tvjany[0]	Left engine jet turning angle (xy plane)	deg
	u[6]: tvjany[1]	Right engine jet turning angle (xy plane)	deg
	u[7]: tvjanp[0]	Left engine jet turning angle (xz plane)	deg
	u[8]: tvjanp[1]	Right engine jet turning angle (xz plane)	deg
	u[9]: pcthlc[0]	Left throttle position command	%
	u[10]: pcthlc[1]	Right throttle position command	%
Output	y[0]: thx	Thrust force in x-body axis	[lb]
	y[1]: thy	Thrust force in y-body axis	[lb]
	y[2]: thz	Thrust force in z-body axis	[lb]
	y[3]: thl	Thrust moment around x-body axis	[ft-lb]
	y[4]: thm	Thrust moment around y-body axis	[ft-lb]
	y[5]: thn	Thrust moment around z-body axis	[ft-lb]
	y[6]: FG(1)	Left engine gross thrust	[lbf]
	y[7]: FG(2)	Right engine gross thrust	[lbf]

Block N.4: Aerodynamic Model (C-Function)

Input	u[0]:	Not Used	
	u[1]:	Not Used	
	u[2]:	Not Used	
	u[3]:	Not Used	
	u[4]:	Not Used	
	u[5]:	Not Used	
	u[6]: p	Roll rate	rad/s
	u[7]: q	Pitch rate	rad/s
	u[8]: r	Yaw Rate	rad/s
	u[9]:	Not Used	
	u[10]:	Not Used	
	u[11]: Altitude	Altitude	ft
	u[12]:	Not Used	
	u[13]: mach	Mach number	-
	u[14]: alp	Angle of attack	rad
	u[15]: bta	Sideslip angle	rad
	u[16]: qbar	Dynamic pressure	slug/(ft*s^2)
	u[17]:	Not Used	
	u[18]: B2V	(Wing Span)/(2*Vt)	-
	u[19]: C2V	(Mean Aerodynamic chord)/(2*Vt)	-
	u[20]: alpdot	Angle of attack rate of change	rad/s
	u[21]: dlefl	Left leading edge flap position	deg
	u[22]: dlefr	Right leading edge flap position	deg
	u[23]: dtefl	Left trailing edge flap position	deg
	u[24]: dtefr	Right trailing edge flap position	deg
	u[25]: dlad	Left aileron position	deg
	u[26]: drad	Right aileron position	deg
	u[27]: dlhtd	Left stabilator position	deg
	u[28]: drhtd	Right stabilator position	deg
	u[29]: drudl	Left rudder position	deg
	u[30]: drudr	Right rudder position	deg
	u[31]: FG(1)	Left engine gross thrust	LBF
	u[32]: FG(2)	Right engine gross thrust	LBF
	u[33]: tvjany(0)	Left engine jet turning angle (xy plane)	deg
	u[34]: tvjany(1)	Right engine jet turning angle (xy plane)	deg
	u[35]: tvjanp(0)	Left engine jet turning angle (xz plane)	deg
	u[36]: tvjanp(1)	Right engine jet turning angle (xz plane)	deg
Output	y[0]: CY	Total side force coefficient	-
	y[1]: CL	Total rolling moment coefficient	-
	y[2]: CN	Total yawing moment coefficient	-
	y[3]: CLFT	Total lift coefficient	-
	y[4]: CM	Total pitching moment coefficient	-
	y[5]: CD	Total drag force coefficient	-
	y[6]: FXAR	Body x-axis force at aero reference	slug*ft/s^2
	y[7]: FYAR	Body y-axis force at aero reference	slug*ft/s^2
	y[8]: FZAR	Body z-axis force at aero reference	slug*ft/s^2
	y[9]: LAR	Aero rolling moment in body x-axis	slug*ft^2/s^2
	y[10]: MAR	Aero pitching moment in body x-axis	slug*ft^2/s^2
	y[11]: NAR	Aero yawing moment in body x-axis	slug*ft^2/s^2

Block N.5: Forces and Moments (Simulink)

Input Vector 1	u[0]: thx	Thrust force in x-body axis	[lb]
	u[1]: thy	Thrust force in y-body axis	[lb]
	u[2]: thz	Thrust force in z-body axis	[lb]
	u[3]: thl	Thrust moment around x-body axis	[ft-lb]
	u[4]: thm	Thrust moment around y-body axis	[ft-lb]
	u[5]: thn	Thrust moment around z-body axis	[ft-lb]
Input Vector 2	y[6]: FG(1)	Left engine gross thrust	[lbf]
	y[7]: FG(2)	Right engine gross thrust	[lbf]
	u2[2]: FZAR	Body z-axis force at aero reference	slug*ft/s^2
	u2[3]: LAR	Aero rolling moment in body x-axis	slug*ft^2/s^2
	u2[4]: MAR	Aero pitching moment in body x-axis	slug*ft^2/s^2
	u2[5]: NAR	Aero yawing moment in body x-axis	slug*ft^2/s^2
Output	y[0]: Fx	Net applied force in the x body axis	slug*ft/s^2
	y[1]: Fy	Net applied force in the y body axis	slug*ft/s^2
	y[2]: Fz	Net applied force in the z body axis	slug*ft/s^2
	y[3]: L	Rolling moment	slug*ft^2/s^2
	y[4]: M	Pitching moment	slug*ft^2/s^2
	y[5]: N	Yawing moment	slug*ft^2/s^2

Block N.6: Equation of Motion: six-dof

Input	u[0]: Fx	Net applied force in the x body axis	slug*ft/s^2
	u[1]: Fy	Net applied force in the y body axis	slug*ft/s^2
	u[2]: Fz	Net applied force in the z body axis	slug*ft/s^2
	u[3]: L	Rolling moment	slug*ft^2/s^2
	u[4]: M	Pitching moment	slug*ft^2/s^2
	u[5]: N	Yawing moment	slug*ft^2/s^2
Output	y[0]: U	Velocity in x body axis	ft/s
	y[1]: V	Velocity in y body axis	ft/s
	y[2]: W	Velocity in z body axis	ft/s
	y[3]: phi	Euler roll angle	rad
	y[4]: theta	Euler pitch angle	rad
	y[5]: psi	Euler yaw angle	rad
	y[6]: p	Roll rate	rad/s
	y[7]: q	Pitch rate	rad/s
	y[8]: r	Yaw rate	rad/s
	y[9]: pos_nord	Position Nord	ft
	y[10]: pos_east	Position East	ft
	y[11]: altitude	Altitude	ft

Block N.7: Output Variables

Input	u[0]: U	Velocity in x body axis	ft/s
	u[1]: V	Velocity in y body axis	ft/s
	u[2]: W	Velocity in z body axis	ft/s
	u[3]: phi	Euler roll angle	rad
	u[4]: theta	Euler pitch angle	rad
	u[5]: psi	Euler yaw angle	rad
	u[6]: p	Roll rate	rad/s
	u[7]: q	Pitch rate	rad/s
	u[8]: r	Yaw rate	rad/s
	u[9]: pos_nord	Position Nord	ft
	u[10]: pos_east	Position East	ft
	u[11]: altitude	Altitude	ft
Output	y[0]: U	Velocity in x body axis	ft/s
	y[1]: V	Velocity in y body axis	ft/s
	y[2]: W	Velocity in z body axis	ft/s
	y[3]: phi	Euler roll angle	rad
	y[4]: theta	Euler pitch angle	rad
	y[5]: psi	Euler yaw angle	rad
	y[6]: p	Roll rate	rad/s
	y[7]: q	Pitch rate	rad/s
	y[8]: r	Yaw rate	rad/s
	y[9]: pos_nord	Position Nord	ft
	y[10]: pos_east	Position East	ft
	y[11]: altitude	Altitude	ft
	y[12]: Vt	Total true airspeed	ft/s
	y[13]: Mach	Mach number	-
	y[14]: alp	Angle of attack	rad
	y[15]: bta	Sideslip angle	rad
	y[16]: qbar	Dynamic pressure	slug/(ft*s^2)
	y[17]: ps	Static pressure	PSF
	y[18]: B2V	(Wing Span)/(2*Vt)	-
	y[19]: C2V	(Mean Aerodynamic chord)/(2*Vt)	-
	y[20]: mu	Flight path angle	rad
	y[21]: gamma	Angle between mu and horizontal plane	rad

Block N.8: Surface Models (Simulink)

Input	u[]: vlefl	Left leading edge command	deg
	u[]: vlefr	Right leading edge command	deg
	u[]: vtefl	Left trailing edge command	deg
	u[]: vtefr	Right trailing edge command	deg
	u[]: vcasail	Left aileron command	deg
	u[]: vcasair	Right aileron command	deg
	u[]: vcashtl	Left stabilator command	deg
	u[]: vcashtr	Right stabilator command	deg
	u[]: vcasrdl	Left rudder command	deg
	u[]: vcasrdr	Right rudder command	deg
Output	y[]: dlefl	Left leading edge position	deg
	y[]: dlefr	Right leading edge position	deg
	y[]: dtefl	Left trailing edge position	deg
	y[]: dtefr	Right trailing edge position	deg
	y[]: dlad	Left aileron position	deg
	y[]: drad	Right aileron position	deg
	y[]: dlhtd	Left stabilator position	deg
	y[]: drhtd	Right stabilator position	deg
	y[]: drudl	Left rudder position	deg
	y[]: drudr	Right rudder position	deg

A-9 SimSim Verification

The SimSim performances were verified using two different types of tests. First a series of lateral and longitudinal maneuvers were performed and the time domain responses were compared to those obtained using the actual NASA Dryden nonlinear flight simulator. Then the response of SimSim to longitudinal and lateral experimental doublets at different altitudes and Mach numbers were compared to the real flight data and to the NASA simulator.

The simulator was run in open loop because in the test we wanted to verify the fidelity of the model of the aircraft only, not of the closed loop system. The open loop plant was driven with the surface commands recorded during the simulation at NASA Dryden.

A-9.1 Pitch Doublets

Several pitch doublets were performed at different Mach numbers and altitudes. In all cases there was an almost perfect match between SimSim and the NASA Dryden Flight Simulator. A summary of the results of the test can be found in Ref. A-4.

A-9.2 Roll Doublets

Roll doublets were also performed in order to compare the lateral directional response of the two simulators. Once again the responses are very similar, almost indistinguishable. A summary of the results of the test can be found in Ref. A-4.

A-9.3 Longitudinal and lateral flight doublets

In order to compare the results of the SimSim simulator with real flight data, a series of pitch and roll doublets at different Mach numbers and altitudes were performed on the F/A-18 SRA. The F-18 SRA is instrumented to record all data necessary to run the open loop SimSim simulator. All the commands to the aerodynamic surfaces and the engine power levels are recorded during flight. These input data were used to run the open loop SimSim.

A description of these tests is give in Ref. A-4. There is a good correspondence between flight data and SimSim data on the axis were the maneuver is performed. Unfortunately there are some annoying discrepancies in the coupling between lateral and longitudinal axes. When a pitch maneuver is performed, there are differences in the lateral states between flight data and simulation data. The same thing happens when a pure roll maneuver is performed. The responses of SimSim are identical to those of NASA simulator but both are different from flight in terms of axis coupling.

A-10 Calculation of Linearized Models

It modern control theory it is often necessary to linearize a nonlinear model around one or several operating points. Built into the Simulink toolbox is a function called *linmod('system')* that allows the linearization of nonlinear plants described as Simulink block diagrams around a defined operating point. In this paragraph we are going to describe how

easily one can calculate a linearized model of the aircraft using SimSim and the function *linmod*. We will also show how the response of the linearized model compares to the response of the nonlinear simulator in the case of a longitudinal pulse input.

The first thing is to define the inputs and outputs of the linear model and to eliminate the states that we don't want to take into account in the linearization. Considering that the actuators' states are already defined in terms of state space models there is no reason to include the block *Surface Models* in the linearization. The linearized model can easily be augmented with the actuator states after the linearization is performed. Due to the fact that most of the control system design is done with fixed throttle also the "engine dynamics" can be omitted from the linear model.

The states and controls are then defined as follows:

$$\underline{x} = [\, q \quad u \quad w \quad \vartheta \quad h \quad p \quad r \quad \beta \quad \varphi \quad \psi \quad Y \quad N] \qquad \text{[A-11]}$$

$$\underline{u} = [\delta_{Ald} \quad \delta_{HTd} \quad \delta_{LEd} \quad \delta_{TEd} \quad \delta_{RDd} \quad \delta_{HTs} \quad \delta_{LEs} \quad \delta_{TEs}] \qquad \text{[A-12]}$$

The subscript *d* used in the control variables stands for differential and identifies the lateral/directional controls while the subscript *s* stands for symmetrical and identifies the longitudinal controls. All the angles are expressed in degrees, the altitude in ft, and the velocity in ft/sec. The linearized model is defined in the standard form:

$$\begin{aligned} \dot{\underline{x}}(t) &= A\underline{x}(t) + B\underline{u}(t) \\ \underline{y}(t) &= C\underline{x}(t) + D\underline{u}(t) \end{aligned} \qquad \text{[A- 13]}$$

The Simulink block diagram used in the linearization is shown in Fig. A-7. There are eight in-ports that correspond to the control inputs defined in equation A-12. The block called *States* in Fig. A-7 selects the output variables so that the eleven states defined in equation A-11 appear at the out-ports.

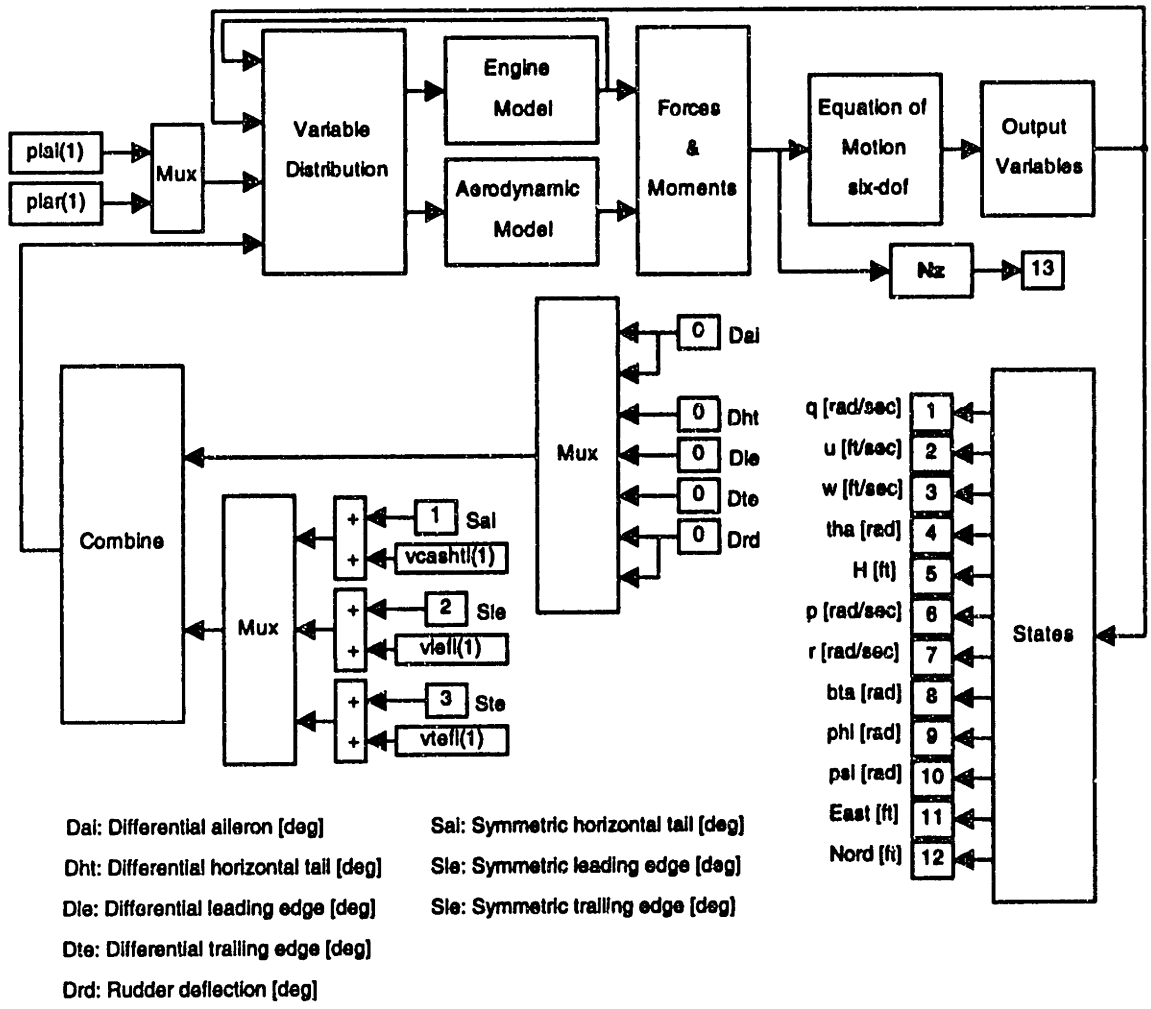

Fig. A-7 Simulink block diagram used for the linearization

As an example we will calculate the linearized models at the flight conditions listed in the following table and then we will show how the response of the linear model to a pulse in the longitudinal axis compare with the response of the nonlinear simulator.

Point	Mach	Altitude [ft]
1	0.6	15000
2	0.7	20000
3	0.7	30000
4	0.8	35000

Tab. A-7 Flight points used for linearization

The longitudinal states are the first five states in equation A-11 and the longitudinal control are the last three variables in the control vector of equation A-12. In addition to the longitudinal states is also necessary to feedback to the longitudinal control augmentation system also the normal acceleration N_z. For this reason the normal acceleration output is added in the outport 13 of Fig. A-7. So the output of the linearized model is be composed of the five longitudinal states plus the normal acceleration.

The longitudinal state space models calculated at the flight conditions listed above are shown in the following tables.

Flight Point N.1 : Mach 0.6 Altitude 15,000 ft

$$\begin{bmatrix} A & B \\ C & D \end{bmatrix} = \left[\begin{array}{ccccc:ccc} -0.3375 & 0.0002 & -0.0073 & 0 & 0.0000 & -0.1475 & -0.0163 & 0.0159 \\ -35.3995 & -0.0089 & 0.0593 & -31.8109 & 0.0000 & 0.0372 & 0.0225 & -0.0278 \\ 629.2496 & -0.0688 & -0.8478 & -1.9627 & 0.0010 & -1.6445 & 0.2585 & -1.8847 \\ 1.0000 & 0 & 0 & 0 & 0 & 0 & 0 & 0 \\ 0 & 0.0562 & -0.9984 & 399.9606 & 0 & 0 & 0 & 0 \\ \hdashline -.0000 & 0 & 0 & 0 & 0 & 0 & 0 & 0 \\ 0 & 1.0000 & 0 & 0 & 0 & 0 & 0 & 0 \\ 0 & 0 & 1.0000 & 0 & 0 & 0 & 0 & 0 \\ 0 & 0 & 0 & 1.0000 & 0 & 0 & 0 & 0 \\ 0 & 0 & 0 & 0 & 1.0000 & 0 & 0 & 0 \\ 0.1291 & 0.0021 & 0.0264 & 0 & 0.0000 & 0.0512 & -0.0080 & 0.0586 \end{array}\right]$$

Flight Point N.2 : Mach 0.7 Altitude 20,000 ft

$$\begin{bmatrix} A & B \\ C & D \end{bmatrix} = \left[\begin{array}{ccccc:ccc} -0.3499 & 0.0002 & -0.0075 & 0 & 0.0000 & -0.1690 & -0.0213 & 0.0186 \\ -35.3404 & -0.0068 & 0.0538 & -31.8410 & 0.0000 & 0.0592 & 0.0334 & 0.0029 \\ 720.8548 & -0.0611 & -0.8640 & -1.7158 & 0.0010 & -1.8147 & 0.2734 & -2.0911 \\ 1.0000 & 0 & 0 & 0 & 0 & 0 & 0 & 0 \\ 0 & 0.0490 & -0.9988 & 388.1785 & 0 & 0 & 0 & 0 \\ \hdashline 1.0000 & 0 & 0 & 0 & 0 & 0 & 0 & 0 \\ 0 & 1.0000 & 0 & 0 & 0 & 0 & 0 & 0 \\ 0 & 0 & 1.0000 & 0 & 0 & 0 & 0 & 0 \\ 0 & 0 & 0 & 1.0000 & 0 & 0 & 0 & 0 \\ 0 & 0 & 0 & 0 & 1.0000 & 0 & 0 & 0 \\ 0.1281 & 0.0019 & 0.0269 & 0 & 0.0000 & 0.0565 & -0.0085 & 0.0651 \end{array}\right]$$

Flight Point N.3 : Mach 0.7 Altitude 30,000 ft

$$\begin{bmatrix} A & B \\ C & D \end{bmatrix} = \left[\begin{array}{ccccc:ccc} -0.2327 & 0.0001 & -0.0042 & 0 & 0.0000 & -0.1099 & -0.0153 & 0.0124 \\ -50.9995 & -0.0009 & 0.0175 & -31.7308 & -0.0001 & 0.0137 & 0.0706 & -0.0422 \\ 691.8357 & -0.0643 & -0.5822 & -2.5646 & 0.0011 & -1.1918 & 0.1660 & -1.3354 \\ 1.0000 & 0 & 0 & 0 & 0 & 0 & 0 & 0 \\ 0 & 0.0735 & -0.9973 & 394.2306 & 0 & 0 & 0 & 0 \\ \hdashline 1.0000 & 0 & 0 & 0 & 0 & 0 & 0 & 0 \\ 0 & 1.0000 & 0 & 0 & 0 & 0 & 0 & 0 \\ 0 & 0 & 1.0000 & 0 & 0 & 0 & 0 & 0 \\ 0 & 0 & 0 & 1.0000 & 0 & 0 & 0 & 0 \\ 0 & 0 & 0 & 0 & 1.0000 & 0 & 0 & 0 \\ 0.0830 & 0.0020 & 0.0181 & 0 & 0.0000 & 0.0371 & -0.0052 & 0.0415 \end{array}\right]$$

Flight Point N.4 : Mach 0.8 Altitude 35,000 ft

$$\begin{bmatrix} A & B \\ C & D \end{bmatrix} = \left[\begin{array}{cccccc:ccc} -0.2328 & -0.0014 & -0.0051 & 0 & 0.0000 & -0.1181 & -0.0189 & 0.0133 \\ -52.2569 & -0.0048 & 0.0400 & -31.7603 & -0.0001 & 0.0072 & 0.0778 & -0.0477 \\ 774.0359 & -0.0697 & -0.5699 & -2.3510 & 0.0012 & -1.2327 & 0.1605 & -1.3776 \\ 1.0000 & 0 & 0 & 0 & 0 & 0 & 0 & 0 \\ 0 & 0.0673 & -0.9977 & 372.2033 & 0 & 0 & 0 & 0 \\ \hdashline 1.0000 & 0 & 0 & 0 & 0 & 0 & 0 & 0 \\ 0 & 1.0000 & 0 & 0 & 0 & 0 & 0 & 0 \\ 0 & 0 & 1.0000 & 0 & 0 & 0 & 0 & 0 \\ 0 & 0 & 0 & 1.0000 & 0 & 0 & 0 & 0 \\ 0 & 0 & 0 & 0 & 1.0000 & 0 & 0 & 0 \\ 0.0792 & 0.0022 & 0.0177 & 0 & 0.0000 & 0.0383 & -0.0050 & 0.0429 \end{array}\right]$$

Once the linearized model has been calculated we can simply create a new Simulink block diagram where instead of the nonlinear simulator we have a linear state space model of the longitudinal dynamics. Some attention must be put in connecting and feeding back the correct variables, but at the end we obtain the block diagram of Fig. A-8.

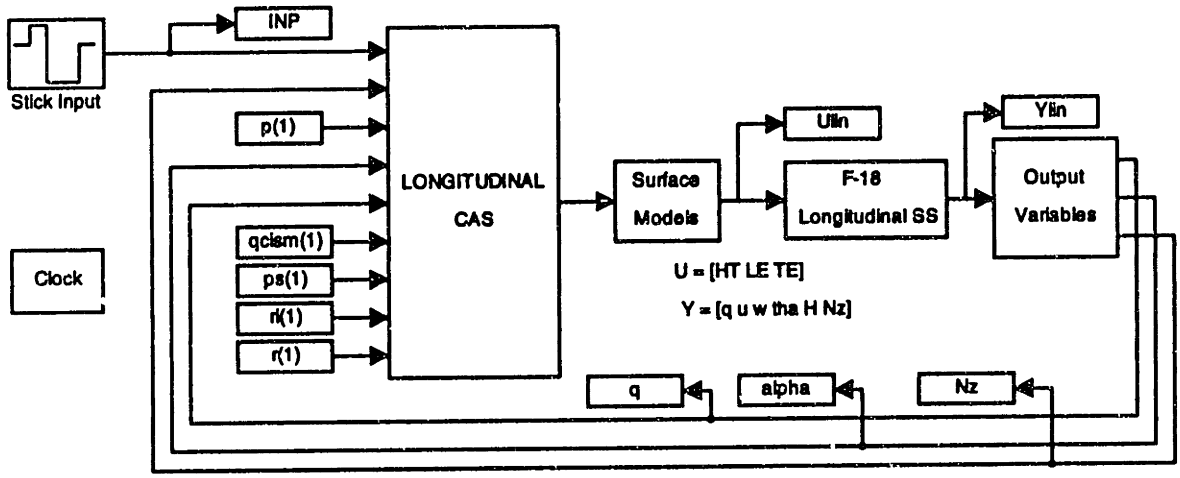

Fig. A-8 Longitudinal Linearized Closed Loop Simulink Block Diagram

In order to show how the linear model compares with the nonlinear model a pulse stick input was simulated at each of the flight point. Fig. A-9 and Fig. A-10 show the time domain responses obtained at flight point 1 and 4 of Tab. A-7. The solid line represent the linear simulation while the dotted line the nonlinear sim. We can see how in general the response of the linear sim follows the one of the nonlinear simulator. At low angle of attack (high altitude and mach) it is almost impossible to distinguish between the two.

With this example we wanted to give only a qualitative idea of how the nonlinear sim can be used for a variety of tasks. The main idea is to have a versatile flight simulator that can

be easily used in flight control law synthesis and analysis. One of the great advantage is the possibility to break the loop in many different points, ask for the linear models of only portion of the overall simulator, inject signal at different locations, test system identification technique, test different control laws, and simulate a variety of maneuvers. We believe that with this flight simulator we have combined the high fidelity of the NASA Dryden flight simulator with all the different capabilities of a modern language as Matlab and Simulink dedicated to control systems analysis and design.

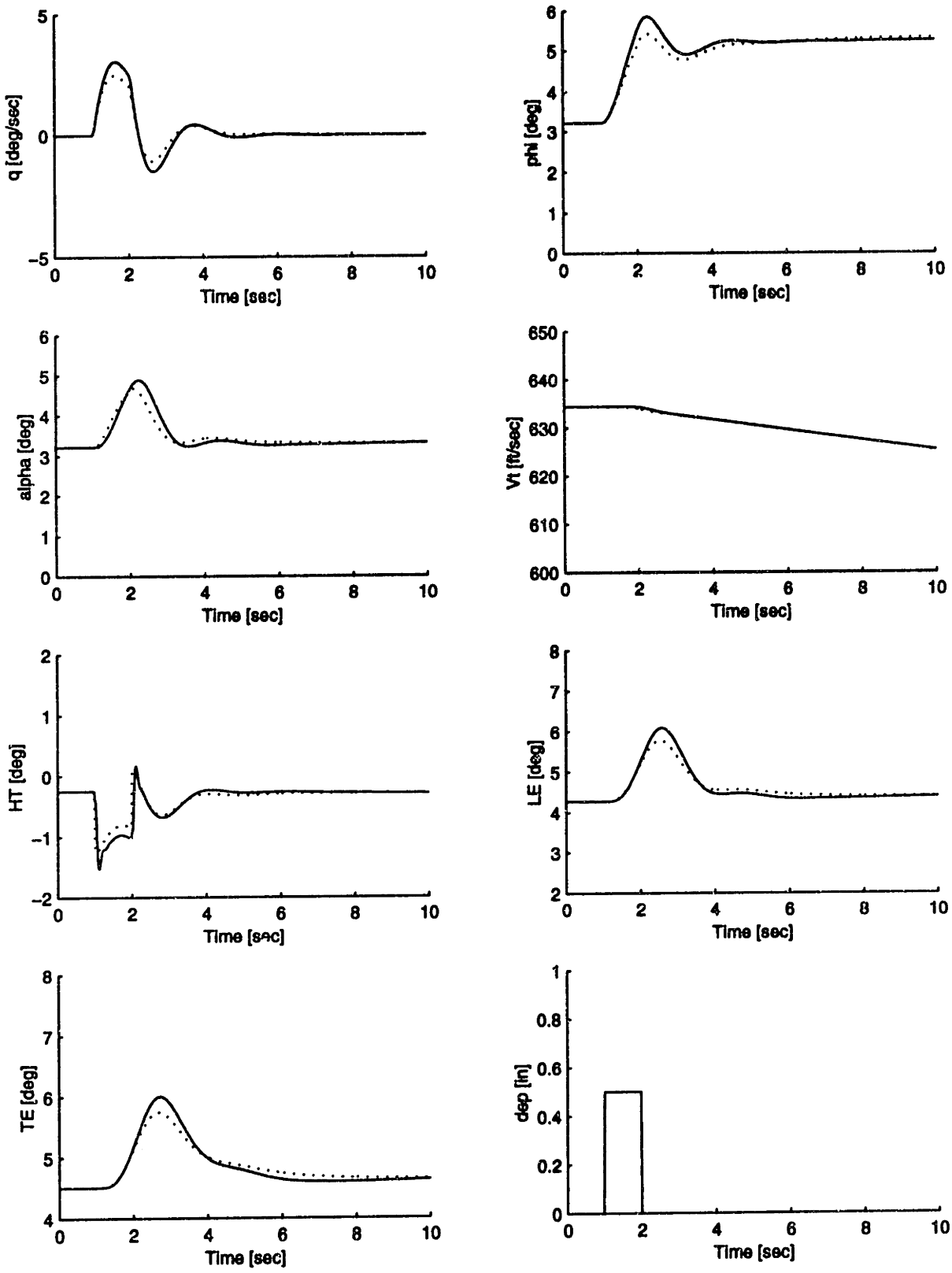

Fig. A-9 Pitch Pulse Response. Mach 0.6 - Altitude 15,000.

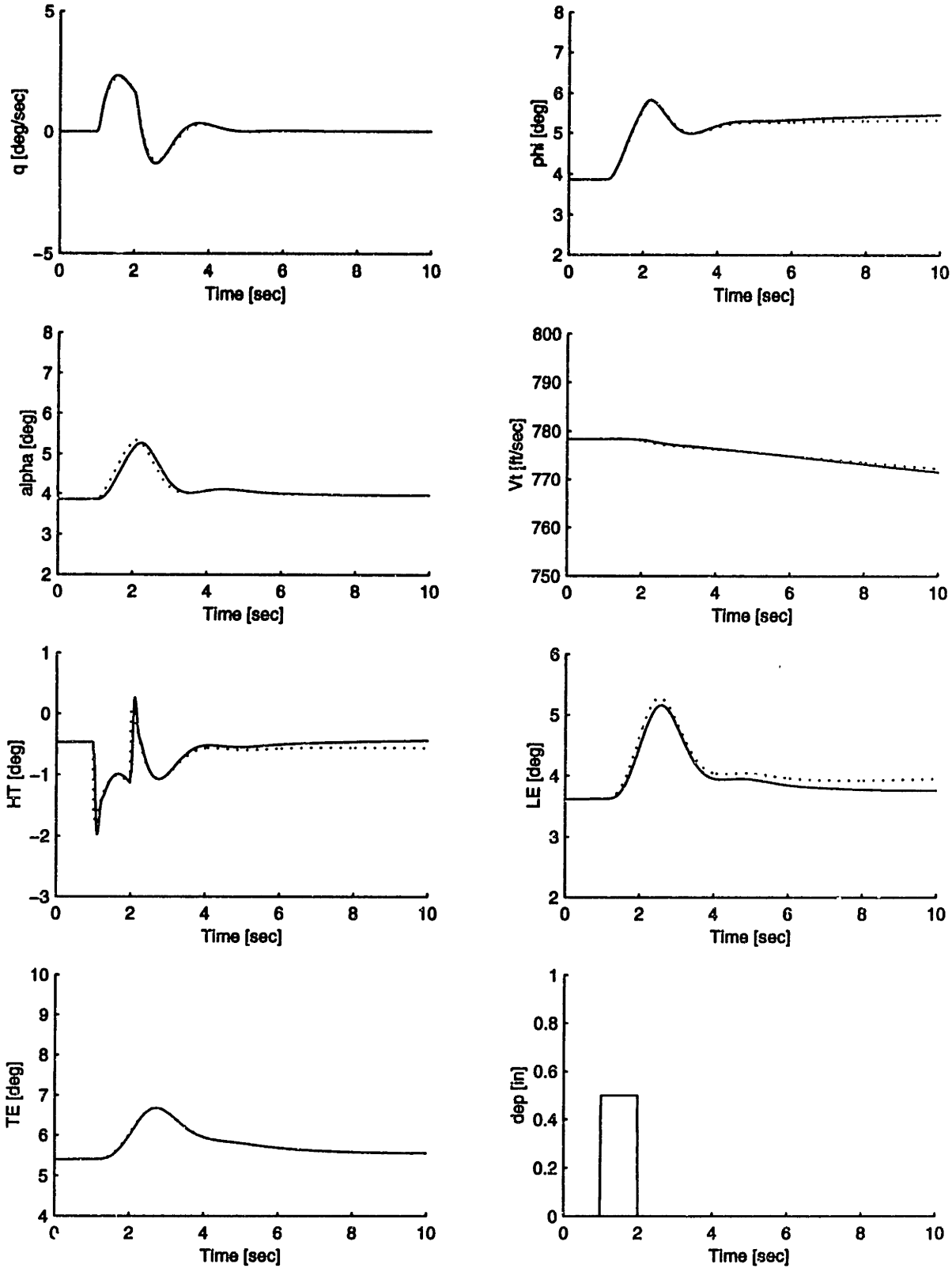

Fig. A-10 Pitch Pulse Response. Mach 0.8 - Altitude 35,000.

A-11 Reference

Ref. A-1 Brian L. Stevens and Frank L. Lewis, *Aircraft Control and Simulation*, John Wiley and Sons, Inc., 1992.

Ref. A-2 R. E. Mc Farland, "A standard kinematic model for flight simulation at NASA Ames," NASA CR-2497, NASA, Washington, D.C., Jan. 1975.

Ref. A-3 D. McRuer, I. Ashkenas, and D. Graham, *Aircraft Dynamics and Automatic Control*, Princeton University Press, Princeton, New Jersey, 1973.

Ref. A-4 P. Miotto and J. D. Paduano, "Nonlinear F/A-18 Simulator for Matlab and Simulink", MIT ICE Lab Internal Note, January 1997.

This page intentionally left blank.

Appendix B

F/A-18 CAS Gain Scheduling

This appendix contains the gain scheduling of the F/A-18 CAS. The scheduling functions resulting from the optimization are shown in their mathematical forms and simulink block diagram implementations. Plots of the gain scheduling as function of static and dynamic pressure are also furnished. These plots show: the original scheduling curve (thick solid line), the new gain scheduling (thin solid line), the optimal gains resulting from a single point design (circles).

The following gains are plotted:

- PK15 Pitch Stick Gain
- PK16 Normal Acceleration Proportional Gain
- PK18 Pitch Rate Proportional Gain
- RK5 Lateral Stick Gain
- RK6 Roll Rate Feedback Gain
- YK13 Lateral Acceleration gain
- YK17 Yaw Rate Feedback Gain
- YK19 Pedal Increment GAIN

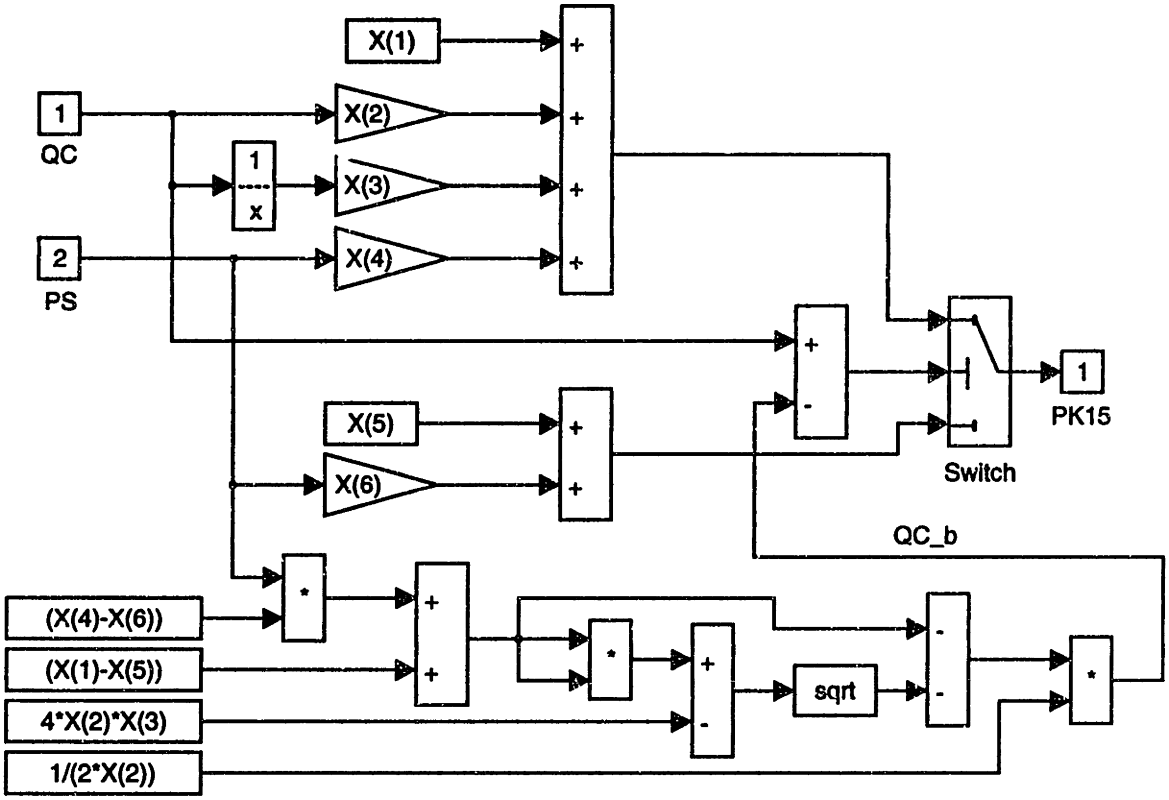

X(1) = -0.0143
X(2) = 1.4721e-005
X(3) = 166.5867
X(4) = -3.2529e-006
X(5) = 0.7000
X(6) = 5.4867e-005

$$PK15 = \begin{cases} X_1 + X_2 * QC + \dfrac{X_3}{QC} + X_4 * PS & QC \geq QC_b \\ X_5 + X_6 * PS & QC < QC_b \end{cases}$$

$$QC_b = \frac{-[(X_1 - X_5) + (X_4 - X_6)PS] - \sqrt{[(X_1 - X_5) + (X_4 - X_6)PS]^2 - 4X_2X_3}}{2X_2}$$

Fig. B-1 PK15: Pitch stick proportional gain, new gain scheduling

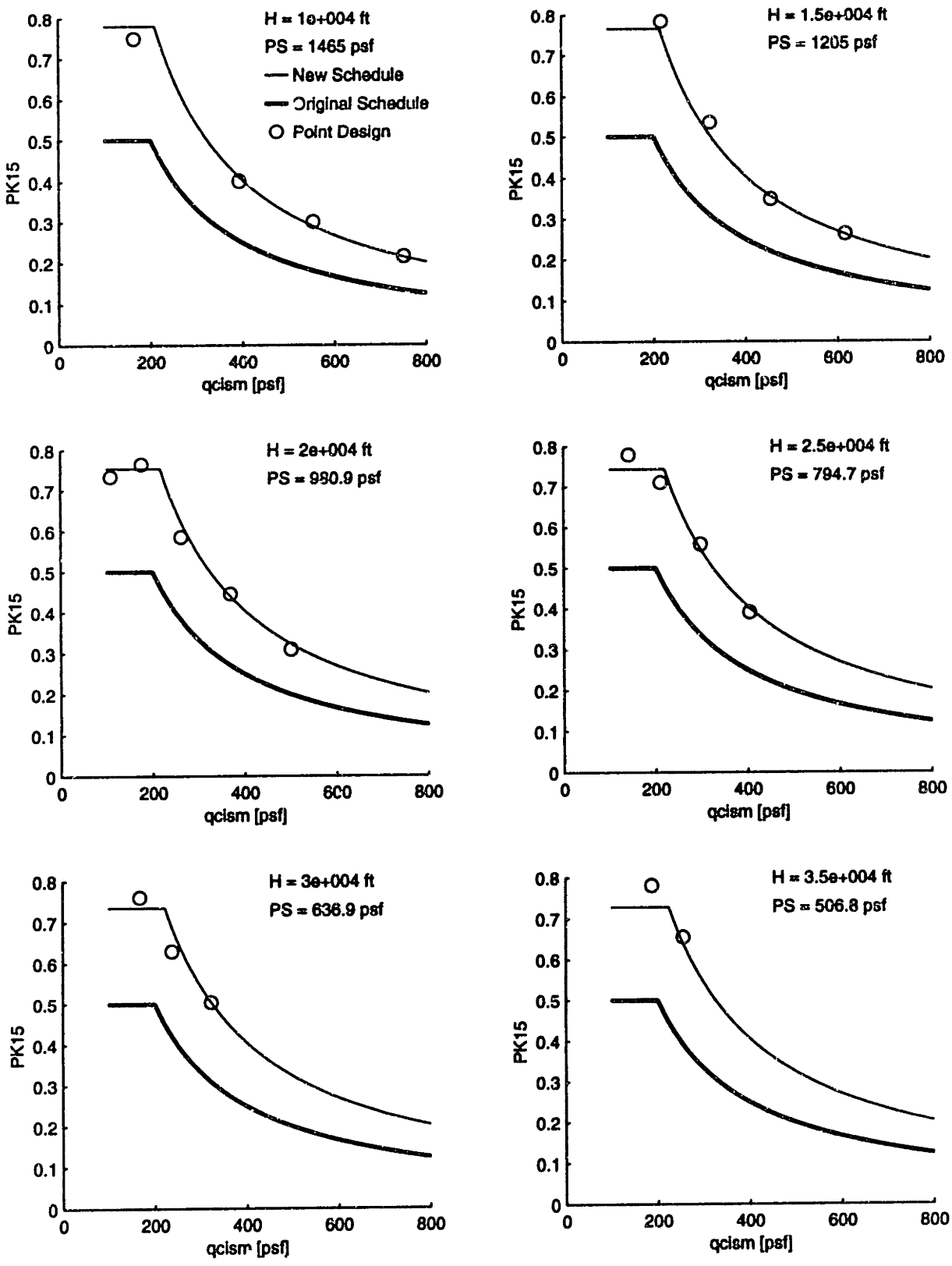

Fig. B-2 PK15: Pitch Stick Proportional Gain Scheduling

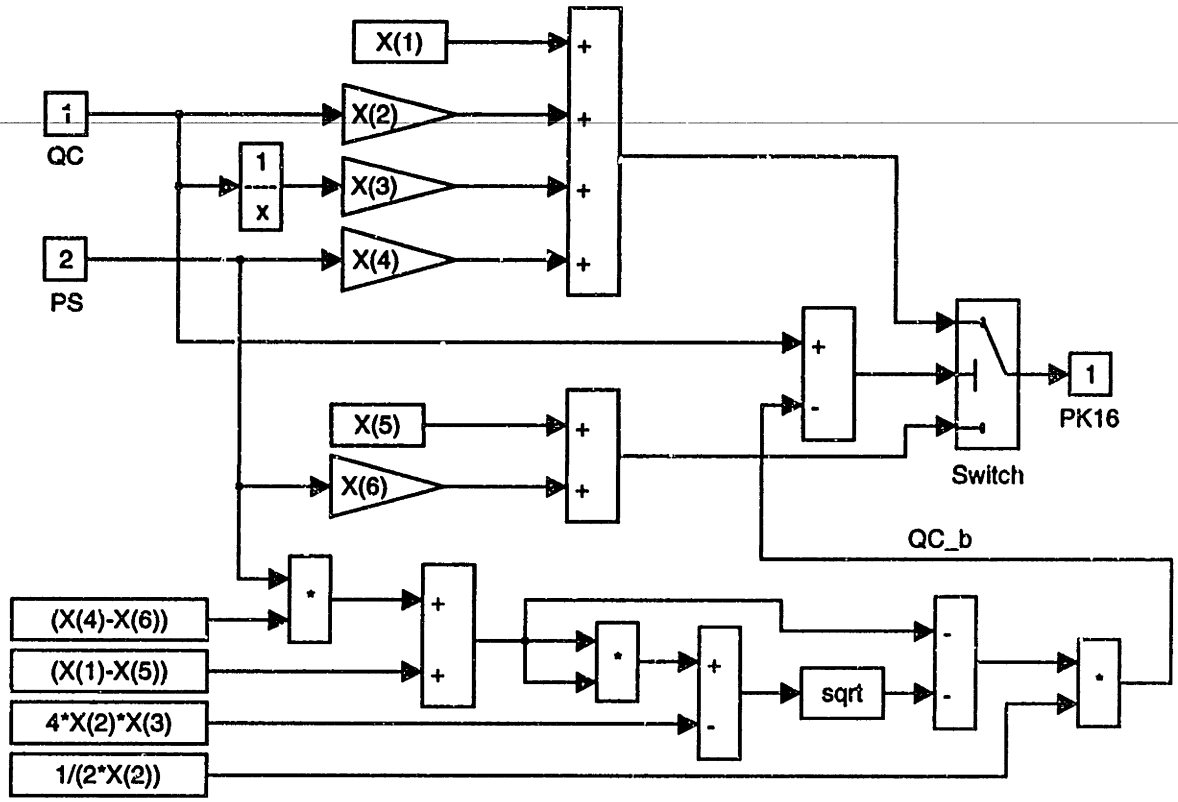

X(1) = -0.5009

X(2) = 3.1995e-004

X(3) = 778.3791

X(4) = -1.0800e-004

X(5) = 3.5490

X(6) = -2.3229e-004

$$PK16 = \begin{cases} X_1 + X_2 * QC + \dfrac{X_3}{QC} + X_4 * PS & QC \geq QC_b \\ X_5 + X_6 * PS & QC < QC_b \end{cases}$$

$$QC_b = \frac{-[(X_1 - X_5) + (X_4 - X_6)PS] - \sqrt{[(X_1 - X_5) + (X_4 - X_6)PS]^2 - 4X_2X_3}}{2X_2}$$

Fig. B-3 PK16: Normal acceleration proportional gain, new gain scheduling

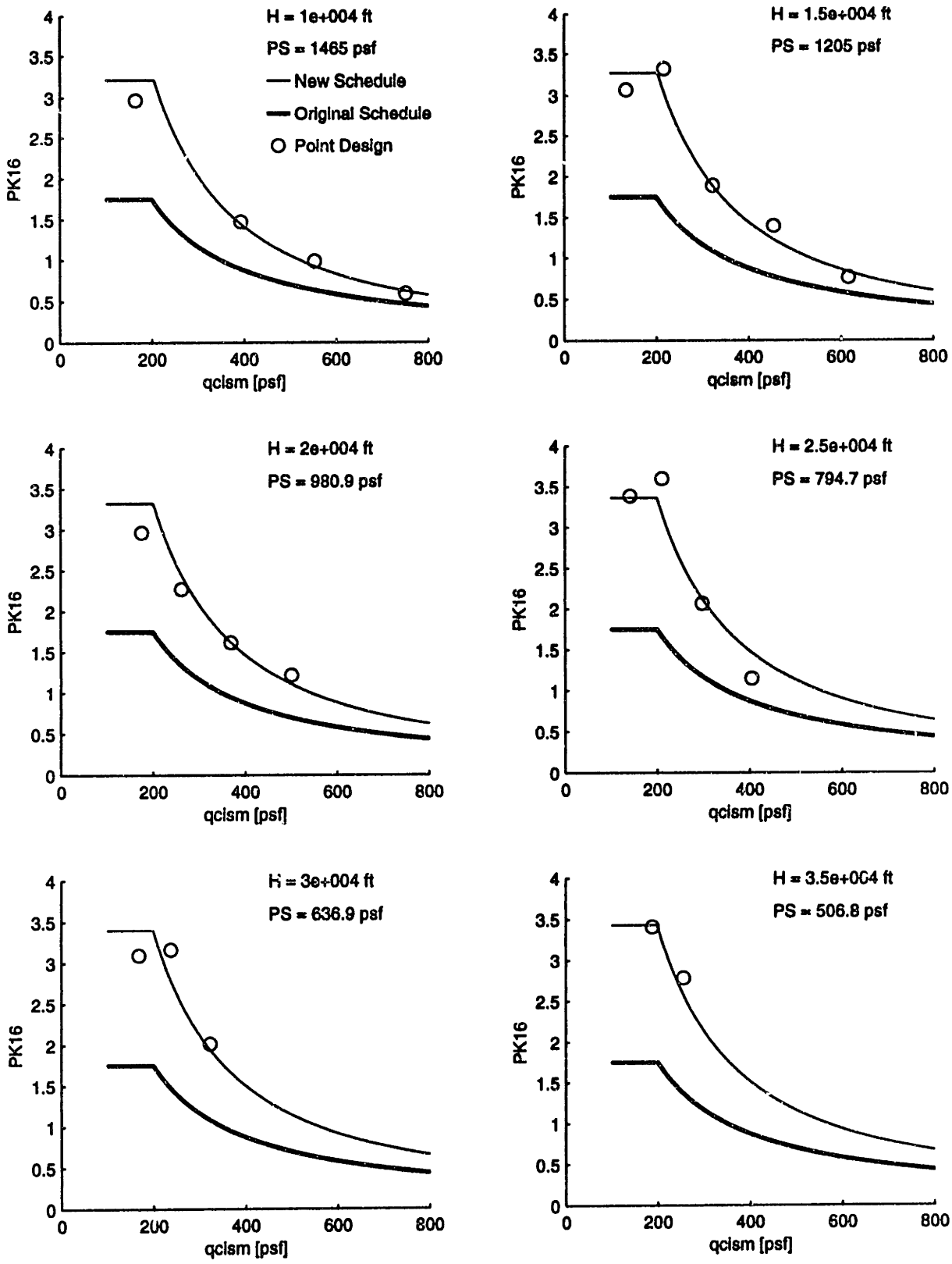

Fig. B-4 PK16: Normal Acceleration Proportional Gain Scheduling

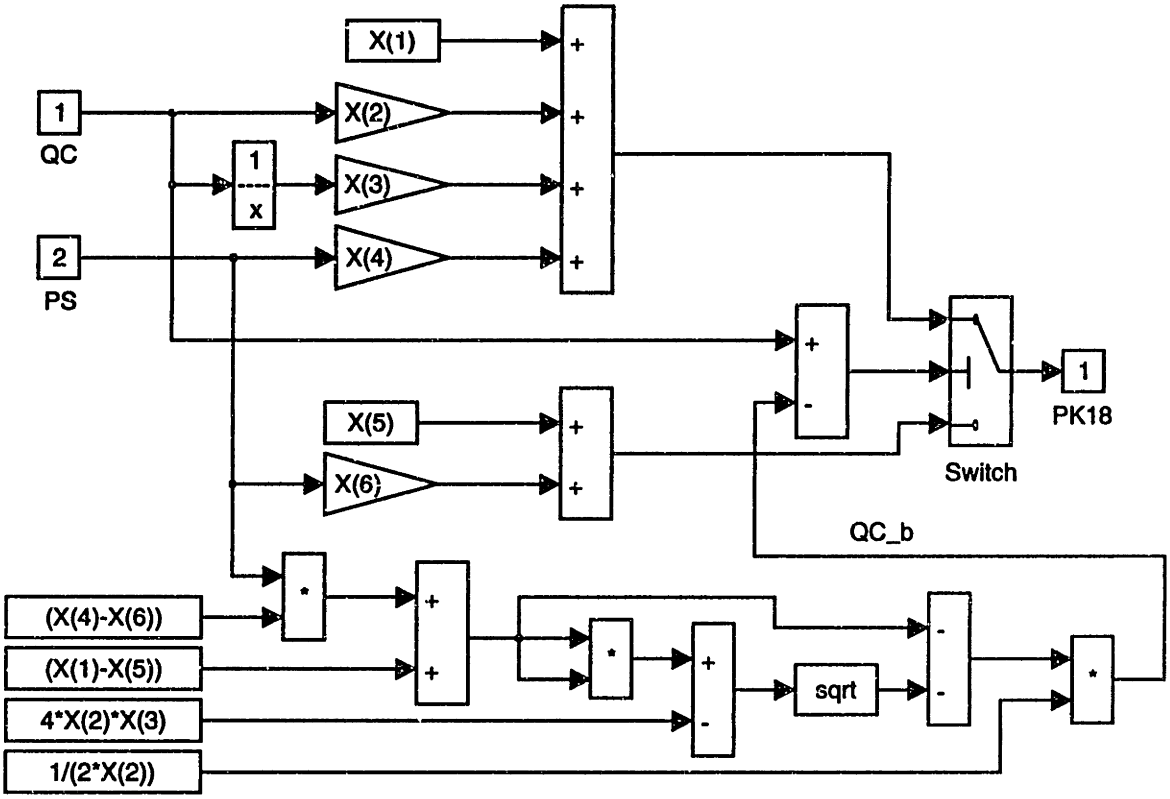

X(1) = -0.1147
X(2) = 4.3174e-004
X(3) = 181.0792
X(4) = -1.3898e-004
X(5) = 0.7678
X(6) = -9.7602e-005

$$PK18 = \begin{cases} X_1 + X_2 * QC + \dfrac{X_3}{QC} + X_4 * PS & QC \geq QC_b \\ X_5 + X_6 * PS & QC < QC_b \end{cases}$$

$$QC_b = \frac{-[(X_1 - X_5) + (X_4 - X_6)PS] - \sqrt{[(X_1 - X_5) + (X_4 - X_6)PS]^2 - 4X_2X_3}}{2X_2}$$

Fig. B-5 PK18: Pitch rate proportional gain, new gain scheduling

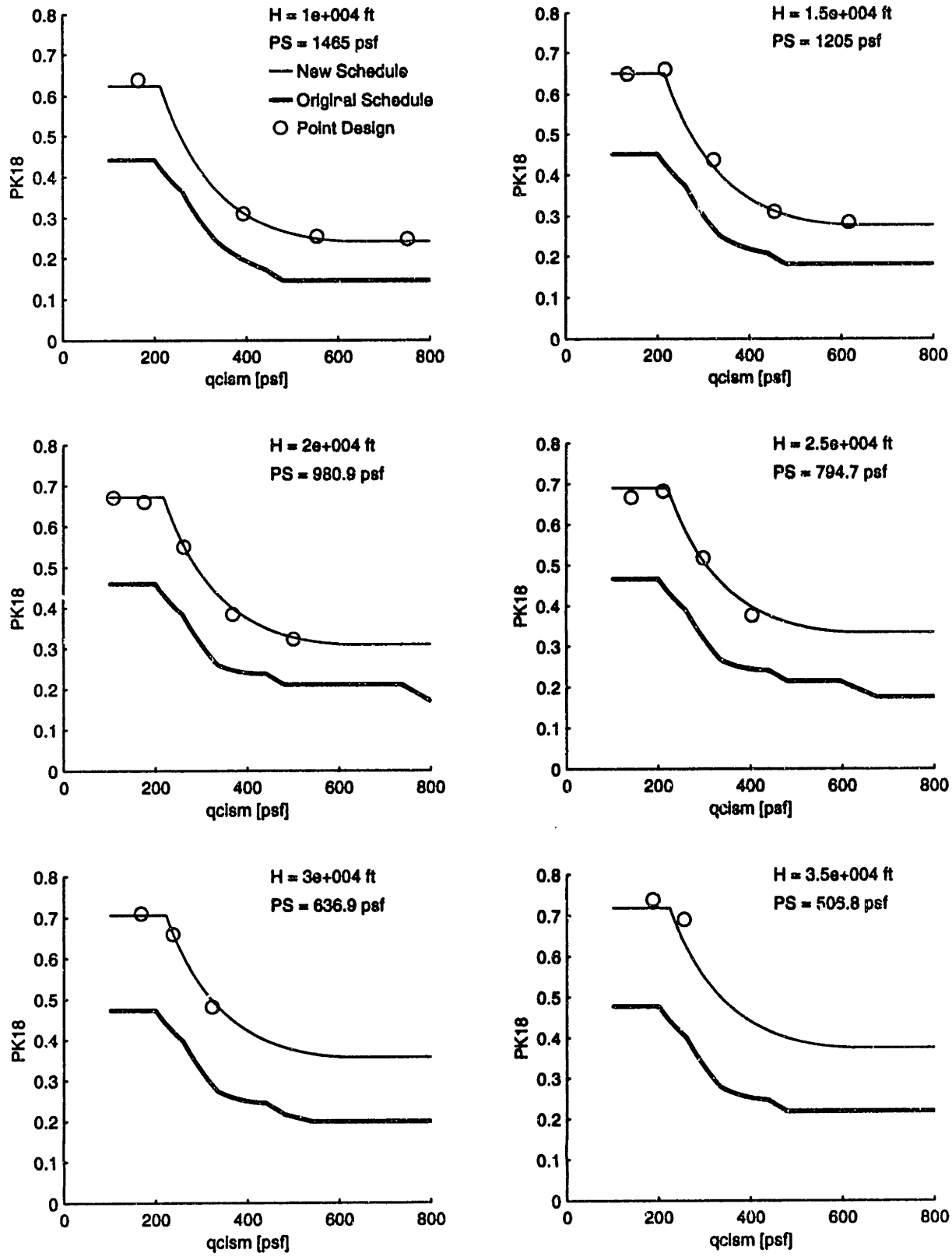

Fig. B-6 PK18: Pitch Rate Proportional Gain Scheduling

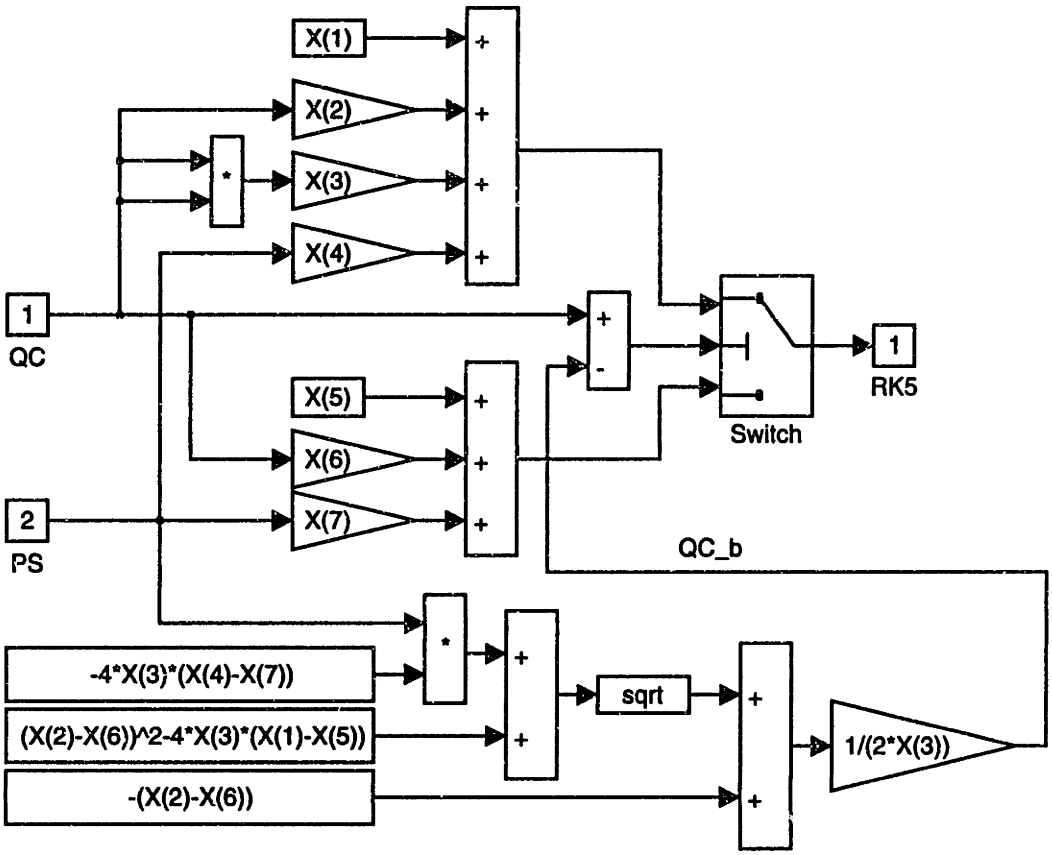

X(1) = 3.0307
X(2) = -0.0024
X(3) = 4.1169e-006
X(4) = -5.4312e-004
X(5) = 6.5021
X(6) = -0.0163
X(7) = 7.9425e-004

$$RK5 = \begin{cases} X_1 + X_2 * QC + X_3 * QC^2 + X_4 * PS & QC \geq QC_b \\ X_5 + X_6 * QC + X_7 * \mathrm{PS} & QC < QC_b \end{cases}$$

$$QC_b = \frac{-(X_2 - X_6) + \sqrt{(X_2 - X_6)^2 - 4X_3(X_1 - X_5) - 4X_3(X_4 - X_7)PS}}{2X_3}$$

Fig. B-7 RK5: Lateral stick gain, new gain schedule

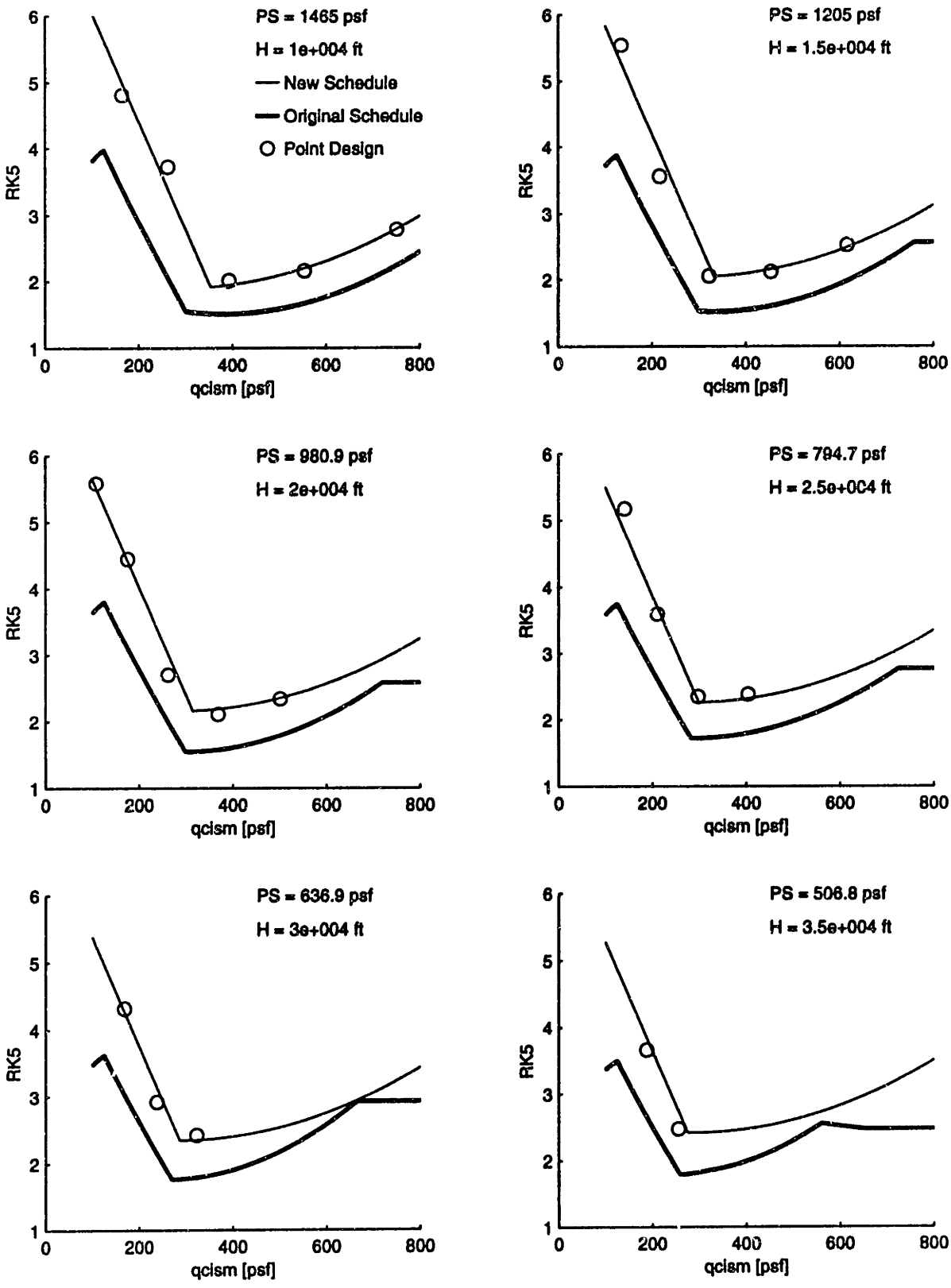

Fig. B-8 RK5: Lateral Stick Gain Schedule

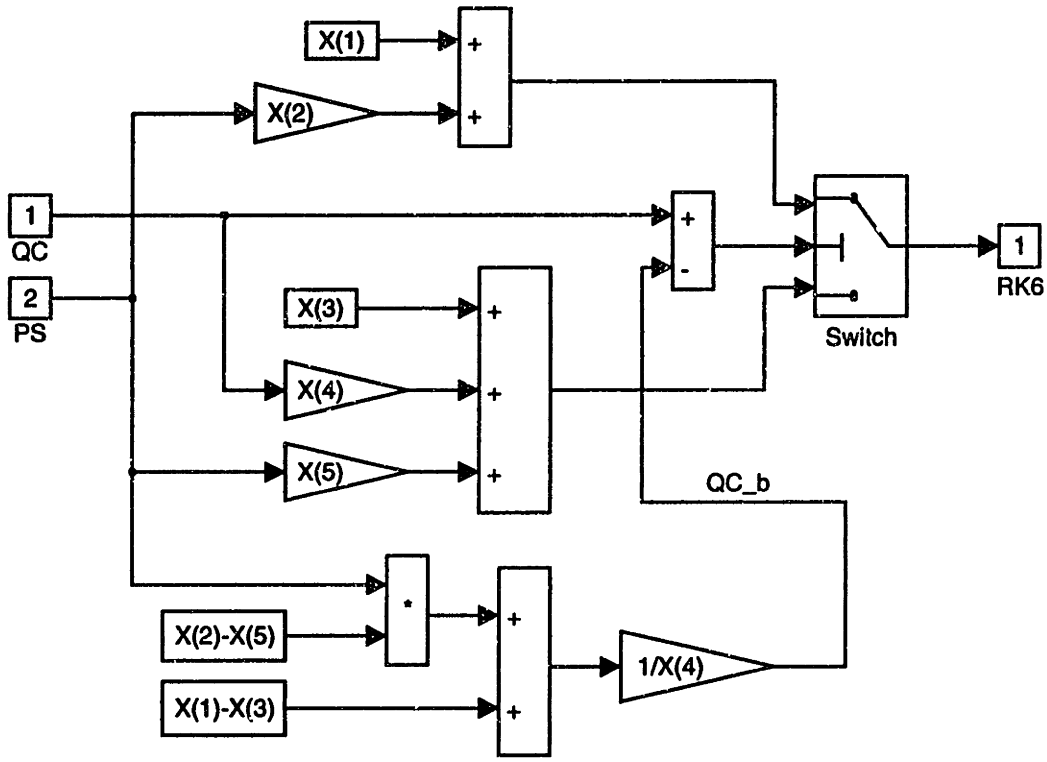

X(1) = 0.0992

X(2) = -3.8879e-005

X(3) = 0.5657

X(4) = -0.0019

X(5) = 5.8588e-005

$$RK6 = \begin{cases} X_1 + X_2 * PS & QC \geq QC_b \\ X_3 + X_4 * QC + X_5 * \mathrm{PS} & QC < QC_b \end{cases}$$

$$QC_b = \frac{(X_1 - X_3) + (X_2 - X_5) PS}{X_4}$$

Fig. B-9 RK6: Roll rate feedback gain, new gain scheduling

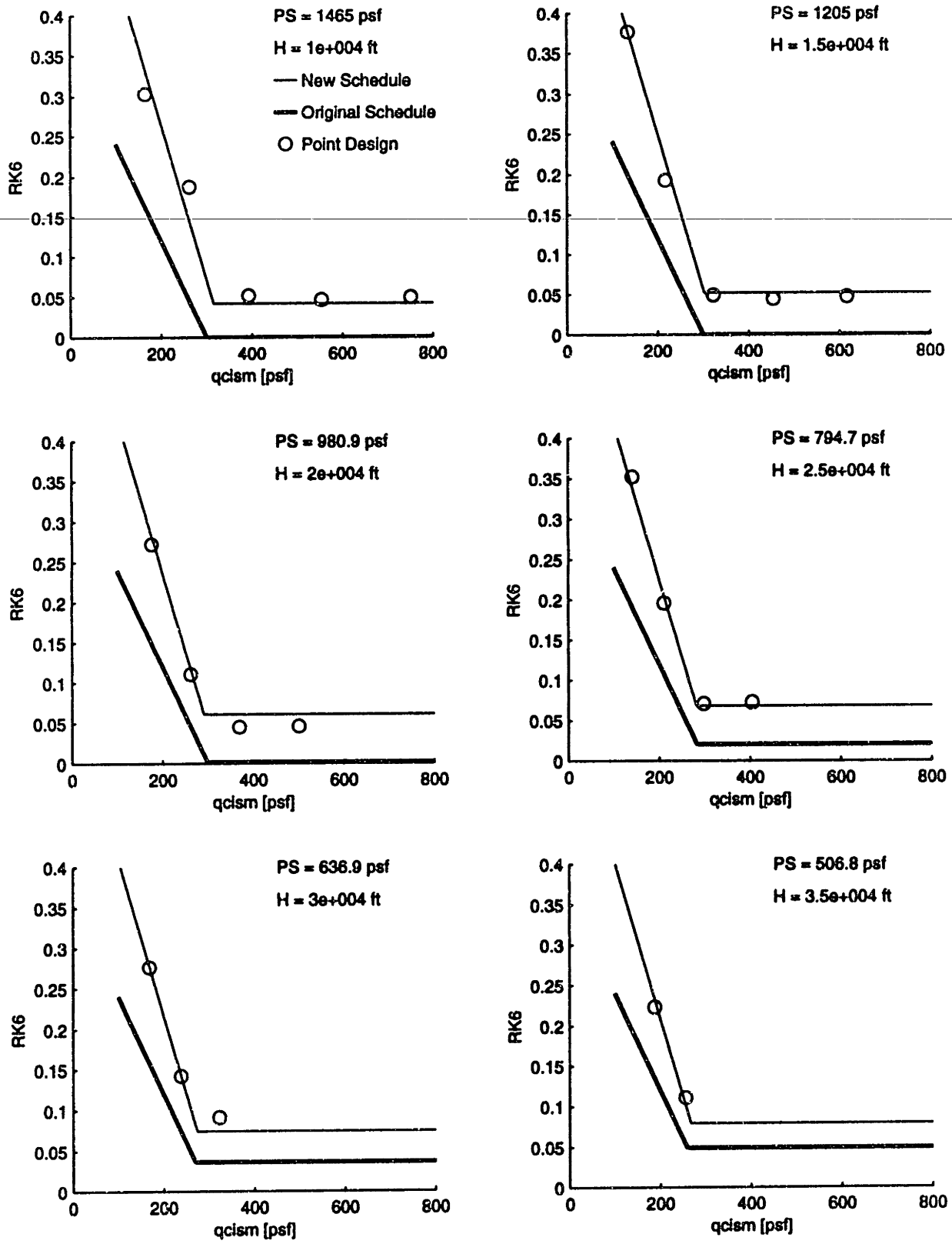

Fig. B-10 RK6: Roll rate feedback gain schedule

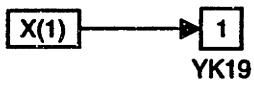

X(1) = 0.6737

$$YK19 = X_1$$

Fig. B-11 YK19: Pedal Increment gain, new gain scheduling

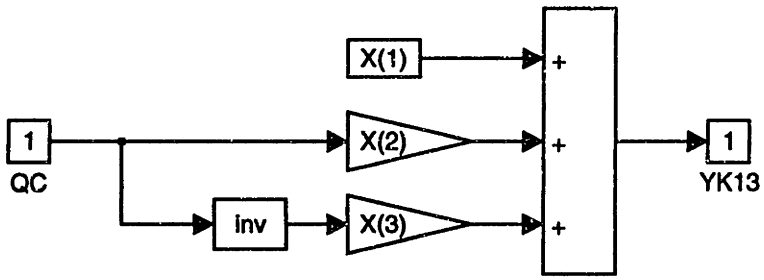

X(1) = 27.0741

X(2) = -0.0109

X(3) = 2.0621e+003

$$YK13 = X_1 + X_2 * QC + \frac{X_3}{QC}$$

Fig. B-12 YK13: Lateral acceleration gain, new gain scheduling

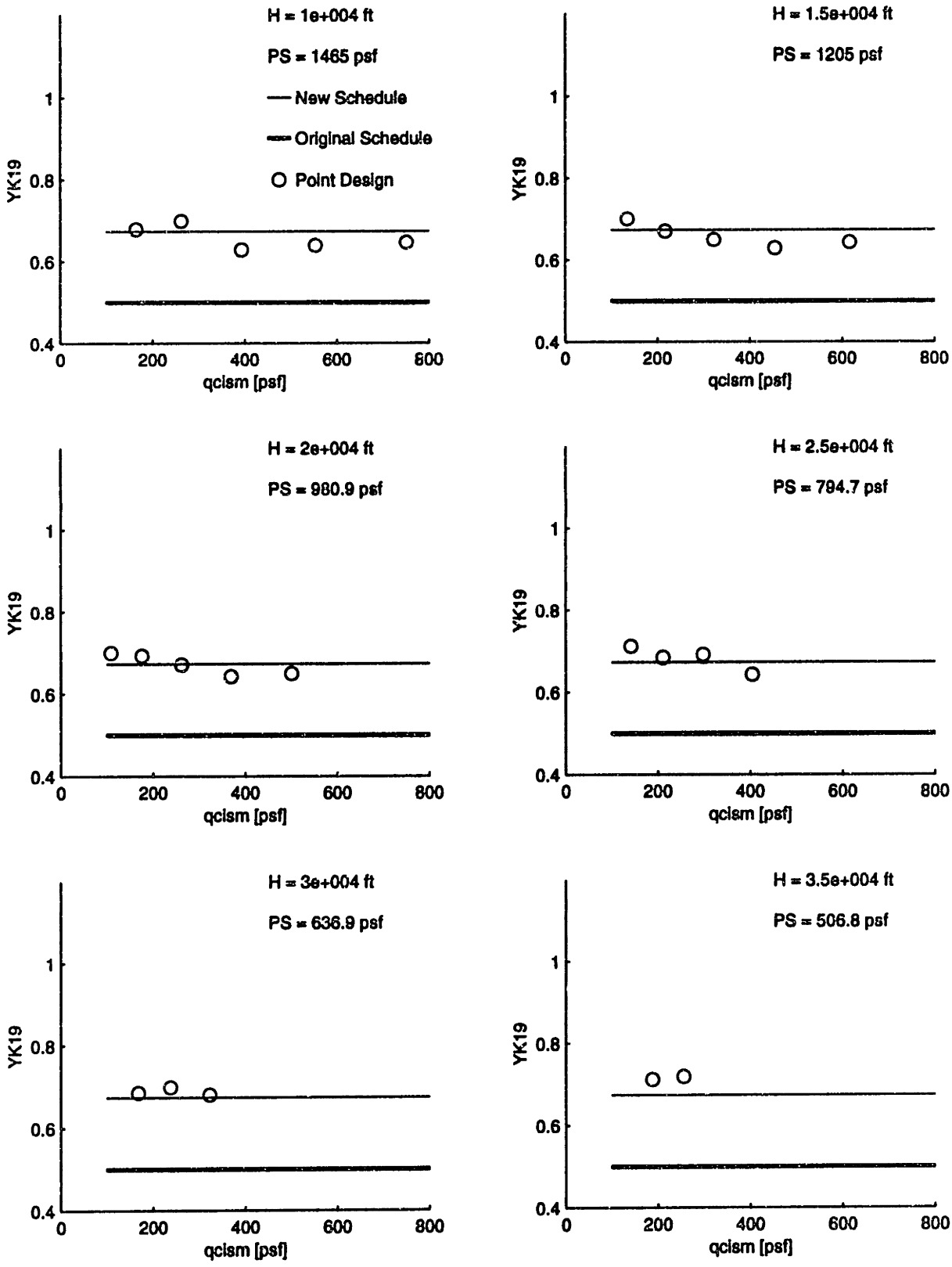

Fig. B-13 YK19: Pedal Increment gain schedule

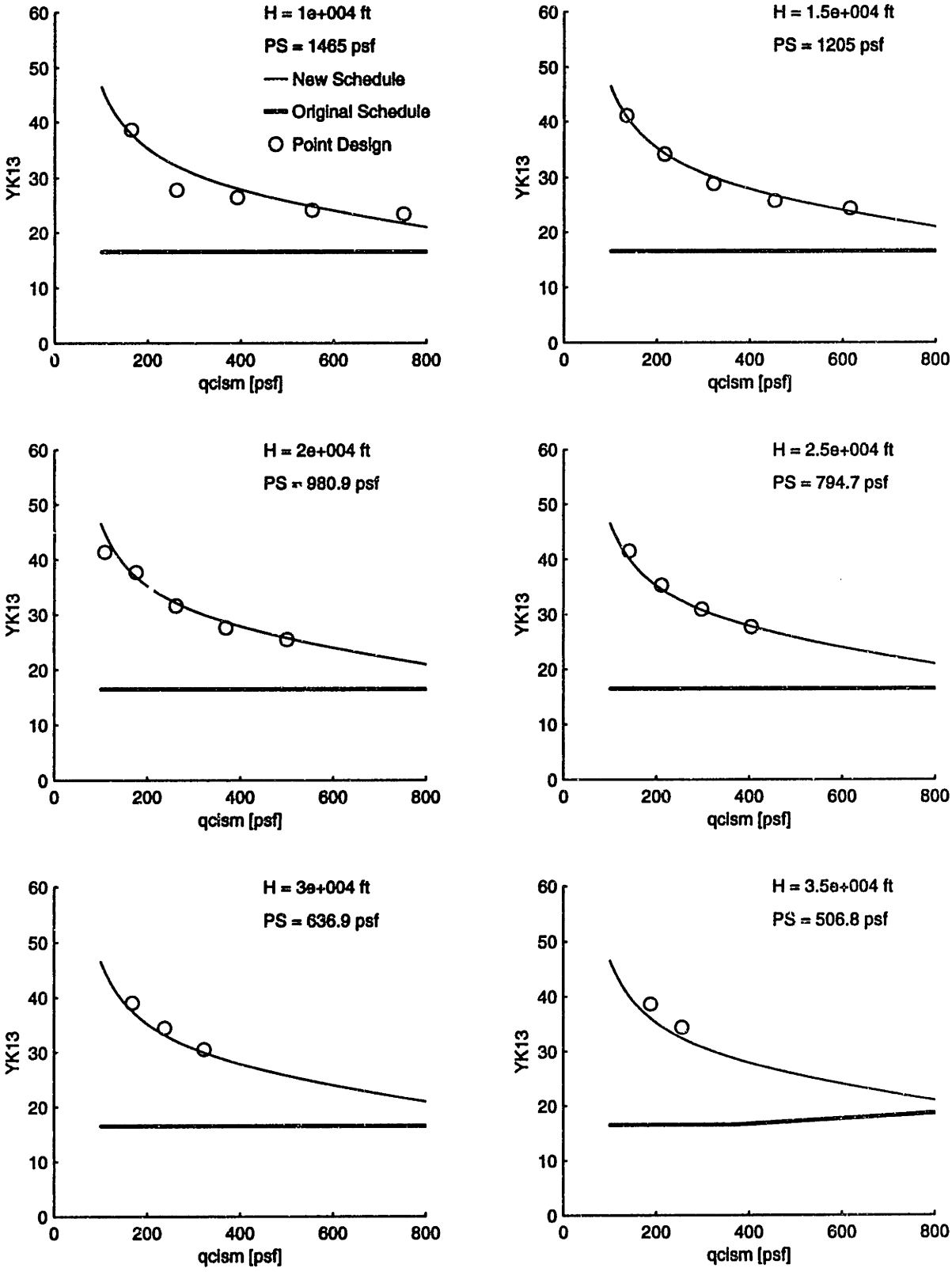

Fig. B-14 YK13: Lateral acceleration gain schedule

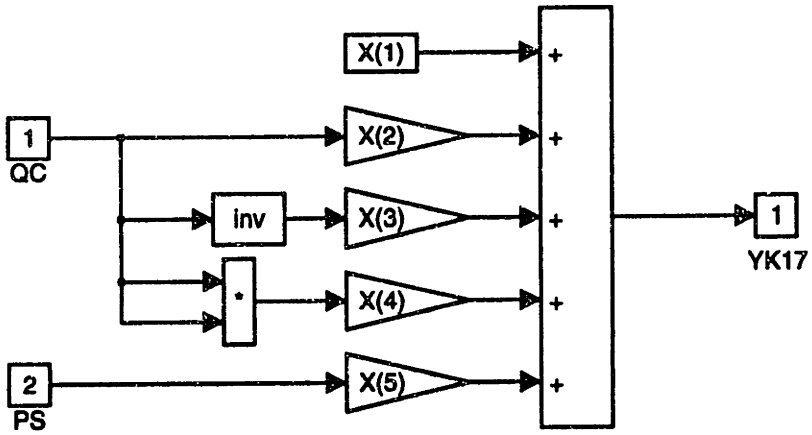

X(1) = 0.7731
X(2) = -2.4934e-004
X(3) = 66.9597
X(4) = 1.7730e-006
X(5) = -2.0759e-005

$$YK17 = X_1 + X_2 * QC + \frac{X_3}{QC} + X_4 * QC^2 + X_5 * PS$$

Fig. B-15 YK17: Yaw rate feedback gain, new gain schedule

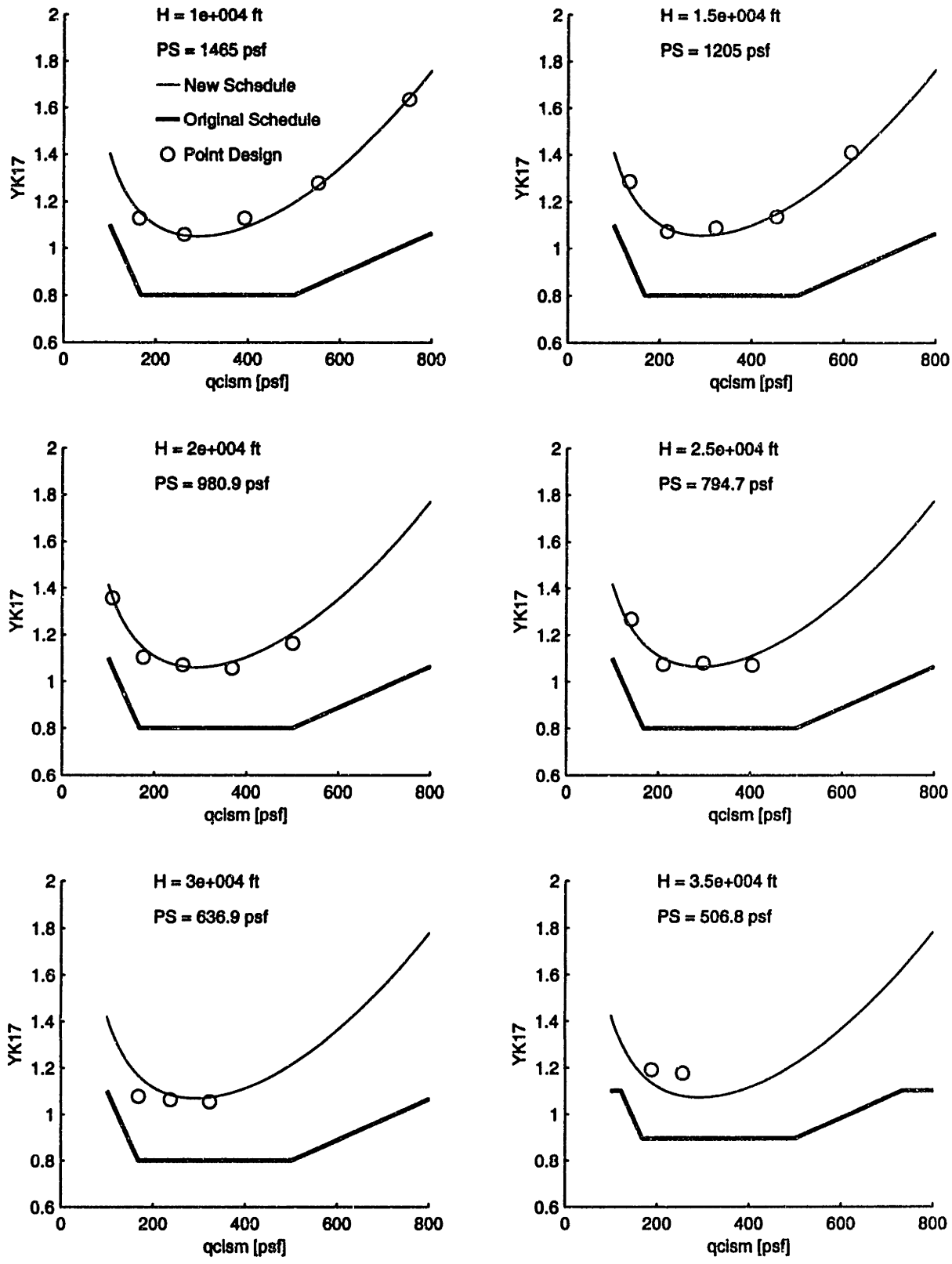

Fig. B-16 YK17: Yaw rate feedback gain schedule

Appendix C

F/A-18 Simulations: Pilots' Comments and CHR

This appendix contains the pilots' comments and Cooper Harper ratings of the simulations performed on the NASA Dryden fixed base flight simulator. There are six tables, one for each pilot.

N.	Maneuver	Aircraft	CH	Comments
1	Level Flight	F/A-18	--	The longitudinal axis looks OK, I have problems with the lateral axis. I expect this to be an F/A-18.
2	Level Flight	F/A-18 HARV	--	The longitudinal axis is not as good as before (1), The lateral axis is still the same.
3	Level Flight	F/A-18 HARV New	--	This is better than the last one (2). I feel that it is much more controllable.
4	Pitch Single Pulse	F/A-18	--	Very nice, a little bit of overshoot but not as much as in the previous one (5).
5	Pitch Single Pulse	F/A-18 HARV	--	This is not very good. There is a large overshoot and a tendency to lag behind. This is the HARV.
6	Pitch Single Pulse	F/A-18 HARV New	--	This is OK, difficult to see any difference from the previous one (4). It is almost better than before (4). This is an F/A-18.
7	Pitch Multiple Pulses	F/A-18	--	Good longitudinal control, I like this response. It is probably an F/A-18.
8	Pitch Multiple Pulses	F/A-18 HARV	--	I don't like this one. There is a high overshoot in the longitudinal axis and it is difficult to stop the oscillations. The most trouble to fly, it must be the HARV.
9	Pitch Multiple Pulses	F/A-18 HARV New	--	Same as the previous one (7). This is another F/A-18. Good longitudinal control.
10	Multiple Acquisitions	F/A-18	--	Longitudinal axis is OK. I have problem in controlling the lateral axis. The maneuver is dominated by lateral oscillations and so it is hard for me to say what is better. Probably an F/A-18, but I'm not sure.
11	Multiple Acquisitions	F/A-18 HARV	--	The previous aircraft (10) was better. The task is too large for me to say. May be this is the HARV, but I'm not sure.
12	Multiple Acquisitions	F/A-18 HARV New	--	Longitudinal is OK. Same overshoot as the first aircraft (10). Basically I like this. This is probably an F/A-18.

Tab. C-1 Pilot A: Cooper Harper rating and comments

N.	Maneuver	Aircraft	CH	Comments
1	Level Flight	F/A-18	2	It is OK, I can fly it easily.
2	Level Flight	F/A-18 HARV	3	This is a little bit harder.
3	Level Flight	F/A-18 HARV New	2	Similar to the first I flew (1). It is OK.
4	Pitch Single Pulse	F/A-18	2	This is very easy to fly.
5	Pitch Single Pulse	F/A-18 HARV	3	I have some difficulties in stopping the oscillations. Oscillations last longer.
6	Pitch Single Pulse	F/A-18 HARV New	2	This looks like the first one (4). Longitudinally is OK, better than before (5).
7	Pitch Multiple Pulses	F/A-18	3	It is fine. The task requires a lot of workload.
8	Pitch Multiple Pulses	F/A-18 HARV	4	Even more workload than before. Probably this is the HARV.
9	Pitch Multiple Pulses	F/A-18 HARV New	3	It looks normal, may be a little bit harder, in general is similar to (7). This is an F/A-18.
10	Multiple Acquisitions	F/A-18	3	It looks easier again. This is very similar to the first one (12).
11	Multiple Acquisitions	F/A-18 HARV	4	A little harder than before. The lateral has problems and there is an annoying delay in the pitch channel. The coupling between pitch and roll is bad.
12	Multiple Acquisitions	F/A-18 HARV New	3	It looks OK. This is probably a standard F/A-18. The task is difficult.
13	Refueling Task	F/A-18	7	This is very hard to fly. The throttle is not realistic, it is too sensitive. A little increase takes you under the tanker. Real refueling is not as difficult.
14	Refueling Task	F/A-18 HARV	6	Still very hard. High workload but the task is feasible in rough parameters.
15	Refueling Task	F/A-18 HARV New	5	Better than before (14) but still very hard to stay on the basket.
16	Gross Task	F/A-18	2	The task is quite simple. The aircraft is easy to fly. This can be an F/A-18.
17	Gross Task	F/A-18 HARV	3	I can perform the task also with this airplane even if it is more sluggish. There is a delay in the longitudinal response.
18	Gross Task	F/A-18 HARV New	2	This is like the first one (16). It is OK.

Tab. C-2 Pilot B: Cooper Harper rating and comments

N.	Maneuver	Aircraft	CH	Comments
1	Level Flight	F/A-18	3	Good response. The aircraft is active and fast to respond to pilot inputs. I think this is an F/A-18.
2	Level Flight	F/A-18 HARV	5	This is definitely more sluggish than before (1). There is a PIO tendency in the pitch channel. The response is slower than before. Probably this is the HARV.
3	Level Flight	F/A-18 HARV New	3	This is the most active. The response is fast, I like this. This can be an F/A-18.
4	Pitch Single Pulse	F/A-18	3	Only a mild compensation is necessary. In general is good. This is an F/A-18.
5	Pitch Single Pulse	F/A-18 HARV	4/5	The aircraft is much more sluggish in the longitudinal channel. I feel that I fall behind and then there is a tendency to overshoot. I think this is the HARV.
6	Pitch Single Pulse	F/A-18 HARV New	3	The response is very similar to the first one (4).
7	Pitch Multiple Pulses	F/A-18	3	This is also OK. It is very similar to the one before (9). I think this is an F/A-18.
8	Pitch Multiple Pulses	F/A-18 HARV	4	Not very different, may be a little more difficul with higher pilot workload.
9	Pitch Multiple Pulses	F/A-18 HARV New	3	This is a normal F/A-18. I like the response, I have nothing to say.
10	Multiple Acquisitions	F/A-18	4	A little tendency to overshoot. Minor but annoying deficiency. This can be an F/A-18.
11	Multiple Acquisitions	F/A-18 HARV	4	Similar to the one before (10). Now the I was closer to the target, this can confuse my judgment.
12	Multiple Acquisitions	F/A-18 HARV New	4	Same comments as before.
13	Refueling Task	F/A-18	5/6	I have serious problems with the throttle. Throttle is too sensitive, in reality it is not like this. The pitch response is OK but I have problems in the lateral axis. This is more sensitive than before (15).
14	Refueling Task	F/A-18 HARV	5/6	It looks better than before (13). It looks more controllable, may be I'm learning. The lateral response has problems.
15	Refueling Task	F/A-18 HARV New	4	This is very simple. The damping is very good. I was able to keep the relative distance within acceptable limits. This one is noticeably easier than (13) and (14). Less tendency to get in the lateral axis.
16	Gross Task	F/A-18	3	Same precision as the first case(18). May be there is more lateral activity. Increased lateral activity.
17	Gross Task	F/A-18 HARV	3	This is definitely the HARV. Heavier stick forces Once the target is acquired it is OK. I still have good precision.
18	Gross Task	F/A-18 HARV New	3	Minimal pilot compensation. There is no tendency to PIO. I can control the flight path marker smoothly and position it precisely.

Tab. C-3 Pilot C: Cooper Harper rating and comments

N.	Maneuver	Aircraft	CH	Comments
1	Level Flight	F/A-18	1/2	The response is OK. The task is not well defined, it is difficult for me to give a CH rating on this task.
2	Level Flight	F/A-18 HARV	2/3	I feel that the aircraft is heavier. Same comment as before about the CH rating.
3	Level Flight	F/A-18 HARV New	1/2	This is as good as the standard F/A-18.
4	Pitch Single Pulse	F/A-18	6	I can stay 80% of the time within the two landing gears of the target aircraft. The response is good. The task is not well defined.
5	Pitch Single Pulse	F/A-18 HARV	8	I can feel a slower frequency response in pitch. It is harder than before.
6	Pitch Single Pulse	F/A-18 HARV New	6	I can stay most of the time within the two landing gears of the target aircraft. This is very similar to the standard F/A-18.
7	Pitch Multiple Pulses	F/A-18	5	It is hard to say. The task is very long and it is not clear what is my objective.
8	Pitch Multiple Pulses	F/A-18 HARV	4	In this case I was further away from the target aircraft, this make the task much easier.
9	Pitch Multiple Pulses	F/A-18 HARV New	3	I prefer this one, it is better than the other two, may be I'm learning.
10	Multiple Acquisitions	F/A-18		
11	Multiple Acquisitions	F/A-18 HARV		
12	Multiple Acquisitions	F/A-18 HARV New		
13	Refueling Task	F/A-18		
14	Refueling Task	F/A-18 HARV		
15	Refueling Task	F/A-18 HARV New		
16	Gross Task	F/A-18		
17	Gross Task	F/A-18 HARV		
18	Gross Task	F/A-18 HARV New		

Tab. C-4 Pilot D: Cooper Harper rating and comments

N.	Maneuver	Aircraft	CH	Comments
1	Level Flight	F/A-18	--	None
2	Level Flight	F/A-18 HARV	--	None
3	Level Flight	F/A-18 HARV New	--	None
4	Pitch Single Pulse	F/A-18	2/3	Not bad. The aircraft is responsive.
5	Pitch Single Pulse	F/A-18 HARV	4/5	More difficult than before. Tendency to oscillate. Difficult to stop.
6	Pitch Single Pulse	F/A-18 HARV New	2/3	This is very similar to the first one (4). This is a standard F/A-18.
7	Pitch Multiple Pulses	F/A-18	3	Tendency to fall behind. I was able to maintain the same distance during the maneuver (tape).
8	Pitch Multiple Pulses	F/A-18 HARV	3	I feel that this is more controllable than before (tape).
9	Pitch Multiple Pulses	F/A-18 HARV New	5/6	I was closer to the target than before and thus the task was more difficult. It was hard for me to do the task.
10	Multiple Acquisitions	F/A-18	3	Better response than before (12).
11	Multiple Acquisitions	F/A-18 HARV	5	This is much harder to fly. The coupling between lateral and longitudinal is bad.
12	Multiple Acquisitions	F/A-18 HARV New	3/4	The roll coupling is dominant in this task. The longitudinal response is not bad.
13	Refueling Task	F/A-18	3	It is hard to control pitch and roll. I can stay on the basket most of the time.
14	Refueling Task	F/A-18 HARV	3	I don't see much of a difference between this and the previous one (13). The task is feasible.
15	Refueling Task	F/A-18 HARV New	3	The pitch response is good. This is better than the other two. But in general I was able to perform the task with all the configurations.
16	Gross Task	F/A-18	3	I'm able to acquire the target and stay stable on it (tape).
17	Gross Task	F/A-18 HARV	4/5	Tendency to fall behind. A little more difficult but still feasible (tape).
18	Gross Task	F/A-18 HARV New	3	Good response. Easy to stay on target. I like this (tape).

Tab. C-5 Pilot E: Cooper Harper rating and comments

N.	Maneuver	Aircraft	CH	Comments
1	Level Flight	F/A-18	--	Response is OK.
2	Level Flight	F/A-18 HARV	--	It does not seem a lot different from before (1). It is hard to say.
3	Level Flight	F/A-18 HARV New	--	Same overshoot as in the first simulation (1).
4	Pitch Single Pulse	F/A-18	3/4	This was smoother than before (6). Less bubble. The task is a little hard. It is satisfactory.
5	Pitch Single Pulse	F/A-18 HARV	2/3	This is good. May be I'm getting used to the task.
6	Pitch Single Pulse	F/A-18 HARV New	5/6	There was more overshoot. It is not as good as number (4). For me it is not obvious from this task to see any difference between the three configurations.
7	Pitch Multiple Pulses	F/A-18	--	The lateral axis is the most difficult to control. Pitch is smooth and very well behaved. Easy to control in pitch.
8	Pitch Multiple Pulses	F/A-18 HARV	--	I cannot see any change in the pitch channel respect before (7). It is hard to say. The lateral axis is bad.
9	Pitch Multiple Pulses	F/A-18 HARV New	--	No major difference. May be this one has a little bit more bubbling. May be here the gains are higher.
10	Multiple Acquisitions	F/A-18	--	It is hard to distinguish between the three. The response in this case is smooth, in general I like it.
11	Multiple Acquisitions	F/A-18 HARV	--	More stick activity. But for me the overall error is the same as before.
12	Multiple Acquisitions	F/A-18 HARV New	--	I cannot say, the response is good.
13	Refueling Task	F/A-18	--	This is a good task. Godd pitch response.
14	Refueling Task	F/A-18 HARV	--	The aircraft is heavier. Sluggish response in pitch.
15	Refueling Task	F/A-18 HARV New	--	Same response as (13).
16	Gross Task	F/A-18	3	This is a very good task. It is hard to see the difference from (15). This task is representative of the level of concentration that you need during refueling.
17	Gross Task	F/A-18 HARV	4	Low frequency PIO in pitch. This has a slower response in pitch. Tendency to low frequency over control in pitch. The pitch channel is definitely sluggish, I'm lagging behind. Among the three I can easily pick up the low frequency aircrfat, the HARV. With the HARV small inputs has apparently no response, for this reason the pilot tends to use larger inputs and starts PIOing. In the other tasks, pitch pulses, it was not obvious to see the difference, now I can.
18	Gross Task	F/A-18 HARV New	3	The lateral axis is hard. It is a demanding task that well represent the refueling. The task is dominated by the for and aft movement. No high frequency bubble. I like this.

Tab. C-6 Pilot F: Cooper Harper rating and comments